DOCTORATE SCHOOL IN

INFORMATION AND COMMUNICATION TECHNOLOGIES

XXVI Cycle

UNIVERSITY OF MODENA AND REGGIO EMILIA

DEPARTMENT OF ENGINEERING “Enzo Ferrari”

Ph.D. DISSERTATION

Models and Algorithms for Powerline Communications

Candidate: Fabio Gianaroli

Advisor: Prof. Giorgio M. Vitetta

Co-Advisor: Prof. Fabrizio Pancaldi

The Coordinator of the Doctorate: Prof. Giorgio M. Vitetta

The Director of the School: Prof. Giorgio M. Vitetta

SCUOLA DI DOTTORATO IN

INFORMATION AND COMMUNICATION TECHNOLOGIES

XXVI Cycle

UNIVERSITÀ DEGLI STUDI DI MODENA E REGGIO EMILIA

DIPARTIMENTO DI INGEGNERIA “Enzo Ferrari”

TESI PER IL CONSEGUIMENTO DEL TITOLO DI DOTTORE DI RICERCA

Modelli e algoritmi per le comunicazioni powerline

Candidato: Fabio Gianaroli

Relatore: Prof. Giorgio M. Vitetta

Correlatore: Prof. Fabrizio Pancaldi

Il Coordinatore del Dottorato:: Prof. Giorgio M. Vitetta

Il Direttore: Prof. Giorgio M. Vitetta

Abstract

In the last few years powerline technology has become a commercially attractive alternative to its wireless counterpart for in-home communications requiring high data rates. This success has fostered research on wideband communication techniques for low voltage powerlines and on the properties of real world powerline channels, since there are substantially different from wireless channels in terms of both system functions and noise characteristics.

This thesis focuses on powerline data communications and, in particular, on: a) the analysis and modeling of the behavior of indoor powerline channels; b) the development of algorithms exploiting the knowledge of channel state to improve the reliability of powerline data communications in indoor scenarios.

In the first part of this thesis the behavior of indoor powerline channels is analyzed under the assumption that they can be modeled as time invariant systems. A novel approach to statistical channel modeling is derived and its application to low-voltage indoor power networks is analyzed in the band 1–30MHz; in addition, the impact of the characterization power loads on the performance of the proposed statistical model is analyzed. Then, different classes of statistical models for the representation of powerline noise are illustrated and their impact on the error performance of an OFDM-based communication system is assessed via computer simulations.

In the second part of this thesis the time varying behavior of powerline channels is investigated. A channel sounding tool based on a FPGA and explicitly designed to analyze the time varying channel response of powerline channels is described. A linear periodically time varying model for indoor PLC channels is developed and its technical relevance is assessed exploiting a set of measurements acquired by means of the developed channel sounder.

Finally, in the last part of the thesis innovative communication algorithms exploiting the knowledge of a time-varying model for powerline channels are devised. More specifically, novel algorithms for data-aided channel estimation, zero forcing equalization and adaptive transmis-

sion are illustrated. The performance of these techniques are assessed and are compared with that offered by other solutions available in the technical literature and not accounting for the time-varying behavior of powerline channels.

Contents

List of Acronyms

ACF	Autocorrelation Function
ACR	Alias Component Representation
A/D	Analog-to-Digital
ADC	Analog to Digital Conversion
AR	Autoregressive
ARIMA	Autoregressive Integrated Moving Average
ARMA	Autoregressive Moving Average
AWGMN	Additive White Gaussian Mixture Noise
AWGN	Additive White Gaussian Noise
BER	Bit Error Rate
BPSK	Binary Phase Shift Keying
CFR	Channel Frequency Response
CIR	Channel Impulse Response
CP	Cyclic Prefix
CRLB	Cramer Rao Lower Bound
CSI	Channel State Information
CTF	Channel Transfer Function

D/A	Digital-to-Analog
DAC	Digital to Analog Conversion
DARMA	Deseasonalized Autoregressive Moving Average
DC-FIFO	Dual Channel First-In First-Out
DFT	Discrete Fourier Transform
DSO	Digital Storage Oscilloscope
EM	Expectation Maximization
EMC	Electromagnetic Compatibility
FD-AWGN	Frequency Domain Additive White Gaussian Noise
FDE	Frequency Domain Estimator
FDNM	Frequency Domain Noise Model
FFT	Fast Fourier Transform
FIR	Finite Impulse Response
FPGA	Field Programmable Gate Array
GM	Gaussian Mixture
GUI	Graphical User Interface
HDR	High Data Rate
ICI	Inter-Carrier Interference
IDFT	Inverse Discrete Fourier Transform
IFFT	Inverse Fast Fourier Transform
iid	independent and identically distributed
IRLS	Iterative Reweighted Least Squares
LDR	Low Data Rate

LNA	Low Noise Amplifier
LPF	Low-Pass Filter
LPTV	Linear Periodically Time-Varying
LS	Least Squares
LSE	Least Square Estimator
LTI	Linear Time Invariant
MA	Moving Average
ML	Maximum Likelihood
MLE	Maximum Likelihood Estimator
MMSE	Minimum Mean Squared Error
MSE	Mean Square Error
NMSE	Normalised Mean Square Error
NSE	Normalised Square Error
NSD	Normalised Standard Deviation
OFDM	Orthogonal Frequency Division Multiplexing
PAFE	Power Analog Front-End
PAPR	Peak-to-Average Power Ratio
PARMA	Periodic Autoregressive Moving Average
PDF	Probability Density Function
PDP	Power Delay Profile
PIO	Parallel Input Output
PLC	Powerline Communications
PSD	Power Spectral Density

PTV	Periodically Time Varying
QAM	Quadrature Amplitude Modulation
rv	random variable
SM	Switching Model
SNR	Signal-to-Noise Ratio
SNR_b	Signal-to-Noise Ratio per bit
STD	Standard Deviation
TDL	Tapped Delay Line
TFS	Time-Frequency Slot
TVPSD	Time-Variant Power Spectral Density
TVTF	Time-Variant Transfer Function
ZB-ZFE	Zadeh-Based Zero Forcing Equalizer
ZF	Zero Forcing
ZFE	Zero Forcing Equalizer
ZR	Zadeh's Representation

Introduction

In the last few years Powerline Communications (PLC) techniques have attracted a lot of attention since they provide commercially appealing solutions data communication problems in a number of scenarios (indoor multimedia communications, broadband Internet access, smart grid applications and home automation). This is mainly due to the fact PLC systems exploit existing powerlines as a communication medium for data transmissions; PLC data signals are generated as high frequency and small amplitude waveform overlapping with power signals at low frequency. Because of the availability of power grids all over the world, PLC technology requires deployment costs comparable to that of wireless communication systems.

Powerline history and technology scenario

The first PLC applications put in place by power utilities involving voice and data communications over high voltage lines date back to 1920 [1]. In those years telephone coverage was very limited, so that PLC systems represented the only way to exchange information for the management of power grids.

An interesting advantage characterizing PLC technologies is represented by the capability of implementing a system to switch on/off appliances responsible for high energy consumption in a cheap way [2]. The first application of PLCs for load managment was implemented in the 1930s [3] to switch off heavy duty appliances in order to avoid peaks in power absorption. Recently, this technology is attracting renewed interest within smart grids to implement demand managment systems.

The systems mentioned above are characterized by low data rates and simple communication techniques; only in 1997 a communication company in the U.K. announced to have developed a PLC technology able to provide access to Internet with a data rate up to 1Mbit/s [2, 4]. Unfortunately, the project was closed early in 1999 for its high costs Electromagnetic

Compatibility (EMC) issues. Other European projects working in the same direction and proposed by Siemens and Ascom were prematurely closed too.

Since 2000, after that problems encountered in the development of Internet access applications based on PLC were solved, the attention of industry focused on in-home applications. This interest has stimulated the birth of several industry alliances, such HomePlug Powerline Alliance, Universal Powerline Association, High Definition Powerline Communication Alliance, etc... Many products have progressively appeared on the market with data rate form 14Mb/s to more than 200Mb/s.

Existing PLC systems can be divided in the following 3 classes.

Ultra narrow band PLC

The ultra narrow band technology operates in the range of ultralow frequencies in the band$[0.3 - 3]$ kHz and in the super low frequencies in the band $[30 - 300]$ Hz[2]. This technology can reach very low data rates ($\sim$ 100bps); an historical example of this technology is represented by the load control based on ripple carrier signaling (this used simple amplitude shift keying modulations in the frequency band $[125 - 2000]$ Hz). This technology is characterized by a very low bit rate, but the transmitted signals can cover distances up to some hundreds of kilometers.

Narrow band PLC

The narrow band technology operates in the very low frequencis, low frequencies and medium frequencies bands in the range $[3 - 500]$ KHz. These systems can be splitted in Low Data Rate (LDR) systems and High Data Rate (HDR) systems. LDR systems exploit single carrier modulations and can reach data rates of some kilobits per second, while HDR systems adopt multicarrier modulations with a maximum data rate around 500Kb/s.

Broad band PLC

The broadband technology operates in the high frequencies and very high frequencies bands in the frequency range $[1.8 - 250]$ MHz and is characterized by data rates ranging from several megabits per second to several hundreds megabits per second.

Contribution and organization

As shown in the previous section, if ultra narrow band systems are neglected, the PLC world can be divided in two families of systems: narrow band systems and broadband systems. Both systems have advantages and disavantages. On the one hand, narrowband systems suffer from a low bit rate, but are characterized by a very large distance of operation and require low cost electronic hardware. On the other hand, broadband systems can reach high data rates, but they are penalyzed by a limited coverage area and a high cost of electronic hardware.

An interesting opportunity in developing new indoor PLC systems is represented by merging the advantages provided by these two technologies. Indeed in the near future applications such as building automation and home appliances networking will be extremely pervasive. The communication technology required by those systems will have to be cheap and reliable. Today, broadband PLC systems require too a high cost too and their coverage area is not large enough, whereas narrow band PLC systems offer a bit rate which is too low for most applications. A possible key to overcome these problems is merging these two technologies to obtain systems characterized by a medium bit rate, an high coverage area and, at the same time, requiring low costs for their hardwares.

The only way to improve the performance of narrow band systems in terms of data rates without increasing their cost is the development of new signal processing algorithms able to exploit powerline channels in a more efficient way. In fact, it is well known that the hardware costs in modem implementation depend on the computational complexity of the algorithms exploited for data communications and on system bandwidth (together the central frequency of the channel). This thesis shows that, if accurate channel models of powerline channels are developed, novel and computationally efficient communications techniques can be devised to reach bit rates above 1Mb/s also and operating at low frequency with a limited bandwidth.

The thesis is divided in 3 part. In its first part the properties of indoor powerline channels are analyzed under the assumption that they can be modelled as time invariant systems. In its second part indoor powerline channels are revisited to develop models accounting for their periodic time variations. Finally, in its third part novel signal processing algorithms based on the proposed channel models and able to improve the performance of PLC systems at a reasonable complexity are illustrated. More specifically, this thesis consists of 9 chapters, whose contents can be summarised as follows. In **Chapter 1** a linear time invariant mathematical model for describing the transfer function of indoor powerline channels is illustrated and its application to low-voltage indoor power networks is analysed in the bandwidth $1 - 30$ MHz. In **Chapter**

2 the impact of load characterization on the statistical modeling of indoor powerline channels is investigated, in terms of average properties of the channel. **Chapter 3** proposes a novel statistical model for the representation of the periodic impulsive noise affecting indoor powerlines; this model is based on a set of experimental results acquired in a measurement campaign and on deseasonalized autoregressive moving average representation of a stochastic process. In **Chapter 4** the impact of statistical noise modelling on the simulated error performance of Orthogonal Frequency Division Multiplexing (OFDM) operating over indoor broadband powerline channels is investigated; in particular, different classes of statistical models suitable to represent powerline noise are illustrated and their impact on the error performance of a specific OFDM system is assessed via computer simulations. **Chapter 5** focuses on the design of a channel sounder based on an Field Programmable Gate Array (FPGA) platform for the characterization of the linear periodically time varying behavior of indoor powerline channels. In **Chapter 6** a powerline channel representation based on so-called Zadeh's series expansion is proposed; moreover, various methods for estimating the parameters of this representation are developed and compared in terms of performance and complexity. **Chapters 7** and **8** illustrate some applications of the devised channel models to the development of algorithms for channel estimation and equalization, and to bit loading techniques, respectively. Finally **Chapter 9** offers some conclusions about this Thesis.

Part I

Linear Time Invariant Modelling of Indoor Powerline Channels

Chapter 1

A Novel Statistical Model for the Transfer Function of Indoor Powerline Channels

In this chapter a acLTI mathematical model for the representation of the transfer function of indoor powerline channels is illustrated and its application to low-voltage indoor power networks is analysed in the bandwidth $1 - 30MHz$*. The proposed model is based on the bifilar model and on a generalization of the so called* N*-branch network topology. It is shown as the model can be exploited to devise an efficient statistical channel simulator predicting the mean impedance matrix and transfer function between an arbitrary couple of plugs in a class of indoor networks sharing multiple parameters (e.g., number of branches, minimum and maximum cable lengths, power loading conditions). Moreover, it is shown that Monte Carlo results generated by that simulator are in good agreement with a set of experimental data acquired in a measurement campaign.*

This chapter is organized as follows. In Section 1.1 a brief introduction at the problem of powerline channel modelling is reported. In Section 1.2 a bifilar model presented in technical litterature is analyzed, a deterministic model of a powerline channel and a statistical simulator are proposed. Section 1.3 presents the experimental set up used to characterize real powerline channels. In Section 1.4 simulation results are compared with experimental data to validate the developed simulator. Finally, Section 1.5 provides some conclusions.

1.1 State of the art

Recently, the interest in high speed data transmission over indoor powerline network has stimulated research in the area of broadband channel modeling for these communication scenarios [6, 7, 8, 9]. Indoor powerline channels are characterized by the multipath phenomenon, but, unlike wireless channels, do not lend themselves to a simple description in the time or in the frequency domains, since their behavior depend on a number of factors (e.g., the topology of the network and the number, arrangement and characteristics of power loads connected to it). For this reason a general channel model encompassing various propagation scenarios cannot be easily derived.

In the last few years various *deterministic* models for indoor powerline channels have been proposed in the technical literature [5, 10, 11, 12, 13, 14]. Most of the available models result from the application of electromagnetic field theory to the problem of wave propagation in a power grid and, consequently, are suitable to the description of specific network topologies [5, 10, 11, 12]. More specifically, a powerline characterization based on a set of network description matrices is illustrated in [10]; this allows to identify the multiple waves travelling along a given powerline and, consequently, to evaluate the multipath response of the given channel. A technique for deriving a channel transfer function from a set of impedance measurements is described in [11]. In [12] the multiconductor transmission line theory is exploited to refine the classic bifilar model of [5]. A conceptually different approach is adopted in [13, 14], where the use of a deterministic Tapped Delay Line (TDL), whose parameters are matched to specific experimental results, is proposed for channel modelling.

An alternative to deterministic models is offered by *statistical* models, which aim at providing a stochastic description of a family of indoor powerline channels. However few contributions about this topic are available in the technical literature at present [15, 16, 17]. In particular, TDL based models have been illustrated in [15, 16], whereas a statistical solution to channel magnitude generation of indoor powerline channels has been described in [17]. The main drawback of the available statistical models is represented by the fact that they usually do not rely on the underlying physical structure of powerline networks, and, consequently, the information they provide are limited to the description of the channel transfer function; in other words, other relevant channel parameters, like, for instance, the input and the output impedance of the channel itself, cannot be extracted from such models.

1.2 Distribuited parameters model

1.2.1 Transmission line parameters

To apply a distribuited paramters model to indoor powerline networks, the powerline cables must be described in terms of transmission lines. In Europe the powerline cables consist of three isolated conductors (phase, neutral and ground) within a *dielectric conduits*; a model for a similar scenario has been adopted in [5], where analytical expressions for the distributed parameters have been derived under the assumption of *metallic conduits* (that reppresent the typical case for indoor powerline cables in Singapore). A change in the nature of the conduit does not influence the resistance, the conductance and the inductance parameters of the powerline. For this reason, following [5], the resistance per unit length R, the inductance per unit length L and the conductance per length unit G can be expressed as

$$R = \frac{1}{\pi a \delta \sigma_c} \left[\frac{\Omega}{m}\right], \tag{1.2.1}$$

$$L = \frac{\mu_c}{\pi}\left[\frac{1}{4} + \ln\left(\frac{D-a}{a}\right)\right]\left[\frac{H}{m}\right] \tag{1.2.2}$$

and

$$G = \frac{\sigma C}{\varepsilon}\left[\frac{\Omega^{-1}}{m}\right] \tag{1.2.3}$$

respectively, where a is the radius of the conductors, δ is the *skin depth* (see [5, p. 1059]), σ_c is the wire conductivity, μ_c is the magnetic permeability of the dielectric, D is the distance between the wires, σ is the electrical conductivity of the insulating coating and C is the capacity per unit length. Note that (1.2.2) represents L as the sum of two contributions, one coming from the self-inductance of single wires, the other one associated with the mutual inductance between them. Finally, the expression of the capacity per unit length is given by

$$C = \frac{3\pi\varepsilon}{2\ln\left[\frac{D}{2a} + \sqrt{\left(\frac{D}{2a}\right)^2 - 1}\right]}\left[\frac{F}{m}\right], \tag{1.2.4}$$

where ε is the dielectric permittivity of the coating insulating the conductors and is different from that derived in [5]. In fact, it accounts for the couplings between phase and neutral, phase and earth, and neutral and earth, but not for those associated with the conduit.

A model based on the expressions (1.2.1)-(1.2.4) is simple, but its accuracy is limited by two factors. In fact, it is not easy to estimate some of its constants, like the dielectric permittivity ε and the electrical conductivity σ of the insulating coating, since this consists of heterogeneous

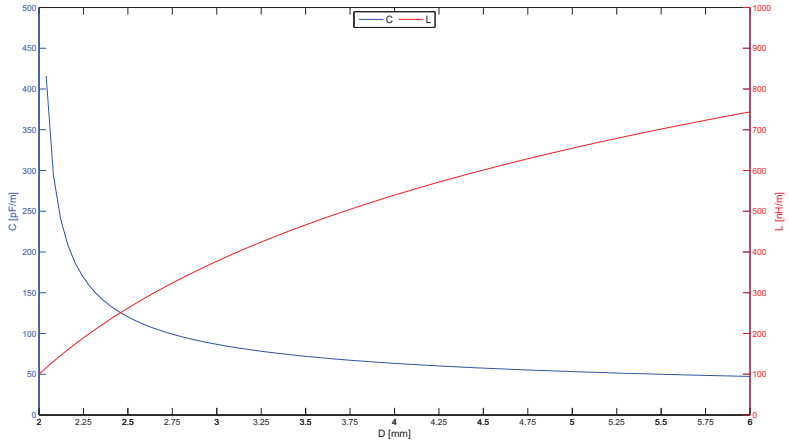

Figure 1.2.1: Inductance per length unit (L) and capacity per length unit (C) as a function of the wire distance D.

materials (insulator and air). In addition, the derivation of (1.2.1)-(1.2.4) is based on the assumption of a constant distance D between the wires of a powerline; unluckily, the cables inside a conduit do not take fixed and rigid positions. It is important to note, however, that

1. the first problem is often encountered in other electromagnetic models and a general solution is still missing;

2. in scenarios of practical interest, changes in the distance D between cables do not entail substantial variations in the inductance per unit length L and in the capacity per unit length C.

The last point can be understood referring to Fig. 1.2.1, which represents L (1.2.2) and C (1.2.4) versus the distance D between the conductors of a powerline having: a) a permeability of the copper cables μ_c equal to the vacuum magnetic permeability μ_0; b) a dielectric permittivity[1] $\varepsilon = 2\varepsilon_0$, where ε_0 is the vacuum dielectric permittivity; c) a diameter $2a$ of the wires equal to 1 mm.

[1]Since cable insulation is composed of both air and PVC, an average value has been adopted for this parameter.

Given the values of the above mentioned distributed constants, the characteristic impedance

$$Z_0 = \sqrt{\frac{R + j\omega L}{G + j\omega C}} \tag{1.2.5}$$

and the propagation constant

$$\gamma = \sqrt{(R + j\omega L)(G + j\omega C)} \tag{1.2.6}$$

of a given powerline can be easily computed. Finally, it is worth mentioning that the characteristic impedance Z_0 and the propagation constant γ can be also evaluated as [5]

$$Z_0 = \sqrt{Z_{io} Z_{is}} \tag{1.2.7}$$

and

$$\gamma = \frac{1}{l} \arctan \sqrt{\frac{Z_{is}}{Z_{io}}} \tag{1.2.8}$$

respectively. Here, l is the length of the powerline, whereas Z_{io} and Z_{is} are the impedances measured at the input of the line when its output is open and shortened, respectively.

1.2.2 Deterministic model

The proposed channel model is based on the following assumptions (see Fig. 1.2.2-a)):

1. the powerline consists of a *backbone* and of a fixed set of *branches* originating from it;
2. each branch terminates with a *plug*, to which a *load* can be connected;
3. the backbone is fed by a signal, which can be received on the plug of any branch;
4. the channel is *static*, so that the possibility of time variations due to the nonlinear behavior of power loads and/or to random changes in their number is not taken into consideration;
5. the number of power loads connected to the network, their impedances and the length of its branches are are input parameters of the simulator.

The model represents the power network as the cascade of *multiple elementary cells*, each including a section of the backbone and a branch, which, in turn, is terminated on a load or left open, as illustrated in Fig. 1.2.3. Therefore, the i-th cell is characterized by the

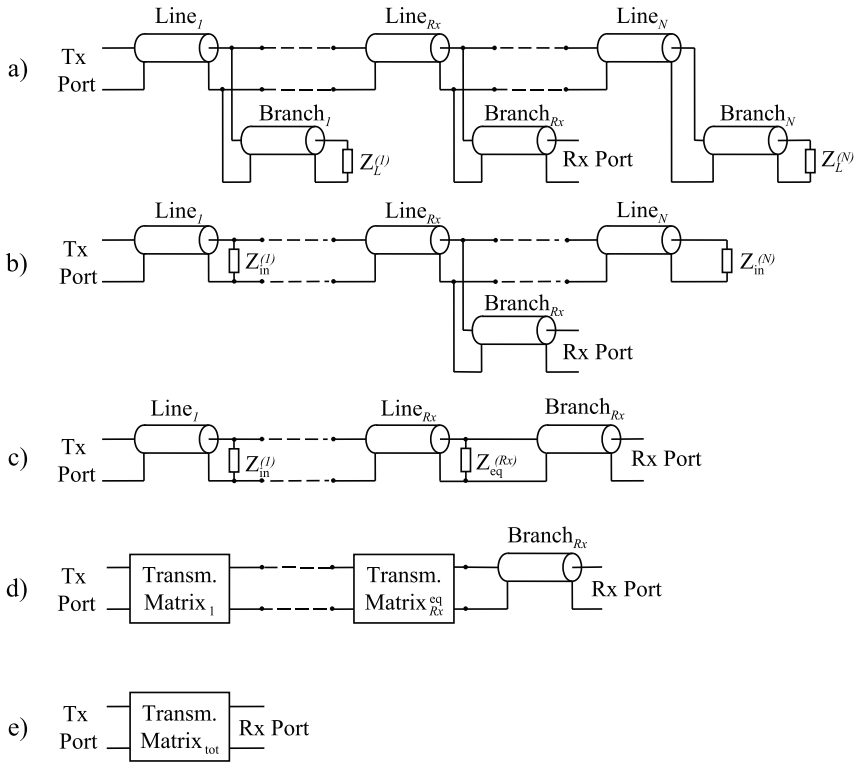

Figure 1.2.2: Equivalent circuits exploited by the proposed channel simulation algorithm: a) initial; b) after the branch substitution step; c) after the substitution of the cells following the receiver branch; d) represented as the cascade of multiple equivalent transmission matrices; e) represented as a single equivalent transmission matrix.

following parameters: a) the length $l_T^{(i)}$ of its piece of backbone; b) the branch length $l_B^{(i)}$; c) the impedance $Z_L^{(i)}$ of the connected load (which, for simplicity, is considered real valued); d) the characteristic impedance Z_0 and the propagation constant γ of the piece of backbone and of each branch. To simplify the analysis, the same values of Z_0 and γ have selected for different cells of the powerline network.

It is important to point out that

1. indoor power networks are often characterized by *star* or *tree* topologies [45], or by a combination of them. In such topologies, however, leafs with the same root, being in parallel, can be easily replaced by a single equivalent branch and a network model similar to that described above can be derived. The proposed algorithm, therefore, can be easily

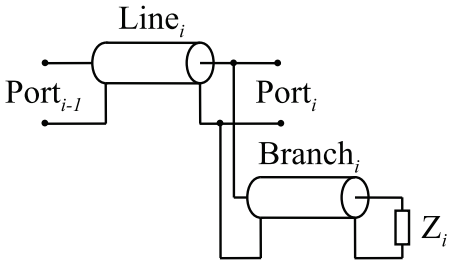

Figure 1.2.3: Structure of the basic cell adopted by the channel simulator algorithm.

extended to account for these topologies (see Chapter 2).

2. The choice of keeping the line parameters constant across the entire network has been dictated mainly by the need of minimising the number of input parameters of the simulator, so reducing its complexity. In principle, the approach to powerline channel modeling works even in the presence of a less restrictive assumption, i.e. when the line characteristics do not change on a given branch, but change from branch to branch. In fact, even in the last scenario, the algorithm illustrated in the following can be still applied.

The powerline model of Figure 1.2.2-a) is useful to derive a simple algorithm computing the equivalent impedance matrix of the communication channel, as illustrated below.

The algorithm for the evaluation of the equivalent channel impedance matrix consists of the following steps:

1. The equivalent impedance characterizing each branch in its point of connection with the backbone is computed for all the branches (excluding that of the receiver); such an impedance is given by

$$Z_{\text{in}}^{(i)} = Z_0 \frac{Z_L^{(i)} + Z_0 \tanh\left(\gamma l_B^{(i)}\right)}{Z_0 + Z_L^{(i)} \tanh\left(\gamma l_B^{(i)}\right)} \tag{1.2.9}$$

for the i-th branch, where $l_B^{(i)}$ is the branch length and $Z_L^{(i)}$ is the impedance of the load connected to it. Then, substituting each branch with its equivalent impedance leads to the equivalent model shown in Fig. 1.2.2-b).

2. The equivalent input impedance $Z_{\text{eq}}^{(\text{Rx})}$ of the subnetwork following the receiver branch is computed, so that the model of Fig. 1.2.2-b) can be turned into its equivalent representation of Fig. 1.2.2-c).

3. Fig. 1.2.2-c) represents the channel as the cascade of multiple sections, each consisting of a piece of the backbone and of a load connected in parallel at its end. Each section can be described by its equivalent transmission matrix $\mathbf{T}^{(i)}$ (also called $ABCD$ matrix),

$$\mathbf{T}^{(i)} = \begin{bmatrix} A^{(i)} & B^{(i)} \\ C^{(i)} & D^{(i)} \end{bmatrix}$$

with its element defined as

$$\begin{aligned} A^{(i)} &= \left.\frac{V_1^{(i)}}{V_2^{(i)}}\right|_{I_2^{(i)}=0}, \quad C^{(i)} = \left.\frac{V_1^{(i)}}{I_2}\right|_{V_2^{(i)}=0}, \\ B^{(i)} &= \left.\frac{I_1^{(i)}}{V_2^{(i)}}\right|_{I_2^{(i)}=0}, \quad D^{(i)} = \left.\frac{I_1}{I_2}\right|_{V_2^{(i)}=0}, \end{aligned} \tag{1.2.10}$$

where $V_1^{(i)}$ ($V_2^{(i)}$) is the input (output) voltage and $I_1^{(i)}$ ($I_2^{(i)}$) is the input (output) current of each section. It can be shown that these coefficients are given by

$$A^{(i)} = e^{\gamma l_T^{(i)}} \frac{\left(1 + \rho_L^{(i)} e^{-2\gamma l_T^{(i)}}\right)}{(1 + \rho_L^{(i)})} \tag{1.2.11}$$

$$B^{(i)} = Z_0 \left(1 - e^{-2\gamma l_T^{(i)}}\right) e^{\gamma l_T^{(i)}}, \tag{1.2.12}$$

$$C^{(i)} = \frac{1}{Z_0} \frac{\left(1 - \rho_L e^{-2\gamma l_T}\right) e^{\gamma l_T}}{1 + \rho_L} \tag{1.2.13}$$

$$D^{(i)} = -\frac{\left(1 + e^{-2\gamma l_T}\right) e^{\gamma l_T}}{2} \tag{1.2.14}$$

where $l_T^{(i)}$ is the line length and $\rho_L^{(i)} = (Z_{\text{in}}^{(i)} - Z_0)/(Z_{\text{in}}^{(i)} + Z_0)$ is the reflection coefficient. Given the transmission matrices of all the sections, the model of Fig. 1.2.2-c) can be replaced by its equivalent of Fig. 1.2.2-c).

4. The cascade of multiple transmission matrices can be replaced by their product; this yields the simplified model represented in Fig. 1.2.2-e) and characterized by a single transmission matrix.

5. The elements of the equivalent impedance matrice $\mathbf{Z}$ can be computed as

$$\begin{aligned} Z_{1,1} &= \frac{A}{C} \\ Z_{1,2} &= \frac{AD - BC}{C} \\ Z_{2,1} &= \frac{1}{C} \\ Z_{2,2} &= \frac{D}{C} \end{aligned}$$

where $Z_{1,1}, Z_{1,2}, Z_{2,1}, Z_{2,2}$are the elements of the matrice $\mathbf{Z}$ and A, B, C, D are the elements of the transmission matrix of the previous point.

This algorithm can be easily exploited to develop a computer based channel simulator. This allows to analyse both the impedance properties and the filtering characteristics of powerline channels in indoor scenarios, as shown in the following Paragraph.

1.2.3 Statistical channel simulator

A stochastic channel simulator based on the algorithm described above has been developed. Its input data are:

- the characteristic impedance Z_0 and the propagation constant γ of each cable;
- the number N of branches (cells) of the power grid;
- the minimum and the maximum length of the portion of main cable included in each cell;
- the minimum and the maximum length of the cable included in the branch of each cell;
- the minimum ($P_{\min}$) and the maximum power ($P_{\max}$) absorbed by the set of loads connected to the network;
- the probability P_{open} of having an open plug in a branch.

Given these data, the following parameters are generated in a random fashion:

1. The location of the powerline output[2] (i.e., of the receiver).
2. The length of all the cables contained in the network. In particular, the length of each cable, given its minimum ($l_{\min}$) and maximum ($l_{\max}$) values, is uniformly distributed[3] over the interval ($l_{\min}, l_{\max}$); in addition, the lengths of distinct cables are modelled as *independent* random variables.
3. The overall power P absorbed by the loads connected to the network. This parameter P is uniformly distributed over the interval ($P_{\min}, P_{\max}$).

[2]The location of its input (i.e., of the transmitter) is always assumed at the beginning of the backbone.

[3]The use of a uniform distributions for the cable lengths and for the powers absorbed by network loads may look unsuitable to indoor scenarios; note, however, that identifying a proper distribution is not easy in this case.

4. The power assigned to each load connected to the powerline. Since any plug (excluding that of the receiver) can be connected to a load with a probability $(1-P_{\text{open}})$, the overall number N_{lp} of loaded plugs is random. Given $N_{\text{lp}} < N$, a real weight w_i, uniformly distributed over the interval $(0, 1)$, is assigned to the i-th loaded plug (with $i = 1, 2, ..., N_{\text{lp}}$). Then, the power absorbed by this plug is evaluated as $P_i = w_i \cdot P \cdot \left(\sum_{i=1}^{N_{lp}} w_i\right)^{-1}$ and the equivalent resistance is computed, assuming a 50Hz power signal with a root mean square voltage equal to 220V.

In particular any plug (excluding that of the receiver) can be connected to a load with a probability $(1-P_{\text{open}})$, the overall number N_{lp} of loaded plugs is random and changes in each simulation.

Different samples of the above mentioned random variables lead to distinct realizations of a power grid with a fixed number of cells. For each of these realizations, the developed channel simulator computes the equivalent impedance matrix between the input and output ports exploiting the algorithm described above.Then, from the set of acquired data various statistical information about the given scenario, like the mean impedance matrix, the mean input and output impedances, and the mean channel transfer function, can be easily obtained.

1.3 Experimental set up

To assess the quality of the numerical results generated by the channel simulator, a measurement campaign has been conducted in the research labs of the department of engineering "Enzo Ferrari" (DIEF) at the University of Modena and Reggio Emilia. In this campaign, experimental data about the channel transfer function have been acquired connecting a network analyser HP 8753D to the available powerline network through an electrical interface, as illustrated in Fig. 1.3.1. This interface has been implemented on the basis of the electrical diagram represented in Fig. 1.3.2 and introduces a deep attenuation at 50 Hz, but exhibits a flat amplitude response in the frequency range of interest (1 − 30MHz). It consists of a band-pass LC filter and of a group of 4 protecting diodes. Note that the filter inductance is introduced by a transformer T1-1-X65 [21], having passband 150 kHz-400MHz and whose complete equivalent circuit is available in the application note [22]. In the frequency interval 1–30MHz[19], an approximate analysis of the inductive behavior of the circuit can be made taking into consideration the primary (L_1), the secondary (L_2) and the mutual (M) inductances of the transformer only; this leads to the frequency response

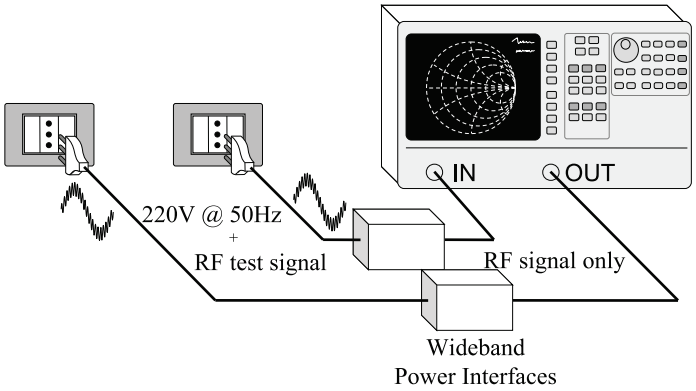

Figure 1.3.1: Measurement setup.

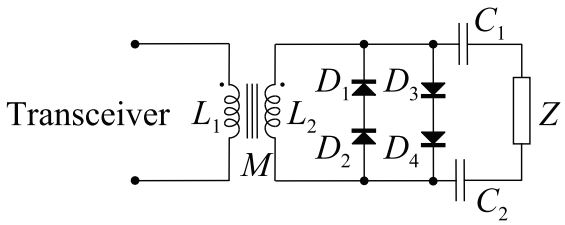

Figure 1.3.2: Electrical circuit of the implemented wideband interface.

$$F(\omega) = \frac{M}{L}\left[\frac{j\omega CZ}{1 + j\omega CZ - \omega^2 C\left(L - \frac{M^2}{L}\right)}\right], \tag{1.3.1}$$

expressing the complex ratio between the output and the input voltage of the interface. Here, Z is the load impedance of the interface, C consists of the series of the two capacitors C_1 and C_2 shown in Fig. 1.3.2 and the term $(L - M^2/L)$ represents the equivalent magnetization inductance of the transformer. It is usually assumed that $C_1 = C_2$, so that $C = C_1/2$; moreover, being the turn ratio unitary, we have that $L_1 = L_2 = L$. The impedance Z is of primary importance for the interface design and, since the circuit is bidirectional, Z can be either the input impedance of the channel or the input impedance of a quadrupole connected to that port (i.e., the input impedance of a Low Noise Amplifier (LNA) of a receiver).

From (1.3.1) it is easily inferred that Z affects the amplitude of the passband response. In addition, the capacitors in the circuit of Fig. 1.3.2 need to be properly selected to a ensure a cut-off frequency of the LC filter lower than 1MHz. In our lab tests, given the equivalent

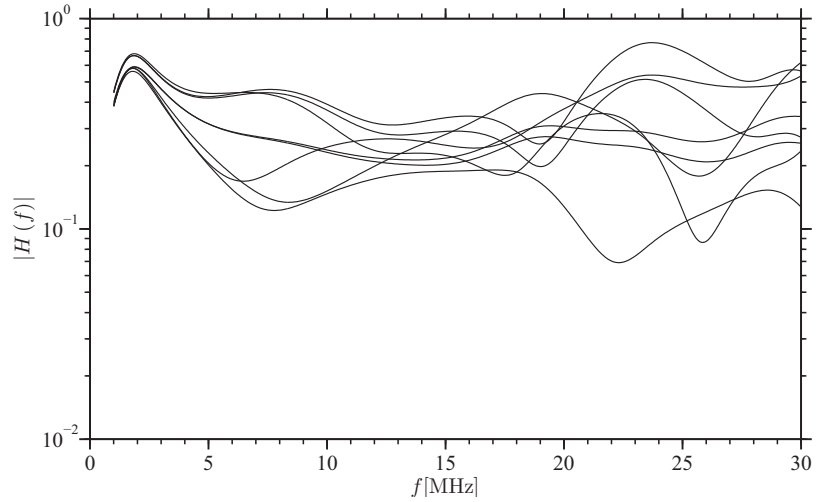

Figure 1.3.3: Transfer function of the front end connected to different realization of the power network.

magnetization inductance $L - M^2/L = 0.41\mu$H [21] and assuming a real load impedance Z, $C_1 = C_2 = 22$ nF have been selected.

Fig. 1.3.1 shows the amplitude response of the proposed interface loaded by the impedance Z_{11} generated in different runs of our channel simulator (the simulation scenario refers to a network characterized by 18 branches and described in detail in the following Section). These results show that the interface works properly in the range $1 - 30$MHz when connected to the electrical network. Note that:

- The presence of some notches in the amplitude response of the interface bipole can be related to the presence of sudden changes in the input impedance of the powerline network; in fact, if the input impedance of the network becomes low, or a particular resonance establishes between the capacitors C_1, C_2 and the input impedance of the network Z, the current flow causes a voltage drop between the interface ports;

- The leakage inductance of the transformer contained in our interface introduces a pole whose characteristic frequency is larger than 30 MHz. This results in a passband behavior of the power interface, which, however, is not visible in Fig. 1.3.1.

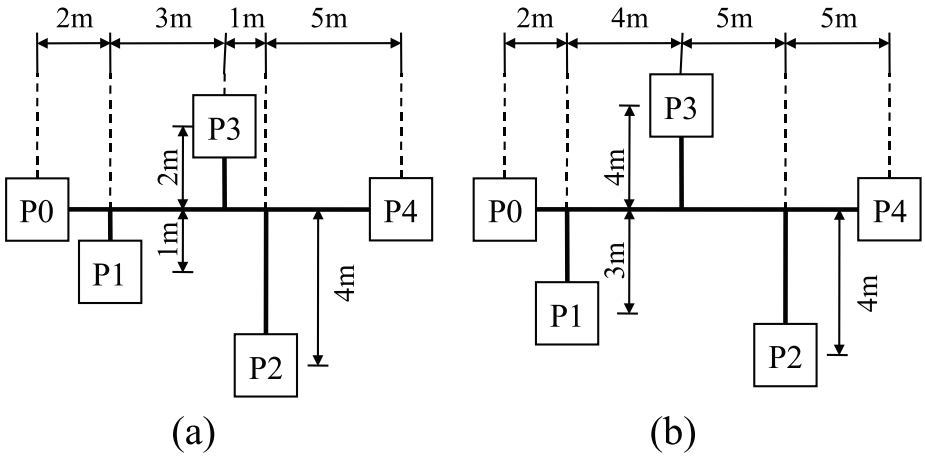

Figure 1.4.1: Topology of the network in scenario #1 (a) and scenario #2 (b).

1.4 Numerical results

In this Section some results extracted from the data acquired in the measurement campaign are compared with those generated by the channel simulator for the same scenarios. Two types of experiments were carryed out to validate the results of the simulator: on one hand two specific powerline networks were arranged in laboratory, on the other hand some meausures were acquired on the powerline networks of the laboratory. For the first type of experiments the following scenarios were considered:

- a powerline having the topology of Fig. 1.4.1(a) and whose cables consist of three insulated wires, tied up with adhesive tape and each with section of 2.5mm^2 (scenario #1);
- a powerline having the topology of Fig. 1.4.1(b) and whose cables consist of three insulated wires, contained in an insulating coating and each with section of 1.5mm^2 (scenario #2).

In both cases all the branch plugs (excluding that of the receiver) have been left open (i.e., unloaded) and the network analyser has been used to measure the channel amplitude transfer functions[4] in the frequency range 1–30 MHz between the plugs P0 and P1, and between P0

[4]The channel phase response has not been plotted, since, for a given indoor powerline channel, its impact on multicarrier data communications is certainly of minor importance with respect to that of the amplitude response.

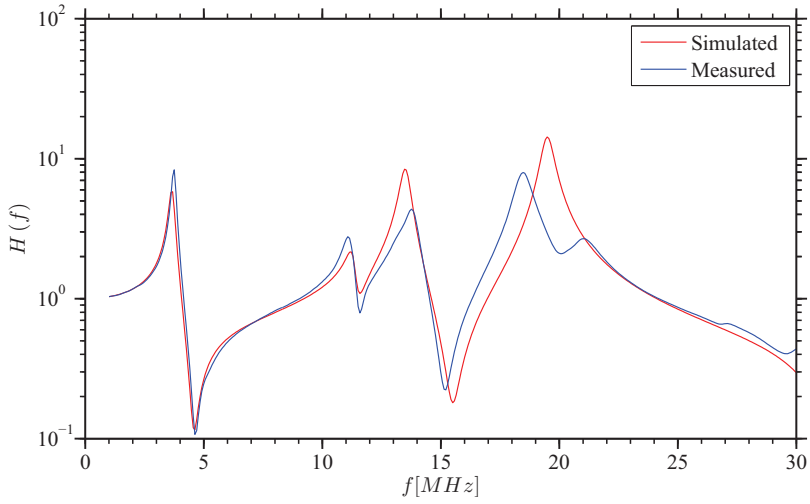

(a)

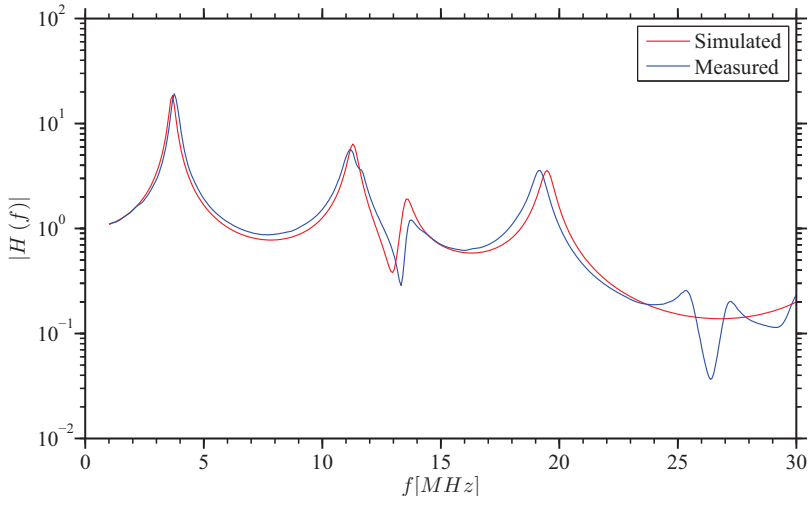

(b)

Figure 1.4.2: Comparison between the measured and the simulated channel amplitude responses between plugs P0 and P1 (a), and between plugs P0 and P4 (b) in scenario #1.

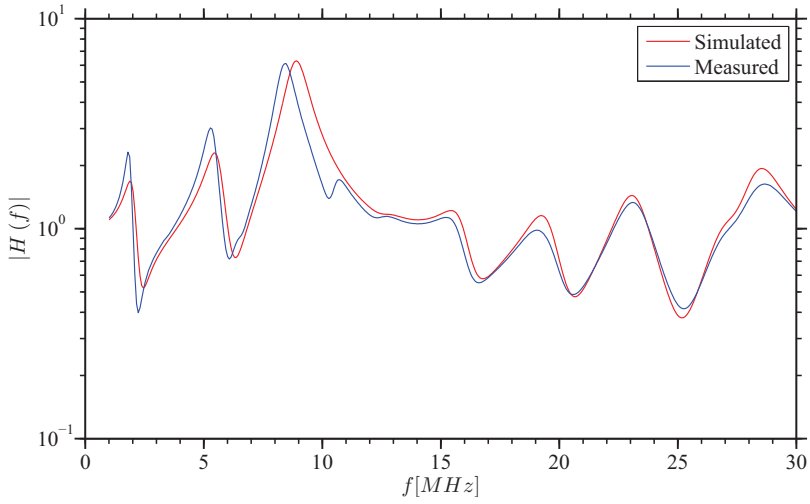

(a)

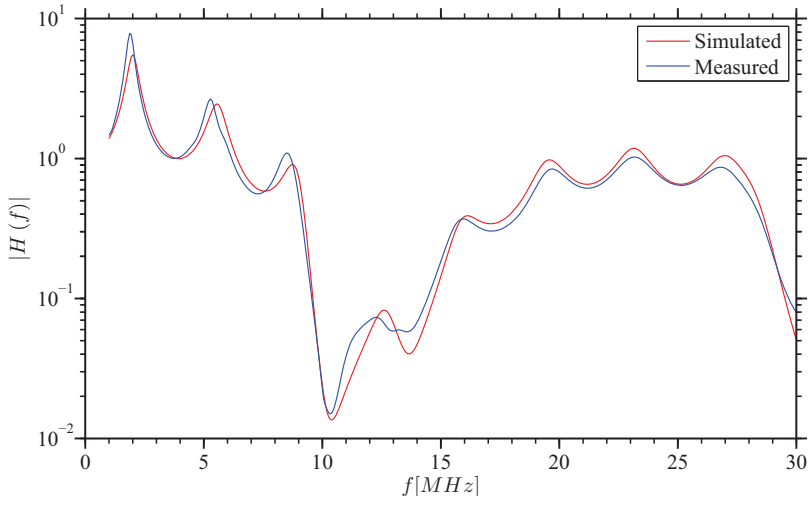

(b)

Figure 1.4.3: Comparison between the measured and the simulated channel amplitude responses between plugs P0 and P1 (a), and between plugs P0 and P4 (b) in scenario #2.

and P4. The channel behavior in both topologies has been also analysed using the proposed channel simulator; producing numerical results the following characteristic impedance and propagation constant have been adopted:

- $R(f) = 5.48 \cdot 10^{-4} \sqrt{f}$ Ω/m, $L = 702$nH and $C = 32.9$pF for scenario #1;
- $R(f) = 1.017 \cdot 10^{-3} \sqrt{f}$ Ω/m, $L = 493$nH and $C = 76$pF for scenario #2;

In fact, it has been found that these specific choices ensure that best match in the minimum mean square sense between experimental and computer generated results. Note that, given the above assumption, the simulator can be used to generate a single channel realization for each scenario, since the network topologies are fixed and perfectly known.

Figs. 1.4.2 and 1.4.3 compare the measured channel amplitude response with that generated by the channel simulator in scenario #1 and in scenario #2, respectively. Those results assume that the Channel Transfer Function (CTF) $H(f)$ is evaluated as the ratio between the receiver input voltage (plugs P1 or P4) and the transmitter output voltage (plug P0) when the input signal is produced by an ideal generator (having a null output impedance) and the output signal is collected by a receiver with an infinite input impedance[5]. In addition, Figs. 1.4.2-a and 1.4.3-a (1.4.2-b and 1.4.3-b) refer to the channel between the plugs P0 and P1 (P0 and P4) indicated in Fig. 1.4.1 (a) and (b). These results evidence a good agreement between computer generated and measured results; it is also interesting to note that the larger gap between measured and simulated data in Fig. 1.4.2 with respect to that of Fig. 1.4.3 derives from the difficulty of keeping a uniform distance between the conductors contained in the cables used in scenario #1.

A set of experimental data has also been acquired in another scenario, involving the real electrical system of a room of our labs; the adopted measurement setup in this case is illustrated in Fig. 1.4.4. In this case the total number of available plugs is 6, even if Fig. 1.4.4 indicates only those employed for the measurements. In addition, the exact network topology is unknown, so that measured data should be compared with simulated results from a statistical viewpoint. Running the simulations the following assumptions have been made: a) the cable model is the same as that used in scenario #1; b) the overall number of branches is 6; c) the minimum (maximum) length of the main cable and of the branch in each cell is equal to 3 m (12 m); d) the minimum (maximum) total power is equal to 0.5KW (3kW); ; e) the probability of

[5]Different values of the transmitter and the receiver impedance can be easily accounted for in the evaluation of the CTF after evaluating the equivalent transmission matrix of the network.

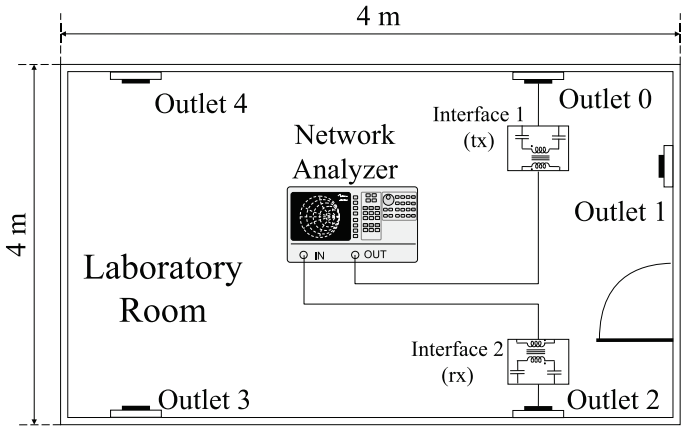

Figure 1.4.4: Measurement setup for acquiring a set of experimental data in our laboratory.

having an open plug is $P_{open} = 0.3$; f) the overall number of realizations generated to estimate channel statistics is equal to $3 \cdot 10^4$; g) the network interface described in the previous Section is connected both at the transmitter and receiver side. Significant statistical information about the behavior of the CTF of the simulated channel are provided by the mean amplitude response, by the distribution function

$$F_H(f,h) = \Pr\{|H(f)| \leq h\} \tag{1.4.1}$$

and by the associated Probability Density Function (PDF) $p_H(f,h)$. Fig. 1.4.5-a shows (on a logarithmic scale) the function $p_H(f,h)$ generated by the channel simulator in the considered scenario, whereas Fig. 1.4.5-b compares the average amplitude response of considered scenario with three different responses (associated with various couples of outlets) acquired in the measurement campaign; in the same figure, two dashed curves representing the mean amplitude response minus (plus) its Standard Deviation (STD) for each frequency are also shown to describe the spread of the simulated channel realizations. These data evidence: a) the reasonable behavior of the computer generated channel transfer functions, which exhibit a similar behavior as the measured ones; b) the average value of the simulated $|H(f)|$ is almost equal to 0.3 and its std gets larger with the frequency.

To assess the impact of the number of branches and of their length on the channel behavior, channel simulations have been repeated after tripling the number of branches (so that the overall number of branches becomes 18) and dividing by 3 the mean length of the branches (i.e., reducing the minimum to 1m and the maximum to 4m), so that the total mean length

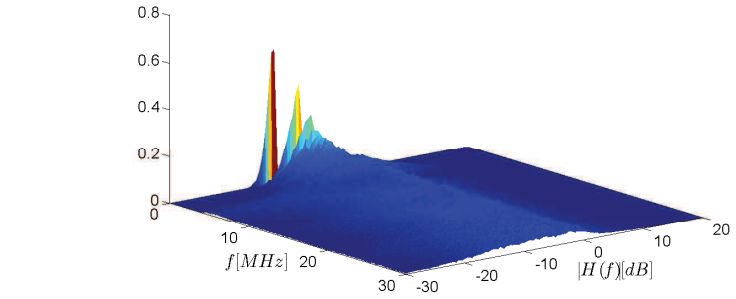

(a)

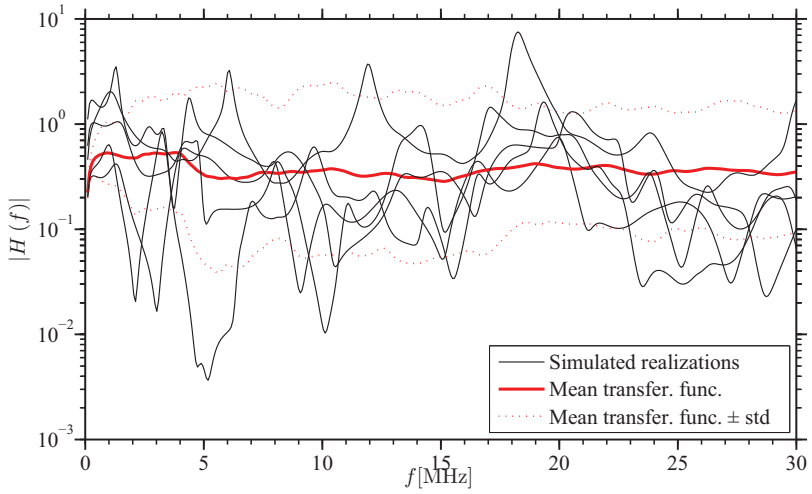

(b)

Figure 1.4.5: Representation of: a) the pdf $p_H(f, \log(h))$; b) the computer generated mean amplitude response and some measured amplitude responses. A powerline with 6 branches is assumed.

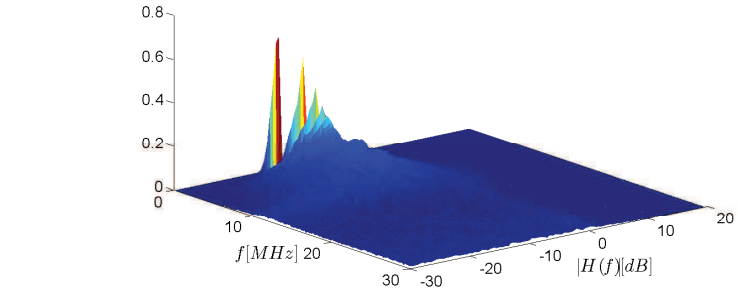

(a)

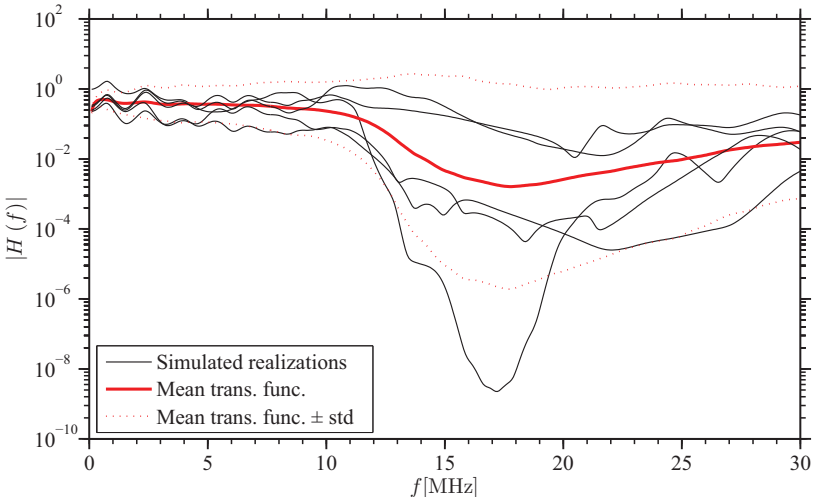

(b)

Figure 1.4.6: Representation of: a) the pdf $p_H(f, \log(h))$; b) the computer generated mean amplitude response and some computer generated realizations. A powerline with 18 branches is assumed.

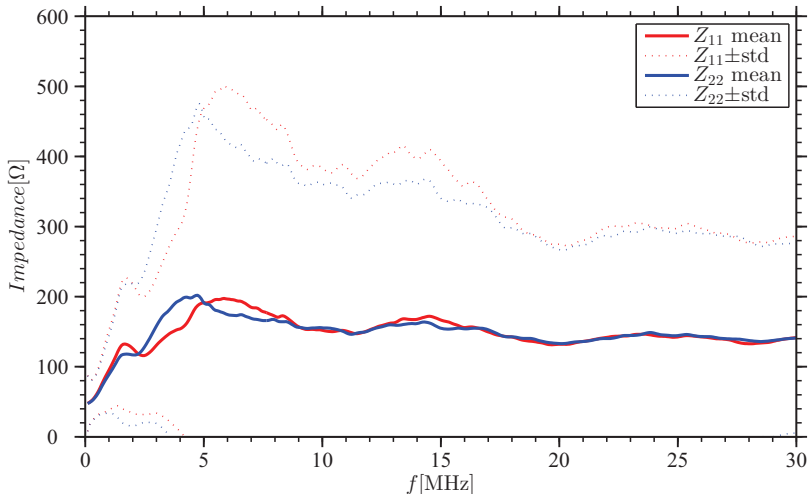

(a)

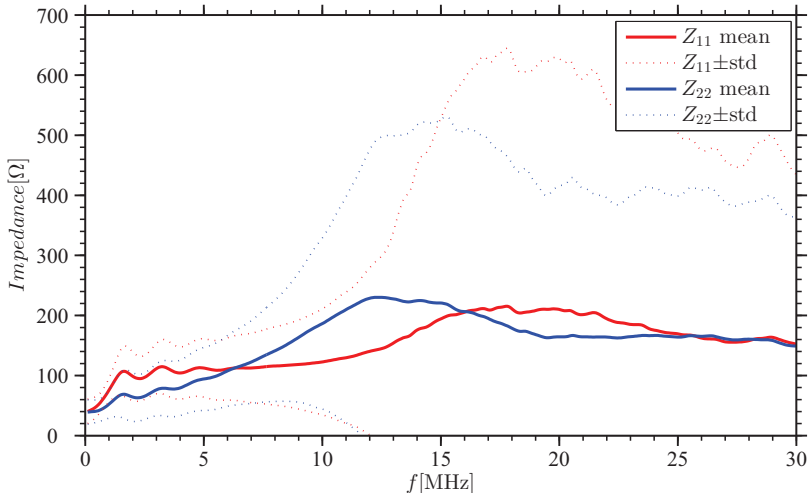

(b)

Figure 1.4.7: Representation of $|Z_{11}|$ and $|Z_{22}|$ versus frequency for a powerline with 6 branches (a) and with 18 branches (b).

of the backbone remains unchanged. Some simulation results are illustrated in Figs. 1.4.6 (a) and (b), providing the same type of information as Figs. 1.4.5 (a) and (b). Note, however, that since no experimental data are available for the network consisting of 18 branches, in Fig. 1.4.6-(a) some channel realizations generated by our simulator have been plotted. A comparison of these data with the previous ones evidences that:

1. The channel behavior in both cases is similar up to about 12MHz (its attenuation ranges between 0 and 10^{-2}); this is mainly due to the reduced length of the network branches, which do not produce strong reflections at low frequencies.

2. As the frequency gets larger (and, in particular, beyond 12MHz) the channel gain in the case of 18 branches exhibits a substantial reduction in its average values and an increase in its standard deviation. This behavior, however, is not observed in the previous case, i.e. in the presence of 6 branches only.

The channel simulator has been exploited to analyse the behavior of the amplitude of the coefficients Z_{11} and Z_{22} contained in the equivalent channel impedance matrix versus the measurement frequency. The computer generated data are shown in Fig. 1.4.7 for both the cases of 6 and 18 branches. Note that the mean absolute value for both Z_{11} and Z_{22} is approximately equal to 150Ω with slight variations in the two cases, especially as far as the standard deviation of these parameters is concerned.

1.5 Conclusions

In this chapter a novel approach to channel modelling for powerline communications has been proposed. A new recursive algorithm for the evaluation of the equivalent channel impedance matrix has been proposed and has been exploited to develop an efficient channel simulator. Computer generated results are in excellent agreement with a set of data acquired in an experimental campaign conducted in different scenarios.

Finally, it is important to point out that the proposed methodology for evaluation of the properties (in terms of both impedance and frequency response) of a powerline channel can be very useful in the design of the electronic front-end of digital modems for powerline communications and in the selection of proper transmission techniques for these applications.

Chapter 2

The Impact of Load Characterization on the Response of Indoor Powerline Channels

In this chapter the impact of load characterization on the statistical modeling of indoor powerline channels is investigated in the bandwidth $[100kHz - 50MHz]$*. The proposed analysis refers to the mean properties of the channel (so that its time-varying features are ignored) and is based on: a) the use of the statistical channel simulator introduced in Chapter 1 and described in [39]; b) the availability of an experimental data base of input impedances of various appliances.*

This chapter is organized as follows. Section 2.1 illustrates the state of the art. The hardware tools developed to acquire some experimental data about the impedance of various commercial appliances are described in Section 2.2, where some considerations about such data are also provided. In Section 2.3, after illustrating the essential features of the adopted channel simulator, various numerical results generated by it in two different scenarios are analysed. Finally, some conclusions are provided in Section 2.5.

2.1 State of the art

In principle, the properties of a powerline channel model are influenced by the type and the position of the connected loads; in fact, in any scenario, the channel transfer function between two distinct outlets depends not only on the powerline topology/cables, but also on

the loads connected to the other taps of the same network. It is worth noting that, in indoor powerlines, channel appliances may exhibit substantially different and time-varying behaviors at high frequencies; in addition, their position may be unknown. These considerations suggest that the assumptions about the loads connected to powerlines may substantially influence the characteristics of the adopted channel model.

In *deterministic* channel modelling the number, the type (resistive or reactive) and the magnitude of load impedances connected to the grid outlets can be taken as model inputs [11, 12, 14, 31, 37]; for instance, purely resistive loads with arbitrary magnitudes have been adopted in [10, 27, 35]. Other solutions to the problem of deterministic modelling of powerline channels rely on fitting mathematical representations of the propagation medium to experimental data (e.g., see [5, 13, 25, 28, 33, 36]). These include: a) the time-domain model and the frequency-domain model developed in [13] (based on representing the propagation medium as a tapped-delay line and as a cascade of a given number of independent series resonant circuits, respectively); b) the model developed in [33] and based on factoring the channel time-variant frequency response in two components (the amplitude and the phase characteristics); c) some models based on transmission line theory [5, 25, 36]; d) the model proposed in [28], representing powerline channels as linear periodically time-varying systems, so that their short term behavior can be accounted for. It is also worth mentioning that an accurate characterization of various appliances, extracted from a set of experimental data, has been illustrated in [25] and [28]; note, however, that on the one hand, such data have been employed to feed a deterministic channel model in [25], whereas, on the other hand, they have been used to motivate the adoption of a linear periodically time-varying model in [28].

In various *statistical* models all the outlets, except those employed by the transmitter and the receiver for powerline communications, are assumed open [15], [16] or connected to purely resistive loads [39]. Other statistical models do not rely on explicit assumptions about the loads and are based on experimental data, or result from different theoretical approaches [30, 34, 38, 41, 42]. Here we mention: a) the models proposed in [30, 34] and based on transmission line theory; b) the models developed in [38] and based on a statistical study of the widths, the heights, and the numbers of peaks and notches in the channel transfer function; c) the tapped delay line model described in [41] and characterized by correlated lognormal tap gains; d) the novel random topology model illustrated in [42].

Even if a significant portion of the above mentioned papers exploits a set of experimental data to validate different channel models (e.g., see [5, 13, 30, 33, 34, 36, 38, 41, 42]), as far as we know, few of them tackle the *specific problem of the accurate characterization of grid*

loads [25, 28, 43, 45]; at the same time none of them tries to extract some general indications about *the impact of load characterization on channel modelling*. These considerations have motivated our work, which tries to shed some light on the last problem. In particular, in our research work some experimental data about the impedance of various appliances in the band 100 kHz – 50 MHz have been acquired. Then, these have been processed by the statistical channel simulator developed in Chapter 1 [39] to assess various first and second order statistics referring to the input impedance and the channel impulse/frequency response of propagation medium; more specifically, the following statistics have been evaluated: a) the mean and the Normalised Standard Deviation (NSD) of the *input impedance* to the network at a given plug; b) the mean and the NSD of the Channel Frequency Response (CFR), the Power Delay Profile (PDP) and the CFR Autocorrelation Function (ACF) for a given couple of outlets of the grid. Then, these statistics have been compared with their counterparts evaluated by our channel simulator in a scenario characterised by purely resistive loads, in order to infer some general rules about the impact of load characterization on the average behavior of powerline channels. It is also worth pointing out that: (a) in this work loads have been characterized both in the *on state* and in the *off state*, since their impedance can appreciably change with their state [25, 28]; b) the time-varying nature of the powerline channel has not been taken into account (i.e., a purely frequency selective channel has been considered), since I was interested in certain average (i.e., statistical) properties of the propagation medium only.

2.2 Load characterization set-up

A specific electrical circuit was designed to acquire the input impedance of home ampliances, its electric diagram is illustrated in Fig. 2.2.1. The circuit is characterized by the *ports* A, B an C, connected to the power grid, to a network analyzer (the instrument HP8753D was used in our measurement campaign) and to a given load (i.e., to the appliance of interest), respectively. To understand the behavior of this circuit, let us assume now to modify it removing both *block A* and *block B*, so that the impedance between the nodes a and b is given by the parallel of the input impedance[1] of the grid, of the input impedance of the network analyzer and of the impedance of the load to be measured. Note that in this case the appliance impedance cannot be easily estimated processing the data acquired by the network analyzer, since such data are influenced by a time-varying unpredictable term introduced by the power network. For this reason the block A, which "shields" the load from the grid, has been included. In fact, the task

[1] Note that this impedance is unknown and *time-varying*.

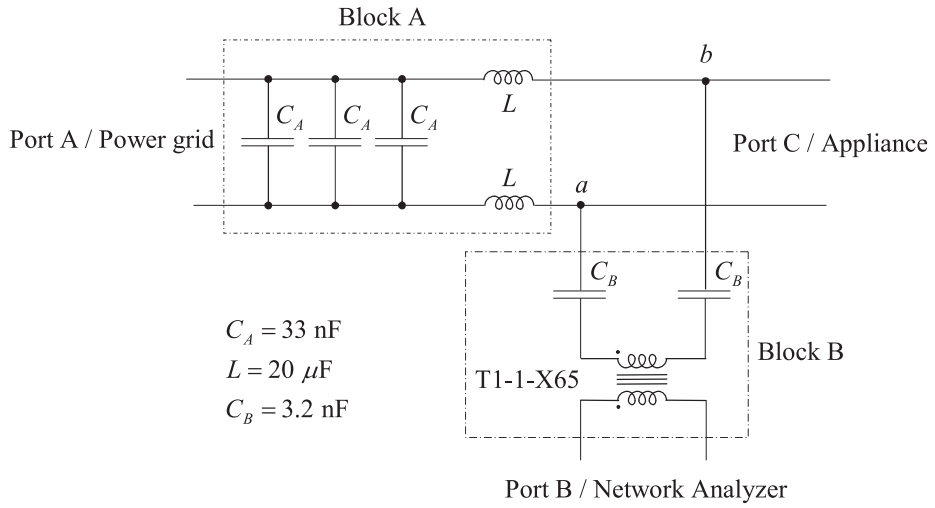

Figure 2.2.1: Electric diagram of the designed circuit and measurement setup.

of the three capacitors C_A is to short circuit the power grid, whereas that of the inductors L is to "insulate" the system under test. It is worth mentioning that the load under test must be properly supplied by the mains, so that its behavior can be analysed both in the *on state* and in the *off state*. For this reason, the impedance of the inductors L needs to be negligible at the mains frequency (50 or 60Hz), but appreciable in the band of interest; similar considerations can be expressed for the capacitors C_A. Finally, block B (composed by two capacitors C_B and by the high frequency transformer T1-1-X65) implements an high pass filter to protect the network analyzer from the mains and, at the same time, to pick up the information signal in the band of interest $100\text{KHz} - 50\text{MHz}$ with negligible attenuation. Moreover the effects of *blocks* A and B can be automatically compensated for calibrating the network analyzer directly on port C *in the absence of the mains* (i.e., with Port A disconnected from the power grid, so that current absorption is limited). This requires connecting three different loads to port C, namely a short circuit, an open circuit and 50Ω resistance. It is also worth mentioning that: a) a proper calibration is achieved in the conditions described above if the current level required to saturate the inductors L of Fig. 1 is larger than that absorbed by the appliance under test; b) the proposed calibration can be also used when the circuit is fed by the mains, provided that the inductors L do not saturate.

For each appliance under test, the network analyzer provides an estimate of the reflection coefficient ρ versus the measurement frequency f; then, the load impedance Z_L can be estimated

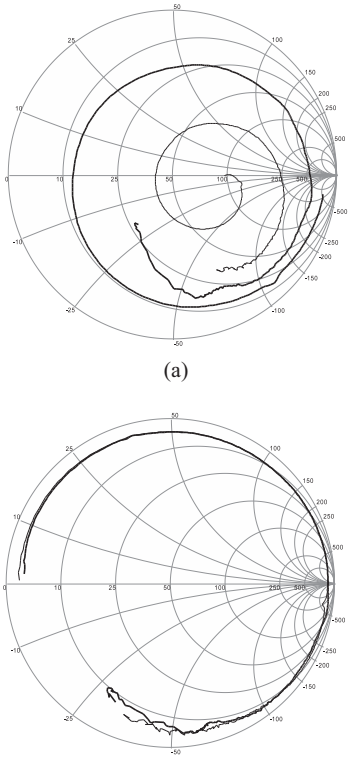

(a)

(b)

Figure 2.2.2: Impedance of an halogen lamp (a) and of an electric knife (b) in the ON state (thick line) and OFF state (thin line).

as

$$Z_L(f) = Z_n \frac{1+\rho(f)}{1-\rho(f)}, \tag{2.2.1}$$

where Z_n is the normalization impedance of the network analyzer.

The hardware tools described above have been employed to characterize different commercial appliances, namely an halogen lamp, an electric knife, a fridge, a mixer, an electric shaver, an hair dryer and an analog TV set. The impedances acquired for an halogen lamp and for an electric knife in the band of interest are shown in Figs. 2.2.2-(a) and 2.2.2-(b), respectively. These results show that:

- the impedance of each appliance exhibits a significant dependence on frequency and is complex;

- the impedance of the halogen lamp in its *on* state is larger than its counterpart in its *off* state because of the Joule effect;
- the impedance of the electric knife does not change appreciably switching from its *off* state to its *on* state; this is probably due to the appliance power supply which hides the effect of the internal circuits on the overall impedance.

2.3 Channel simulation

To assess the impact of power loads characterization on the accuracy of the statistical channel model, the true input impedance of power loads must be introduced in the model. For this reason, the experimental data acquired for various types of appliance have been organized in a database; then a proper channel simulator suitable to exploit the (complex) measured impedances as power loads has been developed.

The developed channel simulator adopts the well known *tree topology*[2] for indoor powerline networks of [29, pp. 47-48] (such a topology is illustrated in Fig. 2.3.1), characterized by: a) multiple "backbones" departing from a single point (namely the meter unit); b) multiple branches originating from each backbone and leading to power loads. Note that each backbone can represent the power network of a distinct floor in a building.

In practice, in the simulations the tree topology is obtained connecting multiple backbones whose specific features are generated by the channel simulator described in [39]. The branches, of the computer generated topology, departing from each backbone terminate on a plug, which can be open or connected to a power load. No branches originate from another branch, i.e. the model is characterized by only two hierarchical levels, namely the level of the backbones and that of the branches.

The simulator can operate in two different modes, one characterized by a *variable topology*, the other one by a *fixed topology* of the power grid. In the *first* mode, a different topology is generated at each run and the statistical channel simulator includes two distinct forms of randomness since:

1. each outlet can be open or connected to one of the (complex) measured impedances;
2. the length of the backbones and of the branches as well as the position of the branches with respect to the backbone is generated stochastically.

[2] This may also be dubbed *star topology*, since multiple branches originate from the same point.

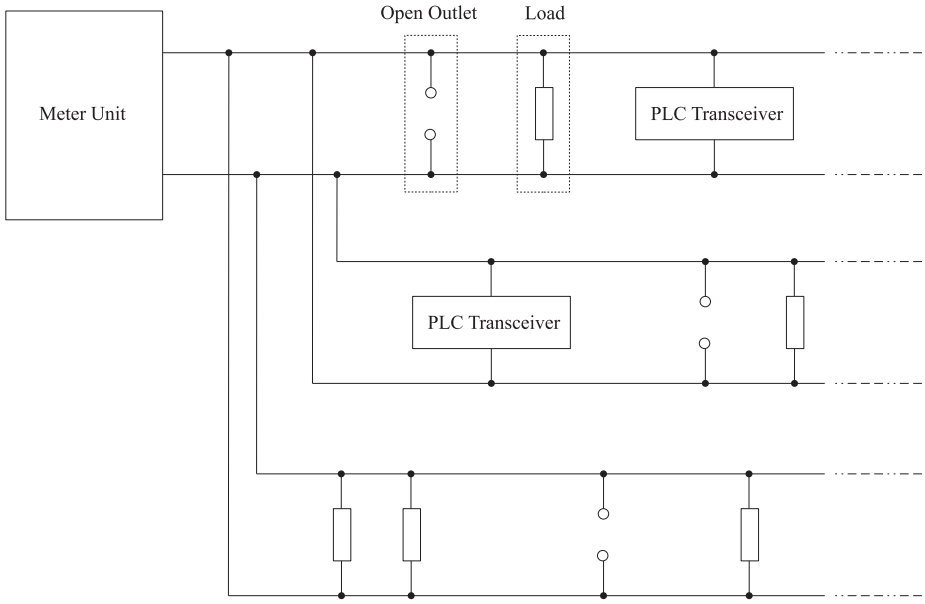

Figure 2.3.1: Example of a random generation of a powerline network characterized by a tree topology.

In the *second* mode, instead, the network topology is randomly generated once and for all at the beginning of the simulation, so that randomness is limited to the assignment of loads to the available plugs in each run. The goal of the last mode is to investigate the long term time variability of a PLC channel, due to switching on and off the appliances connected to a power grid.

2.4 Simulation results

All the numerical results illustrated in this Section mainly refer to certain first order and second order statistics of indoor poweline channels and aim at evidencing: 1) the degree of statistical similarity existing between channel families characterized by different load conditions; 2) the consistency of some numerical results generated by a software simulator with various experimental results acquired in a measurement campaign accomplished in the laboratories of DIEF. Statistical data about families of powerline channels have been generated under the following assumptions (unless differently stated):

- the CFR $H(f)$ is defined as the ratio between the voltage measured at the receiver and

the voltage generated by the transmitter;

- the transmitter and the receiver are connected to two plugs randomly selected in the power network;
- the CFR and the input impedance have been averaged over $N_R = 1000$ channel realizations;
- 3 backbones depart from the meter unit, unless otherwise specified;
- the number of branches per backbone is uniformly distributed between 4 and 8, unless otherwise specified;
- the length of the backbone portion between two adjacent branches is uniformly distributed between 2 m and 5 m, unless otherwise specified;
- the length of each branch is uniformly distributed between 1 m and 5 m, unless otherwise specified;
- the number of branches originating from each backbone and their lengths, and the length of the backbone itself are statistically independent random variables;
- the probability of having an open plug in each branch is equal to 0.3;
- the cable inductance per length unit is equal to 702 nH/m;
- the cable capacity per length unit is equal to 33 pF/m;
- the cable resistance per length unit is given by $0.548\sqrt{f}$ $m\Omega$/m .

It is also important to mention that:

1. When *measured* (*reactive*) *loads* are taken into consideration, each outlet is characterized by a probability mass function describing the associated load. In particular, in the simulations, every outlet is open with a probability equal to 0.3, whereas each of the 7 characterized appliances is connected to that outlet with a probability equal to 0.1.
2. When *resistive loads only* are assumed, such loads are uniformly distributed[3] between $4k\Omega$ and $6k\Omega$. This range has been empirically selected to minimize the difference

[3]Please note that the following interval refers to the impedance characterizing appliances in the band of interest (100kHz − 50MHz); in fact, at the mains frequency the typical impedance of appliances is much smaller, amounting to few tens of Ohm.

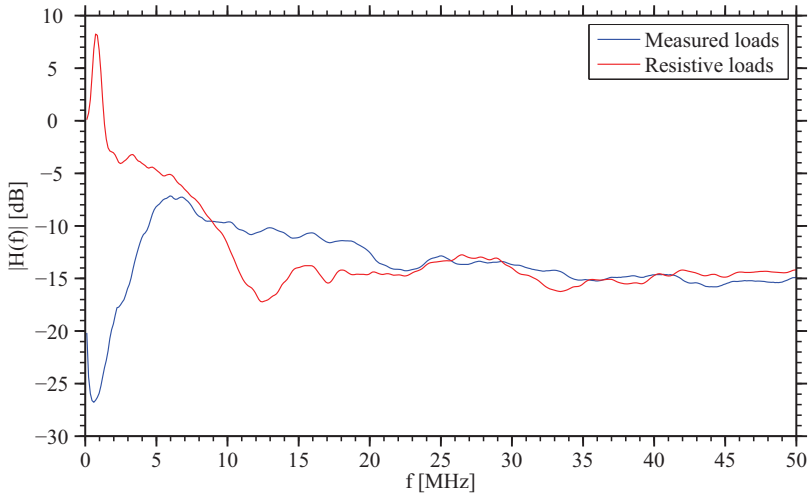

Figure 2.4.1: Mean channel frequency response in the presence of resistive loads and of measured impedances. A variable topology is assumed for the power network.

between the CFR obtained in the presence of resistive loads and that found in the presence of measured loads.

3. The above mentioned parameters have been selected in order to simulate a propagation scenario similar to an *in-home* power network; however, at the end of this Section, a different scenario is introduced to simulate the power grid of the labs and to compare the simulated results with the experimental data acquired on the field.

4. The adopted cable model is based on a set of experimental data acquired in our laboratories. Note that the presence of grounding wires has been taken into consideration in our characterization (see [39, Section II]).

5. The mean attenuation of the powerline channel heavily depends on the cable inductance, capacity and resistance per length unit.

The absolute value of the mean CFR (of the mean input impedance Z_{in}) evaluated in the presence of resistive loads only and that evaluated on the basis of the experimental database are compared in Fig. 2.4.1 (Fig. 2.4.2), where a variable topology mode has been selected for

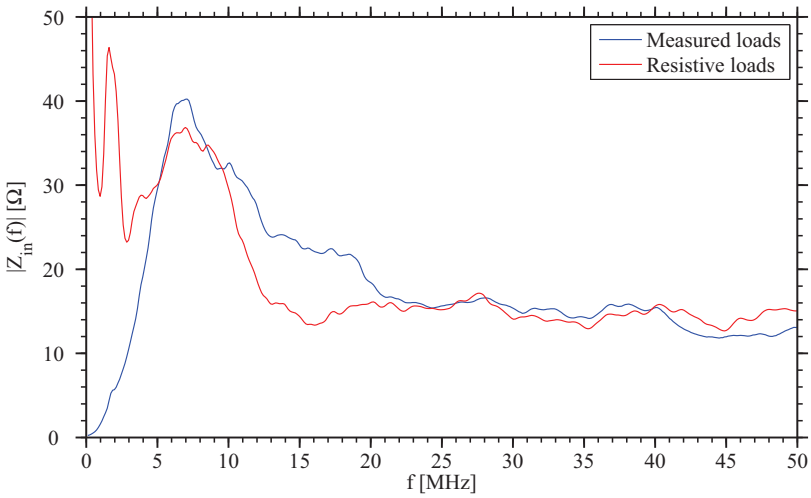

Figure 2.4.2: Mean input impedance in the presence of resistive loads and of measured loads. A variable topology is assumed for the power network.

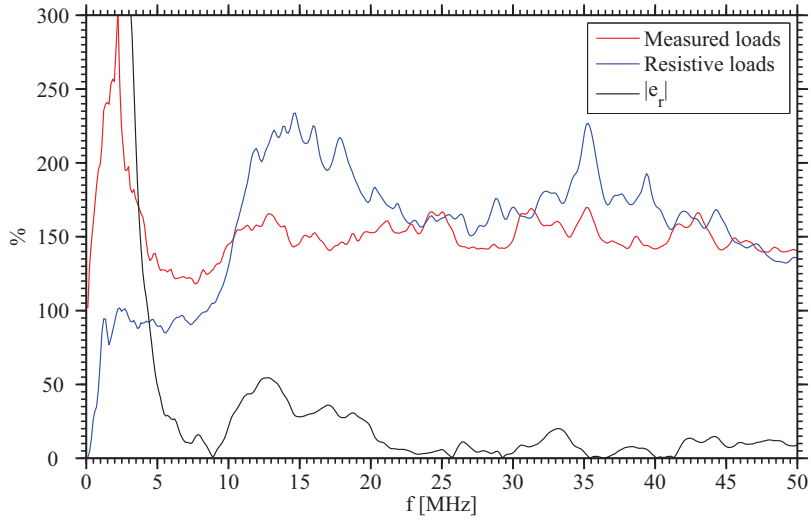

Figure 2.4.3: Relative error and NSD of the mean CFR in the presence of resistive loads and of measured loads. A variable topology is assumed for the power network.

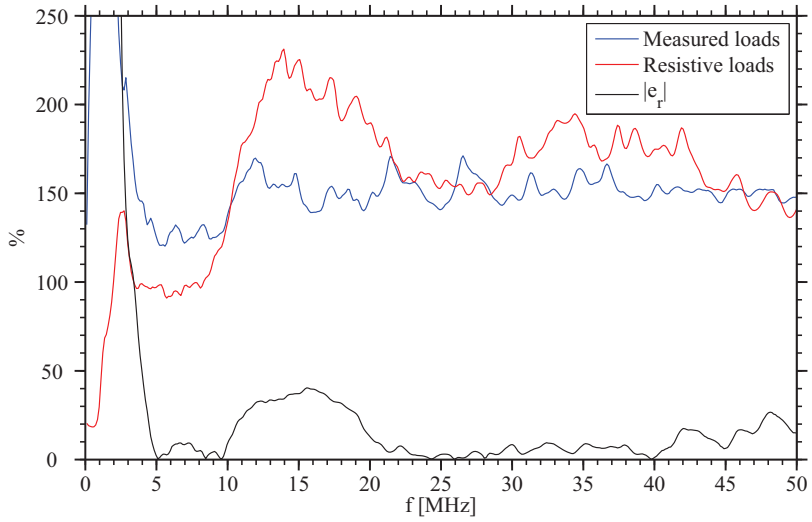

Figure 2.4.4: NSD of the mean input impedance in the presence of resistive loads and of measured loads. A variable topology is assumed for the power network.

the simulator. Moreover, the *relative error*[4] e_r and the NSD[5] of the absolute value of the mean CFR and of the absolute value of mean input impedance Z_{in} are shown in Fig. 2.4.3 and in Fig. 2.4.4, respectively, in the case of resistive loads only and in the case of measured loads. All these results evidence that:

- the relative error e_r between the mean CFR evaluated in the presence of resistive loads and the mean CFR evaluated on the basis of the experimental database is significant in the bandwidth $0.1 - 5$ MHz, is smaller than 50 % in the bandwidth $5 - 20$ MHz and is smaller than 20 % in the bandwidth $20 - 50$ MHz;

- the relative error e_r between the mean input impedance evaluated in the presence of resistive loads and the same quantity evaluated on the basis of the experimental database is appreciable in the bandwidth $0.1 - 4$ MHz, is smaller than 50 % in the bandwidth $4 - 20$ MHz and is smaller than 20 % in the bandwidth $20 - 50$ MHz;

[4]The relative error is defined as the absolute value of the difference between the results obtained with measured loads and the results obtained with resistive loads, normalised to the results obtained in the first case.

[5]This parameter is defined as the standard deviation of a random quantity normalized to its mean value.

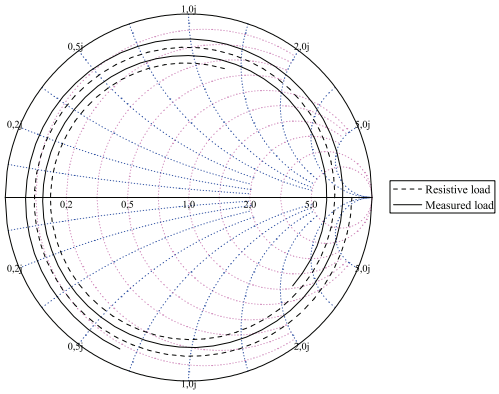

Figure 2.4.5: Plot of the normalized input impedance of a given branch versus the branch length at 25 MHz. The branch load is represented by electric knife or a resistor with resistance $R = 4\ k\Omega$.

- the mismatch between simulated and experimental results is significant in the bandwidth $0.1 - 5$ MHz and is moderate in the bandwidth $5 - 20$ MHz;
- the results obtained with resistive and measured loads are similar in the bandwidth $20 - 50$ MHz;
- the mean CFR is not characterized by deep frequency notches because it results from averaging over $N_R = 1000$ channel realizations;
- the attenuation in the mean CFR depends on the adopted cables model and is similar to that illustrated in [47, 48];
- the NSD evaluated in the presence of the resistive loads and that evaluated on the basis of the measured loads exhibit similar behavior for both the mean CFR and the mean input impedance;
- the large NSD in both cases stems from the intrinsic nature of the statistical channel simulator.

The close average behaviors in the frequency range $20 - 50$ MHz as well as the mismatch found in the range $0.1 - 5$ MHz lend themselves to a simple interpretation, which is provided

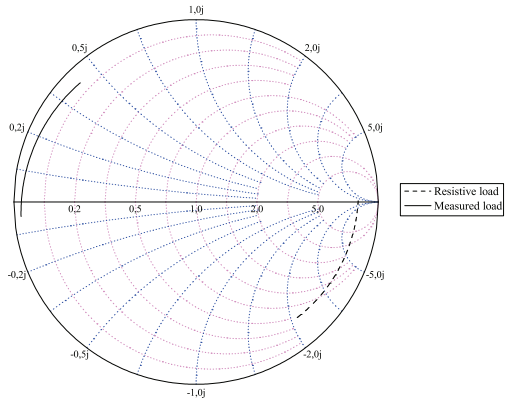

Figure 2.4.6: Plot of the normalized input impedance of a given branch versus the branch length at 1 MHz. The branch load is represented by electric knife or a resistor with resistance $R = 4\,k\Omega$.

in the following. Let us consider a branch consisting of cables with length l_b terminating on an impedance Z_L. The input impedance Z_{in} of the branch is given by

$$Z_{in} = Z_0 \frac{Z_L + Z_0 \tanh(\gamma l_b)}{Z_0 + Z_L \tanh(\gamma l_b)}, \tag{2.4.1}$$

where γ is the branch *propagation constant*. This formula shows that each branch loads the power network with a *complex* random impedance depending on both the load impedance Z_L and the product γl_b. To further clarify the implications of this result, the input impedance Z_{in}, normalized to the characteristic impedance Z_0 of the considered branch, has been represented in the Smith charts of Fig. 2.4.5 and Fig. 2.4.6 (referring to the frequencies 25MHz and 1MHz, respectively) for a cable length l_b ranging from 1 to 5m; two cases are considered in each figure, one in which Z_L is the impedance of an electric knife (measured load), the other one in which the load is purely resistive with resistance $R = 4\,k\Omega$. Note that the input impedance evaluated in the two above mentioned cases exhibits similar behaviors at 25MHz; however, a significant mismatch is found at 1 MHz. This is due to the fact that in the model the branch leading to a given outlet introduces a complex component whose effect gets more significant as the frequency and the length l_b of the wiring increase. Consequently, the actual impedance of the appliance Z_L is "randomized" by the branch *at large frequencies* (e.g., in the band $20 - 50$MHz); this explains why, in this scenario, an accurate characterization of loads has a secondary impact on statistical channel modeling. In fact, the inaccuracies origi-

nating from the rude assumption of purely resistive loads are hidden by the complex random impedances associated with the cables of our statistical channel model. On the contrary, *at low frequencies* (i.e., in the band $0.1-5$MHz), the effect of the complex component introduced by power cables becomes negligible with respect to the impact of the actual load impedance, so that the inaccuracies in the load model appreciably affect the CFR and the input impedance of the network. These properties of indoor powerline channels have to be carefully kept into account in designing the analog front-end of PLC equipment, since this should be able to properly interface with a communication channel behaving differently in the presence of distinct configurations of loads and distinct frequencies. Further work, not illustrated here in detail for space limitations, has evidenced that this problem can be mitigated by inserting a proper low-pass LC filter between each plug of the grid and the appliance connected to it. In fact, such a filter is able to make the CFR $H(f)$ and the input impedance of an indoor power grid *approximately constant* (for a given network topology and independently of the number and of the arrangement of the connected loads), making the design of the analog front-end of PLC equipment substantially simpler. It should be kept in mind, however, that the adoption of this strategy has certain practical drawbacks, since the inductors of low-pass filters can undergo saturation (being excited by a power signal), short circuit at high frequencies because of their parallel parasitic capacity and can introduce an appreciable energy loss because of their serial parasitic resistance.

In this analysis further significant information have been provided by the *power delay profile* (PDP) $P_h(\tau)$ and the CFR ACF $R_H(f)$ of the powerline channel. A comparison between the PDP (the absolute value of the ACF) assessed in the presence of resistive loads only and that resulting from the use of the measured loads is shown in Fig. 2.4.7 (Fig. 2.4.8). Note that, since the Channel Impulse Response (CIR) is computed as the *inverse Fourier transform* of the CFR generated by the channel simulator, the error between the two CFRs in the band $0.1-20$ MHz is spread over the whole time support of the CIR, so that an appreciable difference in the PDPs has been found. This is also confirmed by the fact that, if the considered frequency range is limited to $20-50$MHz, strong similarities between the PDPs are found[6]. Similarly, the error between the two CFRs in the band $0.1-20$ MHz yields a significant difference in the ACFs.

From Fig. 2.4.8 the coherence bandwidth B_{th} of the communication channel can be easily inferred for a given threshold th. In particular, $B_{0.9} = 455$ kHz has been found in the presence

[6]Numerical results concerning the PDPs evaluated in the band $20-50$ MHz are not shown for space limitations.

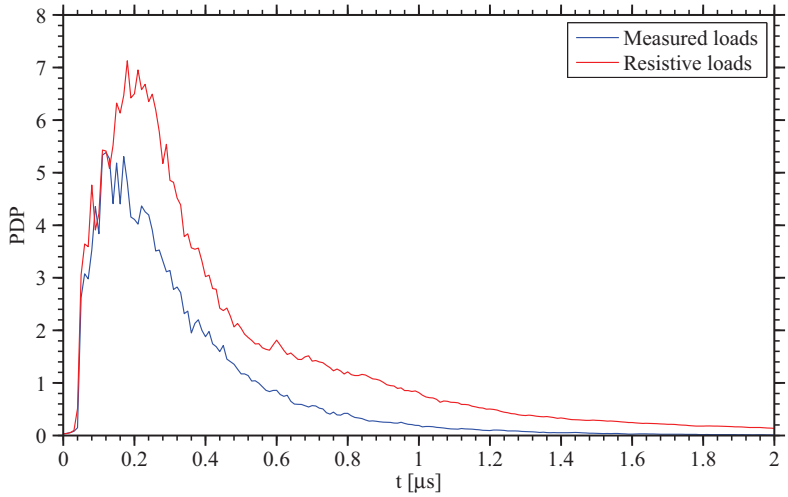

Figure 2.4.7: PDP assessed in the presence of resistive loads and measured loads. A variable topology is assumed for the power network.

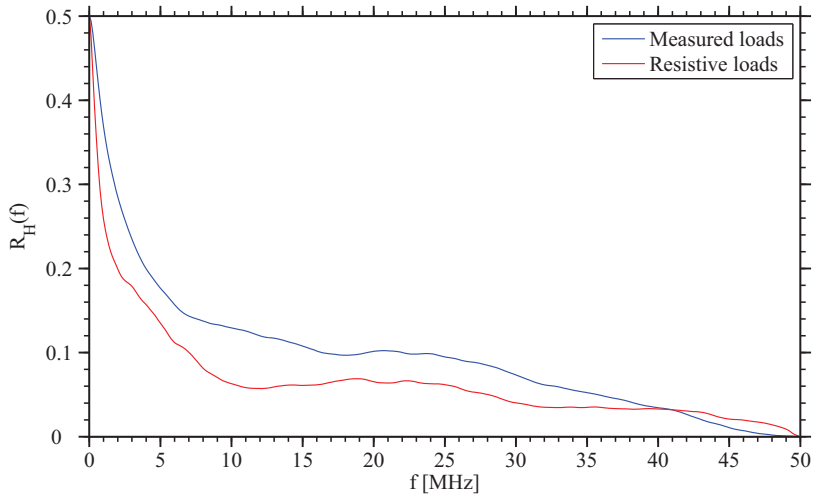

Figure 2.4.8: Absolute value of the channel ACF evaluated in the presence of resistive loads and measured loads. A variable topology is assumed for the power network.

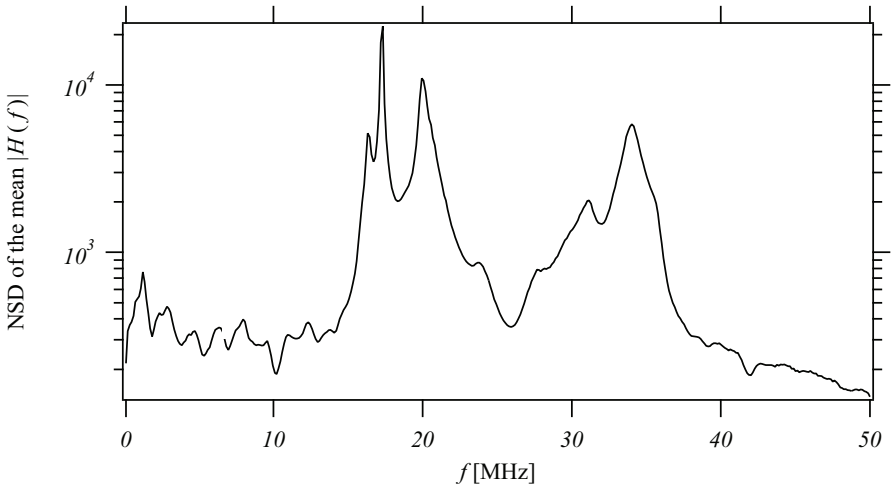

Figure 2.4.9: NSD of the mean CFR. A fixed topology is assumed for the power network.

of the measured loads. To assess the correctness of these results, we have also related the coherence bandwidth and the delay spread σ_τ defined as [49, eqs. (1)-(3)]. If the measured loads are employed in our channel simulations $\sigma_\tau = 284$ ns can be inferred from the simulated PDP, so that the equality

$$\sigma_\tau \simeq \frac{0.129}{B_{0.9}} \tag{2.4.2}$$

holds; this formula is similar to eqs. (5) of [47] and (15) of [18], which have been obtained in environments similar to the simulated one.

The impact of multiple appliances being turned on and off on the daily variability of the CFR has been assessed running the proposed channel simulator in the fixed topology mode and evaluating the NSD of the the absolute value of the mean CFR. Some results are shown in Fig. 2.4.9, which evidences the presence of large variations in the CFR.

Finally, some numerical results generated by the adopted channel simulator in the variable topology mode have been compared with a set of measured data acquired according to the set-up illustrated in Fig. 2.4.10. More specifically, in our measurement campaign the following specific choices have been made: a) two ports of the network analyzer have been connected to distinct outlets of a power network through two wideband interfaces, whose structure is described in [39] (the passband of these interfaces is represented by the interval 100 kHz – 50 MHz); b) the network analyzer has been calibrated at the input of the plugs, in order to compensate for the effect of the transfer function of the above mentioned interfaces. In

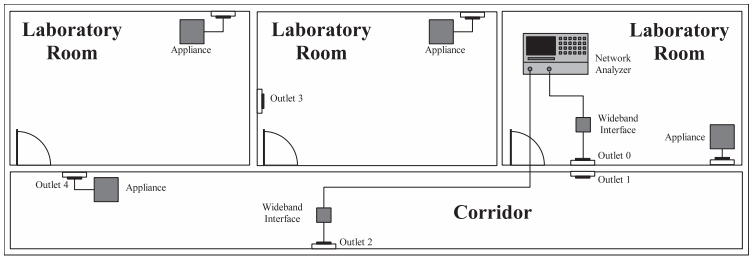

Figure 2.4.10: Experimental set-up for the measurement of the CFR between two plugs of a power network.

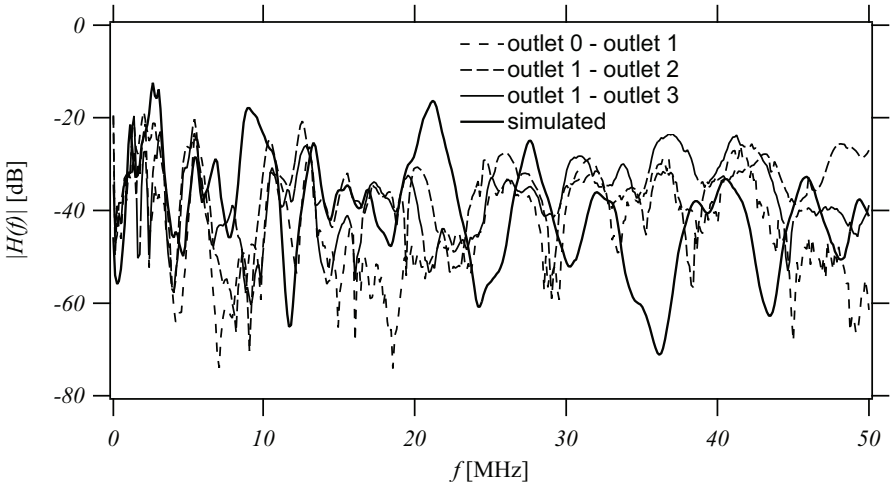

Figure 2.4.11: Comparison between the CFR measured between outlet 0 and outlet 2, outlet 1 and outlet 2, outlet 1 and outlet 3 with a single realization provided by our channel simulator.

addition, the input parameters of our channel simulator have been modified to match the characteristics of our experimental environment; in particular, it has been assumed that the length of the backbone portion and that of each branch are uniformly distributed between 5 m and 20 m. Note that the goal of this task was not extracting other channel statistics, but verifying that the numerical results (i.e., the channel realizations) generated by our channel simulator are *consistent* with measurement results, i.e. exhibit a similar behavior; however, a close match between computer generated data and experimental data should not be expected in this case, since the channel simulator is not deterministic. Some results are shown in Fig. 2.4.11, which compares the CFR's measured between outlet 0 and outlet 2, outlet 1 and outlet 2, outlet 1 and outlet 3 with a single realization of the CFR produced by our channel simulator

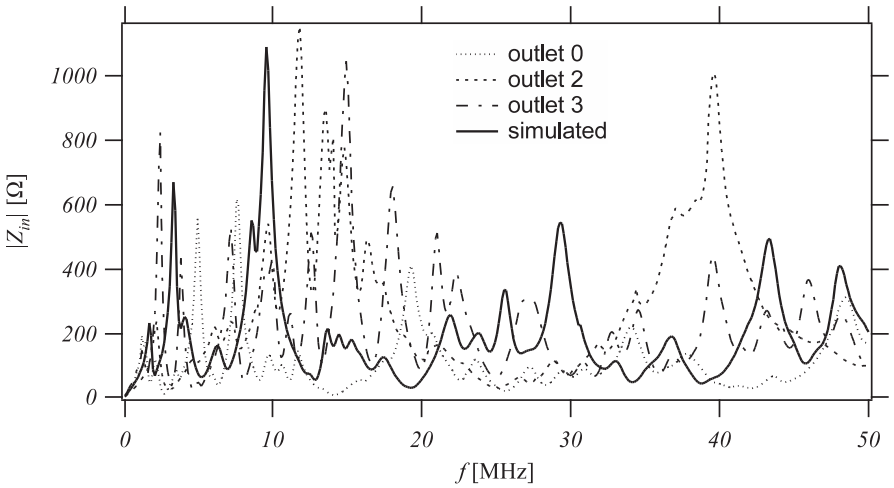

Figure 2.4.12: Comparison between the input impedance measured at outlet 0, outlet 2, outlet 3 and a single realization provided by our channel simulator.

in one of its runs. Similarly, in Fig. 2.4.12 the impedances measured at the input of outlet 0, outlet 2, outlet 3 are compared with a single realization of the impedance evaluated by our simulator. These results evidence that the simulated data are *consistent* with measurements, confirming the technical relevance of the proposed approach to channel modelling.

2.5 Conclusions

In this chapter the effect of the characterization of power loads on the statistical modelling of an indoor power grid has been analysed. This investigation has benefited from the availability of: a) a database of experimental results, showing the behavior of different commercial appliances in the band 100kHz – 50MHz; b) a statistical channel simulator which can be fed by the acquired experimental data. Numerical and experimental results have evidenced that, on the one hand, an accurate characterization of power loads has a marginal effect on the properties of statistical channel models for frequencies exceeding 20MHz, since the effect of power cables prevails over that of load impedance and the random procedure adopted in generating network topology hides the potential inaccuracies of the adopted load model. On the other hand, in the band $0.1 - 5$MHz, the effect of power cables is negligible with respect to that due to load impedance, so that the characterization of the loads connected to a power network can appreciably affect the accuracy of a statistical channel model.

Chapter 3

Statistical Modeling of Periodic Impulsive Noise in Indoor Powerline Channels

In this Chapter some new statistical models for the representation of the periodic impulsive noise generated by power loads connected to power grids in indoor scenarios are developed. Their derivation is based on a set of experimental results acquired in a measurement campaign and on Deseasonalized Autoregressive Moving Average (DARMA) modeling of cyclostationary random processes. Numerical results evidence that the proposed models can provide an accurate stochastic representation of the periodic impulsive noise generated by specific appliances in the 1–30*MHz band, at the price of a limited computational complexity.*

This Chapter begins with an analysis of noise models already available in the technical literature. The measurement set-up adopted exploited for the acquisition of channel noise is illustrated in Section 3.2, whereas the mathematical model proposed for periodic impulsive noise is derived in Section 3.3. Some experimental and numerical results are shown in Section 3.4. Finally, some conclusions are provided in Section 3.5.

3.1 State of the art

Recently, the strong interest in the development of high speed data communication systems exploiting power cables as a communication medium inside apartments and buildings has fos-

tered a number of research activities on the characterization of indoor powerline channels. Such channels suffer from various impairments, among which noise plays a fundamental role in determining the achievable error performance. Unluckily, noise in PLCs originates from different sources and does not lend itself to a simple statistical characterization. In the technical literature, to ease the development of statistical models, powerline noise is usually represented as the superposition of multiple heterogeneous components, namely *colored background noise*, *narrowband noise*, *periodic impulsive noise asynchronous to the mains frequency*, *periodic impulsive noise synchronous to the mains frequency* and *asynchronous impulsive noise* [14]. In the last years significant attention has been paid to the problem of modeling the periodic impulsive components, which usually originate from the appliances and the power suppliers connected to powerline networks. In particular, the Power Spectral Density (PSD) of this component and the cyclic short term variations of this PSD have been analysed in [28, 76] respectively; then, the results of [28] have been exploited to develop a comprehensive channel simulator for PLC [30]. Further experimental results about the main features of the periodic impulsive noise, like the PSD and the properties of noise pulses (namely, their repetition rate, shape, duration and amplitude) have been provided in [40, 77, 78, 79], where noise models fitting such results have been also derived. Note, however, that only [79] has developed a fully statistical model of the periodic impulsive noise, representing it as a sequence of pulses whose duration, amplitude and interarrival time obey certain statistical laws. In [80, 81] other statistical models, based on Poisson processes, have been proposed for this type of noise, but, unluckily, they do not rely on experimental data.

In this Chapter novel statistical models for periodic impulsive noise generated by power loads in indoor scenarios in the 1–30MHz band are presented. These models are characterized by the following features: a) they are based on a set of experimental results acquired in laboratories (where a proper measurement set-up has been developed to suppress the noise coming from the power network in the band of interest, so that only the noise contribution originating from the appliance under test is kept into account); b) they are based on Autoregressive Moving Average (ARMA) modeling of time series[1] and, consequently, they lend themselves to a simple implementation. Note that, since periodic impulsive noise is cyclostationary [40], in principle some specific models of the ARMA family, namely Autoregressive Integrated Moving Average (ARIMA), Periodic Autoregressive Moving Average (PARMA) and DARMA, can be adopted for its representation. However, in practice, in our scenario, only the DARMA approach allows

[1] As far as we know, ARMA models have not been previously applied to the problem of noise modeling in indoor PLCs.

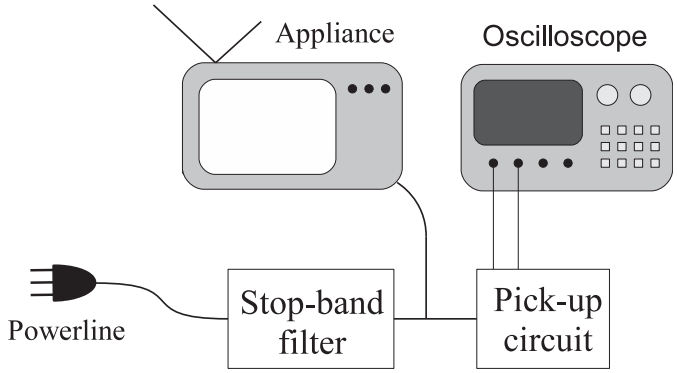

Figure 3.2.1: Experimental set-up for the acquisition of the periodic impulsive noise generated by a given appliance.

to develop accurate statistical models requiring a low implementation complexity. In fact, on the one hand, ARIMA models are not suitable to fit a set of experimental data since they are based on differentiating the acquired time series to remove the unstationarity affecting it and this does not efficiently remove the periodicity of time series itself. On the other hand, PARMA models can be employed to model periodic time series, but they represent a practical solution to a modeling problem only when the set of acquired samples is small.

3.2 Experimental set-up and acquisition procedure

A number of realizations of the impulsive noise generated by different appliances under test has been acquired resorting to the experimental set-up illustrated in Fig. 3.2.1; this consists of a stop-band filter, a pick-up circuit and a Digital Storage Oscilloscope (DSO) DSO6052A manufactured by Agilent Technologies. The stop-band filter has been designed to suppress the noise coming from the power network in the band of interest (1–30MHz), so that the only source of periodic impulsive noise reaching the oscilloscope is represented by the appliance under test; note, however, that this filter does not affect the mains signal (characterized by a frequency of 50 Hz in Europe), which can still feed the given appliance. The pick-up circuit has a threefold goal:

1. to protect the DSO from the mains;

2. to accomplish pass-band filtering so that signal acquisition is limited to the band of interest only;

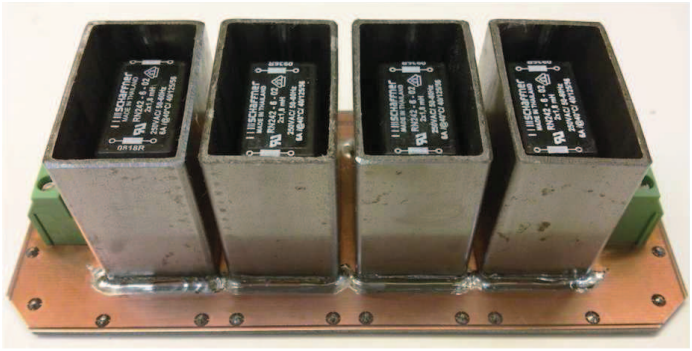

Figure 3.2.2: Stop-band filter employed in the experimental set-up of Fig.3.2.1.

3. to provide the DSO with a time trigger related to the mains frequency (50/60 Hz).

As far as the implementation of the system of Fig. 3.2.1 is concerned, some details are given in the following. The stop-band filter is a fifth order passive filter (see Fig. 3.2.2) and is implemented as the cascade of two equal low-pass T networks (see, for instance, [82]). Its inductors are able to both operate at high frequencies and support large currents (on the order of a few Amperes) without undergoing saturation. Note that in this case more classical and efficient stop-band filtering schemes cannot be employed to meet the design constraints and that the inductors we employed are shielded by ferromagnetic cases to avoid mutual coupling and, hence, to improve the selectivity of the filter.

The pick-up circuit has been implemented according to the electrical diagram shown in Fig. 3.2.3. This interface is endowed with three ports paired with three distinct functional blocks (denoted *A*, *B* and *C* in Fig. 3.2.3) it consists of. In particular, ports *J1*, *J2* and *J3* are connected with a powerline (coming from the output of the stop-band filter and feeding the appliance; see Fig. 3.2.1), with the DSO input and with the DSO input for the trigger signal, respectively. The different blocks of the pick-up circuit play the following roles:

1. Block *A* (power section) accomplishes high-pass filtering and, more precisely, establishes the lower cut-off frequency of the band of interest to 1 MHz (note that it removes the mains signal, so that the DSOO is protected).

2. Block *B* (acquisition section) accomplishes low-pass filtering and, in particular, sets the higher cut-off frequency of the band of interest to 30 MHz; this block is decoupled by the wideband transformer for small signals *XFR1* [21] from the power section (Block *A*).

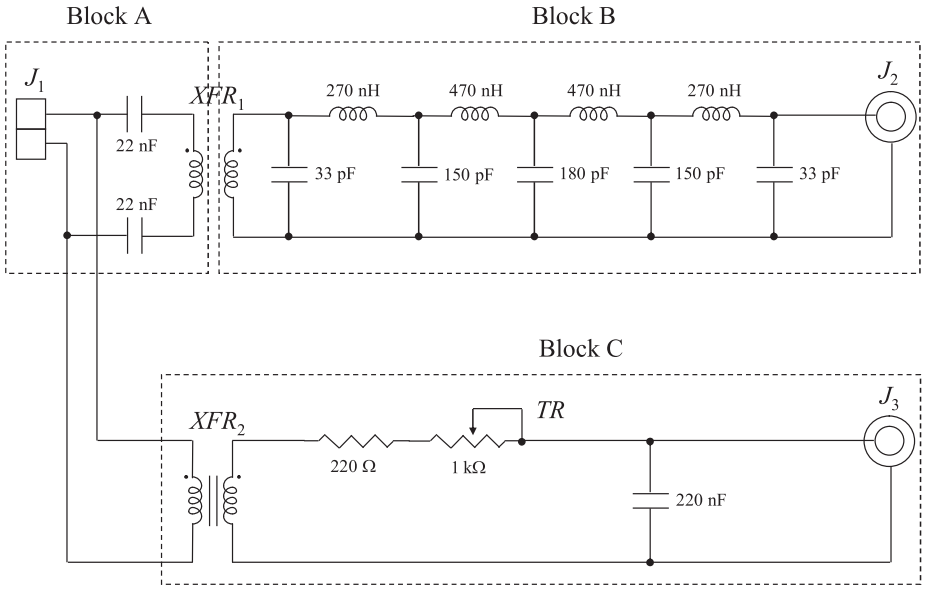

Figure 3.2.3: Electric diagram and connections of the pick-up circuit employed in the experimental set-up of Fig. 3.2.1.

3. 3. Block *C* (trigger section) provides the DSO with a trigger signal which enables the acquisition of the periodic impulsive noise synchronously with the mains frequency. In this block the power transformer *XFR2* aims at generating an attenuated version of the mains, to be low-pass filtered, so that possible spikes are smoothed (these might lead to unwanted triggering events). Note that the trimmer TR allows fine calibration of the triggering instant.

Finally, it is worth pointing out that:

1. The experimental set-up can be used to analyse both types of periodic impulsive noise described in [14].

2. The storage memory of the employed DSO is limited to $8 \cdot 10^6$ samples and this limits the acquisition time. For this reason, in our measurement campaign sequences of noise lasting 80ms (corresponding to 4 periods of the mains) have been acquired at sampling rate $f_s = 80$ MHz.

3.3 DARMA models for periodic impulsive noise

Generally speaking, the DARMA approach to the modeling of a time series consists of: 1) devising a proper one-to-one mathematical transformation which is able to remove the cyclostationarity of the analysed process; 2) exploiting this transformation to generate a stationary series; 3) employing an ARMA model to fit the last series; 4) restoring cyclostationarity via an inverse transformation to generate a new sequence exhibiting similar statistical properties as the original sequence. In practice, the procedure summarized by the flow diagram shown in Fig. 3.3.1 has been adopted to implement DARMA models for the noise processes of powerline channels.

First of all the sequence $\{u_n\}$ acquired from the DSO connected to the pick-up circuit (with a sampling frequency $f_s = 80$ MHz) is passed through a Finite Impulse Response (FIR) pass-band filter selecting the spectral components falling in the band of interest (1–30 MHz); note that, in particular, this filter suppresses both the components below 1 MHz coming from the power network and the noise beyond 30 MHz (possibly generated by the appliance under test). Then, the filtered sequence $\{w_n\}$ is processed to compute the *cyclic autocorrelation function*

$$R_w(\alpha_k, \tau) = \frac{1}{N} \sum_{n=0}^{N-1} w_n w_{n+\tau} e^{-j2\pi\alpha_k n} \tag{3.3.1}$$

where $\alpha_k \doteq k/Nf_s$ (with $k = 0, 1, ..., N-1$) denotes the the k-th cyclic frequency and the parameter τ is the *lag*. Note that, in principle, the interference generated by each appliance can be characterized by multiple cyclostationarity periods; each period is uniquely identified by a *peak* in $R_w(\alpha_k, \tau)$. In practice, however, in the appliances under test in our laboratories two main peaks have been found: one associated with a low cyclostationarity frequency (typically 100 Hz), which originates from the mains, and another one associated with a substantially higher cyclostationarity frequency (on the order of 1–100kHz); the last contribution derives from the use of a switching supply or can be explained analysing the operating principle of the power load under test. It is important to point out that the former contribution appears as an amplitude modulation of the noise pulses, whereas the latter one can be related to the presence of short bursts of pulses occurring with a certain periodicity. An accurate modeling of the periodic impulsive noise should aim at jointly representing both cyclostationary phenomena for each appliance under test. In our work, however, separate DARMA models of these two contributions have been developed for simplicity, so that any possible correlation between them has been ignored. In practice, in all the considered cases, it has been found

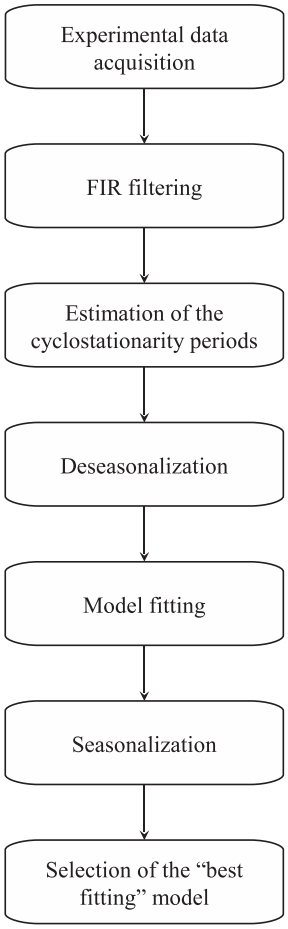

Figure 3.3.1: Flow diagram of the proposed technique for the extraction of DARMA models from the acquired experimental data.

that the cyclostationarity period Y_L (measured in number of samples) associated with the low cyclostationarity frequency is given by

$$Y_L = \frac{1}{100\,\text{Hz}} \cdot 80\,\text{Msamples/s} = 800000\,\text{samples} \tag{3.3.2}$$

Instead, the cyclostationarity period Y_H associated with the high cyclostationarity frequency (and measured in number of samples) has been evaluated as

$$Y_H = arg \underset{k}{max} R_w\left(\alpha_k, \tau\right) \tag{3.3.3}$$

with $k = 1, 2, ..., N-1$ and $\tau = 0$. The last expression deserves the following comments:

1. The stability of the period Y_H can be influenced by time-varying phenomena in the appliance under test. A good stability is evidenced by the presence of sharp peaks in $R_w(\alpha_k, \tau)$ and improves the performance of the proposed algorithm, which assumes a *time invariant* cyclostationarity period Y_H.

2. Generally speaking, sampling a continuous-time cyclostationary process generates an almost-cyclostationary time series (unless the cyclostationarity period is a multiple of the sampling period) [83]; therefore, even if the periodic impulsive noise is cyclostationary in a strict sense, the cyclic autocorrelation function is not characterized by lines placed at the cyclic frequencies. In other words, the peaks are intrinsically smoothed by sampling.

Since our DARMA models developed for the representation of the high cyclostationarity frequency do not aim at capturing the possible variations of Y_H, they can be classified as *short-term models* (in other words, they provide a proper representation of the periodic noise component over a limited time interval). On the contrary, the DARMA models describing the low frequency cyclostationarity can be considered as *long-term models*.

After evaluating the two cyclostationary periods Y_{L} (3.3.2) and Y_{H} (3.3.3), the *deseasonalization* technique illustrated in [84, pp. 464-466] is applied to the sequence $\{w_n\}$ for each of such periods, so that the associated cyclostationary component is removed producing a *stationary* sequence. For a given cyclostationarity period Y (measured in number of samples) this procedure can be summarized as follows. First of all, the time index n of the sequence $\{w_n\}$ is expressed as

$$n = y \cdot Y + s \tag{3.3.4}$$

where $y \doteq \lfloor n/Y \rfloor$ ($\lfloor \cdot \rfloor$ denotes the *floor function*) and s is an integer parameter whose values belong to the set $\{0, 1, ..., N-1\}$; note that: a) for a given sample w_n , y and s represent the *period* (dubbed *year*) and the position within the period (called *season* in the following), respectively, which this sample belongs to; b) if the representation (3.3.4) is adopted, the sample $w_n = w_{y \cdot Y + s}$ can be denoted $w_{y,s}$. Then, for a given season s, the mean value μ_s and the standard deviation σ_s can be computed as

$$\mu_s \doteq E_y(w_{y,s}) = \frac{1}{\lfloor N/Y \rfloor} \sum_{y=0}^{\lfloor N/Y \rfloor - 1} w_{y,s} \tag{3.3.5}$$

and

$$\sigma_s \doteq \sqrt{\frac{1}{\lfloor N/Y \rfloor} \sum_{y=0}^{\lfloor N/Y \rfloor - 1} (w_{y,s} - \mu_s)^2} \tag{3.3.6}$$

respectively, and the cyclostationarity can be removed employing the one-to-one transformation

$$z_{y,s} \doteq G(w_{y,s}) = \frac{w_{y,s} - \mu_s}{\sigma_s} \tag{3.3.7}$$

This produces the stationary sequence $\{z_{y,s}\} = \{z_{y \cdot Y + s}\} = \{z_n\}_{n=0}^{N-1}$ (see eq. (3.3.4)), for which AR(p), MA(q) and ARMA(p, q) models can be developed. It is worth mentioning that the ARMA(p, q) model for a random process $\{z_n\}$ can be represented as [84, 85]

$$(z_n - \mu) - \phi_1 (z_{n-1} - \mu) - \cdots - \phi_p (z_{n-p} - \mu) = a_n - \theta_1 a_{n-1} - \cdots - \theta_q a_{n-q} \tag{3.3.8}$$

where μ denotes the expected value of $\{z_n\}$, and $\{\phi_i\}_{i=1}^{p}$ and $\{\theta_j\}_{j=1}^{q}$ are the parameters of the (p-th order) AR and (q-th order) MA part, and $\{a_n\}$ is a real white Gaussian process whose samples have zero mean and variance σ^2. Since the expected value of $\{a_n\}$ is zero, the ARMA(p, q) model (3.3.8) can be also put in the form

$$z_n = a_n - \sum_{j=1}^{q} \theta_j a_{n-j} + \sum_{i=1}^{p} \phi_i z_{n-i} \tag{3.3.9}$$

from which, if $\{\theta_j\}_{j=1}^{q} = 0$ ($\{\phi_i\}_{i=1}^{p} = 0$) is selected, an AR(p) (MA(q)) model is obtained. In the above described procedure for DARMA modeling the coefficients of (3.3.8) have been evaluated as follows. The parameters $\{\theta_j\}_{j=1}^{q}$ of the MA(q) model have been computed recursively via the *innovations algorithm* of [85, p. 245], i.e. using the recursive expression

$$\theta_{q-k} = v_k^{-1} \left[R_z(q-k) - \sum_{j=0}^{k-1} \theta_{q-j} \theta_{k-j} v_j \right] \tag{3.3.10}$$

for $k = 0, 1, ..., q-1$, with $v_0 = R_z(0)$ and

$$v_k = R_z(0) - \sum_{j=0}^{k-1} \theta_{k-j}^2 v_j \tag{3.3.11}$$

for $k \geq 1$ (note that v_q corresponds to σ^2, i.e. to the variance of the samples of the process $\{a_n\}$ feeding the MA model), where

$$R_z(\tau) \doteq E[z_n z_{n+\tau}] = \frac{1}{N}\sum_{n=1}^{N-\tau} z_n z_{n+\tau} \tag{3.3.12}$$

denotes the autocorrelation of the stationary sequence $\{z_n\}$. The evaluation of the parameters $\{\phi_i\}_{i=1}^{p}$ of the AR(p) model is based, instead, on the *Yule-Walker equations* (e.g., see [84, pp. 96-97]); in other words the vector of the unknown parameters $\mathbf{\Phi}_p \doteq [\phi_1, \phi_2, \ldots, \phi_p]^T$ is computed as

$$\mathbf{\Phi}_p = \mathbf{P}_p^{-1}\mathbf{R}_p \tag{3.3.13}$$

where $\mathbf{R}_p \doteq [R_z(1), R_z(2), \ldots, R_z(p)]^T$is a p-dimensional vector,

$$\boldsymbol{P}_p \doteq \begin{bmatrix} 1 & R_z(1) & \cdots & R_z(p-1) \\ R_z(1) & 1 & \cdots & R_z(p-2) \\ R_z(2) & R_z(1) & \ddots & \vdots \\ \vdots & \vdots & \ddots & \vdots \\ R_z(p-1) & R_z(p-2) & \cdots & 1 \end{bmatrix} \tag{3.3.14}$$

is a $p \times p$ symmetric matrix; note that, in this case, the variance of the samples of $\{a_n\}$ is evaluated as

$$\sigma^2 = R_z(0) - \sum_{i=1}^{p} \phi_i R_z(i) \tag{3.3.15}$$

Generally speaking, the computation of the parameters of an ARMA(p, q) model is not as easy as that of its AR and MA counterparts, because of numerical stability problems [86, 87]. To overcome this problem, in the modeling procedure the Matlab function `armax.m` [88] has been exploited (such a procedure is based on an iterative algorithm for estimation of ARMA parameters [89]).

Any (AR(p), MA(q) or ARMA(p, q)) model based on the procedure illustrated above can be used to generate a stationary sequence $\hat{z}_n = \hat{z}_{y,s}$ (see eq. (3.3.4)) according to (3.3.9). Then, the cyclostationarity property can be restored through the inverse transformation $G^{-1}(\cdot)$ (see (3.3.7)); this generates the sequence

$$\hat{w}_{y,s} \doteq G^{-1}(\hat{z}_{y,s}) = \hat{z}_{y,s}\sigma_s + \mu_s \tag{3.3.16}$$

which represents a noise sequence whose statistical properties are similar to those of $\{w_n\}$.

The above mentioned procedure can be applied for any value of the model orders p and q. This raises the problem of selecting proper values for these parameters; unavoidably such values represent a tradeoff between statistical accuracy and computational complexity. In practice, in this model an index of the statistical accuracy is provided by the error

$$e_s \doteq \sum_{\tau=0}^{\tau_{order}-1} |R_{\hat{z}}(\tau) - R_z(\tau)| \tag{3.3.17}$$

between the autocorrelation function of the given model $R_{\hat{z}}(\tau)$ and that of the stationary sequence $\{z_n\}$ evaluated for $\tau = 0, 1, ..., \tau_{order}$ (here τ_{order} denotes the maximum lag for which the constraint (3.3.17) is set). For this reason, the orders (p, q) of the ARMA model (3.3.8) have been selected in a way that their sum $(p + q)$ is minimized, provided that the error e_s (3.3.17) remains below a given threshold $\bar{R}_s$, i.e.

$$e_s < \bar{R}_s \tag{3.3.18}$$

The same approach has been also adopted in the cases of AR(p) and MA(q) modeling; note that the adopted criterion always allows to identify the minimum order of the model characterized by a desired degree of statistical similarity with the deseasonalized sequence.

The modeling techniques described above is exploited to develop two distinct models, namely a short-term model and a long-term model. The final step of the procedure consists to select the model that best fits the acquired data; to this end, the model minimizing the error

$$e_c \doteq \sum_{\tau=0}^{\tau_{model}-1} |R_{\hat{w}}(\tau) - R_w(\tau)| \tag{3.3.19}$$

between the autocorrelation function $R_{\hat{w}}(\tau)$ of the devised DARMA model and that of the acquired sequence $\{w_n\}$ for $\tau = 0, 1, ..., \tau_{model}$ is selected (here τ_{model} denotes the maximum lag for which the autocorrelations appearing in (3.3.19) are evaluated). Note that:

- eqs. (3.3.17) and (3.3.19) are mathematically similar because both express a degree of statistical accuracy;
- in principle, the maximum lags τ_{order} (see (3.3.17)) and τ_{model} (see (3.3.19)) take on different values, since the former is related to the derivation of the model order, whereas the latter is involved in the selection between short-term model and the long-term counterpart.

In summary, the approach to noise modeling we propose evolves through the following steps:

1. The acquired noise sequence is passed through a proper band-pass FIR filter to generate the sequence $\{w_n\}$.

2. The long cyclostationarity period Y_L is selected according to (3.3.2) and the short cyclostationarity period Y_H is estimated according to (3.3.3).

3. The one-to-one mathematical transformation defined by eqs. (3.3.4)-(3.3.7) is applied to deseasonalise $\{w_n\}$.

4. For each cyclostationarity period (Y_L and Y_H):

   a) The parameters of the AR, MA or DARMA model ($\{\phi_i\}_{i=1}^{p}$ and/or $\{\theta_j\}_{j=1}^{q}$) are estimated on the basis of eqs. (3.3.10)-(3.3.11), (3.3.13)-(3.3.15) or the Matlab function `armax.m` [88], respectively; given the threshold $\bar{R}_s$, the orders (p and/or q) of AR, MA or ARMA models are derived in a way that the sum $(p+q)$ is minimized under the constraint (3.3.18).

   b) A new stationary sequence $\hat{z}_n = \hat{z}_{y,s}$ is generated through the devised model.

   c) The inverse transformation (3.3.16) is applied to $\{\hat{z}_{y,s}\}$ and the modeled periodic impulsive noise $\{\hat{w}_{y,s}\}$ is generated.

5. The short term and long term models are compared and the model minimizing eq. (3.3.19) is selected.

3.4 Numerical and experimental results

The procedure described in previous Section has been applied to develop statistical models for the periodic impulsive noise generated by the CRT LG FLATRON 795FT PLUS monitor. During the experimental campaign multiple sample functions of the impulsive noise process generated by this device have been acquired exploiting the measurement set-up described in Section 3.2. Each sample function has been passed through a 200 taps FIR pass-band filter, limiting the spectral components to the interval 1–30 MHz. The importance of filtering can be understood comparing Fig. 3.4.1, showing a portion of an acquired sample function before FIR filtering, with Fig. 3.4.2, illustrating a sample function after filtering; note that, in this case, pass-band filtering suppresses the residual power signal at $5\,Hz$ and the noise generated

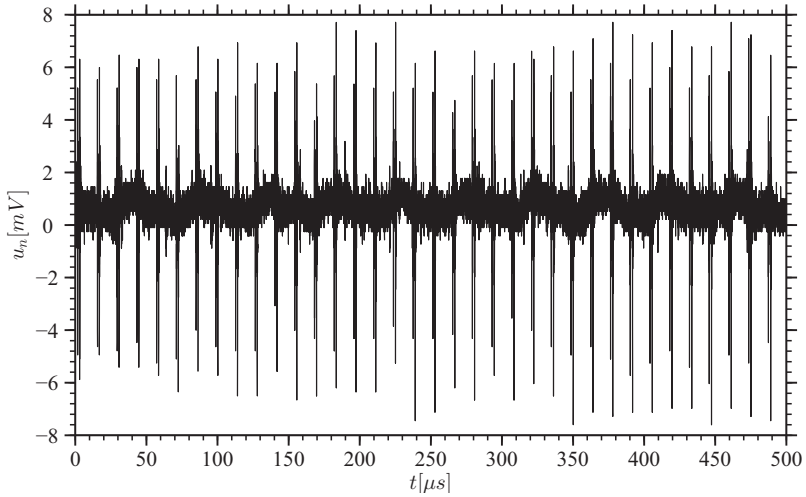

Figure 3.4.1: Sample function of the periodic impulsive noise process generated by a monitor.

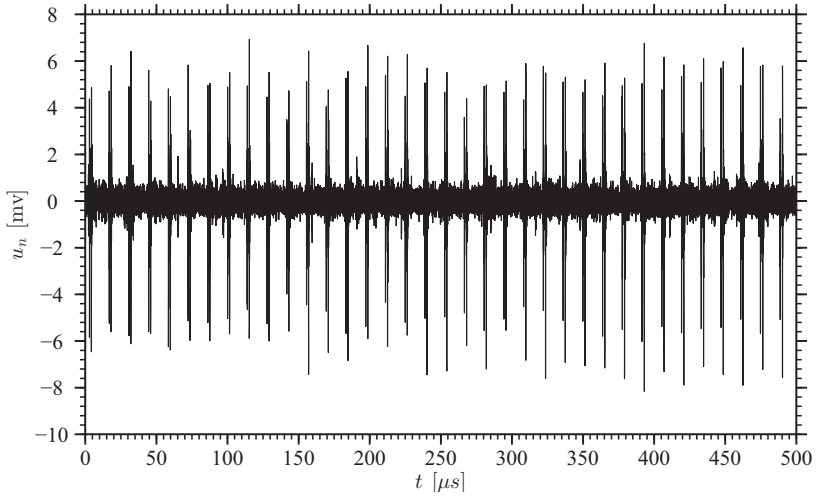

Figure 3.4.2: Output signal of a pass-band filter fed by the periodic impulsive noise generated by a monitor.

by switching supplies at few tens of kHz. Then, the sequence $\{w_n\}$ of filtered noise samples has been processed to assess the cyclic autocorrelation function $R_w(\alpha_k, \tau)$ (3.3.1); the contour plot of this function, shown in Fig. 3.4.3, has allowed us to establish that the short cyclostationarity period Y_H (3.3.3) corresponds to 1111 sampling intervals, i.e. it is associated with a cyclic frequency equal to 72 kHz. Given Y_L (3.3.2) and Y_H the deseasonalization method of eqs. (3.3.4)-(3.3.7) has been applied to develop a long term model and a short term model, respectively. In the following, for simplicity, the analysis is mainly focused on the short term model, the same considerations tare valid for the long term model. The deseasonalized time series referring to the short term model is illustrated in Fig. 3.4.4. A statistical analysis of this sequence has evidenced its wide-sense stationarity and its Gaussianity; it has been also found out, however, that the samples of this sequence are correlated, so that it cannot be modeled as a white process. Finally, AR, MA and ARMA models have been developed for the deseasonalized sequence, assuming a threshold $\bar{R}_s = 0.05$ (see eq. (3.3.18)) and $\tau_{order} = 71$. Unluckily, our analysis has shown that applying the deseasonalization method described by eqs. (3.3.4)-(3.3.7) to the whole acquired sequence leads to poor statistical accuracy because of the time instability of the cyclostationary statistics. In order to circumvent this problem, the deseasonalization method has been applied on a block-by-block basis, assuming that each block consists of the samples collected over 4 consecutive cyclostationarity periods (i.e., it consists of 4444 samples). The autocorrelation functions $R_{AR(56)}(\tau)$, $R_{MA(63)}(\tau)$ and $R_{ARMA(19,11)}(\tau)$ of the resulting AR(56), MA(63) and ARMA (19,11) models are compared with the autocorrelation function $R_z(\tau)$ of the deseasonalized model in Fig. 3.4.5. These results evidence that the developed ARMA model is more efficient than its AR and MA counterparts, since it satisfies the constraint (3.3.18) with a lower overall order.

A white Gaussian process having zero mean and variance $\sigma^2_{AR(56)}$, $\sigma^2_{MA(63)}$ and $\sigma^2_{ARMA(19,11)}$ has been adopted as an excitation signal for the AR(56), MA(63) and ARMA(19,11) models, respectively, and cyclostationarity has been reintroduced resorting to the inverse transformation (3.3.16). The autocorrelation functions $R_{\widehat{AR(56)}}(\tau)$, $R_{\widehat{MA(63)}}(\tau)$ and $R_{\widehat{ARMA(19,11)}}(\tau)$ characterizing the seasonalized models are compared with the autocorrelation function of the acquired sequence $R_w(\tau)$ in Fig. 3.4.6. These results show that a substantial accuracy is achieved by the noise simulator in the short term, i.e. for $\tau_{model} \leq 8000$. Note, however, that the parameters of the above mentioned models have been computed applying the deseasonalization method to short blocks, so that the long term statistical properties of the periodic noise process are not properly represented. In fact, further results (not shown here for space limitations) have evidenced that the autocorrelation of these short term models for large lags

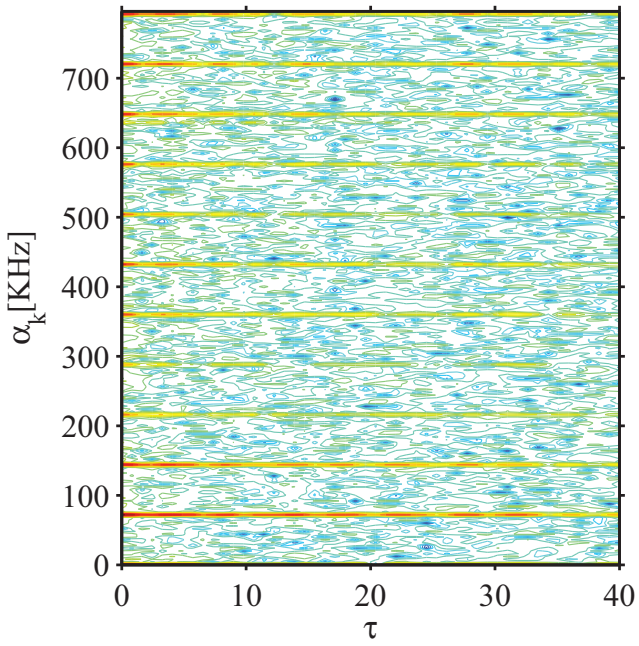

Figure 3.4.3: Contour plot of the cyclic autocorrelation function $R_w(\alpha_k, \tau)$ of the impulsive noise generated by a monitor.

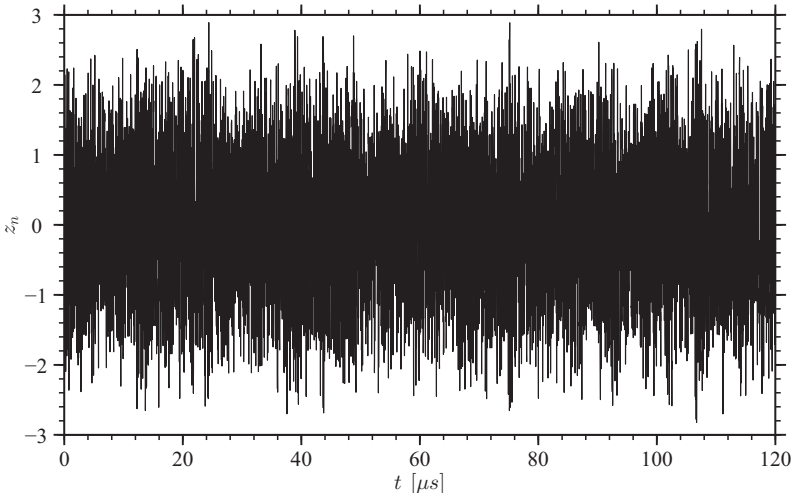

Figure 3.4.4: Deseasonalized sequence $\{z_n\}$.

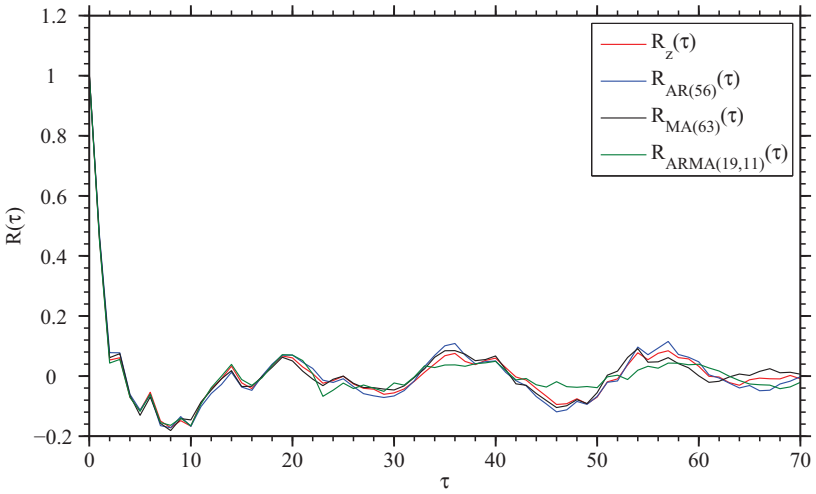

Figure 3.4.5: Comparison between the autocorrelation function $R_z(\tau)$ of the deseasonalized sequence $\{z_n\}$ and the autocorrelation functions $R_{AR(56)}(\tau)$, $R_{MA(63)}(\tau)$ $R_{ARMA(19,11)}(\tau)$ characterizing the developed statistical models.

($\tau_{model} > 20000$) does not carefully match that of the original time series.

Finally, we would like to mention that in our work models for the periodic impulsive noise generated by a portable fridge Ardes TK58 have been also developed. In this case we found out that the long term model provides a better statistical accuracy than its short term counterpart independently of the considered lag τ_{model}. This result can be motivated analysing the contour plot of the time-variant cyclic autocorrelation function

$$R_w(\alpha_k, \tau, t) = \frac{1}{2N_1+1} \sum_{n=t-N_1}^{t+N_1} w_n w_{n+\tau} e^{-j2\pi\alpha_k n} \tag{3.4.1}$$

for $\tau = 0$ and $N_1 = 50000$ (see Fig. 3.4.7). This function shows that the *noise statistics at high frequency evolve periodically and, in particular, are synchronous with the mains frequency.* In fact, the main cyclic frequency varies between 80 kHz and 100 kHz (the mean value is about 90 kHz) with a periodicity of 10 ms and the same periodicity is found for the absolute value of the cyclic autocorrelation function. These results lead to the conclusion that *the periodic impulsive noise generated by certain appliances is not cyclostationary in a strict sense*, so that the assumption of cyclostationarity, commonly made in the technical literature, may be questionable in some cases. A MA(100) long term model has been developed for the fridge under test; the accuracy of this model is evidenced by Fig. 3.4.8-(a) in the short period and

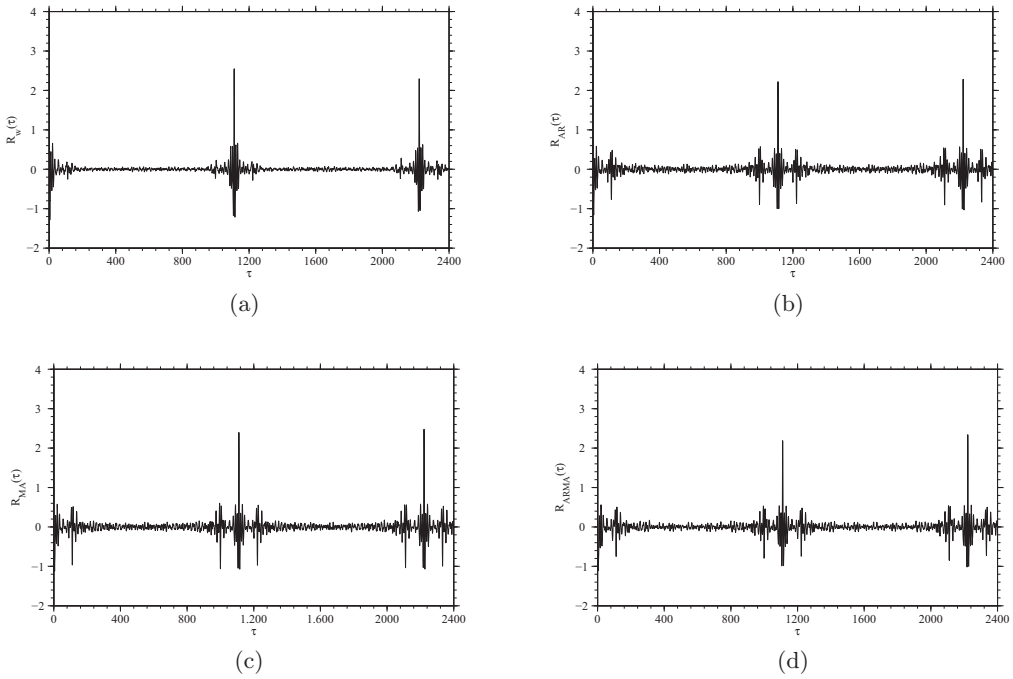

Figure 3.4.6: Comparison between the autocorrelation function $R_w(\tau)$ of the acquired sequence and the autocorrelation functions $R_{\widehat{AR}(56)}(\tau)$, $R_{\widehat{MA}(63)}(\tau)$ and $R_{\widehat{ARMA}(19,11)}(\tau)$ characterizing the developed seasonalized models.

by Fig. 3.4.8-(b) in the long period, comparing a sample function of the acquired noise with a sample function of the simulated noise.

3.5 Conclusions

In this chapter a novel approach to the problem of modeling the periodic noise that affects powerline communications in indoor scenarios and in the 1–30 MHz band has been illustrated. The presented approach relies on a large set of noise sample functions acquired in the laboratories of DIEF and on deseasonalized autoregressive moving average modeling of cyclostationary random processes. It has been shown that, given a set of experimental data, a simple automatic procedure can be used to extract AR, MA and ARMA models from them, capturing the short term or the long term statistical properties of the acquired periodic noise. The numerical results have evidenced that the proposed procedure can lead to simple and accurate models

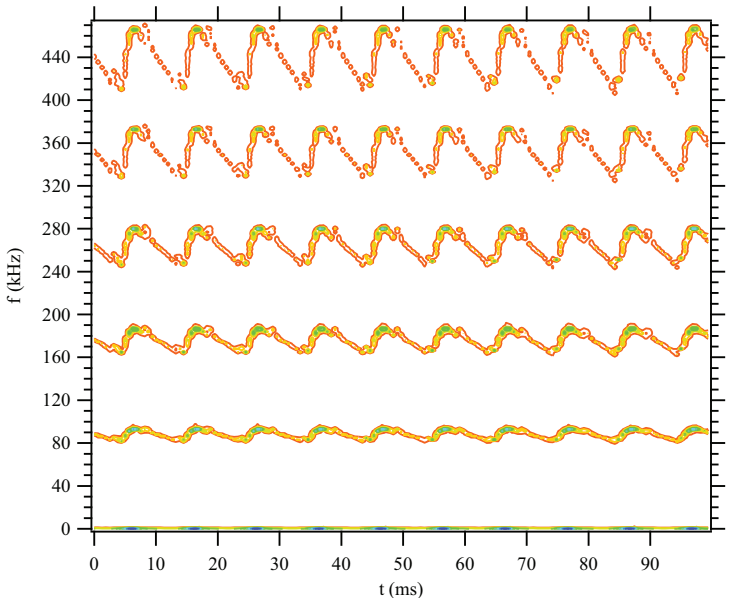

Figure 3.4.7: Time-variant cyclic autocorrelation function $R_w(\alpha_k, \tau, t)$ of the periodic impulsive noise generated by a fridge for $\tau = 0$.

and, consequently, is of great interest for emulating noise effects in computer simulations of powerline communication systems.

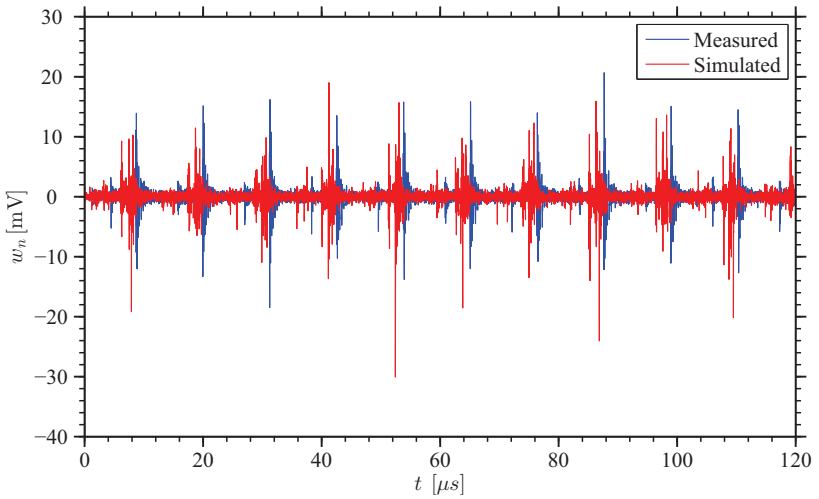

(a)

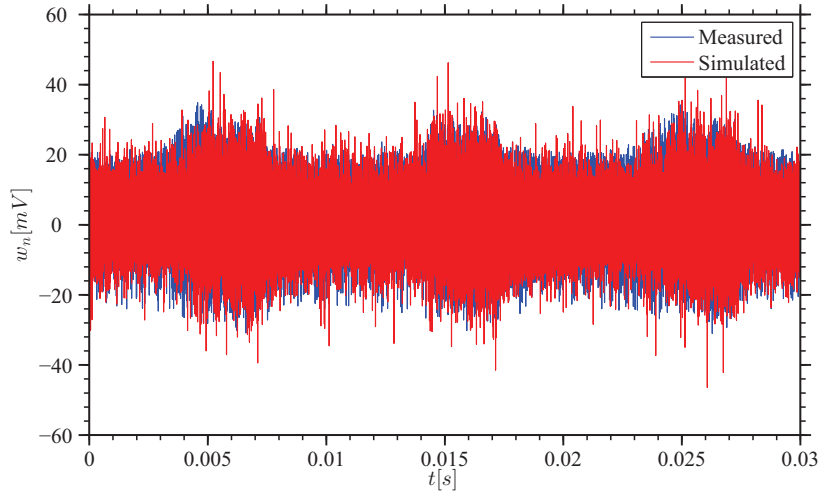

(b)

Figure 3.4.8: Comparison between a sample function of the periodic impulsive noise generated by a fridge with the sample function of a MA(100) noise model ((a) and (b) differ for the time scale only).

Chapter 4

Noise Modelling in OFDM Powerline Communication Systems

In this Chapter the impact of statistical noise modelling on the error performance achieved by OFDM over indoor broadband powerline channels is investigated. Different classes of statistical models suitable to represent powerline noise are illustrated and their impact on the error performance of a specific OFDM system is assessed via computer simulations. Numerical results generated by computer simulation are compared with the error performance provided by the same system in the presence of measured powerline noise; this evidences that a realistic indication of error performance can be achieved only if the power spectral density of the adopted noise model exhibits a good match with that of the measured noise. In practice, this result can be achieved modelling the poweline noise as a Moving Average (MA) random process of proper order; however a satisfying match can be achieved if other simple noise models available in the technical literature are adopted.

This Chapter is organized as follows. A brief summary of the noise models avalaible in the technical literature is given in Section 4.1, whereas in Section 4.2 the method exploited to analyse the error performance provided by OFDM systems in the presence of such models is described.Section 4.3 provideds a detailed description of the OFDM-based communication system considered in computer simulations. In Section 4.4 some indications about the experimental set-up adopted in acquiring a set of channel noise realizations in an indoor scenario are provided, whereas an overview of the statistical noise models considered in this Chapter is given in Section 4.5. The error performance achieved by the analyzed communication system in the presence of measured and model-based channel noise is analyzed in Section

4.6. Finally, some conclusions are given in Section 4.7

4.1 State of the art

Recently, the growing recent interest in PLC has fostered research activities on channel modelling for indoor power grids [90, 96]. Various research results available in the technical literature evidence that the properties of indoor powerline channels are usually very different from their wireless counterparts. In fact, such channels should be often modelled as Linear Periodically Time-Varying (LPTV) systems (e.g., see [50, 74, 91, 92] and references therein); in addition, the noise process affecting them is not usually stationary [28, 75, 93, 94, 95, 96], white [40, 78, 79, 98, 99] and Gaussian [76, 80, 100, 129], and should be represented as the superposition of distinct components, characterized by different statistical features. Despite the apparent complexity of noise modelling, various attempts have been made to develop simplified parametric statistical models for this channel impairment. In particular, cyclostationary models, based on adapting the instantaneous PSD of channel noise to experimental measurements, have been proposed in [28, 75, 78, 93, 94, 95, 96, 97, 99]. Other contributions in this research field have aimed at providing an accurate characterization of the *probability density function* (pdf) of the impulsive component of powerline noise [79, 80, 100, 129]. It is also worth mentioning that in most of the available technical literature the parameters of the proposed noise models are extracted from a set of experimental data; then, the impact of such models on the performance of specific PLC systems is assessed by means of computer simulations [79, 80, 95, 97, 129, 153].

4.2 Introduction

This Chapter analysis the problem of statistical noise modelling for powerline data communications based on OFDM[1] from a perspective different from that commonly taken in the technical literature. In fact, the investigation aims at showing which statistical noise models should be adopted in the simulation of an OFDM-based communication system operating in indoor scenario when a realistic estimate of its Bit Error Rate (BER) performance has to be acquired. To this aim the following procedure has been adopted:

[1]The interest in this modulation format is motivated by the fact that it has been adopted in modern broadband PLC standards (e.g., IEEE P1901 and HomePlug).

1. Various realizations of the channel noise affecting powerline communications in the band $2 - 30$ MHz have been acquired by means of the broadband channel sounder described in [50, 91] and have been stored in a database.

2. A computer-based simulator of an OFDM-based communication system for indoor data communications has been developed. Then, the BER performance of the considered system has been assessed in the presence of the measured channel noise and in the presence of a channel transfer function represented by the realistic statistical model proposed in [39].

3. The noise masurements have been processed to estimate the parameters of various noise models available in the technical literature. Then, such models have been incorporated in the system simulator and the BER system performance has been assessed for each of them. This has allowed to compare the gap between the performance achieved in the presence of measured channel noise and that resulting from its model-based counterparts, and, consequently, to assess the accuracy of the considered noise models from a system performance perspective.

4.3 System model

In this Section a brief description of the OFDM-based communication system implemented in the developed software simulator is provided.

The adopted OFDM modulator, whose block diagram shown in Fig. 4.3.1a, generates the transmitted signal directly in pass-band, so avoiding an explicit frequency up-conversion; this choice is motivated by the fact that the bandwidth of the modulated signal (28 MHz, if the band $2 - 30$ MHz is employed for powerline communications, as already mentioned above) is comparable with its center frequency (16 MHz in this case). The modulator operates as follows. Its input binary stream is partitioned in blocks, each consisting of $\log_2(M)$ bits, and every block is mapped to a channel symbol belonging to an M-ary Quadrature Amplitude Modulation (QAM) constellation. The resulting stream of channel symbols undergoes a serial-to-parallel conversion which generates a sequence of N_c-dimensional vectors, each containing N_c consecutive channel symbols: let $\mathbf{c}_{N_c}^{(l)} \triangleq [c_0^{(l)}, c_1^{(l)}, ..., c_{N_c-1}^{(l)}]^T$ denote the lth transmitted vector. Then, for any l, the vector $\mathbf{c}_{N_c}^{(l)}$ is processed as follows. First of all, a prefix of N_{pre} null symbols and a postfix of N_{post} null symbols are attached to $\mathbf{c}_{N_c}^{(l)}$. This ensures that: a) the given N_c data symbols are transmitted over N_c adjacent subcarriers frequen-

cies in the band $2-30$ MHz; b) $N_{sc}=N_{pre}+N_{post}$ subcarriers are suppressed in the band $0-f_s/2$, where $f_s=100$ MHz is the maximum sampling frequency of the OFDM simulator (see Section 4.4). This yields the vector $\mathbf{c}^{(l)}_{N_{FFT}/2}\triangleq[\mathbf{0}_{N_{pre}},\mathbf{c}^{(l)}_{N_c},\mathbf{0}_{N_{post}}]$, where $\mathbf{0}_N$ denotes a N-dimensional null row vector and $N_{FFT}\triangleq 2(N_c+N_{sc})$. Then, a prefix, generated by reversing the order and taking the conjugate of all the elements of $\mathbf{c}^{(l)}_{N_{FFT}/2}$, is attached to $\mathbf{c}^{(l)}_{N_{FFT}/2}$. This yields the N_{FFT} dimensional vector $\mathbf{c}^{(l)}_{N_{FFT}}$ characterized by an Hermitian symmetry, so that undergoing the vector $\mathbf{c}^{(l)}_{N_{FFT}}$ to an Inverse Fast Fourier Transform (IFFT) of order N_{FFT} leads to the real vector $\mathbf{d}^{(l)}_{N_{FFT}}$. Appending a Cyclic Prefix (CP) of N_{cp} symbols to $\mathbf{d}^{(l)}_{N_{FFT}}$ produces the cyclically extended vector $\mathbf{d}^{(l)}_{N_{FFT}+N_{cp}}$. After parallel-to-serial conversion, the vector $\mathbf{d}^{(l)}_{N_{FFT}+N_{cp}}$ undergoes digital-to-analog conversion at a symbol frequency equal to $f_s=1/T_s$ (where T_s denotes the sampeling period), transmit filtering with impulse response $p(t)$ (a bandpass Butterworth having order 100 and pass band $2-30$ MHz has been employed) and power amplification (the amplifier gain is denoted G_T in the following). This yields the OFDM real signal $s(t)$ containing N_c distinct subcarriers centered at the frequencies $\{f_k=k/(N_{FFT}T_s),\ k=N_{pre},N_{pre}+1,...,N_{pre}+N_c-1\}$. The real signal $s(t)$ feeds a powerline network characterized by the following relevant properties:

- it can be modelled as a linear time invariant system during the transmission of each OFDM symbol (in the following $h(t)$ and $H(f)$ denote the impulse response and the frequency response of the powerline channel);
- its impulse response changes in an independent fashion from symbol to symbol (i.e., a quasi static channel model is used);
- it introduces additive noise;
- it is structured according to a *branched-bus topology* [102, pp. 47-48].

The last assumption entails that the analyzed power network consists of multiple "backbones" (each representing, for instance, the power network of a distinct floor of a given building) departing from a single point to which a metering unit is connected; multiple branches originate from each backbone and lead to various power plugs. More specifically, the power network is characterized by the following features: a) it contains N_{BB} backbones, each having an overall number of branches ranging from $N_{B_{min}}$ to $N_{B_{max}}$; b) the distance that separates branches belonging to the same backbone is uniformly distributed over the interval $[L_{BC_{min}},L_{BC_{max}}]$; c) the length of each branch is uniformly distributed over the interval $[L_{B_{min}},L_{B_{max}}]$; d) each

of its power plugs may be either open with probability P_{open} or closed on a resistive load, whose resistance is uniformly distributed over the interval $[R_{min}, R_{max}]$.

The OFDM receiver, whose block diagram is shown in Fig. 4.3.1b, is endowed with an ideal timing reference and a perfect knowledge of the channel response (i.e., with ideal channel state information). In addition, it operates on a symbol by symbol basis; for this reason, in the following the analysis is carried out on the detection of a single symbol, namely $\mathbf{c}_{N_s}^{(0)}$ (denoted $\mathbf{c}_{N_s}$ in the following, for simplicity). When detecting $\mathbf{c}_{N_s}$, the received signal is first passed through a filter matched to the transmit filter (so that its impulse response is equal to $p(-t)$) and amplified (the amplifier gain is denoted G_R in the following). This produces the filtered received signal

$$r(t) = s(t) \otimes h(t) \otimes p(-t) + n(t) \tag{4.3.1}$$

where $n(t)$ denotes the filtered channel noise. The signal $r(t)$ (4.3.1) is uniformly sampled at the frequency f_s and $N_{cp} + N_{FFT}$ consecutive samples are acquired (an infinite precision is assumed in the digital-to-analog conversion). After discarding the first N_{cp} received signal samples (which are associated with the cyclic prefix), the remaining N_{FFT} samples undergo serial-to-parallel conversion and are collected in the vector $\mathbf{r}_{N_{FFT}} = [r_0, r_1, ..., r_{N_{FFT}-1}]^T$. This vector feeds a Fast Fourier Transform (FFT) of order N_{FFT} generating the frequency-domain vector $\mathbf{R}_{N_{FFT}} = [R_0, R_1, ..., R_{N_{FFT}-1}]^T$. It is not difficult to show that (e.g., see[101])

$$R_k = H_k c_k + N_k \tag{4.3.2}$$

for $k = N_{pre}, N_{pre} + 1, ..., N_{pre} + N_c - 1$, where

$$H_k = G_T G_R H(f_k) |P(f_k)|^2 \tag{4.3.3}$$

denotes the overall frequency response of the communication system evaluated at the kth subcarrier,

$$N_k = \sum_{m=0}^{N_{FFT}-1} n_m \exp(-j2\pi km/N_{FFT}) \tag{4.3.4}$$

represents the noise sample affecting R_k (4.3.2), and n_m is the sample of the channel noise process $n(t)$ affecting r_m (with $m = 0, 1, ..., N_{FFT} - 1$). Then, a portion of the vector $\mathbf{R}_{N_{FFT}} = [R_0, R_1, ..., R_{N_{FFT}-1}]^T$, namely the vector $\mathbf{R}_{N_c} = \left[R_{N_{pre}}, R_{N_{pre}+1}, ..., R_{N_{pre}+N_c-1}\right]^T$, is processed on a subcarrier-by-subcarrier basis. In particular, each element of $\mathbf{R}_{N_c}$ undergoes *zero-forcing* linear equalization and minimum Euclidean distance detection; this produces an estimate $\hat{\mathbf{c}}_{N_c} \triangleq [\hat{c}_0, \hat{c}_1, ..., \hat{c}_{N_c-1}]^T$ of $\mathbf{c}_{N_c}$. Then, each element of $\hat{\mathbf{c}}_{N_c}$ is demapped into $\log_2 M$

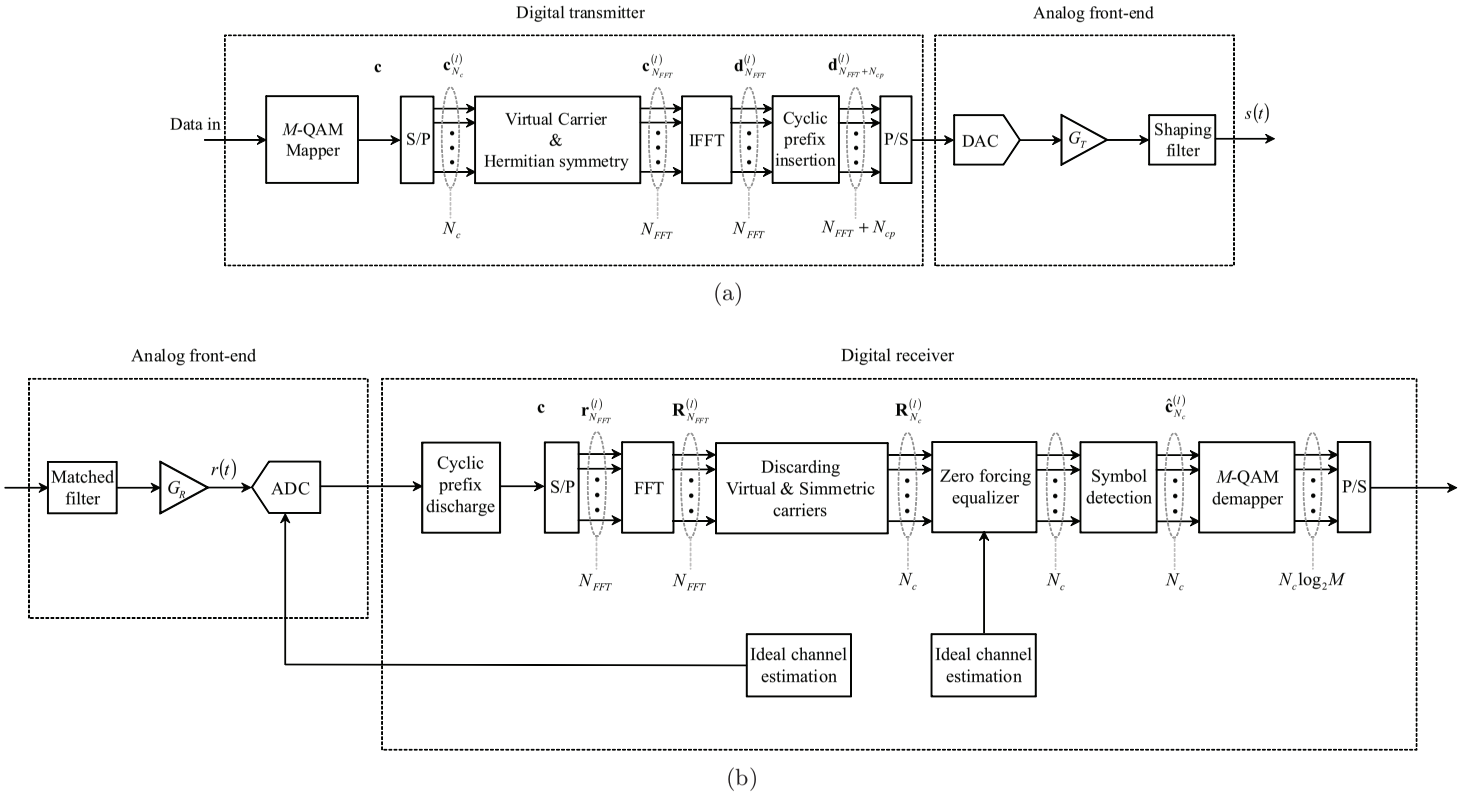

Figure 4.3.1: (a) Block diagram of the OFDM transmitter. (b) Block diagram of the OFDM receiver.

bits and the resulting $N_c \log_2 M$ bits undergo parallel-to-serial conversion, thus generating an estimate of the stream of transmitted bits.

Finally, it is worth pointing out that:

- Minimum Mean Squared Error (MMSE) equalization has not been employed in the receiver, since in a non-stationary scenario, the estimation of the variance of the noise affecting multiple subcarriers of the transmitted OFDM signal can represent a complicated task.

- The adopted detection strategy, being based on the minimization of an Euclidean distance, is optimal only in the presence of Additive White Gaussian Noise (AWGN); unluckily, as already mentioned in the Introduction, the powerline noise $n(t)$ is usually coloured and non-Gaussian. However, the derivation of an optimal detection strategy in the considered scenario is a complicated problem and is well beyond the scope of this analysis.

4.4 Experimental set-up

As already mentioned in the Introduction, the error performance of the communication system described in the previous Section has been assessed in the presence of powerline noise acquired in a real world scenario (namely, in the laboratories of the DIEF). The tool which has been employed during the measurement campaign to acquire a set of realization of the filtered channel noise $n(t)$ (see (4.3.1)) is the broadband powerline channel sounder described in the chapter 5 and in [91] (the adopted experimental set-up is shown in Fig. 5.7.1). This channel sounder consists of the following four basic blocks: 1) an analog front-end (right); 2) an ADC/DAC board (bottom) operating at the sampling frequency of $f_s = 100$ Msamples/s with a resolution of 14 bits; 3) a Stratix III EP3SL150F1152 development board (center); 4) personal computer (left).

In the first part of the measurement campaign our channel sounder has been employed to acquire various sample functions of the noise processes affecting different power plugs of the same environment (which includes a number of academic laboratories and offices). Then, these preliminary measurements have been analyzed to characterize the most significant noise components, namely synchronous impulsive noise, asynchronous impulsive noise and colored background noise.

4.5 Powerline noise models

It is well known that powerline noise can be represented as a combination of different random processes [76, 103], namely background noise, narrowband interference, synchronous periodic impulsive noise, asynchronous periodic impulsive noise and asynchronous impulsive noise. This makes the development of a unified statistical model accounting for the noise properties a formidable task. For this reason, in recent years different statistical models able to capture specific features of powerline noise have been developed. In this Section we analyze three important classes of statistical noise models, namely:

1. Models based on fitting the pdf of powerline noise samples [76, 80, 81, 100, 103, 104, 105, 106, 129].

2. Models based on fitting the PSD of powerline noise [98, 99, 33, 107, 108, 109].

3. Models based on fitting the statistical properties of powerline noise at the input of the hard decision device of a digital receiver [101, 129].

The selected classes of models deserve the following comments:

- On the one hand, in developing the first class of models it is assumed that the sequence of time domain noise samples $\{n_k\}$ extracted from filtered noise process $n(t)$ consists of independent and identically distributed (iid) *random variables* (rvs). On the other hand, the noise samples are modelled as *correlated* rvs in the study of the second class of models.

- The above mentioned classes of models share the following favorable features: the evaluation of their parameter requires a computationally easy fitting procedure and the resulting fitting error can be reduced to a fixed level quite easily. For this reason, in evaluating the error performance of a powerline communication system any gap between the performance achieved in the presence of measured noise and that achieved in the presence of the corresponding model can be usually ascribed to the nature of the model itself and not to the fitting procedure.

- In Section 4.6 it is shown that for an OFDM-based communication system a good match between the performance achieved with measured noise and that with modelled noise is provided by the second class of models. For these reasons, more complex noise models

(e.g., those based on Markov chains [93, 110] or on Poisson distributions [80, 111, 153]) have not been taken into consideration in our study.

In the following three Paragraphs a description of each of the above mentioned models is provided and their match with the experimental results is analyzed in detail.

4.5.1 Models based on pdf fitting

As already mentioned above, for this class of models it is assumed that the time domain sequence $\{n_k\}$ of noise samples consists of iid rvs, i.e. that its elements belong to a *white* random process. Unfortunately, experimental data have evidenced that such random variable (rv)s are not Gaussian [40, 78, 76, 100, 129]. However, in many cases a Gaussian Mixture (GM) [112, Chapt. 9] can be adopted to model each noise sample, so that its pdf can be expressed as

$$f_n(w) = \sum_{l=1}^{N_M} \frac{\lambda_l}{\sqrt{2\pi\sigma_l^2}} \exp\left(-\frac{(w-\mu_l)^2}{2\sigma_l^2}\right), \tag{4.5.1}$$

where N_M is the number of components of the mixture, whereas λ_l, μ_l and σ_l^2 are the probability, mean and variance associated with the lth Gaussian component, respectively. It is worth mentioning that this model is able to effectively approximate a large class of distributions (e.g., see [113] and the so called *Fan theorem* [114]). In addition, its parameters can be easily estimated resorting to the Expectation Maximization (EM) algorithm [115]. In principle, other distributions, like the Nakagami [76], the Middleton class A [104, 105] and the generalized Gaussian [129] distributions, could be employed to model powerline noise samples; however, in our investigation such models have been discarded for the following reasons:

1. The Nakagami distribution is suitable to model the amplitude of impulsive noise [76], but does not provide any information about the phase of noise pulses.

2. The Middleton class A distribution [104] has been introduced to describe man-made interference and has been exploited to assess the capacity of powerline channels affected by impulsive noise in [105]. This distribution relies on representing powerline noise as the superposition of a Gaussian process (background noise) with one or more impulsive random components. For this reason, its use requires identifying the number of impulsive components and evaluating so called Gaussian-to-impulsive power ratio; unluckily, these

tasks are not easy. In addition, it is known that a Middleton class A distribution can be accurately approximated by a GM distribution (e.g., see [116]).

3. The generalized Gaussian model has been introduced in [129] to model the noise affecting each subcarrier of an OFDM system employing Binary Phase Shift Keying (BPSK), i.a. a monodimensional constellation on each subcarrier. When bidimensional constellations (e.g., square constellations) are used, bivariate modelling is required to describe the joint statistical behavior of the in-phase and quadrature components of (complex) noise. Unluckily our results have evidenced that extending the approach proposed in [129] to the case of bidimensional constellations may lead to significant errors, especially when the distribution of measurements is appreciably non-Gaussian and/or multimodal.

4.5.2 Models based on PSD fitting

This class of models is based on representing the powerline noise as a coloured, wide-sense stationary, Gaussian random process with a given PSD. For this reason, such models are able to capture the correlation between noise samples, but usually do not account for the pdf characterizing each noise sample. This class is exemplified by the so called *Esmalian model* [107, 108], characterized by the single sided PSD

$$PSD_n(f) = A + B \cdot f^C \left[\frac{\text{dBm}}{\text{Hz}}\right], \tag{4.5.2}$$

where A, B and C are real parameters and by the so called *Omega model*, characterized by the PSD

$$PSD_n(f) = 10\log_{10}\left(\frac{1}{f^x} + 10^y\right)\left[\frac{\text{dBm}}{\text{Hz}}\right], \tag{4.5.3}$$

where x and y are real parameters. It is worth mentioning that $C = -1/2$ is often assumed in (4.5.2), so that this PSD becomes

$$PSD_n(f) = A + \frac{B}{\sqrt{f}}\left[\frac{\text{dBm}}{\text{Hz}}\right]. \tag{4.5.4}$$

Experimental campaigns have evidenced an exponential decrease of noise PSD as frequency gets larger; for this reason, the PSD expression

$$PSD_n(f) = N_0 + N_1 \exp\left(-\frac{f}{f_1}\right)\left[\frac{\text{dBm}}{\text{Hz}}\right], \tag{4.5.5}$$

has been proposed by Philipps; here, N_0 is the one-sided PSD of the (background) white component, whereas N_1 and f_1 are proper real parameters whose values are selected in a way to approximate the noise PSD at low frequencies.

The models (4.5.2)-(4.5.5) are simple but, unluckily, are unable to account for the presence of narrowband interferers that can play a significant role in some cases. For these reason, (4.5.5) has been modified as [109]

$$PSD_n(f) = N_0 + N_1 \exp\left(-\frac{f}{f_1}\right) + \sum_{k=1}^{N_I} A_k \exp\left(-\frac{(f-f_{0,k})^2}{2B_k^2}\right), \tag{4.5.6}$$

where A_k, $f_{0,k}$ and B_k represent the amplitude, frequency and bandwidth, respectively, of the kth interferer, with $k = 1, 2, ..., N_I$, and N_I denotes the overall number of narrowband interferers. In [109] a two-step procedure based on a median filter followed by a nonlinear filter has been proposed to separate the background noise from the narrowband interferers; however, no guidelines have been provided for the design of these filters and this has prevented us from considering the model (4.5.6) in this study. Despite this, some ideas illustrated in [109] have suggested us to adopt a MA model of order p [85] to represent the powerline noise in the same scenario as that for which the model has been devised (4.5.6). This model has the relevant feature that its parameters can be estimated through standard algorithms (e.g., the so called innovations algorithm [75]).

4.5.3 Models based on fitting the statistical properties of noise at the input of an hard detector

In assessing the error performance of an OFDM system via computer simulations, the frequency domain model (4.3.2) is often generated directly, i.e. the subcarrier gains $\{H_k,\ k = N_{pre}, N_{pre}+1, ..., N_{pre}+N_c -$ and the noise samples in the frequency domain $\{N_k,\ k = N_{pre}, N_{pre}+1, ..., N_{pre}+N_c-1\}$ are generated according to given distributions. For instance, in the field of wireless communications the noise samples $\{N_k\}$ are often modeled as iid Gaussian complex rvs; however the suitability of such a model to powerline communications has not been carefully investigated yet. For this reason, the following three features have been extracted from the measurements (all the parameters of the considered communication system are provided in Section 4.6):

1. The pdfs of the frequency domain noise samples for each subcarrier, in order to assess their degree of similarity with a bivariate Gaussian pdf.

2. The covariance

$$C_{m,k} = E\left\{(N_m - \mu_m)(N_k - \mu_k)\right\} \tag{4.5.7}$$

between the noise samples affecting the mth and the kth subcarriers, where μ_p denotes the mean of the noise samples $\left\{N_p^{(l)},\ l=0,1,...\right\}$ affecting the pth subcarrier in subsequent OFDM symbols; the estimation of this second order statistic is required to unveil if the property of "local" wide sense stationarity holds for the discrete time stochastic process $\left\{N_p^{(l)},\ l=0,1,...\right\}$.

3. The correlation coefficient
$$\rho_{m,k}=\frac{C_{m,k}}{\sigma_m\sigma_k}, \tag{4.5.8}$$
where σ_p denotes the standard deviation of the noise samples $\left\{N_p^{(l)},\ l=0,1,...\right\}$, with $m\neq k$; this coefficient allows us to assess the correlation degree between noise samples affecting close subcarriers.

First of all, in processing the noise samples affecting the kth subcarrier (with $k=N_{pre},N_{pre}+1,...,N+N_c$), the pdf of the noise sequence $\left\{N_k^{(l)},\ l=0,1,...\right\}$ has been estimated as the GM with $N_M=3$ components achieving the best match with experimental data; this has lead us to generating a family of functions $\left\{\hat{f}_k\left(n\right),\ k=N_{pre},N_{pre}+1,...,N_{pre}+N_c-1\right\}$, where $\hat{f}_k\left(n\right)$ denotes an estimate of the noise pdf $f_k\left(n\right)$ for the kth subcarrier. Our results have evidenced that:

- The estimated pdfs usually exhibit substantial deviations from a bivariate Gaussian PDF.
- On most of the subcarriers the noise pdf exhibits a multimodal behavior and a good match with experimental data is provided by a bivariate GM model characterized by few components; this is exemplified by Fig. 4.5.1, showing GM models characterized by $N_M=3$ components for a couple of subcarriers (we have accurately checked that no overfitting occurs).
- In our scenario the generalized Gaussian model proposed in [129] achieves poor accuracy.

Then, the covariances $\{C_{m,k}\}$ and the corresponding correlation coefficients $\{\rho_{m,k}\}$ have been evaluated for all the possible couples of useful subcarriers. Our results have shown that:

- A negligible correlation between the samples of frequency domain noise affecting distinct subcarriers is found in the band $12-30\,\mathrm{MHz}$; noise correlation becomes more significant, but is still weak, in the band $2-12\,\mathrm{MHz}$, as evidenced by Fig. 4.5.2 that shows the amplitude of the estimated correlation coefficients $\{\rho_{m,k}\}$;

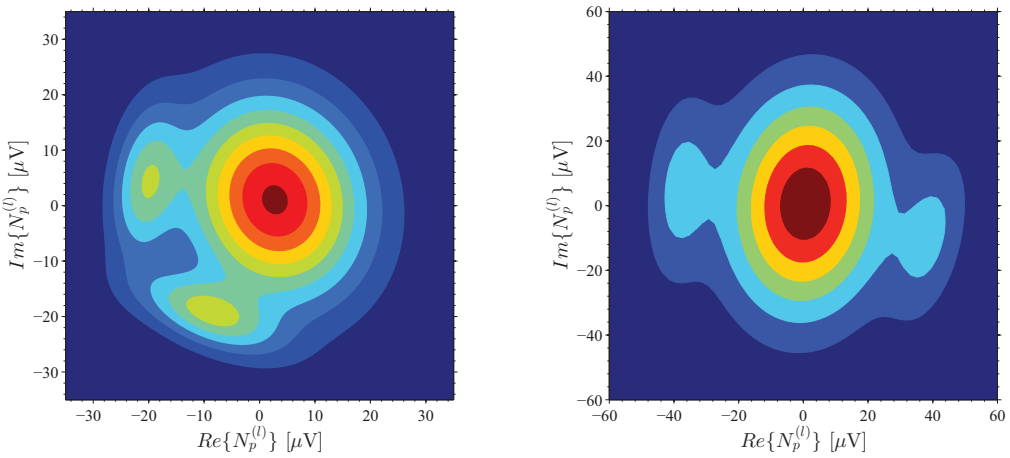

(a) (b)

Figure 4.5.1: GMapproximation for the bivariate pdfs of the complex noise affecting the subcarriers centered at (a) 6.787 MHz ($k = 140$) and (b) 7.812 MHz ($k = 161$) in an OFDM transmission.

- The variance of noise samples may change from subcarrier to subcarrier;
- The correlation between noise samples referring to a given subcarrier, but affecting adjacent OFDM symbols, is negligible.

The above mentioned results have lead us to the conclusion that in the considered scenario a simple Frequency Domain Noise Model (FDNM) can be developed to assess the error performance of an OFDM system; this statistical model has the following properties:

- the noise samples affecting a given subcarrier over consecutive OFDM symbols and the noise samples affecting distinct subcarriers of a given OFDM symbols are statistically independent;
- each noise sample can be accurately represented by a bivariate GM whose parameters change from subcarrier to subcarrier according to the measured PSD.

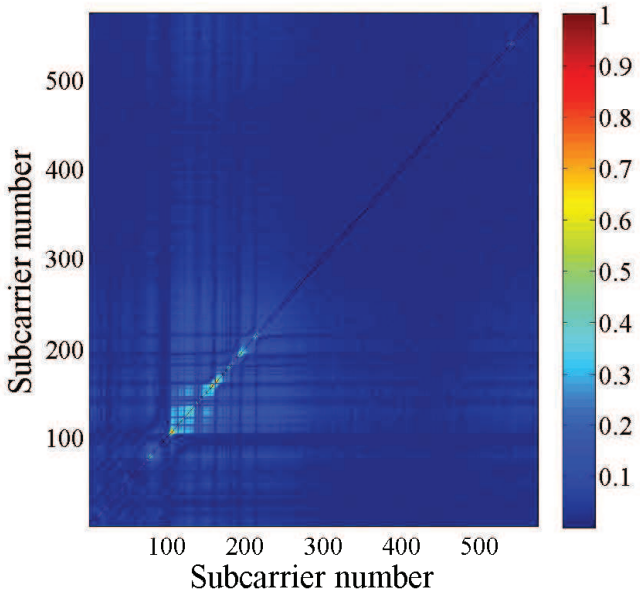

Figure 4.5.2: Absolute value of the cross correlation coefficient $\rho_{m,k}$ evaluated for the noise samples affecting the subcarriers of an OFDM system that operates in the band 2-30 MHz.

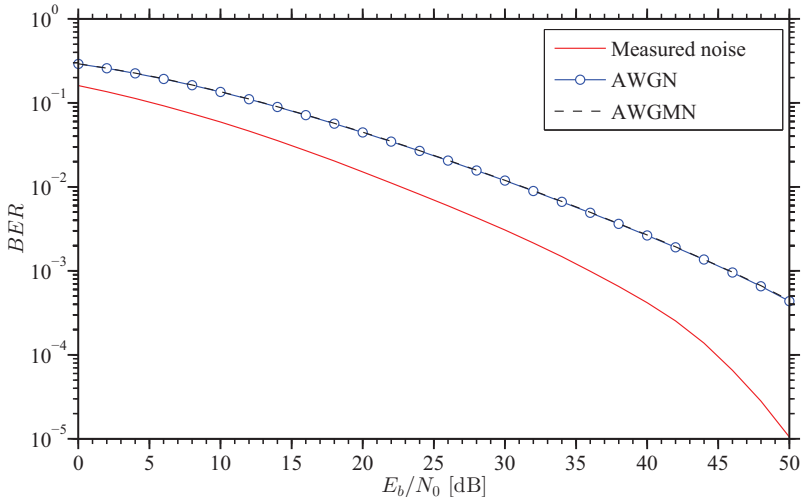

Figure 4.5.3: BER performance assessed in the presence of an AWGN model, an AWGMN model and the measured noise.

4.6 Numerical results

The influence of powerline noise modelling on the error performance of a specific OFDM communication system has been assessed via computer simulation. In particular, the selected OFDM modulation is characterized by the following parameters: a) useful band: $2-30$ MHz; b) symbol period: $T_s = 1/f_s = 10$ ns; c) data rate: 75.3 Mbps; d) FFT order: $N_{FFT} = 2048$; e) number of useful subcarriers: $N_c = 574$ (with $N_{pre} = 39$, $N_{post} = 411$); f) CP length: $N_{CP} = 1000$ (the resulting CP duration is equal to $N_{CP}T_s = 10\,\mu s$); g) constellation: 16-QAM over each subcarrier ($M = 16$).

The simulated powerline communication channel has the following features: a) number of backbones: $N_{BB} = 5$; b) minimum and maximum number of branches for each backbone: $N_{B_{min}} = 1$ and $N_{B_{max}} = 6$, respectively; c) minimum and maximum distance separating two branches on the same backbone: $L_{BC_{min}} = 1$ m and $L_{BC_{max}} = 4$ m, respectively; d) minimum and maximum length of each branch: $L_{B_{min}} = 0.5$ m and $L_{B_{max}} = 2$ m, respectively; e) minimum and maximum resistive load: $R_{min} = 10\,\Omega$ and $R_{max} = 3000\,\Omega$, respectively; f) probability of an open plug: $P_{open} = 0.3$. It is worth pointing out that the root mean square delay spread of the simulated channel is equal to 1.1 μs and is much shorter than the CP duration ($10\,\mu s$), so that inter-block interference is avoided at the receive side.

As far as the simulation of channel noise is concerned, the use of different models has been taken into consideration. First of all, the impact of the pdf selected for the time domain noise samples $\{n_k\}$ on the error rate performance has been assessed considering: 1) a complex AWGN sequence with a given variance; 2) a complex Additive White Gaussian Mixture Noise (AWGMN). The noise variance in the first case and the parameters of the GM (4.5.1) in the second one have been extracted from our measurments. Figure 4.5.3 compares the BER performance assessed in the presence of measured noise with that achieved in the presence of the above mentioned two noise models; note that the Signal-to-Noise Ratio per bit (SNR_b) has been evaluated as the ratio between the average received energy per bit of the useful signal component and the average one-sided noise PSD evaluated over the selected transmission band. These results evidence that: a) an accurate fitting of the noise pdf (via a GM model in this case) has a negligible impact on error performance; b) neglecting the correlation of noise samples (i.e., assuming a flat PSD) may lead to really poor accuracy in the assessment of error performance (the energy gap between measured and estimated performance may be as large as 10 dB). Therefore, to make noise modelling realistic, the correlation of time domain noise samples (or, equivalently, the shape of noise PSD) has to be carefully accounted for. This poses

a serious problem because the powerline noise is not stationary [28, 75, 93, 94, 95, 96, 97] and, in principle, models based on approximating the PSD could not be applied. However, the noise process can be considered almost-cyclostationary with a fundamental frequency of 100 Hz (i.e. twice the mains frequency of 50 Hz) [28, 75, 94, 95, 96, 97], so that the PSD of the noise can be estimated over a time support of 10 ms (corresponding to one period of cyclostationary); note that this approach does not limit the generality of our study, since 10 ms represents a very long time with respect to the OFDM symbol duration of $(N_{IFFT} + N_{CP})\, T_s \simeq 30\, \mu s$. Then, the following approach to PSD fitting and noise modelling has been pursued. First of all, an Autoregressive (AR) model of order p has been considered, and the PSD of the measured noise samples $\{n_m\}$ has been estimated as [85]

$$PSD_{AR}(f) = \frac{\sigma_z^2}{\left|1 - \sum_{m=1}^{p} \phi_m \exp\left(-j2\pi m f T_s\right)\right|^2}, \tag{4.6.1}$$

where σ_z^2 is the variance of the discrete time white noise process feeding the model and $\{\phi_m\}_{m=1}^{p}$ are its taps; note that these parameters can be easily extracted from the acquired samples resorting to the so called Yule-Walker method. Then, the parameters of the Esmalian (4.5.2), Omega (4.5.3), simplified-Esmalian (4.5.4) and Philipps (4.5.5) models have been extracted from $PSD_{AR}(f)$ (4.6.1) using a Least Squares (LS) approach. In practice, for the considered observation interval, the following values have been identified: a) Esmalian model: $A = -144$ dBm/Hz, $B = 443$ dBm/Hz^2, $C = -0.10$; b) simplified-Esmalian model: $A = -156$ dBm/Hz, $B = 521$ dBm/Hz^2; c) Omega model: $x = 2.01$, $y = -14.7$; d) Philipps model: $N_0 = -144$ dBm/Hz, $N_1 = 63$ dBm/Hz, $f_1 = 2.86$ MHz.Finally, the corresponding noise processes have been generated feeding a filter characterized by the frequency response $G(f) = \sqrt{PSD_n(f)}$ with a white Gaussian noise process of proper variance [109], where $PSD_n(f)$ denotes the PSD of one of the above mentioned models.

Fig. 4.6.1 compares the PSD of the measured noise ($p = 100$) and those estimated with the models (4.5.2)-(4.5.5) in the considered scenario. From these results it is easily inferred that the PSD models (4.5.2)-(4.5.5) are unsuitable to provide an accurate representation of the measured PSD shape; this is mainly due to the fact that the related smooth functions cannot adequately account for the presence of narrowband interferers. On the contrary, an accurate approximation is obtained adopting an MA model of proper order; this is exemplified by Fig. 4.6.2, which compares the PSD of the measured noise with that of an MA model of order $p = 1000$ (briefly, an MA(1000) model), whose parameters have been assessed by means of the innovations algorithm illustrated in [75].

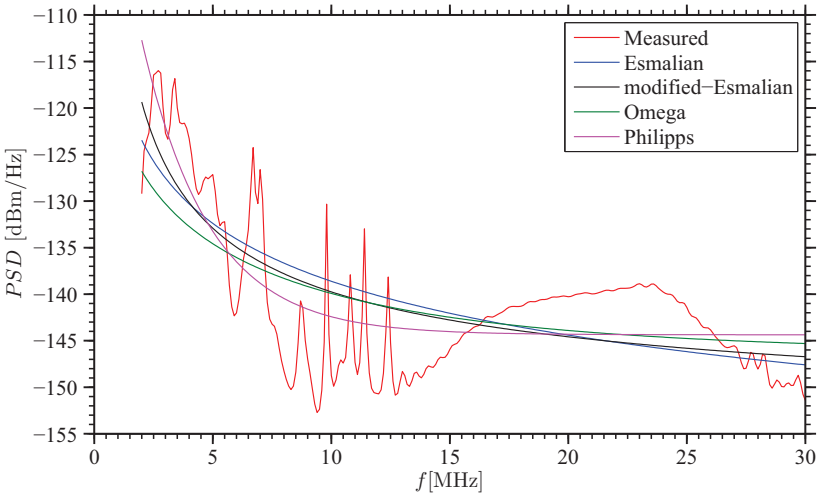

Figure 4.6.1: Comparison between the PSD of the measured noise and that of the models (4.5.2)-(4.5.5).

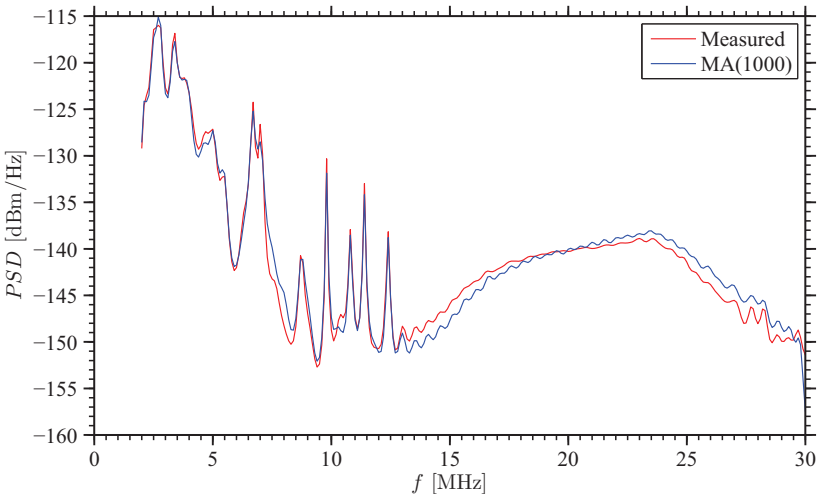

Figure 4.6.2: Comparison between the PSD of the measured noise and that of an MA(1000) model.

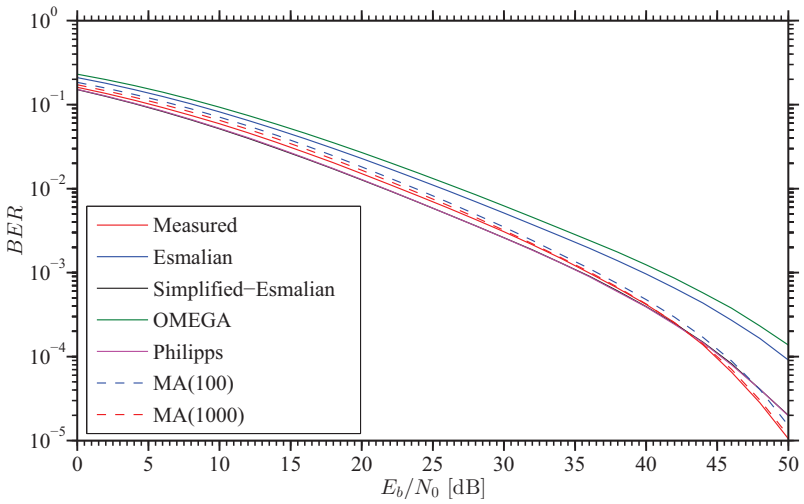

Figure 4.6.3: BER performance achieved in the presence of the measured noise, the noise models based on (4.5.2)-(4.5.5), a MA(100) model and a MA(1000) model.

It should be expected that a substantial mismatch between the PSDD of measured noise and that of a noise model may lead to a relevant performance gap in terms of BER. This idea is exemplified by Fig. 4.6.3, which compares the BER performance of the OFDM system operating in the presence of measured noise with the BER performance achieved in the presence of the PSD models (4.5.2)-(4.5.5), MA(100) model and MA(1000) model. On the one hand, the BER performance achieved with the simplified-Esmalian (4.5.4), Philipps (4.5.5) and MA models is very close to that obtained with the measured noise (the energy gap is limited to ± 1 dB); on the other hand, a substantial mismatch is found with the Esmalian (4.5.2) and Omega (4.5.3) models, since the energy gap is larger than 5 dB. These results evidence that the PSD represents a fundamental property of the noise to be captured by any powerline OFDM simulator, since its shape significantly affects the BER achievable over each subcarrier. For the sake of fairness, it is also important to note that the use of MA models involves a computational complexity by far larger than that required by the simplified-Esmalian (4.5.4) and Philipps (4.5.5) models; however, the computational burden entailed by noise generation is always negligible with respect to that required for OFDM demodulation.

Finally, the impact of the model adopted in generating the frequency domain noise samples $\{N_k\}$ (see (4.3.2)) on the error performance is investigated, since the received signal is often generated directly in the frequency domain. In particular, the BER performance achieved in

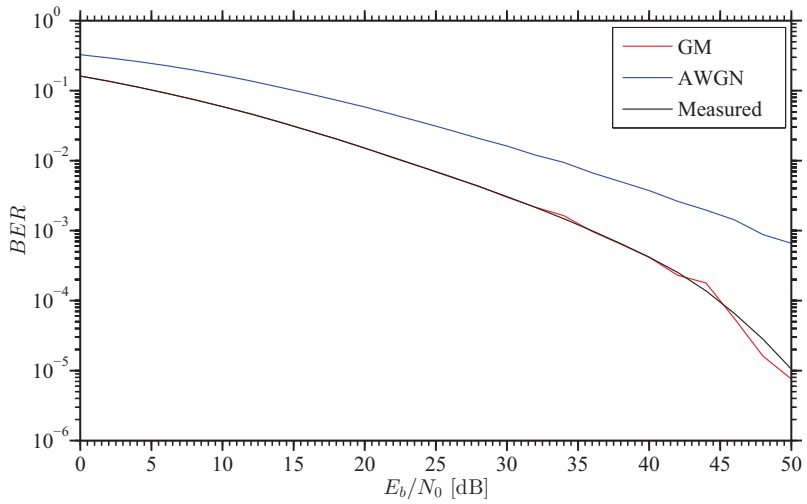

Figure 4.6.4: BER performance achieved in the presence of measured noise, an FDGM model and an FD-AWGN model.

the presence of the FDNM (see Section 4.5.3) has been compared with that usually achieved by OFDM simulators, according to which frequency domain noise samples $\{N_k\}$ can be represented as iid complex Gaussian rvs (this model is dubbed Frequency Domain Additive White Gaussian Noise (FD-AWGN), in the following). The BER performance of the OFDM system employing the noise samples $\{N_k\}$ measured in the frequency domain is considered as reference. Fig. 4.6.4 shows that, on the one hand, an excellent match can be achieved with the FDNM, for which the energy gap is limited to a small fraction of dB; on the contrary, the FD-AWGN model is unable to reproduce the physical behavior of powerline noise, since the energy gap is larger than 15 dB at high SNR_bs.

4.7 Conclusions

In this chapter the impact of statistical noise modelling on the error performance achieved by anFDNM communication system has been investigated. The presented study is based on an experimental database of noise realizations collected in an indoor power grid. The availability of experimental data has allowed to assessFDNM performance in the presence of broadband powerline noise measured in a real world scenario. The results have evidenced that the shape of the noisePSD plays a fundamental role and represents the main feature to be captured by an

accurate noise model. In addition, it has been shown that the commonly adopted FD-AWGN model is unable to account for the BER performance provided by anFDNM system in the presence of broadband powerline noise.

Part II

Time Varying Modelling of Indoor Powerline Channels

Chapter 5

Design and Implementation of a Powerline Channel Sounder

Estimating the input-output behavior of low voltage powerline channels for indoor high speed data communications requires the availability of proper wideband channel sounding tools. In fact, the properties of real world powerline channels are substantially different from those commonly exhibited by their wireless counterparts, so that standard methods for wireless channel sounding cannot be adapted to a powerline scenario. In this Chapter, after providing some general design guidelines for powerline channel sounding, a detailed description of a FPGA-based implementation of a wideband powerline channel sounder is provided. Such a tool is based on low cost hardware and is flexible, since it can be easily customized to user needs using a set of simple graphical user interfaces. Some of its specific applications, namely the estimation of the time-varying transfer function of an indoor powerline channel and the evaluation of the power spectral density of the noise affecting it, are illustrated to show the potentialities of the developed equipment.

This Chapter is organized as follows. Section 5.1 provides a brief overview of the tools for the investigation of powerline channels. In Section 5.2 some design requirements for powerline channel sounding are provided. The architecture of the developed channel sounding tool is described in Section 5.3. Various technical details about this tool are provided in Sections 5.4, 5.5 and 5.6, which focus on its analog front-end, FPGA processing and graphical user interfaces, respectively. Some experimental results are illustrated in Section 5.7, where specific applications of the sounder are taken in consideration; in particular, its use for acquiring the time-variant transfer function of an indoor powerline channel and the power spec-

tral density of the noise affecting it are discussed. Finally, Section 5.8 offers some conclusions.

5.1 State of the art

In the last few years powerline technology has become a commercially attractive alternative to wireless technology for in-home applications requiring high speed data communications. This success has fostered research in wideband communications over low voltage powerlines and, in particular, has motivated the interest in a deeper understanding of the properties of their propagation medium. Unfortunately, the properties of real world powerline channels are substantially different from those of their wireless counterparts in terms of system functions and noise; for instance, the frequency response of such channels is usually periodic [50], so that standard methods for wireless channel sounding (e.g., see [51], [52] and references therein) cannot be adopted for its measurement. This raises the problem of developing new channel sounding tools. Even if some powerline channel emulators have been proposed [53], [54], [55] or have been made available on the market [56], the problem of designing and implementing technical solutions for wideband sounding of powerline channels has not been tackled yet in the technical literature. This chapter aims at filling this gap by providing some design guidelines for powerline channel sounding and by describing a specific low cost FPGA-based implementation of a powerline channel sounder.

5.2 Design requirements for the sounding of wideband powerline channels

Channel sounding tools commonly rely on simple theoretical principles. In fact, the response of a given communication channel can be usually related to its excitation through a specific system function (e.g., the channel transfer function) in a simple fashion. Then, if the excitation (i.e., the *probing signal*) is properly selected, in principle an estimate of the involved system function can be easily extracted from a set of samples of the channel response. However, when applied to wideband sounding of powerline channels, the implementation of this procedure on a digital hardware platform requires addressing carefully various technical issues; these lead to various design requirements, as discussed in detail below.

Signal generation and acquisition - The probing signal generated by a channel sounder is employed to scan a specific portion of the available frequency spectrum. In powerline commu-

nications two different bands have been standardized [57, 58]; one consists of the frequencies lower than 500 kHz (allocated mainly for home and building automation as well as for applications related to the smart grid), whereas the other one covers the frequency range $1.8 - 30$ MHz (devoted to high data rate applications). The channel sounder described in this chapter has been designed to sound powerline channels up to 30 MHz. This entails that, if a digital hardware platform is used for the generation of a probing signal, it has to be equipped with a Digital to Analog Conversion (DAC) device operating at a frequency f_s not smaller than $2 \cdot 30\,\text{MHz} = 60\,\text{MHz}$. In practice, in our channel sounding tool the frequency $f_s = 100\,\text{MHz}$ has been selected; note that this frequency is also employed by an Analog to Digital Conversion (ADC) device when acquiring the channel response to the probing signal. Another important technical issue concerning the probing signal is represented by the selection of its duration. In fact, powerline channels are LPTV [50, 53, 59]; in addition, their variations are synchronous to the mains [59] and are characterized by a period $T_0 = 10$ ms (if the mains frequency is equal to 50 Hz). Therefore, the duration of the probing signal depends on both the desired frequency resolution and the periodicity of time variations; in practice, one or more periods (i.e., $f_s T_0 = 10^6$ samples or a multiple of this quantity) need to be acquired in each measurement interval [50], so that the selected hardware platform has to be endowed with a fast memory access and a proper data storage capability. To address all the above mentioned technical issues, an FPGA Stratix III Digital Signal Processing development board [60] has been employed in the implementation of our tool. This board is based on an EP3SL150F1152 FPGA, which is able to operate at a maximum internal clock speed equal to 600 MHz and a maximum clock speed equal to 400 MHz in interfacing with its DDR2 memory [61]. In addition, the employed board is equipped with: a) one bank of DDR2 memory able to store 1 GByte and two DDR2 memory chips able to store 32 MBytes each (additional details about this are provided in Section); b) a GigaBit Ethernet port for exchanging data with a personal computer.

Coupling of the channel sounder with powerlines - The topology and the properties of cabling in low-voltage powerlines are usually unknown; in addition, the input impedance of the loads (e.g., home appliances) connected to them exhibit an unpredictable frequency dependent behavior. For these reasons, the impedance of powerlines is usually unknown and may undergo significant time variations (due to connection/disconnection of power loads), and, consequently, the output (input) impedance of the channel sounder cannot be matched to the input (output) impedance of the communication medium. This problem has to be carefully taken into account when designing the analog coupling circuit connecting the channel sounder

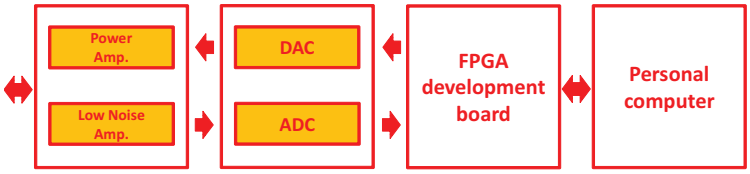

Figure 5.3.1: Block diagram of the developed channel sounder.

to a power network. In particular, a good protection of the low voltage circuitry of the sounder has to be guaranteed and low noise amplification has to be employed in signal acquisition, since probing signals may experience a deep attenuation.

5.3 Architecture of the developed channel sounder

The architecture of the channel sounding tool implemented in our labs is shown in Fig. 5.3.1. The developed tool consists of the following blocks: a Power Analog Front-End (PAFE), an interface for ADC and DAC, an FPGA development board and a personal computer. A description of the tasks accomplished by each block is provided below.

Personal computer - The personal computer provides the FPGA board with a sampled version of the probing signal and process the samples of the corresponding response acquired by the board itself. A software application based on Matlab and running on the personal computer has been developed to ease the use of the channel sounder. This application provides various simple *graphical user interfaces* (GUIs) for handling different high level tasks (e.g., generation of an arbitrary probing signal, start and stop of the measurement procedure and plot of the acquired data).

FPGA *development board* - All the *real-time* critical tasks of the channel sounding procedure are directly managed by the FPGA development board. In particular, during this procedure the FPGA feeds the data conversion interface with the samples of the probing signal to be sent over a powerline channel and at the same time stores in a DDR2 memory the samples of the channel response acquired by the interface itself in one or more consecutive periods (each lasting $T_0 = 10$ ms). At the end of each measurement, the acquired data are moved from the FPGA board to the personal computer through its Gigabit Ethernet interface.

Data conversion interface - The FPGA is equipped with an Altera HSMC data conversion interface [62] employed for the DAC of the probing signal and the ADC of the corresponding channel response. The main components of this interface are two Digital-to-Analog (D/A)

converters and two Analog-to-Digital (A/D) converters, all characterized by a 14 bit resolution and a $[-256, +256]$ mV dynamic range. In addition, the maximum operating frequency is 275 MHz and 150 MHz for the D/A converters and A/D converters, respectively.

The PAFE represents an interface between the powerline network and the data conversion interface. Its tasks are:

- decoupling the data conversion interface from the powerline network at low frequencies in order to prevent damages potentially due to the high voltage of the mains;
- feeding the powerline with a signal of proper amplitude (the output stage of the D/A converter is terminated on a $50\,\Omega$ resistance and is unable to generate an output current larger enough to drive a powerline network);
- amplifying the response of the powerline to the probing signal;
- ensuring impedance matching on the A/D converter input port.

Additional technical details about the PAFE, the FPGA development board and the GUIs are provided in Sections IV, V and VI, respectively.

5.4 Power analog front-end

In this Section the architecture of the PAFE is described first; then some details about its amplification chains and trigger generation are provided.

Front-end architecture

The architecture of the PAFE is illustrated in Figure 5.4.1. This block contains the following elements:

- A *power amplifier* for the signal generated by theD/A converter; this device has a voltage gain equal to $G_a = 1$, but is able to drive the powerline channel even in the presence of a very low input impedance.
- Two LNAs, characterized by the different (and selectable) voltage gains $G_1 = 1$ and $G_2 = 20$.

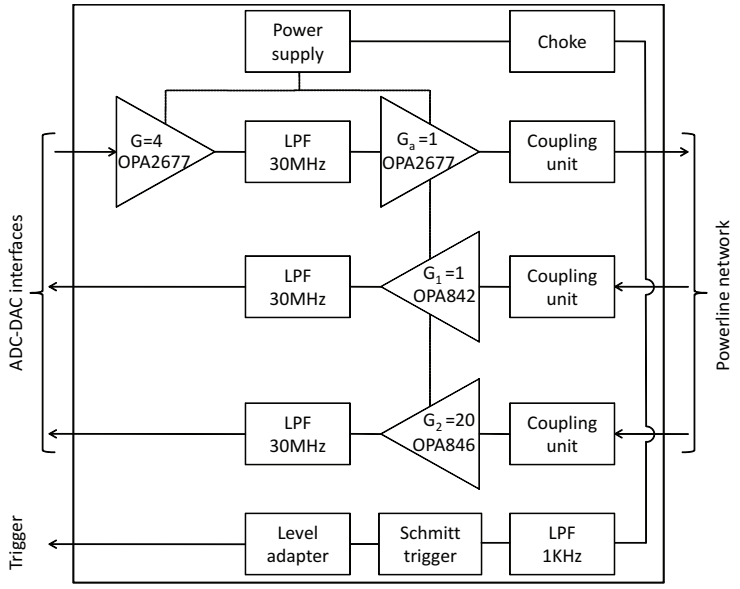

Figure 5.4.1: Block diagram of the PAFE.

- Three *Low-Pass Filters* (LPFs), each having a 30 MHz bandwidth; one of them is the image rejection filter of the D/A converter, whereas the other two are anti-aliasing filters for the A/D converters.

- Three *coupling units* protecting the data conversion interface from the mains voltage.

- A circuit (consisting of a LPF , a Schmitt trigger and a level adapter) for extracting a *trigger* signal from the mains voltage (this provides a useful time reference in the acquisition of the channel response, since channel variations are synchronous with the mains [50, 59][59]).

- A *power supply* section. Note that a choke inductor has been inserted between the PAFE power supply and the powerline network. This choice is motivated by the fact that the input impedance of the power supply, which is in parallel with the impedance of the powerline channel[1], can be quite low. Thanks to the choke, the impedance seen by the power amplifier is roughly equal to the input impedance of the powerline, so that the output signal of the power amplifier never experiences an excessive attenuation.

[1]Detailed information about powerline channel impedance can be found in [39] and [63].

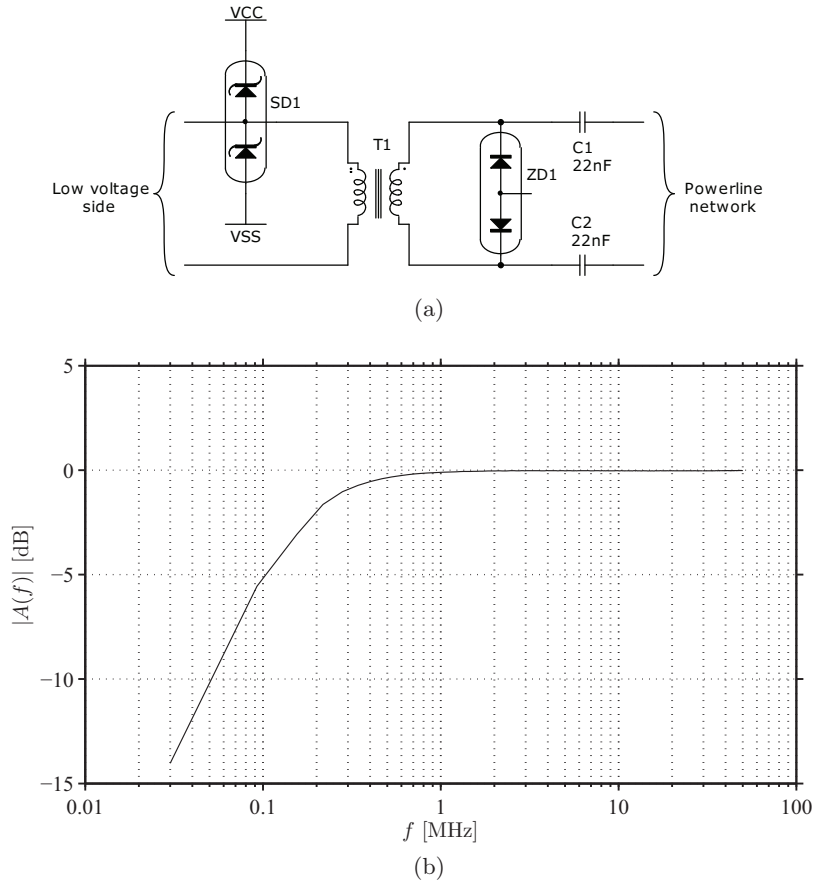

Figure 5.4.2: Electric diagram a) and amplitude response b) of the coupling unit employed in the PAFE.

Further technical details about the amplifiers employed in the PAFE and about its circuit for trigger generation are provided in the following two Paragraphs.

Amplification chains

As shown in Fig. 5.4.1, the same architecture has been adopted for all the amplification chains of the PAFE, since each of them contains a coupling unit, a passive LPF and a (power or low-noise) amplifier. Some details about each of these components are provided below.

Low-pass filters - Each Low-Pass Filter (LPF) is based on a P7LP-306L filter [64]; this allows to implement easily a 7th order filter having a cut off frequency equal to 30 MHz and an (input

and output) impedance matched to a 50 Ω resistance.

Coupling units - Each coupling unit is employed for injecting (or receiving) an high frequency signal into (from) the power network, as well as for protecting the amplifier it feeds (it is fed by) from the mains. For these reasons, each coupling unit behaves as an *high pass filter*. Its electrical diagram is shown in Fig. 5.4.2a. Note that: a) the cut off frequency of this circuit is determined by the dispersion inductance L_p of the primary of transformer T_1 and by the capacitors C_1 and C_2; b) the capacitors C_1 and C_2 need to be properly selected, since they operate in the presence of the mains voltage and their self-resonance frequency, related to their parasitic elements, has to be large enough in order to introduce a negligible attenuation in the band $1.8-30$MHz; c) the high frequency transformer WB1-1SLB [65] has been selected for T_1 in order to ensure a proper galvanic isolation (this component is characterized by the bandwidth $0.15-500$ MHz and a maximum current equal to 250 mA); d) the couple of Zener diodes ZD_1 and and that of Schottky diodes SD_1 are used to reject the high voltage perturbations coming from the powerline under test. The amplitude response of the proposed coupling unit $A(f)$ is shown in Fig. 5.4.2b, from which a cutoff frequency close to 100 kHz is easily inferred.

Amplifiers - The use of two LNAs characterized by different gains and feeding two distinct A/D converters can be motivated as follows. The attenuation experienced by the probing signal on the powerline network depends on a number of factors (e.g. the distance between the couple of plugs under test and the set of loads connected to the network and its topology [63]) and, consequently, it may vary over a wide range. Hence, during the experimental campaign, the availability of a couple of LNAs with gains $G_1 = 1$ and $G_2 = 20$ has been extremely useful to match the dynamic range of the A/D converters and to acquire channel responses characterized by significantly different dynamic ranges.

The two LNAs are based on the operational amplifiers OPA842 [66] and OPA846 [67], both characterized by low distortions, a bandwidth greater than 200MHz and a large input impedance (so that the transfer function of the coupling units are negligibly perturbed by these devices). Note that, on the one hand, the OPA842 [66] ensures a stable unitary gain $G_1 = 1$ and that, on the other hand, the OPA846 [67] has a gain-bandwidth product greater than 1750 MHz, so that it can be adopted to provide the gain $G_2 = 20$.

Finally, it is worth mentioning that the power amplification chain employed for the probing signal is based on the operational amplifier OPA2677 [68]. This device provides a 220 MHz bandwidth and a maximum output current equal to 500 mA. As a result, our channel sounder can effectively cope with powerline channels introducing small and large attenuation.

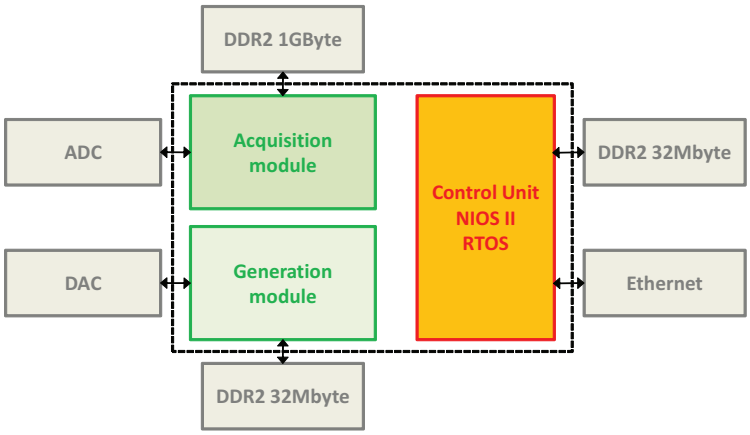

Figure 5.5.1: Block diagram of the FPGA project.

Trigger generation

The trigger circuit consists of three building blocks, namely a LPFs, a Schmitt trigger and a level adapter, as shown in Fig. 5.4.1. The goal of the LPFs is the suppression of any high frequency signal superimposed to the mains (e.g., impulsive noise affecting powerlines and/or the probing signal generated by the channel sounder) potentially leading to a false lock-in of the Schmitt trigger. The comparator thresholds can be properly adjusted, so that the Schmitt trigger output can be synchronized to whatever phase within the mains period. The last stage consists of a level adapter matching the trigger output dynamic range to the digital inputs of the FPGAs.

5.5 FPGA development board

In this Section, after summarizing the tasks assigned to the FPGA development board and the way it manages them, we provide some details about their implementations.

Task management

The FPGA board handles the following three distinct tasks (see Fig. 5.5.1):

1. generation of the samples of a probing signal;

2. acquisition of the samples of the corresponding channel response;

3. management of the acquired data and control of the channel sounding procedure.

The first two tasks need to be accomplished in real-time and, for this reason, they have been implemented in Verilog [69]. Since the data conversion interface is equipped with A/D and D/A converters operating at $f_s = 100$ MHz and offering a resolution $r = 14$ bits/sample, the FPGA is required to manage two distinct data flows (one associated with the probing sequence and the other stemming from the acquired channel response), each characterized by a bit rate $D_r = f_s \cdot r = 1.4$Gbps. Even if the channel response was acquired over small number of periods of the mains, the resulting huge amount of data available at the A/D converter output could not be moved directly from the FPGA board to the personal computer in real time. For this reason, a "store-and-forward" approach has been employed for the data transfer. This approach consists in exploiting a portion of the DDR2 memory banks of the FPGA board as a buffer and benefits from their low access time. In particular, the DDR2 memory device of 1 GB available on the FPGA board has been employed to store the acquired channel response. Then, at the end of the measurement phase, the FPGA development board transfers the acquired data to the personal computer through its Gigabit Ethernet interface. This data transfer is managed by the control module which can operate without real-time constraints. For this reason, the tasks of the control unit are handled by a virtual microprocessor Nios II, running on the FPGA and operating at a clock frequency equal to 150 MHz. Finally, it is worth mentioning that the control unit is also responsible for transferring the probing signal from the personal computer to the DDR2 memory (physically allocated on one of the two 32 MB memory chips) and for managing all internal operations of the channel sounder.

Generation of the probing signal

The generation of the samples of the probing signal (i.e., of the probing sequence) is managed by a specific module, whose structure is shown in Fig. 5.5.2. The main task of this module is handling two distinct data streams, one flowing into the 32 MB DDR2 memory, the other one out of it. In fact, in the initialization phase, the probing sequence is stored in the 32MB DDR2 memory. Note that each sample is represented by 14bits; however, a zero padding is performed to extend the sample representation to 16 bits, so that the logic management of the DDR2 memory is substantially simplified. Then, during channel sounding, the probing sequence is transferred directly from the DDR2 memory to the D/A converter without involving the virtual microprocessor of the control module, so that any potential delay is avoided. Since the DDR2 memory operates at 300 MHz with a data bus width (at physical layer) equal to 8

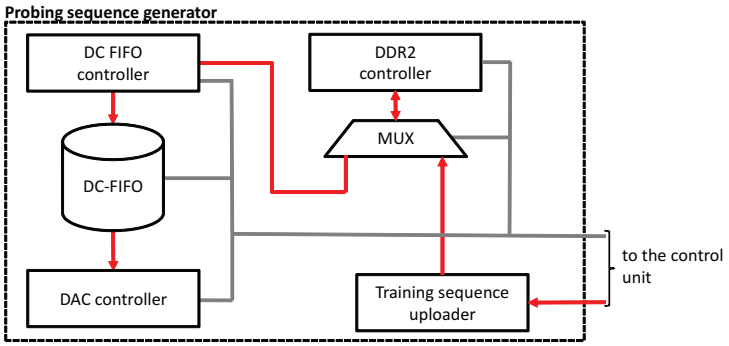

Figure 5.5.2: Block diagram of the module handling the generation of the probing sequence.

bits, in principle the maximum frequency at which the samples of the probing sequence can be read from the memory itself is equal to 150 MHz. This means that the DDR2 memory and the D/A converter operate at different frequencies; in particular, the DDR2 memory can transfer the samples of the probing sequence at a frequency greater than the sample rate of the D/A converter (100 MHz). To overcome this problem a Dual Channel First-In First-Out (DC-FIFO) memory with asynchronous read and write ports has been inserted between the D/A converter and the DDR2 memory. The DC-FIFO memory offers the following advantages:

- Due to its asynchronous ports, it allows to establish a simple connection between the DDR2 memory, which sends the samples of the probing sequence at 150 MHz, and the D/A converter, that converts such samples at 100 MHz.
- Due to its large depth (1024 locations, each of 16 bits), short idle cycles of the DDR2 memory can be tolerated without interrupting the DAC (note that the ratio between the input and output bit rate of the DC-FIFO is equal to 1.5).
- It can automatically perform data alignment (i.e., removal of padding zeros).

Due to the availability of the DC-FIFO memory, the probing signal can be generated as follows:

1. The control module connects the DDR2 multiplexer to the DDR2 memory and transfers the probing sequence to this memory from the personal computer (through the control module).
2. The control module connects the DDR2 multiplexer to the DC-FIFO and resets the DC-FIFO controller.

3. The DC-FIFO controller acquires the length of the probing sequence and starts to transfer the samples (each represented by a word of 16 bits) from the DDR2 memory to the DC-FIFO.

4. When the DC-FIFO memory is full, the control module resets and configures the DAC controller (setting the length of the probing sequence).

5. The DAC controller takes the control of the whole module waiting for a start command from the control module.

6. When the start command is received by the DAC controller, this controller manages the transfer of a given number of samples to the D/A converter at a proper frequency and then stops.

Note that the length of the probing sequence is not limited by the size of the DC-FIFO memory (1024 words) since, when the number of samples available in such a memory drops below half its capacity, the DC-FIFO controller automatically transfers 512 new words from the DDR2 memory to the DC-FIFO memory. It is also worth mentioning that the DAC is never interrupted by this "refresh" procedure since the transfer rate from the DDR2 memory to the DC-FIFO memory is larger than the frequency at which the D/A converter operates. However, the maximum length of the probing sequence cannot exceed 16 Msamples because of the limited size of the DDR2 memory (32 MB). This entails a maximum duration of 160 ms for the probing signal; however, this does not represent an appreciable limitation in case of a periodic probing sequence, since the samples associated with a whole period can be stored in the DDR2 memory and can be cyclically moved to the D/A converter.

Acquisition of the channel response

The architecture of the acquisition module (see Fig. 5.5.3) is very similar to that of the module developed for the generation of the probing sequence (see Fig. 5.5.2), although the direction of the data transfer is opposite. In fact, first of all the acquisition module stores the samples of the channel response in the DDR2 memory; then, at the end of the measurement procedure, it moves all the acquired data from the DDR2 memory to the personal computer. It is important to point out that:

- The size of the DDR2 memory handled by this module is 1 GByte, so that up to $5 \cdot 10^8$ samples can be stored, if each of them is represented by 16 bits. Then, if the A/D

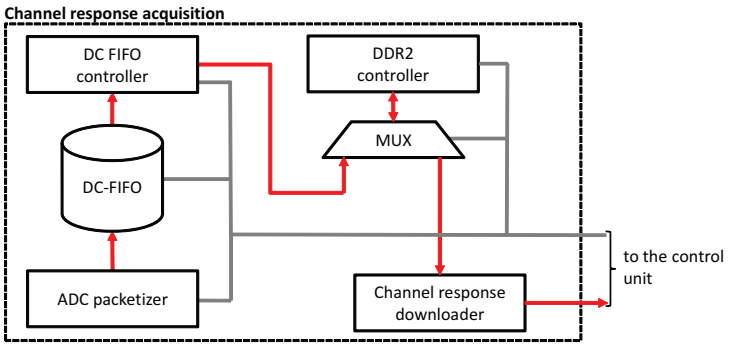

Figure 5.5.3: Block diagram of the acquisition module.

converter operates at 100 MHz, the channel impulse response can be acquired over a time interval whose duration does not exceed 5 seconds.

- The width of the memory data bus is equal to 72 bits.
- The clock frequency of the DDR2 memory is 300 MHz, but the DDR2 controller is configured to operate "at quarter rate mode", so that one memory access is carried out every 4 cycles (as if the memory operated at 75 MHz). In this configuration the data bus width of the DDR2 controller is equal to 288 bits, so that the DDR2 controller can move 4 blocks of 72 bits at each access and a maximum bit rate of 75 MHz $\times$ 288 bits = 21.6 Gbps can be achieved.

The acquisition module, whose core is represented by a DC-FIFO memory (able to store 16 words, each consisting of 288 bits) operates as follows. The samples available at the A/D converter output are queued by the ADC controller (which partitions them into *packets* of 18 consecutive samples, corresponding to $18 * 16 = 288$ bits) and are transferred to the DC-FIFO memory. Then, a packet stored in this memory can be moved by the DC-FIFO controller to the DDR2 memory in a single memory access. During channel sounding, new packets are continuously transferred by the ADC controller to the DC-FIFO memory and, in turn, these data are moved by the DC-FIFO controller to the DDR2 memory. Consequently, the channel acquisition procedure consists of the following steps:

1. The control module resets the acquisition system, commutes the DDR2 multiplexer towards the DC-FIFO controller and informs the DC-FIFO controller about the overall number of samples to be acquired.

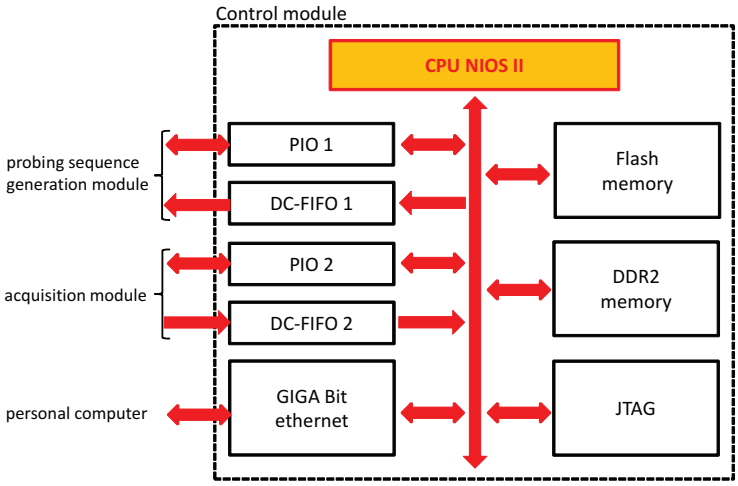

Figure 5.5.4: Block diagram of the control module.

2. When the measurement procedure begins (this event is triggered by the user interface), the ADC controller starts the acquisition of the samples of the channel response.

3. When there is at least one new packet stored in the DC-FIFO memory, the DC-FIFO controller transfers it to the DDR2 memory.

4. At the end of the measurement procedure, the downloading unit takes the control of the whole acquisition module and transfers the content of the DDR2 memory to the control module.

5. The control module transfers the acquired data to the personal computer.

Control module

The block diagram of the developed control module is shown in Fig. 5.5.4. This module represents an interface between the real-time modules implemented in Verilog (for the generation of the probing sequence and the acquisition of the channel response) and the GUIs developed in Matlab to manage the channel sounder. In fact, it translates a set of high level Matlab commands in low level instructions driving the FPGA platform. Note also that, in principle, it can be interpreted as an embedded system whose core is the Nios II microprocessor, and whose peripherals are the real-time modules, the Gigabit Ethernet port and the DDR2 memory.

The control module interacts with the personal computer and with the real time modules as follows. The personal computer sends its commands to the channel sounder through the Gigabit Ethernet port; each command is represented by a data packet of fixed length. Then the control module generates a set of control signals suitable to configure the generation of the probing sequence and the acquisition of the channel response. In particular, two Parallel Input Output (PIO) ports are exploited to send the control signals and to monitor all the flags of the other two modules; note that these PIO ports establish an asynchronous connection, so that the real-time modules and the control module can operate at different rates. The control module is also equipped with two DC-FIFO memories, one allocated to manage the data transfer of the probing sequence, the other one the data transfer of the acquired channel response; both these memories have a data bus width of 32 bits and a size of 8192 words.

Finally, it is important to point out that our approach to the design of a channel sounder provides a number of advantages since: a) all the algorithms devoted to the management of the channel sounder can be developed in C language, which is much simpler than standard FPGA descriptive languages like Verilog and VHDL; b) the structure of real-time modules is not visible to users, who are not required to learn the structure of low-level components; c) the tools made available by the sounder can be easily adapted to user needs, since the control module can be configured in C language through the Nios II microprocessor (see Section 5.6 for further details).

5.6 Graphical user interfaces

The Matlab language has been adopted to develop various Graphical User Interface (GUI)s that ease the use of the channel sounder; moreover, various Matlab scripts have been devised to manage the different tasks which the sounding procedure consists of. It is worth mentioning that this approach simplifies the integration of the GUIs with a set of Matlab functions which can be easily created/modified by the user to cope with a number of specific problems (e.g., processing the channel response according to specific algorithms). Furthermore, any user can interact with the developed GUIs through the Matlab workspace and this makes the sounding tool extremely flexible.

The software architecture of the channel sounder is shown in Fig. 5.6.1 and includes the following four specific GUIs:

1. connection GUI,

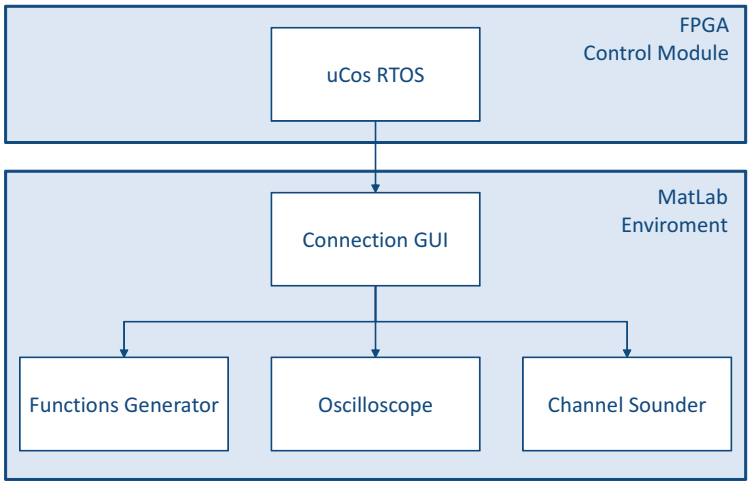

Figure 5.6.1: Software architecture of the channel sounder.

2. function generator GUI,

3. oscilloscope GUI,

4. channel sounder GUI.

The *connection* GUI provides users with a dedicated menu for activating the other GUIs. In addition, it manages the link between the FPGA development board and the personal computer through the GigaBit Ethernet port. To this aim, it allows to set various connection options, like the packet size, the IP address of the FPGA development board and the number of the TCP port from which the kernel of the NIOS II microprocessor waits for data packets.

The other GUIs implement simple virtual instruments based on the developed hardware platform. In particular, the *function generator* GUI allows users to load an arbitrary waveform from a Matlab file .mat and to turn it into the specific format accepted by the control unit for DAC[2]. One of the options provided by this GUI is the cyclic operation mode (see Paragraph 5.5); in this case the D/A converter generates an analog periodic signal (of arbitrary length) in the band $0.1 - 50$ MHz.

A different functionality offered by our tool derives from the possibility of exploiting the acquisition module to set up a virtual digital oscilloscope which operates at a 100 MHz sampling

[2]Note that the channel sounder can operate as a function generator terminated on 50 Ω load if the PAFE is excluded or as a function generator for powerline channels if the PAFE is employed.

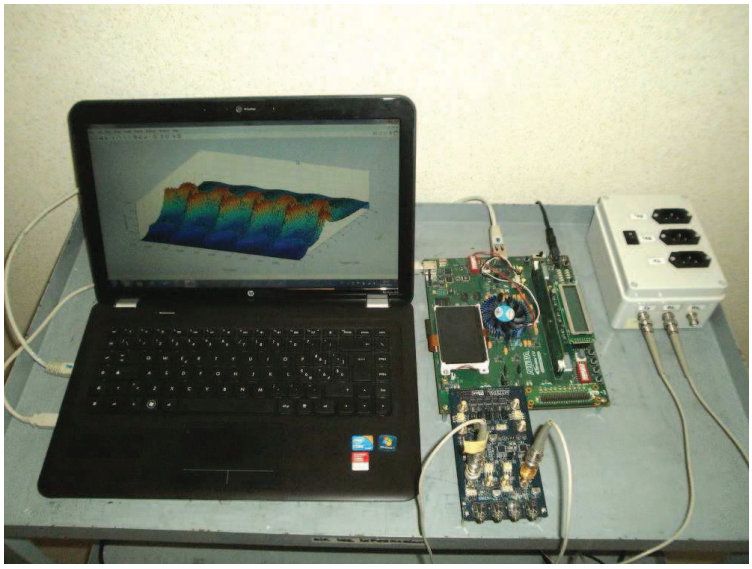

Figure 5.7.1: The developed channel sounder.

frequency. In practice, thanks to the *oscilloscope* GUI, any user is able to define the duration of the sequence to be acquired (setting the number of samples of the input signal). The acquisition can be triggered either manually (pressing a button available on the GUI) or automatically by means of the PAFE (see Section 5.4). Once a sequence has been acquired, each of its samples is converted from the specific format adopted by the FPGA board to a voltage value, that can be processed and saved by Matlab for any purpose. This functionality is very useful, because it makes available a signal sample vector that can be exploited in a number of different applications (e.g., plotting a given signal or analyzing the noise generated by the power network in a given bandwidth).

Finally, the *channel sounder* GUI implements a virtual channel sounder by combining the signal generation and acquisition functionalities. Thanks to this GUI, any user can select an arbitrary sequence (generated by Matlab) for channel sounding and can set the duration of the channel sounding operation (in terms of number of output samples). The acquired channel response can be plotted or processed in Matlab to extract specific channel parameters.

5.7 Experimental results

The channel sounder implemented in the labs of DIEF is shown in Fig. 5.7.1 and, as already mentioned above, includes a personal computer (left), an FPGA development board (center), a DAC-ADC board (bottom) and a PAFE (right). An extensive measurement campaign has been accomplished in the labs and in the building of Department of Engineering "Enzo Ferrari" (University of Modena and Reggio Emilia, Italy) to assess the accuracy of this tool and to analyze the properties of various indoor powerline channels. In the whole campaign a comb of sinusoids has been used to excite powerline channels; this sounding signal encompasses the band (f_L, f_H) and is characterized by a frequency spacing equal to Δf Hz between adjacent tones. In addition, the following choices have been always made for sounding waveforms: a) Δf is a submultiple of the sampling frequency f_s, so that

$$f_s = k\Delta f \tag{5.7.1}$$

where the positive integer k represents the period of the probing sequence; b) the duration of the probing sequence is a multiple of the channel period T_0, so that it consists of

$$N_c = l f_s T_0, \tag{5.7.2}$$

samples (here l denotes a positive integer). When analyzing the channel response to this excitation in the frequency domain, a *short time Fourier transform* [70] processing nonoverlapping sample blocks of size k has been employed; this ensures a frequency resolution equal to Δf. Note that if the Fourier transform of each block is normalized to the Fourier transform of the probing sequence, the so called Time-Variant Transfer Function (TVTF) of the channel under test is assessed[3].

In the first part of our measurement campaign, our instrument has been tested employing a simple circuit designed to emulate the behavior of a periodically time varying system. The electric diagram of this circuit is shown in Fig. 5.7.2, and consists of a fixed resistor (having a resistance equal to $50\,\Omega$) and two JFET J106 transistors, each having a voltage drop between gate and source equal to $V_g(t)$. In practice, the JFETs operate as voltage controlled resistors and their drain-to-source resistance is controlled by the periodic voltage $V_g(t) = -2.5 +$

[3] Any reader can refer to [50, 71, 72, 73, 74] for further analytical details about the identification of LPTV systems.

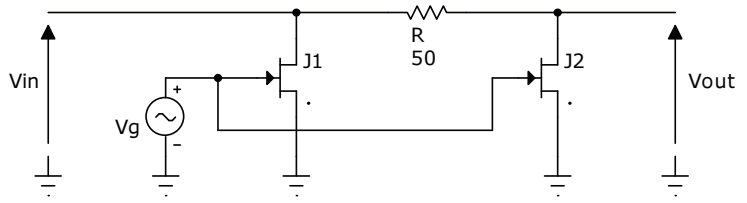

Figure 5.7.2: Electric diagram of the employed test circuit.

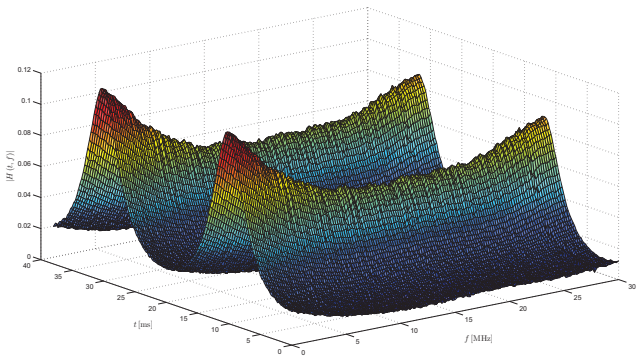

Figure 5.7.3: Amplitude of the TVTF characterizing the test circuit shown in Fig.10.

$1.5\sin(2\pi f_0 t)$ V, with $f_0 = 50$ Hz, so that the drain-to-source resistance of the JFETs varies sinusoidally at the same frequency as the mains voltage. Such a circuit can be driven directly by the HSMC input/output; for this reason, the D/A converter and the A/D converter have been connected to the V_{in} and V_{out} terminals, respectively (in other words, the PAFE has been excluded). In our test this circuit has been excited by a comb of sinusoids characterized by $f_L = 1$ MHz, $f_H = 30$ MHz, $\Delta f = 200$ kHz and $l = 2$. The amplitude of the resulting TVTF $H(t, f)$ computed by the tool is shown in Fig. 5.7.3. This result has been compared with the estimate of the TVTF generated by a Spice simulation of the given circuit and an excellent match has been found; this has confirmed the excellent accuracy provided by our channel sounder.

In the second part of our experimental campaign, various powerline channels available at second floor of the DIEF have been sounded; borrowing the jargon of wireless communications,

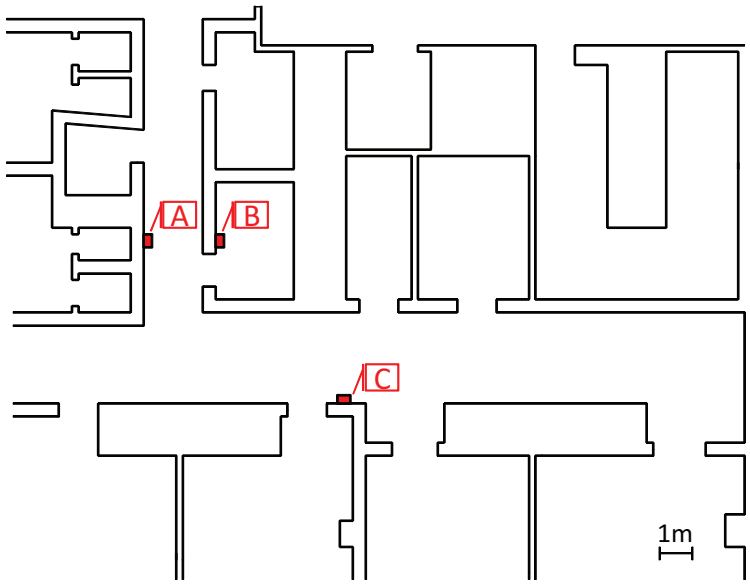

Figure 5.7.4: Portion of the map of the building where our experimental data have been acquired. The plugs selected for our measurements are labeled by red letters.

this propagation environment can be classified as *light commercial*, since it refers to a power network to which various personal computers and electronic devices are connected. The experimental data shown below refer to the plugs labeled by red letters in Fig. 5.7.4, which shows a portion of the map of the above mentioned building. It is important to point out that the function generation section and channel acquisition section of our tool have been implemented on the same FPGA, so that synchronization between them can be easily achieved. However, this entails the need of using two (potentially long) extension cords to connect the PAFE to the couple of selected plugs. This raises the additional problem of assessing the impact of the cable length and properties on our acquired data. Luckily, our measurements have evidenced that the impact of such cords is minor since a) they are usually by far shorter than the cables of the considered power network and b) channel properties mainly depends on the loads connected to the power network under test.

In the experimental campaign the powerline channel has been excited by a comb of sinusoids characterized by $f_L = 0.1$ MHz, $f_H = 1$ MHz, $\Delta f = 10$ kHz and $l = 2$. The amplitude of the TVTFs $H(t, f)$ referring to the couple of plugs (A,B) and (B,C) are shown in Figs. 5.7.5

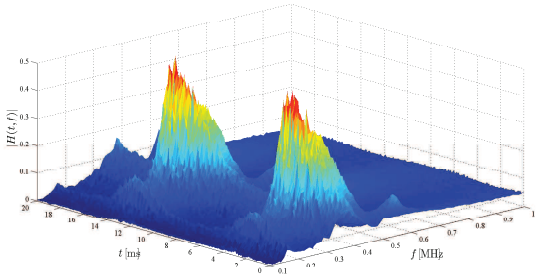

Figure 5.7.5: Amplitude of the TVTF referring to the plugs A and B.

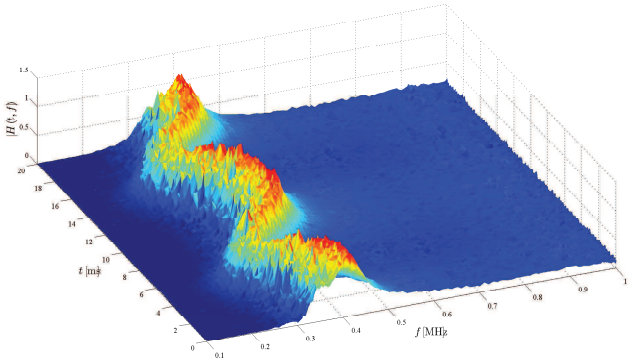

Figure 5.7.6: Amplitudes of the TVTF referring to the plugs B and C.

and 5.7.6, respectively. These results evidence that: a) the transfer function of a broadband indoor powerline channel may exhibit significant variations; b) the transfer function exhibits periodicity with period $1/(100\ \text{Hz}) = 10$ ms. Further experimental results about LPTV powerline channels can be found in [50, 53, 59].

Finally, the developed PLC channel sounder has been employed to analyze the spectral properties of channel noise in the band $0.1 - 1$ MHz; in practice, sequences of $N_c = 5 f_s T_0$ samples have been acquired for different plugs (in the absence of any excitation) and the associated Time-Variant Power Spectral Density (TVPSD) has been estimated applying the Yule-Walker method to multiple signal blocks, each consisting of 10^5 samples. The TVPSDs of the noise

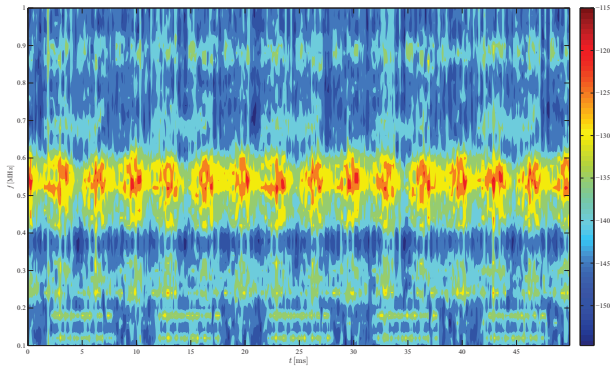

Figure 5.7.7: Estimate of the noise TVPSD referring to plug A.

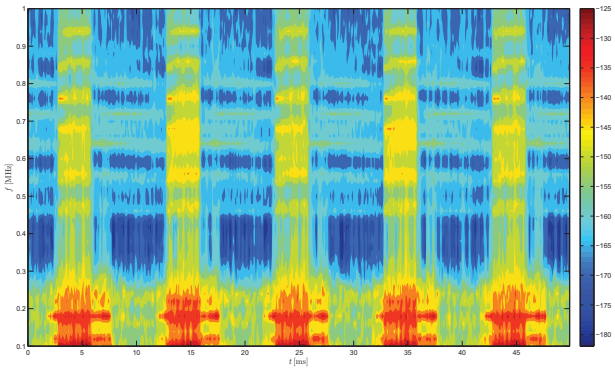

Figure 5.7.8: Estimate of the noise TVPSD referring to plug B.

acquired from the plugs A and B are shown in Fig. 5.7.7 and 5.7.8, respectively. Note that: a) the TVPSD of the noise affecting plug A is periodic and is characterized by a frequency larger than that of the mains; b) the TVPSD of noise acquired from plug B is periodic and synchronous with the mains[4].

[4]Further details on powerline noise modeling can be found in [75] and references therein.

5.8 Conclusions

In this chapter a low cost implementation of a broadband channel sounder for low voltage powerlines has been described. This tool is based on a commercial FPGA board and is very flexible, since it allows its users to excite powerline channels with arbitrary waveforms and to process the resulting channel responses easily, thanks to its Matlab-based interfaces. The developed instrument has been exploited to analyze the TVTF between couples of plugs in an indoor scenario and to estimate the TVPSD of powerline noise. Future applications of our channel sounder concern: a) the analysis of different properties of real world indoor powerline channels; b) the characterization of the impulsive noise affecting powerline communications; c) the development of communication techniques exploiting the periodic behavior of powerline channels.

Chapter 6

LPTV modelling of Indoor Powerline Channels

Indoor powerline channels usually exhibit a cyclic input-output behavior due to the time-varying impedance of power loads. This makes typical time-invariant system models unsuitable to provide a faithful representation of such channels. In this Chapter, starting from the so-called Zadeh's series expansion, a discrete-time parametric representation of a linear periodically time-varying system is developed and it is shown how a reduced complexity version of it can be adopted to model indoor powerline channels. Then, various methods for estimating the parameters of the proposed representation are developed and compared in terms of performance and complexity. Numerical and experimental results evidence that the proposed reduced complexity model is able to provide an accurate representation of indoor powerline channels at the price of a reasonable complexity.

This Chapter is organized as follows. In Section 6.1 an overview of the technical literature on LPTV modelling of powerline channel is provided. A novel LPTV channel model is developed in Section 6.2, whereas the identification of its parameters is analysed in Section 6.3. The computational complexity of the proposed channel model and that of various estimators for channel parameters are compared in Section 6.4, whereas the estimation accuracy is assessed in Section 6.5. Finally, some conclusions are provided in Section 6.6.

6.1 LPTV models for powerline channels: state of the art

In the last few years considerable attention has been paid to the problem of analysing and modelling the channel behavior in indoor powerline data communications. Indoor powerline channels are often represented as Linear Time Invariant (LTI) systems [10, 14, 38, 41, 42, 47, 117, 118, 119]; such representations, however, can only account for the *average* behavior of the communication medium. In fact, any indoor power network usually experiences: a) *long-term variations* due to the switching of the electrical appliances connected to it; b) *short-term variations* originating from the time-vaying input impedance of such appliances. However, the problems of modelling these variations has received very limited attention [27, 120]. In particular, a wavelet-based time-domain model for the representation of long-term variations has been derived in [27], where a broadband powerline channel is described by a two-port equivalent with a given scattering matrix. This model assumes that the long term channel evolution can be seen as a sequence of stationary states and that the transition between two states does not affect data transmissions; note, however, that short term variations are not kept into account and no input-output relationship is provided to describe channel behavior. A conceptually different approach is followed in [120], where a Markov model, representing long-term variations, is combined with a LPTV representation accounting for cyclic short-time changes. In practice, this discrete-time channel model is based on partitioning the mains period T_0 (equal to half period of the mains, i.e. to 10 ms for a mains frequency equal to 50 Hz) in N_0 intervals and on representing the channel as a time-invariant FIR filter over each of them. This channel representation belongs to the class of the so called *switching models* (SMs), where a limited number of invariance intervals (i.e., a small N_0) is usually assumed to limit model complexity, at the price, however, of poor performance in terms of accuracy. On the other hand, very accurate models for broadband powerline channels can be developed resorting to the well known Alias Component Representation (ACR) [71, 73, 122, 123, 124] of LPTV systems. However, this approach entails a huge complexity; for instance, if the sampling frequency $f_s = 100$ MHz is selected to model the channel behavior in the band $0 - 50$ MHz, in principle a bank of $N_0 = T_0 f_s = 10^6$ filters would be necessary to represent a powerline channel.

In this chapter, inspired by some previous work on the use of the *Zadeh's series expansion* [125] for the continuous time representation of powerline channels [121, 126], a novel discrete-time representation of a broadband indoor powerline channel experiencing short term cyclic variations is developed. The proposed model is based on the Fourier expansion of the CIR of a

discrete-time LPTV system and, unlike the models developed in [27, 120], is parsimonious, i.e. it is able to provide a faithful representation of an indoor powerline channel with a reduced number of parameters. The problem of extracting the values of the model parameters from a set of measurements acquired by the broadband channel sounder illustrated in [91] is also investigated; various solutions, based on a Least Square Estimator (LSE), a Huber estimator, a Fair estimator and a Maximum Likelihood Estimator (MLE) are proposed and compared in terms of estimation accuracy and complexity.

6.2 Discrete-time model for indoor powerline channels

Generally speaking, the n-th sample of the output sequence of a discrete-time LPTV system can be expressed as [124]

$$z_n = \sum_{m=-\infty}^{+\infty} h_{n,m} x_{n-m} \tag{6.2.1}$$

where $\{x_n\}$ and $\{h_{n,i}\}$ represent its input sequence and its impulse response (defined as the filter response at time n to a unitary pulse applied $n-i$ samples earlier), respectively. Since the sequence $\{h_{n,m}\}$ is periodic in the time index n, i.e.

$$h_{n,m} = h_{n+kN_0,m} \qquad \forall n, m, k \in \mathbb{Z} \tag{6.2.2}$$

where N_0 denotes its period, it can be represented as

$$h_{n,m} = \sum_{k=0}^{N_0-1} H_{k,m} \exp\left(j\frac{2\pi kn}{N_0}\right) \tag{6.2.3}$$

where

$$H_{k,m} = \frac{1}{N_0} \sum_{n=0}^{N_0-1} h_{n,m} \exp\left(-j\frac{2\pi kn}{N_0}\right) \tag{6.2.4}$$

is the k-th coefficient of the Discrete Fourier Transform (DFT) of $\{h_{n,m}\}$. Substituting (6.2.3) in (6.2.1) yields

$$z_n = \sum_{m=-\infty}^{+\infty} \left(\sum_{k=0}^{N_0-1} H_{k,m} \exp\left(j\frac{2\pi kn}{N_0}\right) \right) x_{n-m} \tag{6.2.5}$$

$$= \sum_{k=0}^{N_0-1} \left[\sum_{m=-\infty}^{+\infty} H_{k,m} x_{n-m} \right] \exp\left(j\frac{2\pi kn}{N_0}\right). \tag{6.2.6}$$

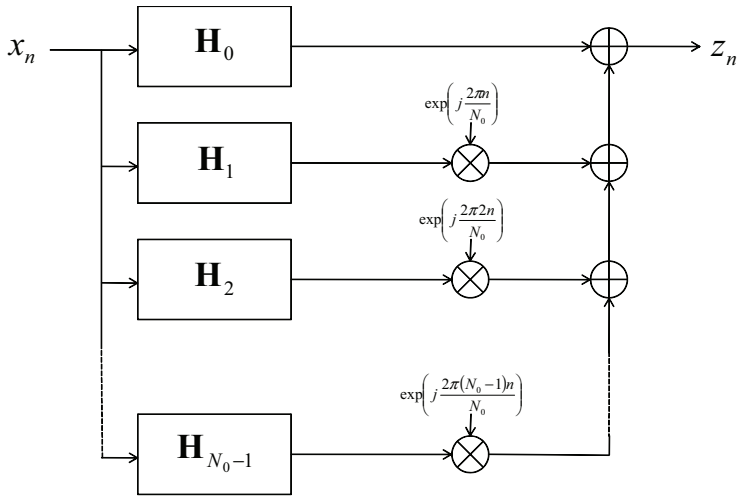

Figure 6.2.1: Graphical representation of the discre-time Zadeh's series expansion.

The last expression, which represents the discrete-time counterpart of the Zadeh's series expansion for the output of a continuous-time LPTV [125], shows that the system output sequence $\{z_n\}$ can be obtained as the superposition of the responses of N_0 LTI filters that are all fed by the input sequence $\{x_n\}$ and have infinite memory (see Fig. 6.2.1). It is worth pointing out that the k-th FIR filter (with $k = 0, 1, ..., N_0 - 1$) is characterized by the impulse response $\left\{h_m^{(k)} \triangleq H_{k,m}\right\}$ and its output is modulated by the complex exponentials $\left\{s_n^{(k)} \triangleq \exp\left(j\frac{2\pi kn}{N_0}\right)\right\}$ to account for time variations. Let us apply now the representation (6.2.6) to describe the samples of the useful signal component available at the output of a powerline channel characterized by the following properties: a) it is affected by the additive noise process $\{w_n\}$; b) it is causal; c) its memory is *finite*. In the following we always assume a sampling frequency equal to f_s Hz, a channel memory of M taps and $N_0 = T_0 f_s$, where T_0 is the period characterizing the cyclic behavior of the powerline channel. Then, the n-th sample of the channel output sequence can be expressed as (see (6.2.6))

$$y_n = \sum_{k=0}^{N_0-1} \left[\sum_{m=0}^{M-1} H_{k,m} x_{n-m}\right] \exp\left(j\frac{2\pi kn}{N_0}\right) + w_n. \tag{6.2.7}$$

A further simplification is still possible since experimental data have evidenced that only $(2Z + 1)$ (where Z denotes the so-called *order* of our system model) of the N_0 LTI filters provide a relevant contribution to $\{z_n\}$. For this reason, if the periodicity of $\{H_{k,m}\}$ in the

index k (with period N_0) is kept into account, (6.2.7) can be rewritten as

$$y_n = \sum_{k=-Z}^{Z} \left[\sum_{m=0}^{M-1} H_{k,m} x_{n-m} \right] \exp\left(j \frac{2\pi k n}{N_0} \right) + w_n \tag{6.2.8}$$

Finally, since $H_{-k,m} = H_{k,m}^*$ for the Hermitian symmetry of DFT coefficients, (6.2.8) can be easily put in the form

$$\begin{aligned} y_n &= \sum_{m=0}^{M-1} \mathrm{Re}\{H_{0,m}\} x_{n-m} \\ &+ 2 \sum_{k=0}^{Z} \left[\sum_{m=0}^{M-1} \mathrm{Re}\{H_{k,m}\} \cos\left(\frac{2\pi k n}{N_0} \right) x_{n-m} \right] \\ &- 2 \sum_{k=1}^{Z} \left[\sum_{m=0}^{M-1} \mathrm{Im}\{H_{k,m}\} \sin\left(\frac{2\pi k n}{N_0} \right) x_{n-m} \right] + w_n \end{aligned} \tag{6.2.9}$$

where $\mathrm{Re}\{x\}$ and $\mathrm{Im}\{x\}$ denote the real and imaginary part of a complex number x, respectively[1]. The last model, which is represented by the block diagram shown in Fig. 6.2.2 (where $\mathbf{H}_k \triangleq [H_{k,0}, H_{k,1}, ..., H_{k,M-1}]^T$ for $k = 0, 1, ..., Z$), involves real quantities only and, consequentely, lends itself to a practical implementation on programmable hardware. The identification of the parameters M and Z, as well as that of the $M(2Z+1)$ real taps $\{\mathrm{Re}\{H_{k,m}\}, \mathrm{Im}\{H_{k,m}\}\}$ of the filter bank is studied in the following Section.

6.3 System identification

In this Section various techniques, for the pilot-aided estimation of the $M(2Z+1)$ real coefficients characterizing the FIR filter bank, are illustrated; in doing so, that both the order Z and the memory M of the FIR filter bank are assumed known. Then, the section focus on the problem of estimating these parameters.

6.3.1 Pilot-aided estimation of the filter coefficients

In this Paragraph the problem of estimating the taps of the FIR filters contained in the model (6.2.9) is formulated and various solutions are developed. It is assumed that the considered powerline channel is excited by a periodic known (pilot or training) sequence $\{x_n\}$ having a period equal to N_0, so that, in the absence of noise, it generates the periodic response $\{z_n\}$,

[1]Note that $\mathrm{Im}\{H_{0,m}\} \equiv 0$.

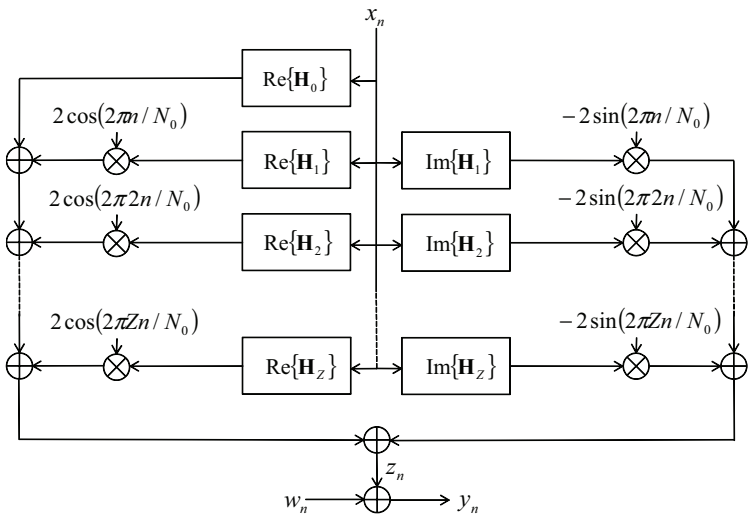

Figure 6.2.2: Discrete-time model of a powerline channel.

characterized by same period as $\{x_n\}$. Then, the n-th signal sample available at the channel output is given by (see (6.2.6) and (6.2.7))

$$y_n = z_n + w_n \tag{6.3.1}$$

where w_n denotes the contribution of channel noise. The channel estimation algorithms illustrated below process the N_s-dimensional vector (with $N_s \leq N_0$)

$$\mathbf{y}_{N_s} \triangleq \left[y_{l_0}, y_{l_1}, ..., y_{l_{N_s-1}}\right]^T \tag{6.3.2}$$

which consists of the channel output samples available at the instants $\{l_k,\ k = 0, 1, ..., N_s - 1\}$, all belonging to the same period (we comment on the criteria for the selection of N_s and $\{l_k,\ k = 0, 1, ..., N_s - 1\}$ later). From (6.2.9) it can be easily inferred that

$$\mathbf{y}_{N_s} = \mathbf{ZH} + \mathbf{w}_{N_s} \tag{6.3.3}$$

where $\mathbf{w}_{N_s} \triangleq \left[w_{l_0}, w_{l_1}, ..., w_{l_{N_s-1}}\right]^T$ is a vector of noise samples,

$$\begin{aligned} \mathbf{H} &= \left[H_0, H_1, ..., H_{M(2Z+1)-1}\right]^T \\ &\triangleq \left[\mathrm{Re}\left\{\mathbf{H}_0^T\right\}, \mathrm{Re}\left\{\mathbf{H}_1^T\right\}, ..., \mathrm{Re}\left\{\mathbf{H}_Z^T\right\},\right. \\ &\quad \left.\mathrm{Im}\left\{\mathbf{H}_1^T\right\}, \mathrm{Im}\left\{\mathbf{H}_2^T\right\}, ..., \mathrm{Im}\left\{\mathbf{H}_Z^T\right\}\right]^T, \end{aligned} \tag{6.3.4}$$

$(\cdot)^T$ denotes the transpose operator and $\mathbf{Z}$ is a $N_s \times M(2Z+1)$ matrix depending on both the training sequence and the complex exponentials $\left\{s_n^{(k)}\right\}$. In particular, it is not difficult to show that

$$\mathbf{Z} = \mathbf{X} \odot \mathbf{P} \tag{6.3.5}$$

where $\odot$ denotes the Hadamard product,

$$\mathbf{X} \triangleq \left[\underbrace{\mathbf{x}, ..., \mathbf{x}}_{(2Z+1)}\right] \tag{6.3.6}$$

is a $N_s \times M(2Z+1)$ matrix,

$$\mathbf{x} \triangleq \begin{bmatrix} x_{l_0} & x_{l_0-1} & \cdots & x_{l_0-M+1} \\ x_{l_1} & x_{l_1-1} & \cdots & x_{l_1-M+1} \\ \vdots & \vdots & \ddots & \vdots \\ x_{l_{N_s-1}} & x_{l_{N_s-1}-1} & \cdots & x_{l_{N_s-1}-M+1} \end{bmatrix} \tag{6.3.7}$$

is a $N_s \times M$ matrix properly collecting the samples of the training sequence $\{x_n\}$, and

$$\mathbf{P} = [\mathbf{C}_0, \mathbf{C}_1, ..., \mathbf{C}_Z, \mathbf{S}_1, \mathbf{S}_2, ..., \mathbf{S}_Z] \tag{6.3.8}$$

is a $N_s \times M(2Z+1)$ matrix resulting from the concatenation of the $N_s \times M$ matrices $\mathbf{C}_k = \left[c_i^{(k)}\right]$ (with $c_i^{(k)} = \cos(2\pi k l_i / N_0)$, $i = 0, 1, ..., N_s - 1$), and $\mathbf{S}_k = \left[s_i^{(k)}\right]$ (with $s_i^{(k)} = \sin(2\pi k l_i / N_0)$, $l_i = 0, 1, ..., N_s - 1$).

In the following some specific techniques for estimating the channel parametrs from $\mathbf{y}_{N_s}$ are presented(6.3.3).

Least square estimation - If channel noise is neglected (i.e., it is assumed that $\mathbf{w}_{N_s} = \mathbf{0}_{N_s}$), equation (6.3.3) can be interpreted as a system of N_s linear equations in $M(2Z+1)$ real unknowns $\{\mathrm{Re}\{H_{k,m}\}, \mathrm{Im}\{H_{k,m}\}\}$. Achieving an acceptable performance in channel estimation (see Section 6.5) requires: a) the system (6.3.3) to be over-determined, i.e. the inequality $N_s > M(2Z+1)$ to hold; b) the N_s samples of $\mathbf{y}_{N_s}$ to be uniformly spaced over an entire period so that a good numerical stability is achieved. If all this occurs, the solution of such a system can be evaluated as

$$\hat{\mathbf{H}} = \mathbf{Z}^{\dagger} \mathbf{y}_{N_s} \tag{6.3.9}$$

where $\mathbf{Z}^{\dagger}$ denotes the pseudo-inverse of $\mathbf{Z}$. It is not difficult to show that $\hat{\mathbf{H}}$ (6.3.9) coincides with the *least square* (LS) estimate[2]

$$\hat{\mathbf{H}}_{LS} \triangleq \arg\min_{\tilde{\mathbf{H}}} |\mathbf{e}|^2 \tag{6.3.10}$$

where $|\mathbf{x}|$ denotes the Euclidean norm of the vector $\mathbf{x}$ and

$$\mathbf{e} = \left[e_{l_0}, e_{l_1}, ..., e_{l_{N_s-1}}\right]^T \triangleq \mathbf{y}_{N_s} - \mathbf{Z}\tilde{\mathbf{H}}. \tag{6.3.11}$$

The accuracy of the LSE (6.3.9) can be improved modifying the way the N_s-dimensional vector of channel output samples is generated. In fact, the CIR and the noise statistics exhibit *long term* variations [120], whereas, as evidenced by our measurement campaign in an indoor scenario, the variations of the channel impulse response are much slower than those of the noise statistics. Consequently, it should be expected that the effects of powerline noise can be mitigated by averaging the channel output over N_p consecutive periods of the mains, i.e. by replacing $\mathbf{y}_{N_s}$ (6.3.2) with

$$\bar{\mathbf{y}}_{N_s}(N_p) \triangleq \left[\bar{y}_{l_0}(N_p), \bar{y}_{l_1}(N_p), ..., \bar{y}_{l_{N_s-1}}(N_p)\right]^T \tag{6.3.12}$$

where

$$\bar{y}_{l_k}(N_p) = \frac{1}{N_p}\sum_{i=0}^{N_p-1} y_{l_k+iN_0}. \tag{6.3.13}$$

with $k = 0, 1, ..., N_s - 1$. It is worth mentioning that: a) the noise affecting the average output vector $\bar{\mathbf{y}}_{N_s}(N_p)$ tends to become Gaussian as $N_p \to \infty$, so that the LSE approaches optimal Mean Square Error (MSE) performance, provided that the channel impulse response does not change over the selected observation interval; b) in principle, any channel estimator described below can benefit from the use of $\bar{\mathbf{y}}_{N_s}(N_p)$ (6.3.12), but the largest performance improvement has to be expected for the LSE, since it does not take into consideration the presence of the impulsive noise affecting powerlines.

M-estimation - The effects of impulsive noise can be mitigated through the use of a data-aided *M-estimator* [130, 131]. In this case the metric to be minimised is not the squared Euclidean norm of the vector $\mathbf{e}$ (6.3.11), but the function

[2]Note that the solution to the problem (6.3.10) can be derived iteratively, so avoiding the direct computation of the pseudo-inverse $\mathbf{Z}^{\dagger}$ [127].

$$J_{Me}(\mathbf{e}) = \sum_{k=0}^{N_s-1} \rho(e_{l_k}) \tag{6.3.14}$$

where $\rho(\cdot)$ denotes an even function such that $\rho(0) = 0$, and $\rho(x) > 0$ for $x \neq 0$. Therefore, the optimal channel estimate is evaluated as

$$\hat{\mathbf{H}}_{Me} = \arg\min_{\tilde{\mathbf{H}}} J_{Me}(\mathbf{e}). \tag{6.3.15}$$

The solution of the minimization problem (6.3.15) can be evaluated recursively resorting to an Iterative Reweighted Least Squares (IRLS) procedure; the l-th step of this procedure generates the estimate

$$\hat{\mathbf{H}}_{Me}^{(l)} = \arg\min_{\tilde{\mathbf{H}}} \sum_{k=0}^{N_s-1} \varphi\left(e_{l_k}^{(l-1)}\right) e_{l_k}^2 \tag{6.3.16}$$

of $\hat{\mathbf{H}}_{Me}$, where

$$\mathbf{e}^{(l-1)} = \left[e_{l_0}^{(l-1)}, e_{l_1}^{(l-1)}, ..., e_{l_{N_s-1}}^{(l-1)}\right]^T \triangleq \mathbf{y}_{N_s} - \mathbf{Z}\hat{\mathbf{H}}_{Me}^{(l-1)}. \tag{6.3.17}$$

and

$$\varphi(e) \triangleq \frac{1}{e}\frac{\mathrm{d}\rho(e)}{\mathrm{d}e} \tag{6.3.18}$$

represents the so called *weight function*. It is not difficult to show [127] that $\hat{\mathbf{H}}_{Me}^{(l)}$ (6.3.16) can be evaluated as

$$\hat{\mathbf{H}}_{Me}^{(l)} = \left(\mathbf{Z}^T\boldsymbol{\Phi}^{(l-1)}\mathbf{Z}\right)^{-1}\mathbf{Z}^T\boldsymbol{\Phi}^{(l-1)}\mathbf{y}_{N_s} \tag{6.3.19}$$

with $l = 0, 1, ...$; here $\boldsymbol{\Phi}^{(l)} \triangleq \mathrm{diag}\left\{\varphi\left(e_{l_k}^{(l-1)}\right)\right\}$ (with $k = 0, 1, ..., N_s - 1$) and $\mathrm{diag}\{\mathbf{x}\}$ denotes the diagonal matrix having the elements of the vector $\mathbf{x}$ on its main diagonal.

In this work the Huber [130] and Fair [131] estimators, characterized by the parametric functions $\rho(\cdot)$ and $\varphi(\cdot)$ listed in Table 6.1, have been taken into consideration. Unluckily, general guidelines for the selection of the parameters β and γ are not available in the technical literature. In our work the values $\beta = 1.345\sigma_N$ and $\gamma = 1.3998\sigma_N$, where σ_N^2 denotes the noise variance, have been selected; note that this choice ensures a 95% asymptotic efficiency for the selected estimators if the channel noise is Gaussian with variance σ_N^2 [130, 131]. It is also

	Huber	Fair
$\rho(x)$	$\begin{cases} \frac{x^2}{2} & \lvert x\rvert \le \beta \\ \beta\left(\lvert x\rvert - \frac{\beta}{2}\right) & \lvert x\rvert \ge \beta \end{cases}$	$\gamma^2\left[\frac{\lvert x\rvert}{\gamma} - \log\left(1+\frac{\lvert x\rvert}{\gamma}\right)\right]$
$\varphi(x)$	$\begin{cases} 1 & \lvert x\rvert \le \beta \\ \frac{\beta}{\lvert x\rvert} & \lvert x\rvert \ge \beta \end{cases}$	$\frac{1}{1+\frac{\lvert x\rvert}{\gamma}}$

Table 6.1: Functions $\rho(\cdot)$ and $\varphi(\cdot)$ characterizing the Huber and Fair M-estimators (see eq. (6.3.15) and eq. (6.3.16), respectively).

worth mentioning that the variance σ_N^2 is the only form of *a priori* information about the channel noise sequence $\{w_n\}$ required for a proper use of the proposed algorithms.

Maximum likelihood estimation - If the joint statistical behavior of additive noise samples $\{w_n\}$ is known, in principle *a* Maximum Likelihood (ML) approach to channel estimation can be employed. Based on the measurements acquired in our experimental campaign, the following assumptions have been made: a) the noise samples $\{w_n\}$ are iid rvs); b) a good approximation of the pdf of each noise sample is achieved by a GM with a proper number of components. This means that the PDF

$$\begin{aligned} f_{GM}(x) &= \sum_{i=1}^{N_c} f_{G,i}(x) \\ &= \sum_{i=1}^{N_c} \frac{\lambda_i}{\sqrt{2\pi\sigma_i^2}} \exp\left(-\frac{(x-\mu_i)^2}{2\sigma_i^2}\right) \end{aligned} \tag{6.3.20}$$

is adopted for the noise samples, where N_c represents the number of GM components and λ_i, μ_i and σ_i^2 denote the *a priori* probability, mean and variance of the ith Gaussian component, respectively, for $i = 1, 2, ..., N_c$. Then, the channel MLE [106] can be formulated as

$$\begin{aligned} \hat{\mathbf{H}}_{MLE} &= \arg\max_{\tilde{\mathbf{H}}} \prod_{k=0}^{N_s-1} f_{GM}(e_{l_k}) \\ &= \arg\max_{\tilde{\mathbf{H}}} \sum_{k=0}^{N_s-1} \log\left[\sum_{i=1}^{N_c} \frac{\lambda_i}{\sqrt{2\pi\sigma_i^2}} \exp\left(-\frac{(e_{l_k}-\mu_i)^2}{2\sigma_i^2}\right)\right]. \end{aligned} \tag{6.3.21}$$

A lower bound to the MLE performance is provided by the Cramer Rao Lower Bound (CRLB), which establishes that

$$var\{H_i\} \ge CRLB\{H_i\} = \left[\mathbf{J}^{-1}\right]_{ii} \tag{6.3.22}$$

with $i = 0, 1, ..., M(2Z+1)-1$, where $var\{H_i\}$ denotes the variance of any unbiased estimate of H_i (6.3.4) and $\mathbf{J}$ is the so called *Fisher information matrix* for the considered estimation problem. The element on the i-th row and j-th column of $\mathbf{J}$ is given by

$$[\mathbf{J}]_{ij} = E\left\{\left(\frac{\partial \log\left(f_{GM}(x)\right)}{\partial x}\right)^2\right\}\sum_{k=0}^{N_s-1}\left(\frac{\partial\left[\mathbf{Z}_k\mathbf{H}\right]}{\partial H_i}\frac{\partial\left[\mathbf{Z}_k\mathbf{H}\right]}{\partial H_j}\right), \tag{6.3.23}$$

where $\mathbf{Z}_k = \left[Z_{k0}, Z_{k1}, ..., Z_{k[M(2Z+1)-1]}\right]$ is the kth row of $\mathbf{Z}$ (6.3.5) and $E\{\cdot\}$ represents the statistical expectation operator. It is not difficult to prove that the first factor appearing in (6.3.23) is given by

$$E\left\{\left(\frac{\partial \log\left(f_{GM}(x)\right)}{\partial x}\right)^2\right\} = \int_{-\infty}^{+\infty}\frac{\left[\sum_{i=1}^{N_c} f_{G,i}(x)\frac{(x-\mu_i)}{\sigma_i^2}\right]^2}{\sum_{i=1}^{N_c} f_{G,i}(x)}dx \tag{6.3.24}$$

whereas

$$\frac{\partial\left[\mathbf{Z}_k\mathbf{H}\right]}{\partial H_i} = \begin{cases} x_{l_k-i} & 0 \le i,k \le M-1 \\ 2x_{l_k-i}c_{i,k} & M \le i,k \le M(Z+1)-1 \\ -2x_{l_k-i}s_{i,k} & M(Z+1) \le i,k \le M(2Z+1)-1 \\ 0 & \text{elsewhere} \end{cases}. \tag{6.3.25}$$

Frequency domain estimation - An alternative to the time domain channel estimators described above is represented by channel estimation techniques operating in the frequency domain. The Frequency Domain Estimator (FDE) described below processes the DFT of the vector $\bar{\mathbf{y}}_{N_0}(N_p) \triangleq [\bar{y}_0, \bar{y}_1, ..., \bar{y}_{N_0-1}]^T$, which consists of N_0 consecutive samples $\bar{y}_n$ generated according to (6.3.13); note that, unlike the output vector $\mathbf{y}_{N_s}$ (6.3.12), which is processed by the proposed time-domain estimators and whose size N_s is always smaller than N_0, the size of $\bar{\mathbf{y}}_{N_0}(N_p)$ is equal to the channel period N_0.

It is not difficult to show that the ξ-th element of the DFT of $\bar{\mathbf{y}}_{N_0}(N_p)$ can be expressed as

$$
\begin{aligned}
Y_\xi &\triangleq \frac{1}{N_0}\sum_{n=0}^{N_0-1}\bar{y}_n \exp\left(-j\frac{2\pi\xi n}{N_0}\right) \\
&= \frac{1}{N_0}\sum_{n=0}^{N_0-1}\left\{\sum_{k=-Z}^{Z}\left[\sum_{m=0}^{M} H_{k,m}x_{n-m}\right]\exp\left(j\frac{2\pi kn}{N_0}\right)\right\} \\
&\quad \cdot \exp\left(-j\frac{2\pi\xi n}{N_0}\right) + W_\xi \\
&= \sum_{k=-Z}^{Z} X_{\xi-k}\mathcal{H}_{k,\xi-k} + W_\xi
\end{aligned} \tag{6.3.26}
$$

where W_ξ is the ξth element of the N_0-point DFT of the noise vector affecting $\bar{\mathbf{y}}_{N_0}(N_p)$,

$$
X_\xi = \frac{1}{N_0}\sum_{n=0}^{N_0-1} x_n \exp\left(-j\frac{2\pi\xi n}{N_0}\right), \tag{6.3.27}
$$

and

$$
\mathcal{H}_{k,\xi} = \sum_{m=0}^{N_0-1} H_{k,m}\exp\left(-j\frac{2\pi\left(\xi-k\right)m}{N_0}\right) \tag{6.3.28}
$$

having defined $H_{k,m}=0$ for $m>M$ without loosing any generality. The expression (6.3.26) lends itself to a simple interpretation, since it shows that the useful component of the response of a LPTV channel (having a period $N_0 = f_sT_0$) at the frequency $f_\xi = \frac{\xi}{T_0}$ is given by the superposition of the contributions coming from $(2Z+1)$ different harmonics, whose frequencies are $f_k = f_\xi + kf_0$ with $k=-Z,-Z+1,...,Z$ and $f_0 = 1/T_0$.

The proposed FDE is based on the idea that, if a LPTV channel described by (6.3.26) is fed by a comb of sinusoids characterized by a frequency spacing $\Delta f < Zf_0$, then it generates multiple harmonics that do not overlap in the frequency domain. In this case, if the frequency spacing Δf is selected in a way that that $\Delta_f = f_s/N_L$ and the channel noise contribution is neglected, an estimate $\hat{\mathcal{H}}_{k,l}$ of the coefficient $\mathcal{H}_{k,l}$ can be evaluated as

$$
\hat{\mathcal{H}}_{k,l} = \frac{Y_{k+l\Delta_f}}{X_{l\Delta_f}}. \tag{6.3.29}
$$

for $k=-Z,-Z+1,...,Z$ and $l=0,1,...,N_L-1$. Finally, the parameters of the Zadeh's representation can be estimated by taking the N_L-point Inverse Discrete Fourier Transform (IDFT) of $\left\{\hat{\mathcal{H}}_{k,l}\right\}$, i.e. as

$$
\hat{H}_{k,m} = N_L\sum_{l=0}^{N_L-1}\hat{\mathcal{H}}_{k,l}\exp\left(j\frac{2\pi\left(l-k\right)m}{N_L}\right) \tag{6.3.30}
$$

for $k = -Z, -Z+1, ..., Z$ and $m = 0, 1, ..., M$.

6.3.2 Pilot-aided estimation of the filter memory and order

The filter memory M can be estimated experimentally operating in the time domain. In fact, if the powerline channel under test is fed by a pulse train and the spacing between consecutive pulses of the train itself is progressively increased, M is identified by the minimal spacing ensuring the absence of inter-symbol interference in the output sequence.

The order Z, instead, can be assessed in the frequency domain; the adopted approach is inspired by the results on channel estimation in the frequency domain illustrated in the previous paragraph. In particular the adopted procedure consists of the following steps:

1. set $\tilde{Z} = 1$ and the value of a threshold t_{dB};
2. feed the powerline channel under test with a comb of sinuoids characterized by a frequency spacing $\Delta f = 2\tilde{Z} f_0$;
3. evaluate the DFT of the system output according to (6.3.26);
4. estimate
$$k = \arg \max_{\xi,k} \left(|Y_{\xi+k}|_{dB} > |Y_{\xi}|_{dB} - t_{dB} \right); \tag{6.3.31}$$
5. if $k > \tilde{Z}$, then set $\tilde{Z} = \tilde{Z} + 1$ and go back to step 2), otherwise stop.

In practice, the distance between adjacent suinusoids contained in the pilot signal is progressively increased in each recursion (see steps 2) and 6)) until the spectral contributions associated with the terms $X_{\xi-k}\mathcal{H}_{k,\xi-k}$ (see (6.3.26)) are non-overlapping for $k = Z$. Finally, it is worth mentioning that the estimated order of the Zadeh's representation Z (and, consequently, the accuracy of the model as a consequence) depends on the threshold t_{dB}, since a smaller t_{dB} may entail a larger estimate of Z.

6.4 Complexity

This Section is devoted to: a) comparing the computational complexity required by the implementation of different models for a given powerline channel; b) providing some quantitative indications about the computational complexity of pilot-aided channel estimators based on such models (i.e., about the complexity of the estimators of model parameters). As already

mentioned in the Introduction, alternatives to the channel model developed in this manuscript are given by the ACR [73] and the SM [120]. The ACR is based on N_0 time-invariant FIR filters, each having M complex-valued taps. The estimation of the N_0M filter tap gains involves the inversion of a complex-valued matrix whose size is not smaller than $N_0M \times N_0M$, so that the complexity of this task increases as $O\left[(N_0M)^3\right]$. This explains why a large complexity should be expected if the ACR is employed when the channel period N_0 is large (i.e., when the band of the channel and, consequently, the sampling frequency at the receive side are large). The overall complexity of the channel model can be reduced if a SM is adopted for the representation of a powerline channel[120], since this model is based on $N_{LTI} < N_0$ independent linear time-invariant FIR filters, each having M real-valued taps. The estimation of the $N_{LTI}M$ filter parameters requires the inversion of a real matrix whose minimum size is $N_{LTI}M \times N_{LTI}M$, so that the complexity of this task increases as $O\left[(N_{LTI}M)^3\right]$; note also that a SM may require a large N_{LTI} if a good accuracy in channel representation is required. The channel representation proposed in this manuscript is based on $2Z+1$ time-invariant FIR filters (each filter has M real-valued taps) and is characterized by a small complexity if the channel order Z is small. As far as the complexity of channel estimation is concerned, the LSE, the Huber estimator and the Fair estimator require the inversion of the $N_s \times M\,(2Z+1)$ matrix $\mathbf{Z}$ (e.g., see (6.3.9)) with $N_s > M\,(2Z+1)$, so that their complexity is upper bounded by $O\left[(N_s)^3\right]$. These findings are summarized in Table 6.2. In particular, on the one hand, the complexity of a channel model is given by the number of real taps required to generate a single sample at the channel output. On the other hand, the complexity of a channel estimator is evaluated as a number of *floating point operations* (FLOPs) required for the estimation of all the channel taps, where one FLOP is defined as a complex-valued multiplication followed by a complex-valued addition. Note that: a) the complexity of the MLE has not been specified since its implementation relies on the MATLAB routine `fmincon` (which is based on a sequential quadratic programming algorithm) whose complexity cannot be easily assessed; b) the complexity required by an N_L-point IDFT (see (6.3.30)) in the FDE increases as $O\left[N_L \log\left(N_L\right)\right]$.

6.5 Numerical results

In our work the time-varying behavior of real world indoor powerline channels has been analysed exploiting the channel sounder described in [91] and illustrated in Fig. 5.7.1.

All experimental results have been acquired at the second floor of the DIEF. During the

Algorithm	Channel model	Channel estimator
ACR	$N_0 M$	$O\left[(N_0 M)^3\right]$
SM	$N_{LTI} M$	$O\left[(N_{LTI} M)^3\right]$
ZR - LSE	$M(2Z+1)$	$O\left[(N_s)^3\right]$
ZR - Huber estimator	$M(2Z+1)$	$O\left[(N_s)^3\right]$
ZR -Fair estimator	$M(2Z+1)$	$O\left[(N_s)^3\right]$
MLE	$M(2Z+1)$	
FDE	$M(2Z+1)$	$O\left[N_L \log(N_L)\right]$

Table 6.2: Computational complexity of different channel models and channel estimators.

measurements the channel sounder has transmitted an analog signal $x(t)$ associated with a pilot sequence $\{x_n\}$ over the selected power network and has acquired the output sequence $\{y_n\}$ sampling the corresponding channel response $y(t)$. The sounder has been also used to collect multiple realizations of the noise sequence $\{w_n\}$, i.e. the channel output in the absence of any excitation. The measurements have evidenced that:

- The periodic time variations of indoor powerline channels are significant only in the lower portion of the considered band [91]; for this reason, our analyis has been restricted to the band $80 - 700$ kHz. This has allowed us to reduce the sampling frequency to $f_s = 2$ Msps, so that $N_0 = T_0 f_s = 2 \cdot 10^4$ samples are contained in a channel period.
- $M = 100$ can be assumed for the memory of the considered powerline channels in the band of interest.

In this case the implementation of the ACR would require the inversion of a complex-valued matrix having size $2{\cdot}10^4 \times 2{\cdot}10^4$. Since this is unfeasible in practice, the ACR has been excluded from our analysis, which has focused on the SM and on the proposed Zadeh's Representation (ZR). To compare these models, the following procedure has been followed:

1. A single realization of the received vector $\mathbf{y}_{N_s}$ (see (6.3.12)) has been acquired on a specific power tap in the considered scenario by means of the channel sounder described above.
2. A LS method has been employed to estimate the parameter vector $\mathbf{H}$ (6.3.4) of the ZR (the resulting estimate $\hat{\mathbf{H}}_{LS}$ is expressed by (6.3.10)) and the $N_{LTI}M$-dimensional

parameter vector $\mathbf{H}_{SM}$ of the SM (the corresponding estimate is denoted $\hat{\mathbf{H}}_{SM}$ in the following).

3. The channel output vectors $\hat{\mathbf{y}}_{N_s}^{LS}$ and $\hat{\mathbf{y}}_{N_s}^{SM}$ have been generated feeding the derived ZR and SM, respectively, with the training sequence $\{x_n\}$ used for channel sounding.

4. For each of the considered models, the Normalised Square Error (NSE) has been assessed as

$$\text{NSE} = \frac{\|\hat{\mathbf{y}}_{N_s} - \mathbf{y}_{N_s}\|^2}{\|\mathbf{y}_{N_s}\|^2} \tag{6.5.1}$$

where $\hat{\mathbf{y}}_{N_s}$ coincides with $\hat{\mathbf{y}}_{N_s}^{LS}$ or $\hat{\mathbf{y}}_{N_s}^{SM}$ and $\|\mathbf{x}\|^2 \triangleq \mathbf{x}^H\mathbf{x}$ denotes the squared Euclidean norm of a complex vector $\mathbf{x}$.

It is important to point out that:

- The selected training sequence $\{x_n\}$ is periodic with period N_0 and its samples are generated as iid rvs; in particular the samples are extracted from a uniform distibution in the interval [−256mV, 256mV], so that the dynamic range of the channel sounder front-end is not exceeded.

- One branch of the ZR entails the same complexity of one stationary state of the SM, since $M = 100$ has been set for both systems.

- The maximum number of stationary states in the SM is $N_{LTI}^{max} = \frac{N_0}{M} = 200$.

- The computational complexity required for generating the LS estimates $\hat{\mathbf{H}}_{LS}$ and $\hat{\mathbf{H}}_{SM}$ is the same ($O\left(N_s^3\right)$).

Fig. 6.5.1 shows the NSE (6.5.1) versus the channel model complexity evaluated for the ZR and the SM; note that: a) these results refer to specific vectors $\mathbf{y}_{N_s}$ characterized by different lengths in the ZR case; b) the complexity of the channel estimator associated with a given representation depends on N_s. These results evidence that the ZR outperforms its counterpart in terms of both accuracy and complexity. In fact, on the one hand, for a given complexity of the channel model, the ZR outperforms its SM counterpart in term of accuracy even when the complexity of the associated channel estimator is by far smaller. On the other hand, for a given NSE, the ZR entails a computational complexity (both in the channel model and in the estimation of its parameters) by far smaller that that required by its SM counterpart.

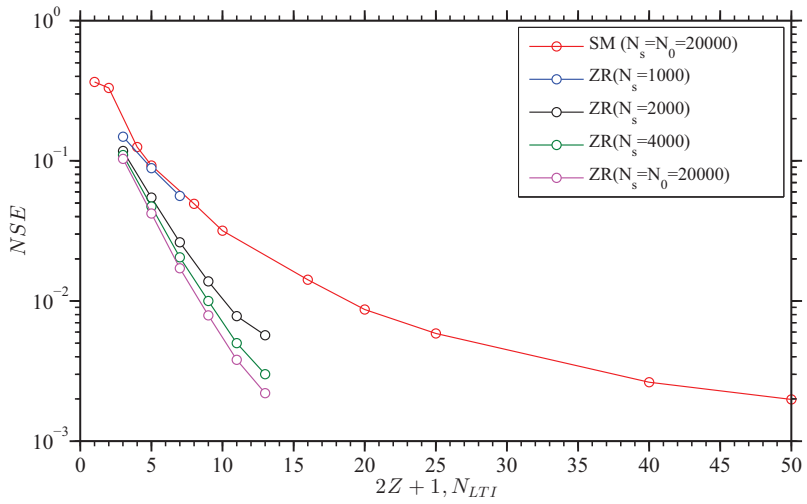

Figure 6.5.1: NSE performance comparison between powerline channel models based on the ZR and a SM.

The performance of the channel estimators described in Section 6.3 has been also compared. In this case the following procedure has been adopted:

1. In the selected scenario a single realization of the powerline response $\mathbf{y}_{N_s}$ to our training sequence and multiple realizations of the powerline noise[3] have been acquired by means of our channel sounder (the amplitude of the TVTF, of the considered powerline channel is shown in Fig. 6.5.2).

2. For the acquired vector $\mathbf{y}_{N_s}$ the parameters of the Zadeh's model $\mathbf{H}$ (6.3.4) have been evaluated by means of the FDE described in the previous Section (the resulting estimate is denoted $\hat{\mathbf{H}}_{FDE}$).

3. The vector $\hat{\mathbf{H}}_{FDE}$ has been processed to estimate the CIR of the channel under test; this estimated CIR has been assumed to be the true CIR of the selected powerline channel.

4. A new received vector $\tilde{\mathbf{y}}_{N_s}$ has been generated superimposing the result of the convolution between the true CIR and the same training sequence as step 1) with one of the acquired noise sequences.

[3] A detailed analysis of the statistics of the powerline noise acquired in our laboratories can be found in [128].

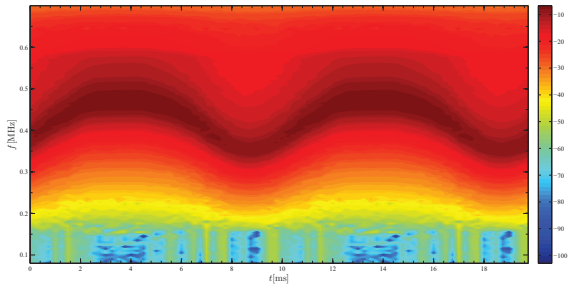

Figure 6.5.2: Amplitude of the TVTF of the powerline channel considered in the assessment of the NSE performance shown in Fig. 6.5.3 (a dB scale is used in this representation).

5. The parameters of the Zadeh's representation have been estimated from $\tilde{\mathbf{y}}_{N_s}$ by means of the time domain techniques described in the previous Section.

6. Steps 4) and 5) have repeated $N_E = 40$ times.

7. For each of the above mentioned estimation techniques, the Normalised Mean Square Error (NMSE) has been evaluated as

$$\text{NMSE} = \frac{1}{N_E} \sum_{n=1}^{N_E} \frac{\left\| \hat{\mathbf{H}}^{(n)} - \mathbf{H} \right\|^2}{\|\mathbf{H}\|^2} \tag{6.5.2}$$

   where $\hat{\mathbf{H}}^{(n)}$ denotes the parameters of the Zadeh's representation estimated at the nth simulation run.

This approach deserves the following two important comments:

- Since the CIR experimentally acquired at step 1) is unavoidably affected by channel noise, an error is unavoidably introduced when exploiting the parameters derived at step 2) to generate the *true* CIR as a reference for step 3). An alternative to this approach consists of adopting a CIR generated by a computer on the basis of a given statistical model for the considered communication channel; however, even the last procedure introduces an error, since, in practice, a non negligible mismatch between any statistical model and the real properties of powerline channels should be expected.

- In the simulations the power of the noise sequence is properly adjusted at step 4) so that the accuracy of the considered channel estimators at a specific Signal-to-Noise Ratio (SNR) can be estimated.

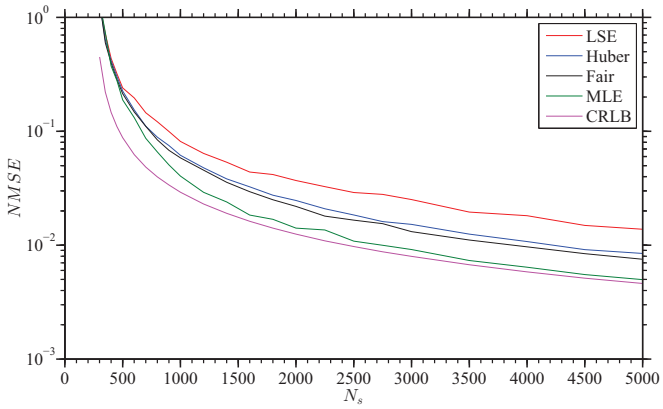

Figure 6.5.3: NMSE performance of the LSE, Huber estimator, Fair estimator and MLE; the CRLB is also shown for comparison.

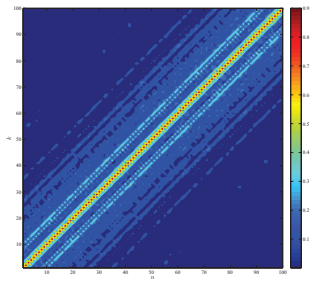

Figure 6.5.4: Amplitude of the cross-correlation coefficient $\rho_{n,k}$ (6.5.3) referring to 100 consecutive samples of powerline noise.

The NMSE versus the length N_s of the observed vector $\mathbf{y}_{N_s}$ is shown in Fig. 6.5.3 for the LSE, the Huber estimator, the Fair estimator and MLE with SNR = 5 dB. These results evidence that:

- Since the powerline noise is far from being Gaussian, the LSE is outperformed by both the Huber estimator (with $\gamma = 0.0346$) and the Fair estimator (with $\beta = 0.0332$).
- The MLE (adopting the following parameter values: $N_c = 3$, $\lambda_0 = 0.2678$, $\mu_0 = -0.0025$, $\sigma_0^2 = 0.0016$, $\lambda_1 = 0.0082$, $\mu_1 = 0.0719$, $\sigma_1^2 = 0.0015$, $\lambda_2 = 0.7240$, $\mu_2 = 0.0001$ and $\sigma_2^2 = 0.001$) achieves the best accuracy and, in particular, approaches the CRLB even for moderate lengths N_s.

As far the last point is concerned, it worth mentioning that the CRLB has been derived under the assumption of iid noise samples, all distributed according to a GM. In this work the existence of a statistical correlation between consecutive samples of channel noise has been investigated; in particular, the cross correlation coefficient

$$\rho_{n,k} = \frac{\mathrm{E}\left\{\left(w_m - \mu_m\right)\left(w_k - \mu_k\right)\right\}}{\sigma_m \sigma_k}, \tag{6.5.3}$$

has been evaluated for a set of 100 consecutive noise samples, where μ_m and σ_m denote the mean and standard deviation of the noise sample w_m, respectively. The amplitude of $\rho_{n,k}$ (6.5.3) for the considered noise process is shown in Fig. 6.5.4; from these results it is easily inferred that channel noise cannot be deemed white. Therefore, the real CRLB should be expected to be lower than that shown in Fig. 6.5.3.

The effects of the noise mitigation technique proposed in Section 6.3.1 (see eqs. (6.3.12)-(6.3.13)) can be assessed analysing the results of Fig. 6.5.5, which illustrates the pdf $f_W(w)$ of the noise affecting the elements of the vector $\bar{\mathbf{y}}_{N_s}(N_p)$ (6.3.12) for $N_p = 1, 2, 5$ and 10; note that the quality of its Gaussian fitting (red line) improves quickly as N_p increases. The improvement is confirmed by the performance results shown in Fig. 6.5.6 for the LSE, where the NMSE is assessed employing the observed vector $\bar{\mathbf{y}}_{N_s}(N_p)$ (see (6.3.12)) instead of $\mathbf{y}_{N_s}$ in the LS strategy (6.3.10). As expected, the NMSE decreases as N_p gets larger and, surprisingly, the LSE accuracy approaches that of the MLE even for $N_p = 2$ and outperforms it for $N_p > 2$.
$P_W(\omega)$

Finally, the NMSE performance of the FDE has been assessed feeding the selected powerline channel with a training sequence generated by sampling a combs of sinusoids with frequency spacing Δf equal to 2.5 kHz, 5 kHz, 10 kHz and 20 kHz. The numerical results shown in Fig. 6.5.7 (referring to SNR = 5 dB and $N_P = 1, 2, 5, 10$) evidence that the FDE can outperform its time domain counterparts even for $N_p = 1$, i.e without resorting to noise mitigation. This result can be explained as follows. The training sequence employed by the estimators (6.3.10), (6.3.15) and (6.3.21) consists of iid rvs, so that the its energy is uniformly distributed over the whole band of interest ($80 - 700$ kHz); on the other hand, the energy of the comb of sinusoids can be concentrated on frequencies close to that characterizing the Zadeh' representation (see eqs. (6.3.29) and (6.3.30)), thus improving the performance of the channel estimator exploiting the pilot signal. Finally, it is wort noting that the NMSE of the FDE does not significantly decrease when the frequency spacing Δf is lower than 10 kHz; this is likely to be due to the fact that the coherence bandwidth of the powerline channel belongs to the interval $10 - 20$ kHz.

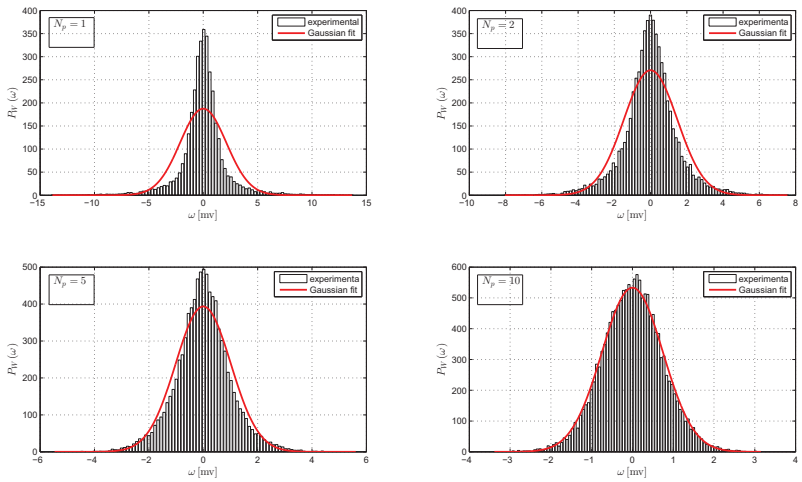

Figure 6.5.5: Pdfs of the noise affecting the elements of the vector $\bar{\mathbf{y}}_{N_s}(N_p)$ (6.3.12) for $N_p = 1, 2, 5, 10$ periods; its Gaussian fitting is also shown for comparison.

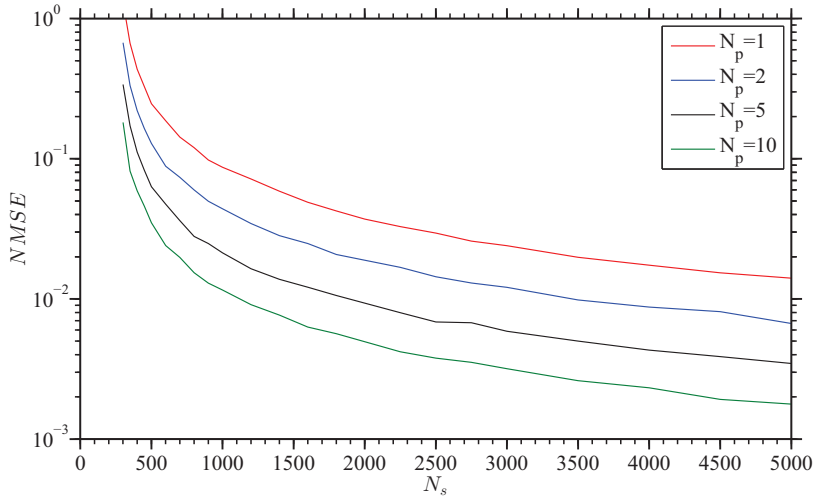

Figure 6.5.6: NMSE performance provided by the LSE when the observed vector $\bar{\mathbf{y}}_{N_s}(N_p)$ (6.3.12) is employed; $N_P = 1, 2, 5$ and 10.

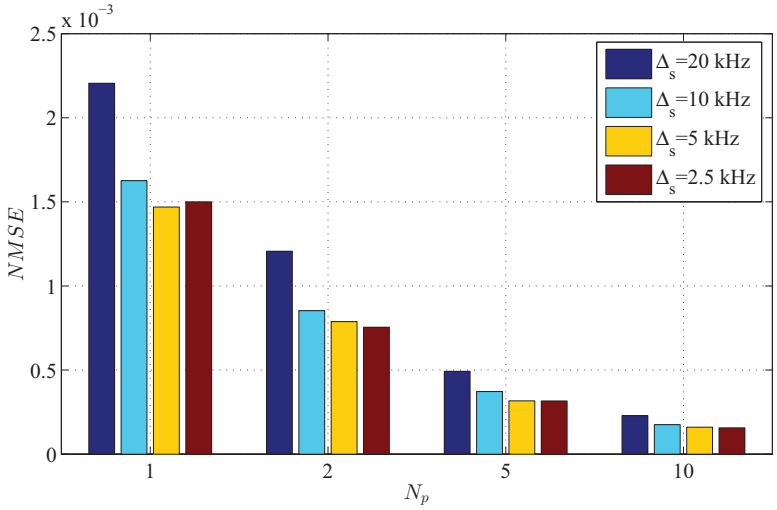

Figure 6.5.7: NMSE performance provided by the FDE for $\Delta f = 2.5, 5, 10, 20$ kHz and $N_P = 1, 2, 5, 10$.

6.6 Conclusions

Modelling powerline channel as LPTV systems may entail a huge complexity if an alias component representation is adopted or may lead to a limited accuracy if the switching model is employed to lower the complexity of channel representation. In this chapter it has been shown that a simple discrete-time model inspired by the Zadeh's representation can achieve excellent performance in terms of both complexity and accuracy. The problem of estimating the parameters of channel models has been also investigated and it has been shown that, if the proposed channel model is adopted, a simple frequency domain estimator, outperforming its time domain counterparts, can be devised.

Part III

Commmunication Techniques Based on LPTV Modelling of Indoor Powerline Channels

Chapter 7

A Zadeh-Based Approach to Channel Estimation and Equalization in OFDM Communications over Indoor Powerline Channels

This chapter represents a follow up to Chapter 6 where it is shown that a faithful representation of a periodically time varying powerline channel is provided by a discrete-time model based on the so Zadeh's series expansion. In fact, it applies this model to the development of novel channel estimation and equalization techniques for orthogonal frequency division multiplexing over indoor powerline channels. Simulation and experimental results evidence that these techniques can significantly outperform their conventional counterparts, which do to account for the time-varying behavior of the channel within each symbol, at the price of a very limited increase in computational complexity.

The rest of this chapter is organized as follows.In Section 7.1 the state of the art of powerline channel equalization in analyzed. The PLC system considered in this work is illustrated in Section 7.2, where frequency domain models based on the Zadeh's representation are also developed for the received signal. Novel data-aided channel estimation and ZF equalizer are derived in Section 7.3, whereas their error performance is assessed in Section 7.4. Finally, some conclusions are offered in Section 7.5.

7.1 State of the art

It is well known that reliable detection of OFDM over indoor powerline channels requires specific channel estimation and equalization techniques which may appreciably differ from their counterparts developed for wireless channels. This is mainly due to the fact that: a) the standard AWGN model is far from the describing the statistical properties of real world powerline noise; b) powerline channels exhibit a cyclically time-varying input-output behavior synchronous with the mains. Therefore, the development of novel techniques for OFDM PLCs requires the availability of accurate channel models accounting for both the peculiar statistical properties of poweline noise and channel double selectivity (i.e., frequency and time selectivity). Unluckily, modelling of powerline noise is still an open issue [128], since this process, being not Gaussian, almost-cyclostationary and colored, does not lend itself to a simple and comprehensive statistical representation. On the other contrary, accurate mathematical models are already available to describe system functions (e.g., impulse response and frequency response) of powerline channels, since such channels, as evidenced by various experimental campaigns, behave as LPTV systems synchronized to the mains frequency, at least for some periods of the mains [28, 50, 132]. In fact, various models, namely the *switching* [120], the *alias component* [73] and the *Zadeh's representations* [50, 132], are already available in the technical literature for the description of the input-ouput behavior LPTV systems. However, in principle, the exploitation of these models for the design of channel estimation and equalization techniques may not be easy; in fact, generally speaking, this design problem can be easily tackled if the selected channel model depends on a limited (and, possibly, small) set of real or complex parameter, i.e. if it provides a *parsimonious representation* of a powerline channel. In this manuscript, after showing that the Zadeh's representation has this favorable feature, we exploit it to derive novel algorithms for data-aided LS channel estimation and Zero Forcing (ZF) equalization to be employed in OFDM transmissions over powerline channels. The experimental and simulation results, referring to PLCs over the band[1] $200 - 500$ kHz in specific indoor scenarios, show that these techniques substantially outperform standard counterparts developed for wireless channels at the price of a limited increase in computational complexity. It is important to point out that, as far as we know, the problem of channel estimation and equalization of LPTV channels has been previously investigated in [144] only; in that reference, however, a blind channel estimator based on the cyclostationary properties of a wireless channel output is developed and channel equalization is based on the Viterbi

[1] The interest in this band is motivated by the fact that it is currently under investigation by various working groups for low-to-medium data rate PLCs [96].

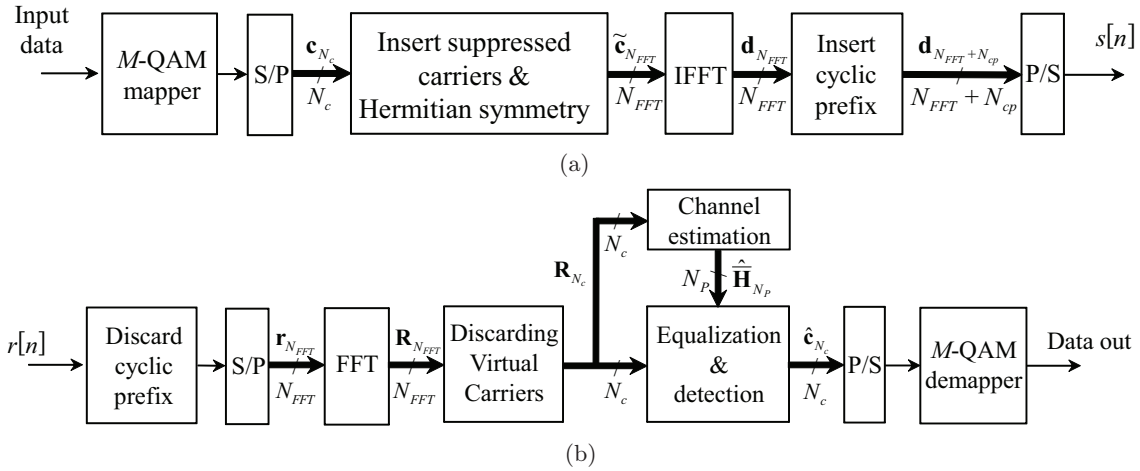

Figure 7.2.1: Block diagram of the OFDM transmitter (a) and receiver (b).

algorithm or on a MSE approach. In fact, other equalization algorithms explicitly developed for multicarrier transmissions assume a stationary channel (e.g., see [139, 140] and [141, 142, 143] where neural and fuzzy tecniques, respectively, are considered); in addition, some of them refer to specific multicarrier formats (e.g., OFDM/OQAM [137, 138])

7.2 System and signal model

The digital parts of the OFDM transmitter and receiver adopted in the powerline communication systems are illustrated in Fig. 7.2.1-(a) and 7.2.1-(b), respectively. Note that, since in the considered scenario the bandwidth B of the transmitted signal is comparable to its central frequency f_c, the transmitted signal is generated directly in pass-band, so that no frequency upconversion is required; similarly, no downconversion is employed at the receive side.

The OFDM transmitter operates as follows. The input binary stream is partitioned in blocks, each consisting of $\log_2(M)$ bits, and each block is mapped to a channel symbol belonging to a M-ary QAM constellation. The resulting stream of channel symbols undergoes a serial-to-parallel conversion which produces a sequence of N_c-dimensional vectors, each containing N_c consecutive channel symbols; let $\mathbf{c}_{N_c}^{(l)} \triangleq [c_0, c_1, ..., c_{N_c-1}]^T$ denotes the l-th channel symbol vector, where $()^T$ indicates the transposition operator. Then, for any l the vector $\mathbf{c}_{N_c}^{(l)}$ is processed to generate a larger vector, denoted $\tilde{\mathbf{c}}_{N_{FFT}}^{(l)}$ in the following, which undergoes an *inverse discrete Fourier transform* (in practice, an IFFT) of order N_{FFT}. This processing

is needed since: a) the IFFT output vector $\mathbf{d}_{N_{FFT}}$ is required to be *real*; b) the N_c data symbols forming the vector $\mathbf{c}_{N_c}$ have to be transmitted over N_c adjacent subcarriers and flexibly allocated in the available band (whose lower limit is larger than 0). For these reasons, the N_{FFT}-dimensional OFDM symbol $\tilde{\mathbf{c}}^{(l)}_{N_{FFT}}$ is generated as

$$\begin{aligned}\tilde{\mathbf{c}}^{(l)}_{N_{FFT}} &= \left[\tilde{c}^{(l)}_0, \tilde{c}^{(l)}_1, ..., \tilde{c}^{(l)}_{N_{FFT}-1}\right]^T \\ &= \left[\left(\mathbf{0}_{N_{pre}}\right)^T, \left(\mathbf{c}^{(l)}_{N_c}\right)^T, \left(\mathbf{0}_{2N_{post}}\right)^T, \left(\mathbf{c}^{(l)}_{N_c}\right)^{\ddagger}, \left(\mathbf{0}_{N_{pre}}\right)^T\right]^T \end{aligned} \quad (7.2.1)$$

where $\mathbf{0}_N$ denotes a N-dimensional null column vector, $(\mathbf{x})^{\ddagger}$ denotes the *flipped Hermitian transpose* of the vector $\mathbf{x}$, and N_{pre} and N_{post} are two integer parameters whose sum $N_{sc} \triangleq N_{pre} + N_{post}$ represents the overall number of suppressed subcarriers in the transmitted OFDM signal and $N_{FFT} \triangleq 2N_c + 2N_{sc}$. Note that the specific structure of the vector $\tilde{\mathbf{c}}^{(l)}_{N_{FFT}}$ (7.2.1) ensures that both the above mentioned requirements a) and b) are satisfied since: 1) $\tilde{\mathbf{c}}^{(l)}_{N_{FFT}}$ has the property of Hermitian symmetry; 2) the elements of $\mathbf{c}_{N_c}$ are transmitted over the N_c adjacent subcarrier frequencies $\{f_k = k/(N_{FFT}T_s),\ k = N_{pre}, N_{pre}+1, ..., N_{FFT}-1-N_{post}\}$ (where $T_s \triangleq 1/f_s$ and f_s denotes the frequency at which the IFFT output samples are transmitted over the communication channel) which can be properly allocated in the available band $(0 - f_s/2)$ by adjusting the values of the parameters N_{pre} and N_{post}. Appending a *cyclic prefix* (CP) of N_{cp} symbols to $\mathbf{d}^{(l)}_{N_{FFT}}$ produces the cyclically extended vector $\mathbf{d}^{(l)}_{N_T}$ (with $N_T \triangleq N_{FFT} + N_{cp}$), which after parallel-to-serial conversion feeds a bandpass transmit filter generating the sequence $\{s[n]\}$; this sequence consists of equally spaced samples of the (real) OFDM signal to be sent over the communication channel. Following the Chapter 6 and [50], the poweline communication channel is modelled as a discrete-time LPTV system characterized by a period[2] N_0 and discrete time version of the so called Zadeh's series expansion is adopted to describe its input-output behavior. Then, if $\{h_{n,i}\}$ denotes the time-variant impulse response[3] of the overall communication channel (which includes both the transmit filter and the receive filter matched to it); see 7.2.1-(b)) , the n-th received signal sample $r[n]$ can be expressed as

$$r[n] = \sum_{z=0}^{N_0-1}\left[\sum_{m=-\infty}^{+\infty} H_{z,m}\, s[n-m]\right]\exp\left(j\frac{2\pi z n}{N_0}\right) + w[n] \quad (7.2.2)$$

[2]Note that $N_0 = T_0/T_s$, where T_0 is the period of the time varying impulse response $h(t,\tau)$ of the communication channel.

[3]This is defined as the response at time n to a unitary pulse applied $n-i$ samples earlier.

where

$$H_{z,m} \triangleq \frac{1}{N_0} \sum_{n=0}^{N_0-1} h_{n,m} \exp\left(-j\frac{2\pi zn}{N_0}\right), \tag{7.2.3}$$

is the kth coefficient of the *discrete Fourier transform* (DFT) of $\{h_{n,i}\}$ and $w[n]$ represents the contribution of the filtered additive channel noise. In the following the channel impulse response is assumed causal and with a finite duration, moreover the overall delay introduced by the communication channel is neglected, so that the signal model (7.2.2) can be simplified as

$$r[n] = \sum_{z=0}^{N_0-1} \left[\sum_{m=0}^{M-1} H_{k,m} s[n-m]\right] \exp\left(j\frac{2\pi zn}{N_0}\right) + w[n] \tag{7.2.4}$$

where M denotes the channel memory. The last result lends itself to a simple interpretation. In fact, it shows that the useful component of the sequence $\{r[n]\}$ consists of the superposition of the responses of N_0 LTI filters, all fed by the input sequence $\{s[n]\}$ and whose outputs are modulated by complex exponentials, that account for the time-variant behavior of the channel and whose normalised frequencies are all multiple of the fundamental normalised frequency $1/N_0$. Note that if N_0 is large (i.e., if the channel period T_0 is substantially larger than T_s), the representation of the powerline channel behavior through (7.2.4) may require a substantial complexity. Luckily, experimental results have evidenced that in the considered scenario only $(2Z+1)$ (where Z denotes the so-called *order* of the system model) of the N_0 LTI filters, with $(2Z+1) \ll N_0$, provide a relevant contribution to $r[n]$. Consequently, if the periodicity of $\left\{\tilde{H}_{k,m}\right\}$ in the index k (with period N_0) is kept into account, (7.2.4) can be further simplified as

$$r[n] = \sum_{z=-Z}^{Z} \left[\sum_{m=0}^{M-1} \tilde{H}_{z,m} s[n-m]\right] \exp\left(j\frac{2\pi zn}{N_0}\right) + w[n] \tag{7.2.5}$$

which contains a *parsimonious parametric representation* of the useful component of the received signal.

The proposed OFDM receiver operates on a symbol-by-symbol basis and is endowed with ideal timing synchonization; for this reason, in the following the detection of a single OFDM symbol only, namely on $\tilde{\mathbf{c}}^{(l)}_{N_{FFT}}$ is investigated and it is assumed that the transmission of this symbol starts at the instant $(\beta_l - N_{cp})T_s$, where $\beta_l \triangleq lN_TT_s + \beta$ and β denotes a time offset. To carry out the detection of the l-th OFDM symbol, the receiver process the vector $\mathbf{r}^{(l)}_{N_{FFT}} = \left[r^{(l)}_0, r^{(l)}_1, ..., r^{(l)}_{N_{FFT}-1}\right]^T$ collecting the samples $\{r[n], n = \beta_l, \beta_l+1, \ldots, \beta_l+N_{FFT}-1\}$; note that in the received signal model the N_{cp} samples $\{r[n], n = \beta_l - N_{cp}, \beta_l - N_{cp}+1, ..., \beta_l - 1\}$ correspond to the cyclic prefix of the lth OFDM symbol and are discarded by the receiver.

The vector $\mathbf{r}_{N_{FFT}}^{(l)}$ feeds a *discrete Fourier tranform* (DFT) of order N_{FFT} *(*implemented as a FFT) generating the frequency-domain vector $\mathbf{R}_{N_{FFT}}^{(l)} = [R_0, R_1, ..., R_{N_{FFT}-1}]^T$, where

$$R_q^{(l)} \triangleq \mathrm{DFT}_{N_{FFT}}\left[\mathbf{r}_{N_{FFT}}^{(l)}\right] = \frac{1}{N_{FFT}} \sum_{n=0}^{N_{FFT}-1} r_n^{(l)} \exp\left(-j\frac{2\pi nq}{N_{FFT}}\right) \tag{7.2.6}$$

with $q = 0, 1, ..., N_{FFT} - 1$ (here $\mathrm{DFT}_N[\mathbf{x}]$ denotes the DFT of order N of the vector $\mathbf{x}$). Note that: a) the vector $\mathbf{r}_{N_{FFT}}^{(l)}$ represents the noisy response of the channel to its input samples $\left\{s_{-N_{CP}}^{(l)}, s_{-N_{CP}+1}^{(l)}, \ldots, s_{N_{FFT}-1}^{(l)}\right\}$, where

$$s_n^{(l)} = \sum_{k=0}^{N_{FFT}-1} \tilde{c}_k^{(l)} \exp\left[j\frac{2\pi kn}{N_{FFT}}\right] \tag{7.2.7}$$

for $n = -N_{CP}, -N_{CP}+1, \ldots N_{FFT}-1$; b) the elements of $\mathbf{r}_{N_{FFT}}^{(l)}$ can be related to the above mentioned input samples as

$$r_n^{(l)} = \sum_{m=0}^{M-1} h_{n+\beta_l,m} s_{n-m}^{(l)} + w_n^{(l)} \tag{7.2.8}$$

for $n = -N_{CP}, -N_{CP}+1, \ldots N_{FFT}-1$, provided that the channel memory is shorter than the length of the cyclic prefix (i.e., $M \leq N_{CP}$). Then, substituting (7.2.5) and (7.2.8) in (7.2.6) and keeping into account the Zadeh representation (see (7.2.2) and (7.2.3) yields

$$\begin{aligned} R_q^{(l)} \quad = \tfrac{1}{N_{FFT}} \textstyle\sum_{n=0}^{N_{FFT}-1} \quad & \left\{ \sum_{m=0}^{M-1} \left[\sum_{k=0}^{N_{FFT-1}} \tilde{c}_k^{(l)} \exp\left(-j\frac{2\pi km}{N_{FFT}}\right) \right.\right. \\ & \left. \cdot \exp\left(j\frac{2\pi kn}{N_{FFT}}\right)\right] \sum_{z=-Z}^{Z} H_{z,m} \\ & \left.\cdot \exp\left(j\frac{2\pi z\,(n+\beta_l)}{N_0}\right)\right\} \exp\left(-j\frac{2\pi nq}{N_{FFT}}\right) + W_q^{(l)} \end{aligned} \tag{7.2.9}$$

where

$$W_q^{(l)} \triangleq \frac{1}{N_{FFT}} \sum_{n=0}^{N_{FFT}-1} w_n^{(l)} \exp\left(-j\frac{2\pi nq}{N_{FFT}}\right) \tag{7.2.10}$$

denotes the q-the element of the DFT of the noise component of $\mathbf{r}_{N_{FFT}}^{(l)}$. If the following vector is introduced

$$\mathbf{H}_z^{(e)} \triangleq \left[H_{z,0}^{(e)}, H_{z,1}^{(e)}, ..., H_{z,N_{FFT}-1}^{(e)}\right]^T \tag{7.2.11}$$

for $z = -Z, -Z+1, ..., Z$, with

$$H_{z,m}^{(e)} \triangleq \begin{cases} H_{z,m} & 0 \leq m \leq M-1 \\ 0 & M \leq m \leq N_{FFT}-1 \end{cases} \tag{7.2.12}$$

and the quantity[4]

$$\overline{H}_{z,k} \triangleq \frac{1}{N_{FFT}} \sum_{m=0}^{N_{FFT}-1} H_{z,m}^{(e)} \exp\left(-\frac{j2\pi km}{N_{FFT}}\right) \tag{7.2.13}$$

for $z = -Z, -Z+1, ..., Z$ and $k = 0, 1, ..., N_{FFT}-1$, (7.2.9) can be rewritten, after some manipulation, as

$$\begin{aligned} R_q^{(l)} &= \sum_{z=-Z}^{Z} \sum_{k=0}^{N_{FFT}-1} \overline{H}_{z,k} \tilde{c}_k^{(l)} \exp\left(j\frac{2\pi z\beta_l}{N_0}\right) \\ &\quad \cdot \sum_{n=0}^{N_{FFT}-1} \exp\left(-j2\pi n\left(\frac{q-k}{N_{FFT}} - \frac{z}{N_0}\right)\right) + W_q^{(l)} \end{aligned} \tag{7.2.14}$$

Then, if I define the coefficient

$$\widetilde{A}_{q,k}^{(z)} \triangleq \sum_{p=0}^{N_{FFT}-1} \exp\left(-j2\pi p\left(\frac{q-k}{N_{FFT}} - \frac{z}{N_0}\right)\right) \tag{7.2.15}$$

$$= \exp\left(-j\pi\delta_{q,z,k}\left(N_{FFT}-1\right)\right) \frac{\sin\left(\pi N_{FFT}\delta_{q,z,k}\right)}{\sin\left(\pi\delta_{q,z,k}\right)} \tag{7.2.16}$$

with

$$\delta_{q,z,k} \triangleq \frac{q-k}{N_{FFT}} - \frac{z}{N_0}, \tag{7.2.17}$$

the frequency-domain sample $R_q^{(l)}$ (7.2.14) can be put in the more compact form

$$R_q^{(l)} = \sum_{z=-Z}^{Z} \sum_{k=0}^{N_{FFT}} \overline{H}_{z,k}\, \widetilde{A}_{q,k}^{(z)}\, \tilde{c}_k^{(l)} \exp\left(j\frac{2\pi z\beta_l}{N_0}\right) + W_q^{(l)} \tag{7.2.18}$$

which can be also rewritten as

[4]Note that $\{\overline{H}_{z,k}\}$results from a double DFT of the channel impulse response $\{h_{n,m}\}$.

$$R_q^{(l)} = U_q^{(l)} + I_q^{(l)} + W_q^{(l)} \tag{7.2.19}$$

where

$$U_q^{(l)} \triangleq \tilde{c}_q^{(l)} \sum_{z=-Z}^{Z} \overline{H}_{z,q}\, \widetilde{A}_{q,q}^{(z)}\, \exp\left(j\frac{2\pi z\beta_l}{N_0}\right) \tag{7.2.20}$$

represents the useful signal component (i.e., the contribution originating from the qth channel symbol $\tilde{c}_q^{(l)}$), whereas

$$I_q^{(l)} \triangleq \sum_{z=-Z}^{Z} \sum_{\substack{k=0 \\ k\neq q}}^{N_{FFT}} \overline{H}_{z,k}\, \widetilde{A}_{q,k}^{(z)}\, \tilde{c}_k^{(l)} \exp\left(j\frac{2\pi z\beta_l}{N_0}\right) \tag{7.2.21}$$

represents the Inter-Carrier Interference (ICI) originating from the variations of the communication channel during the transmission of the considered OFDM symbol. It is not difficult to show that from the expression (7.2.18) the matrix model

$$\mathbf{R}_{N_{FFT}}^{(l)} = \mathbf{A}^{(l)}\tilde{\mathbf{c}}_{N_{FFT}}^{(l)} + \mathbf{W}_{N_{FFT}}^{(l)} \tag{7.2.22}$$

can be derived for received signal vector $\mathbf{R}_{N_{FFT}}^{(l)} \triangleq [R_0^{(l)}, R_1^{(l)}, ..., R_{N_{FFT}-1}^{(l)}]^T$; here $\mathbf{W}_{N_{FFT}}^{(l)} \triangleq [W_0^{(l)}, W_1^{(l)}, ..., W_{N_{FFT}-1}^{(l)}]^T$ and $\mathbf{A}^{(l)} = [A_{q,k}^{(l)}]$ is a $N_{FFT} \times N_{FFT}$ matrix depending on the set of $N_{FFT} \cdot (2Z+1)$ channel parameters $\left\{\overline{H}_{z,k}\right\}$ (with $z = -Z, -Z+1, ..., Z$ and $k = 0, 1, ..., N_{FFT}-1$) since (see (7.2.18))

$$A_{q,k}^{(l)} = \sum_{z=-Z}^{Z} \overline{H}_{z,k}\, \widetilde{A}_{q,k}^{(z)} \exp\left(\frac{j2\pi z\beta_l}{N_0}\right) \tag{7.2.23}$$

with $q, k = 0, 1, ..., N_{FFT}-1$.

It is important to point out that in (7.2.22) the dependence of the received signal vector $\mathbf{R}_{N_{FFT}}^{(l)}$ on the l-th symbol $\tilde{\mathbf{c}}_{N_{FFT}}^{(l)}$ involves the matrix $\mathbf{A}^{(l)}$, which, in turn, depends on the parameters of the Zadeh representation in a complicated fashion. It is not difficult to show that the dependence of $\mathbf{R}_{N_{FFT}}^{(l)}$ on these parameters can be clearly evidenced if a different representation is adopted, namely if this vector is expressed as

$$\mathbf{R}_{N_{FFT}}^{(l)} = \mathbf{K}^{(l)}\overline{\mathbf{H}} + \mathbf{W}_{N_{FFT}}^{(l)} \tag{7.2.24}$$

where

$$\overline{\mathbf{H}} \triangleq \left[\left(\overline{\mathbf{H}}_{-\mathrm{Z}}\right)^{\mathrm{T}}, \left(\overline{\mathbf{H}}_{-\mathrm{Z}+1}\right)^{\mathrm{T}}, ..., \left(\overline{\mathbf{H}}_{\mathrm{Z}}\right)^{\mathrm{T}} \right]^{\mathrm{T}} \tag{7.2.25}$$

is a column vector collecting all the channel parameters and $\overline{\mathbf{H}}_z \triangleq \mathrm{DFT}_{N_{FFT}} \left\{ \mathbf{H}_z^{(e)} \right\}$ for $z = -Z, -Z+1, \ldots, Z$, and $\mathbf{K}^{(l)}$ is a $N_{FFT} \times [N_{FFT}\,(2Z+1)]$ matrix which depends on $\tilde{\mathbf{c}}_{N_{FFT}}^{(l)}$, the order Z of the channel model and on transmission instant β_l. More specifically,$\mathbf{K}^{(l)}$is structured as

$$\mathbf{K}^{(l)} \triangleq \left[\mathbf{k}_{-Z}^{(l)}, \mathbf{k}_{-Z+1}^{(l)}, \ldots, \mathbf{k}_{Z}^{(l)} \right] \tag{7.2.26}$$

where

$$\mathbf{k}_z^{(l)} \triangleq \left(\widetilde{\mathbf{C}}^{(l)} \odot \widetilde{\mathbf{A}}_{\mathrm{z}} \right) \exp\left(j \frac{2\pi z \beta_l}{N_0} \right) \tag{7.2.27}$$

is $N_{FFT} \times N_{FFT}$ matrix for $z = -Z, -Z+1, ..., Z$; here $\odot$ denotes the Hadamard product,

$$\widetilde{\mathbf{C}}^{(l)} \triangleq \begin{bmatrix} \widetilde{c}_0^{(l)} & \widetilde{c}_1^{(l)} & \cdots & \widetilde{c}_{N_{FFT}-1}^{(l)} \\ \widetilde{c}_0^{(l)} & \widetilde{c}_1^{(l)} & \cdots & \widetilde{c}_{N_{FFT}-1}^{(l)} \\ \vdots & \vdots & \vdots & \vdots \\ \widetilde{c}_0^{(l)} & \widetilde{c}_1^{(l)} & \cdots & \widetilde{c}_{N_{FFT}-1}^{(l)} \end{bmatrix} \tag{7.2.28}$$

is a $N_{FFT} \times N_{FFT}$ matrix depending on $\tilde{\mathbf{c}}_{N_{FFT}}^{(l)}$ only

$$\widetilde{\mathbf{A}}_{\mathrm{z}} \triangleq \begin{bmatrix} \widetilde{A}_{0,0}^{(z)} & \widetilde{A}_{0,1}^{(z)} & \cdots & \widetilde{A}_{0,N_{FFT}-1}^{(z)} \\ \widetilde{A}_{1,0}^{(z)} & \widetilde{A}_{1,1}^{(z)} & \cdots & \widetilde{A}_{0,N_{FFT}-1}^{(z)} \\ \vdots & \vdots & \vdots & \vdots \\ \widetilde{A}_{N_{FFT}-1,0}^{(z)} & \widetilde{A}_{N_{FFT}-1,1}^{(z)} & \cdots & \widetilde{A}_{N_{FFT}-1,N_{FFT}-1}^{(z)} \end{bmatrix} \tag{7.2.29}$$

is a $N_{FFT} \times N_{FFT}$ matrix accounting for ICI in the received signal. Finally, it is worth to note that the representation (7.2.24) can be easily generalised to encompass the case in which processing involves the signal received over N_s consecutive OFDM symbols, e.g. the set of vectors $\left\{ \mathbf{R}_{N_{FFT}}^{(l)}, l = 0, 1, ..., N_s - 1 \right\}$. In fact, in this case the overall received (column) vector

$$\mathbf{R}_P \triangleq \left[\left(\mathbf{R}_{N_{FFT}}^{(0)} \right)^T, \left(\mathbf{R}_{N_{FFT}}^{(1)} \right)^T, \ldots, \left(\mathbf{R}_{N_{FFT}}^{(N_s-1)} \right)^T \right]^T$$

with $P = N_{FFT} N_s$, can be expressed as

$$\mathbf{R}_P = \overline{\mathbf{K}}\overline{\mathbf{H}} + \mathbf{W}_P \tag{7.2.30}$$

where $\mathbf{W}_P \triangleq [(\mathbf{W}^{(0)}_{N_{FFT}})^T, (\mathbf{W}^{(1)}_{N_{FFT}})^T, \ldots, (\mathbf{W}^{(N_s-1)}_{N_{FFT}})^T]^T$,

$$\overline{\mathbf{K}} \triangleq \left[\left(\mathbf{K}^{(0)}\right)^T, \left(\mathbf{K}^{(1)}\right)^T, \ldots, \left(\mathbf{K}^{(N_s-1)}\right)^T\right]^T \tag{7.2.31}$$

and $\overline{\mathbf{H}}$ is defined by (7.2.25).

7.3 Channel estimation and equalization

The parametric models developed above for the received signal in the frequency domain (see (7.2.22), (7.2.24) and (7.2.30)) can be exploited to devise novel algorithms for a) data-aided channel estimation and b) channel equalization. In doing so, the following features of the considered scenario should be carefully kept into account:

1. Powerline channel noise is not Gaussian and white, and its properties may undergo substantial changes over time, so that stationarity cannot be deemed a realistic assumption, even in a local sense. For this reason, the standard model commonly employed for frequency domain noise samples in OFDM wireless communications cannot be adopted. In other words, the elements of the channel noise vector $\mathbf{W}^{(l)}_{N_{FFT}}$ appearing in (7.2.22) and (7.2.24) (or, equivalently, of $\mathbf{W}_P$ in (7.2.30)) cannot be modelled as independent and identically distributed complex Guassian random variables. Consequently, various standard approaches to estimation, equalization and detection based on the typical properties of channel noise in wireless communications (in particular, Gaussianity and stationarity) cannot be applied to this case.

2. *Signal-to-noise ratios* (SNRs) commonly experienced in indoor powerline links are quite high, so that, in principle, the presence of channel noise could be neglected in algorithm design.

Let us now tackle problem a) and assume that : 1) a *pilot block* consisting of N_s consecutive OFDM training symbols (indexed by $l = 0, 1, ..., N_s - 1$ in the following) is transmitted periodically to allow channel estimation at the receive side; b) the channel estimation algorithm process the received signal samples associated with a single pilot block to extract the channel parameters to be employed for channel equalization of the OFDM data symbols following this

block (and preceding the next pilot block). In this case, the received signal model (7.2.30) holds and, if a LS approach is adopted, an estimate of the vector $\overline{\mathbf{H}}$ (7.2.25) can be evaluated as

$$\hat{\overline{\mathbf{H}}} = \overline{\mathbf{K}}^{\dagger}\mathbf{R}_P, \tag{7.3.1}$$

where $\overline{\mathbf{K}}^{\dagger} \triangleq \left(\overline{\mathbf{K}}^H\overline{\mathbf{K}}\right)\overline{\mathbf{K}}^H$ is the pseudo-inverse matrix of the matrix $\overline{\mathbf{K}}$ (7.2.31) and $(\cdot)^H$ denotes the Hermitian transpose. It is important to note that

1. The computational complexity of the channel estimator (7.3.1) is $\mathcal{O}\left(P^3\right)$.

2. In principle, the vector of channel parameters $\overline{\mathbf{H}}$ (7.2.25) needs to be estimated only once, since the channel is periodic and the Zadeh's representation (7.2.2) holds for a whole period of the channel. However, it is well known that indoor powerline channels usually experience long terms variations (due, for instance, to changes in the connected loads), so that the parameters of any channel model can be deemed static only for few tents of periods of the mains [132]. For these reasons, the estimation of the channel coefficients needs to be accomplished periodically (say, every second) to avoid any substantial mismatch between the channel response and the equalizer.

3. Generally speaking, the channel parameters Z and M (see (7.2.5)) are not known a priori to the receiver, so that they need to be estimated; in the following it will be assumed for simplicity that, unless differently stated, both parameters are known to the receiver. When the receiver will assume a channel order different from the real one in its channel estimator, this parameter will be denoted Z_E.

Once the estimate $\hat{\overline{\mathbf{H}}}$ of $\overline{\mathbf{H}}$ (7.2.25) has been evaluated, eq. (7.2.23) is exploited (with $Z = Z_E$) to evaluate an estimate $\hat{\mathbf{A}}^{(l)} = [\hat{A}_{i,j}^{(l)}]$ of the channel matrix $\mathbf{A}^{(l)}$ referring to all the OFDM information symbols following the pilot block ($l = N_s, N_s+1, ...$ in this case). Given $\hat{\mathbf{A}}^{(l)}$, *zero-forcing* (ZF) equalization can be employed to compensate for channel distortions in $\mathbf{R}_{N_{FFT}}^{(l)}$ (7.2.22) if the effects of channel noise are neglected. This leads to evaluating the vector

$$\mathbf{Z}_{N_{FFT}}^{(l)} \triangleq \left(\hat{\mathbf{A}}^{(l)}\right)^{-1}\mathbf{R}_{N_{FFT}}^{(l)} \tag{7.3.2}$$

and to applying a standard detection strategy to $\mathbf{Z}_{N_{FFT}}^{(l)}$in order to generate an estimate $\hat{\mathbf{c}}_{N_c}^{(l)}$ of $\mathbf{c}_{N_c}^{(l)}$. Note that, in principle, the computational complexity of the Zadeh-Based Zero Forcing Equalizer (ZB-ZFE) (7.3.2) is $\mathcal{O}\left(N_{FFT}^3\right)$, since it requires the inversion of a $N_{FFT} \times N_{FFT}$ square matrix. However, $\mathbf{A}^{(l)}$ (and, consequently, its estimate $\hat{\mathbf{A}}^{(l)}$) is a close to a

banded matrix with small lower and upper bandwidths (in the following these quantities are denoted b_L and b_U, respectively); this is due to the fact that the changes experienced over the duration $N_T T_s$ of OFDM symbols (which is substantially shorter than the channel period T_0) are small, so that the average power of ICI is limited. For this reason, before inverting $\hat{\mathbf{A}}^{(l)}$ we have always reduced it to a banded matrix with $b_L = b_U = b$, so that $\hat{A}_{i,j}^{(l)}$ is always set to zero for $j > i + b$ and $i > j + b$; this reduces the complexity of matrix inversion to $\mathcal{O}\left(N_{FFT}^2\right)$ if algorithms explicitly developed for banded matrices are applied [146]. Conputational complexity is minimized if $b = 0$ is selected, i.e. if all the elements out of the main diagonal are ignored in $\hat{\mathbf{A}}^{(l)}$, so that no matrix inversion is required. In fact, this case

$$\mathbf{Y}_{N_{FFT}}^{(l)} \triangleq \left(\breve{\mathbf{A}}^{(l)}\right)^{-1} \mathbf{R}_{N_{FFT}}^{(l)} \tag{7.3.3}$$

is evaluated in place of $\mathbf{Z}_{N_{FFT}}^{(l)}$ (7.3.2), where $\left(\breve{\mathbf{A}}^{(l)}\right)^{-1}$ is a $N_{FFT} \times N_{FFT}$ diagonal matrix with

$$\left[\left(\breve{\mathbf{A}}^{(l)}\right)^{-1}\right]_{i,i} = 1/\hat{A}_{i,i}^{(l)} \tag{7.3.4}$$

for $i = 0, 1, ..., N_{FFT} - 1$.

7.4 Numerical and experimental results

An extensive work has been accomplished to assess the performance of the developed estimation and equalization algorithms in realistic conditions. The performance results rely on a rich set of experimental measurements acquired by means of the broadband powerline channel sounder described in Chapter 5 and in [91] in two distinct real world scenarios, namely on the second floor[5] of the Department of Engineering "Enzo Ferrari" (University of Modena and Reggio Emilia, Italy) and in a two floor residential house located in Maranello (Modena, Italy).

As far as the first two points are concerned, in the experimental work the channel sounder has employed to acquire: a) the frequency response of the powerline channel referring to several couples of power sockets, usually located in different rooms (the experimental set-up is shown in Fig. 7.4.1); b) multiple realizations of the noise affecting the channel itself. Then, the acquired data have been processed to estimate: a) the parameters of the Zadeh's representation for each considered channel using the frequency domain estimator proposed in Subsection 6.3.1; b) the PSD of indoor powerline noise in the considered scenarios.

[5]Measurements have been been acquired at different power plugs available in the laboratories of that floor.

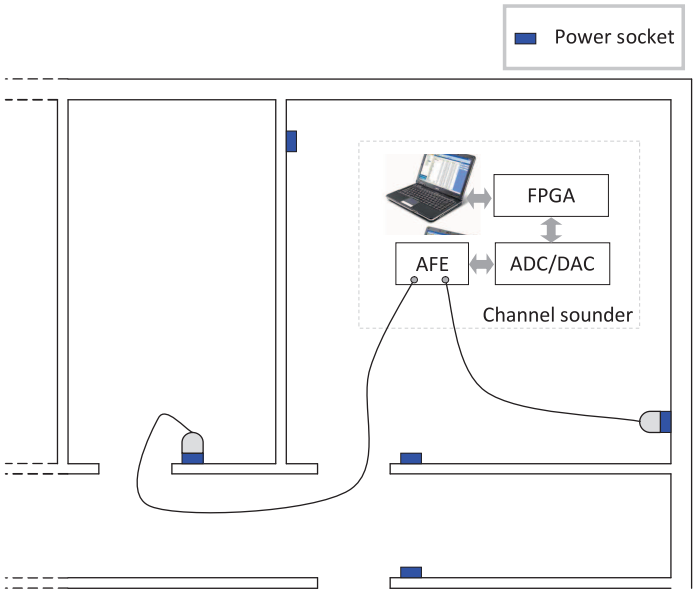

Figure 7.4.1: Experimental set-up for channel sounding.

As far as the third point is concerned, in evaluating the performance of an OFDM-based communication system employing the developed algorithms, the following two distinct approaches have been adopted:

Computer-based approach - A Matlab-based software simulator has been employed to implement the whole communication system, which consists of the following blocks:

- *OFDM modulator* - The following values have been selected for the relevant parameters of the OFDM modulation: $f_s = 2$ MHz, $Q = 64$, $N_{FFT} = 512$, $N_{pre} = 53$, $N_c = 76$, $N_{post} = 127$ and $N_{CP} = 60$. Moreover, in the OFDM transmission pilot symbol blocks, each consisting of N_s consecutive training symbols, alternate with information blocks, each consisting of N_d consecutive data symbols if a ZB-ZFE is used at the receive side; on the contrary, single training symbols alternate with data symbols when a conventional Zero Forcing Equalizer (ZFE) is adopted. A bandpass Butterworth filter having order 100 and pass band $200 - 500$ kHz has been employed for the transmit filter.

- *Channel response emulator* - This implements the Zadeh's representation expressed by eq. (7.2.2); the values of the parameters (7.2.3) have been extracted from experimental measurements of the channel response. It is worth pointing out that experimental data have evidenced that powerline channels associated with distinct couples of power

sockets may exhibit relevant differences in terms of both frequency responses and noise statistics, so that, in principle, drawing general conclusions about the performance of the algorithms from computer simulations would require emulating the behavior of a large number of powerline channels. To simplify this task, at the beginning a specific powerline channel, affected by an appreciable frequency selectivity, has been selected among all those acquired at the the Department of Engineering "Enzo Ferrari", its emulator based on the Zadeh's representation has been implemented, the error performance provided by different equalization algorithms in the presence of this channel has been assessed and, finally, some conclusions about algorithm performance have been inferred from these computer generated results (which are shown in Figs. 7.4.4 and 7.4.5); then, this procedure has been repeated for 24 distinct channels measured in the above mentioned residential scenario, so that the validity of preliminary conclusions could be assessed (the results shown in Fig. 7.4.10 refer to this case). It is also important to mention that each selected channel is characterized by a specific TVTF $H(t, f)$ and that evaluating the parameters of its Zadeh's representation requires the estimation of this system function, as illustrated in detail in the Chapter 6 and [50]. In practice, in this case the TVFT is estimated at the equally spaced frequencies $f_\xi = f_s N_{pre+\xi}/N_{FFT} \qquad \xi = 0, 1, \ldots N_c - 1$ (i.e., at the frequencies of the OFDM active subcarriers) and at 40 instants uniformly distributed over the TVFT period. Estimation for all the selected frequencies at a given instant is accomplished as follows: a) the channel is excited by a comb of N_c sinuosids (probing signal) characterized by the frequencies of interest; b) the steady state channel response to this excitation is sampled at the frequency f_s, so generating the sequence $\{y_n\}$; c) at each of the selected instants the last N_{FFT} samples of $\{y_n\}$ are collected in a vector, which undergoes a DFT of order N_{FFT}; d) the DFT output is compared with the DFT of the sequence feeding the input channel (i.e., the sequence available at the DAC input of the channel sounder) to estimate the TVFT at all the frequencies of interest. The estimated time-varying amplitude response characterizing the specific powerline channel selected for the first performance evaluations is shown in Fig. 7.4.3, from which the approciable frequency selectivity can be inferred (for instance, a 20 dB variation is found in the band $400 - 450$ kHz). From the estimated TVFT it can be inferred that a faithful representation of this specific channel is provided by (7.2.5) with $Z = 2$ and $M = 100$.

- *Channel noise emulator* - Following [128], an AR model of order 200 has been adopted in the generation of the additive Gaussian noise to be superimposed to the channel

response to the OFDM signal. The Yule-Walker method is applied to extract the values of the model parameters from a sequence of measured noise samples in the SNR range $0-40$ dB. This procedure ensures that the PSD of the computer-generated noise follows closely that of the measured powerline noise (see Fig. 7.4.2); note that the last PSD refers to the noise affecting the output of the single communication channel simulated by the channel emulator.

- *Channel estimator* - The channel parameters $\mathbf{H}_{N_P}$ are estimated from each pilot block and exploited in the following information block for equalization;

- *Equalizers and detector* - Standard data detection is accomplished after equalization based on (7.3.2), on (7.3.3) or a *conventional* ZF algorithm [101]. The last equalization algorithm is employed with $N_s = N_d = 1$ only[6] (i.e., each data/pilot block consists of a single OFDM symbol) and operates as follows. If a pilot symbol, denoted $\mathbf{c}_{pilot}^{(l)}$, is transmitted in the lth OFDM symbol interval, the data-aided channel estimate $\check{\overline{\mathbf{H}}}^{(l)}$ is evaluated as[7]

$$\check{\overline{\mathbf{H}}}^{(l)} = \left[\frac{R_0^{(l)}}{c_0^{(l)}}, \frac{R_1^{(l)}}{c_1^{(l)}}, ... \frac{R_{N_{FFT}-1}^{(l)}}{c_{N_{FFT}-1}^{(l)}}, \right]^T . \tag{7.4.1}$$

  Then, this estimate is employed in the next symbol interval to generate the equalized vector

$$\mathbf{X}_{N_{FFT}}^{(l+1)} = \left(\text{diag} \left(\check{\overline{\mathbf{H}}}^{(l)} \right) \right)^{-1} \mathbf{R}_{N_{FFT}}^{(l+1)}, \tag{7.4.2}$$

  feeding the data detector in place of $\mathbf{Z}_{N_{FFT}}^{(l)}$ (7.3.2) or $\mathbf{Y}_{N_{FFT}}^{(l)}$ ((7.3.3)).

Partially experimental approach - In this case the channel sounder has been exploited to generate an OFDM signal, to transmit it over a selected powerline channel and to acquire the channel response to this signal. Then, the acquired response has been processed by the OFDM receiver developed for the previous approach. The interest in this additional approach is motivated by the fact that it allows us to account for the instability of the LPTV channel [8],

[6] This ensures that the channel response during the transmission of the pilot symbol is very close to that experienced during the transmission of the following data symbol, since the OFDM symbol duration is substantially smaller tthan the period of the channel .

[7] Actually, onle the elements of $\check{\overline{\mathbf{H}}}^{(l)}$ associated with useful sucarriers are estimated; all the other elements are set to zero.

[8] It is well known that the period charactering the LPTV model undergoes slight fluctations, but this phenomenon cannot be easily includes in the channel model [75].

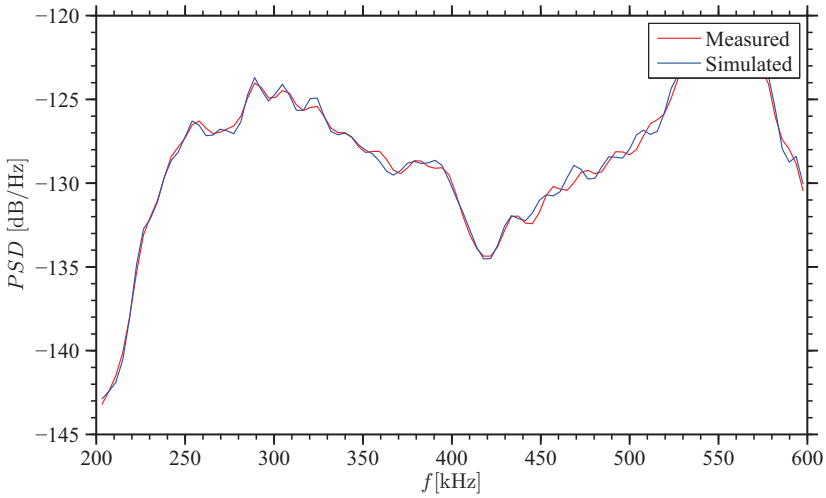

Figure 7.4.2: Comparison between the noise PSD measured in labs and that associated with the AR (200) model approximating it.

for real world powerline noise, and the constraints on the Peak-to-Average Power Ratio (PAPR) of the OFDM signal originating from the limited dynamic range of the transmitter.

In both cases our efforts have mainly aimed at assessing the BER performance versus the SNR, which defined as

$$SNR = \frac{E_b}{E_{noise}}, \tag{7.4.3}$$

where E_b and E_{noise} denote the average received energy per information bit and the mean energy[9] of noise evaluated in the transmission bandwidth, respectively.

Figs. 7.4.4 and 7.4.5 compare the BER performance of the proposed ZB-ZFEs based on (7.3.2) (for $b = 1$ and 2 in the evaluation of the inverse of $\hat{\mathbf{A}}^{(l)}$,) and (7.3.3) (corresponding to $b = 0$) with that provided by the conventional ZFE (7.4.2) in the presence of ideal channel knowlege at the receive side[10] and of an estimated channel response, respectively. The results shown in Fig. 7.4.4 evidence that: a) the error floor of the ZB-ZFEs is substantially lower than that of the conventional ZFE and improves as the value of the parameter b increases; b) this performance

[9] In practice, E_{noise} is expressed by the product between the symbol period and the noise PSD averaged over the transmission band (i.e, over the frequency interval $200 - 500$ kHz) and over half-period of the mains (i.e., over a time interval lasting10 ms).

[10] Note that pilot symbols are not transmitted in this case.

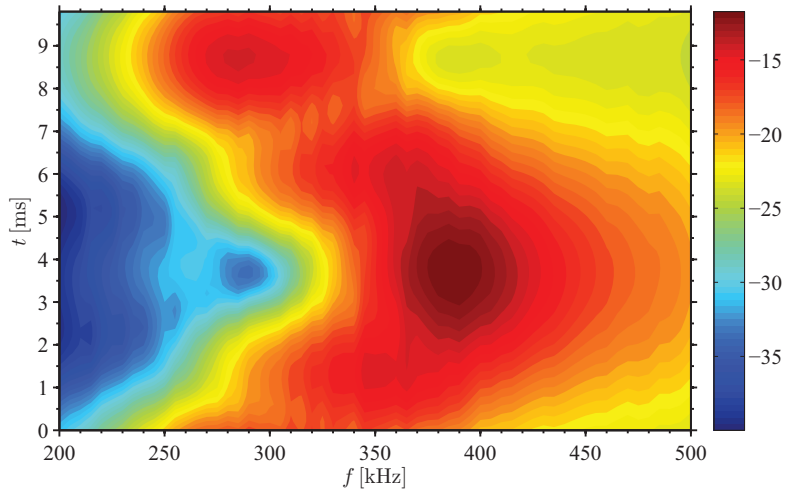

Figure 7.4.3: Representation of the time-varying amplitude response (expressed in dB) of the powerline channel selected for the performance assessment using a computer-based approach. The whole band of interest and a single period of its time evolution are considered.

gap is significant even for $b = 0$. In generating the results shown Fig. 7.4.5 the channel estimation algorithms described in Section 7.3 have been exploited and the transmission of 3496 OFDM symbols covering 100 consecutive periods of the mains (i.e., 1 s) has been simulated. However, when assessing the performance ZB-ZFE, a single pilot plock, consisting of $N_s = 349$ training symbols followed by a single data block made of 3147 OFDM symbols has been transmitted (the corresponding pilot symbol rate 349/3147 entails an energy loss of about 0.51 dB), so that the net data rate is 1.035 Mbps; when simulating the conventional ZFE each training (data) symbol is preceded and followed by a single data (training) symbol (the corresponding pilot symbol rate 1/2 entails an energy loss of about 3.01 dB), so that the net data rate is 575 kbps. The results shown in Fig. 7.4.5 show that: a) the use of channel estimates does not reduce the substantial performance gap existing between a conventional equalizer and ZB-ZFE; b) the error performance of a ZB-ZFE improves when Z_E approaches Z. Moreover, comparing Figs. 7.4.4 with 7.4.5 leads to the conclusion that the quality of channel estimates generated according to (7.3.1) does not entail a substantial degradation on the BER performance of a ZB-ZFE with respect to the case of ideal channel knowledge; on the contrary, the error performance of a conventional ZFE gets worse (in particular, its error floor increases from $2.6 \cdot 10^{-3}$ to $4 \cdot 10^{-2}$).

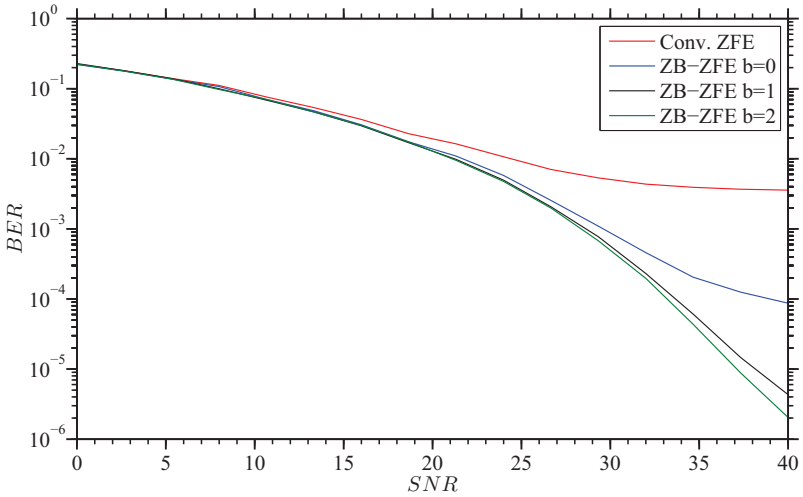

Figure 7.4.4: BER comparison among three ZB-ZFEs (characterized by $b = 0$, 1 and 2) and a conventional ZFE. Ideal channel state information at the receive side is assumed.

The BER performance achieved by the devised algorithms has been assessed also resorting to the partially experimental approach described above. During the experiment the channel sounder has been employed to transmit, like in the previous case, a sequence of 3496 randomly generated OFDM symbols[11] over a specific powerline channel of the considered residential scenario; the time-varing amplitude response of the selected channel is shown in Fig. 7.4.6, whereas the PSD of the noise affecting it and the SNR measured over the OFDM subcarrier frequencies are illustrated in Fig. 7.4.7. It is also worth mentioning that: a) the dynamic range of the DAC of the channel sounder has been properly adjusted to avoid nonlinear distortions in the transmission over the given powerline channel; b) a quantization error is unavoidably introduced; c) the SNR cannot be modified. Fig. 7.4.8 shows the BER performance achieved on each subcarrier-by-subcarrier basis by the ZB-ZFE with $b = 0$ and by a conventional ZFE (numerical results are denoted by labels, whereas lines are darwn to ease the reading). Channel estimation is based on (7.3.1) for the ZB-ZFE, but three different orders, namely $Z_E = 1$, 3 and 5, are assumed by the receiver for the communication channel (whose time variations are accurately represented by a model order Z not smaller than 3); on the contrary, (7.4.1) is employed for generating the channenel estimate feeding the conventional ZFE (7.3.3). From these results it can be inferred that:

[11] A 16 QAM constellation has been always adopted for the OFDM subcarriers. In addition, training and data symbols are arranged in the same way as the previous case.

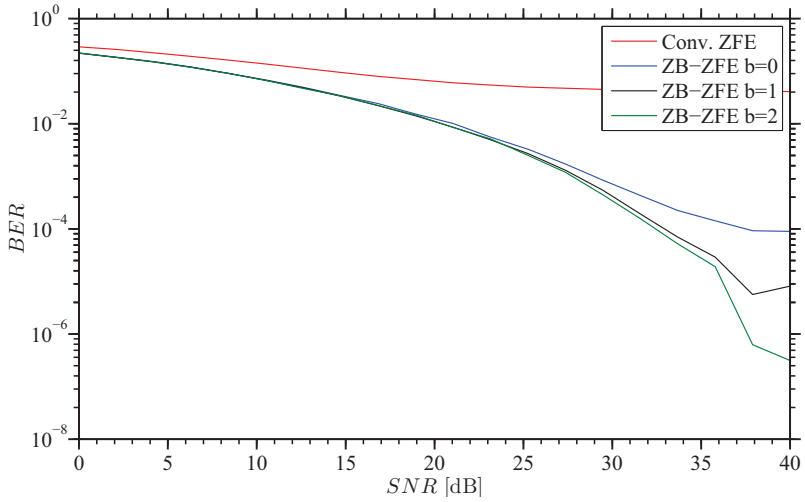

Figure 7.4.5: BER comparison among three ZB-ZFEs (characterized by $b = 0$, 1 and 2) and a conventional ZFE. Channel estimation is accomplished at the receive side.

- The conventional ZFE outperforms the ZB-ZFE with $Z_E = 1$ for some subcarriers belonging to the frequency range $228 - 370$ kHz. This result is motivated by Fig. 7.4.9, showing the absolute values of the channel coefficients $\left\{\overline{H}_{z,k}, z = 0, 1, 2, 3, 4, 5\right\}$ of the Zadeh's representation versus frequency. In fact these results evidence that a significant contribution is provided by the components for $z = 2$ and $z = 3$ in that band, where the channel exhibits relevant time variations.

- The ZB-ZFE with $Z_E = 1$ and 2 substantianlly outperforms the conventional ZFE in the whole band of interest ($200 - 500$ kHz).

- The BER performance achieved by all the equalizers in the band $370 - 500$ kHz is appreciably better than that referring to the band $200 - 370$ kHz. This result can be related to the stastical properties of powerline noise and, in particular, to its correlation properties [128].

Finally, as already mentioned above, the Zadeh-based representation (all with order $Z = 2$) of 24 distinct powerline channels measured in the selected residentail scenario have been inserted in the channel emulator and the computer-based approach has been adopted to assess the BER performance averaged over all these channels of a ZB-ZFE with $Z_E = 1$ and of a conventional ZFE (the values of the simulation parameters are the same as those adopted in assessing the

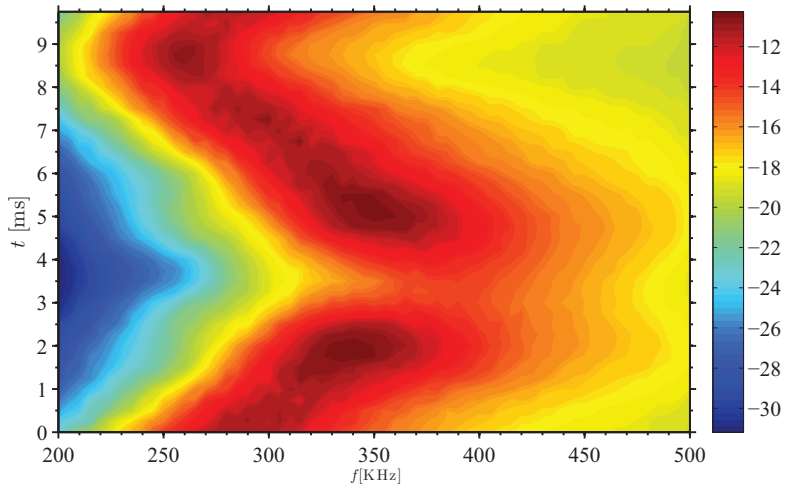

Figure 7.4.6: Representation of the time-varying amplitude response (expressed in dB) of the powerline channel selected for the performance assessment using a partially experimental approach. The whole band of interest and a single period of its time evolution are considered.

error performance previously). In this case error performance is deeply influenced by the poor quality of some channels; however, the ZB-ZFE still significantly outperforms the conventional ZFE in terms of error floor.

7.5 Conclusions

In this chapter the well known Zadeh's representation for LPTV systems has been exploited to develop novel techniques for data-aided channel estimation and ZF equalization to be employed in powerline communications. Numerical simulations and experimental results referring to specific indoor scenarios have shown that the proposed algorithms can substantially outperform standard counterparts in terms of error rate performance at the price of a very limited increase in the computational complexity of the receiver.

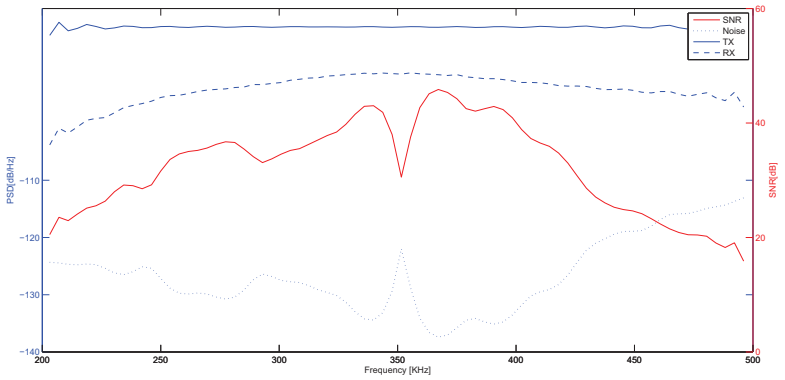

Figure 7.4.7: PSD of the noise of the powerline channel exploited for the experimental validation and SNR.

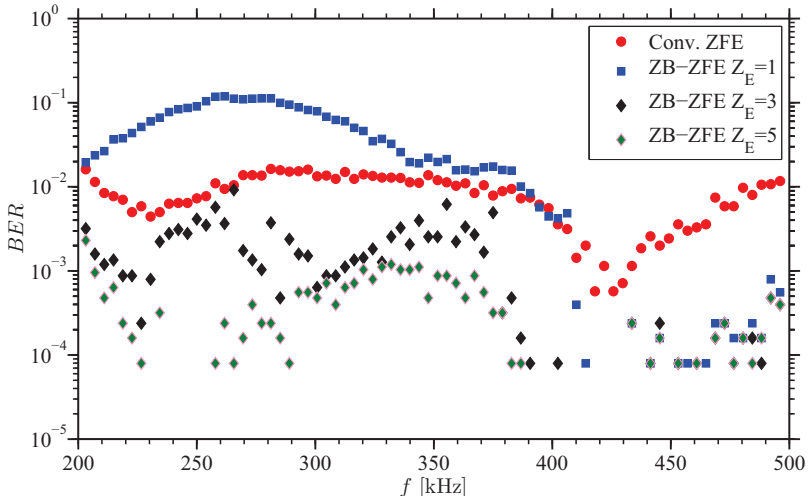

Figure 7.4.8: BER performance versus subcarrier frequency provided by a ZB-ZFE with $Z_E =$ 1, 3 and 5, and by a conventional ZFE

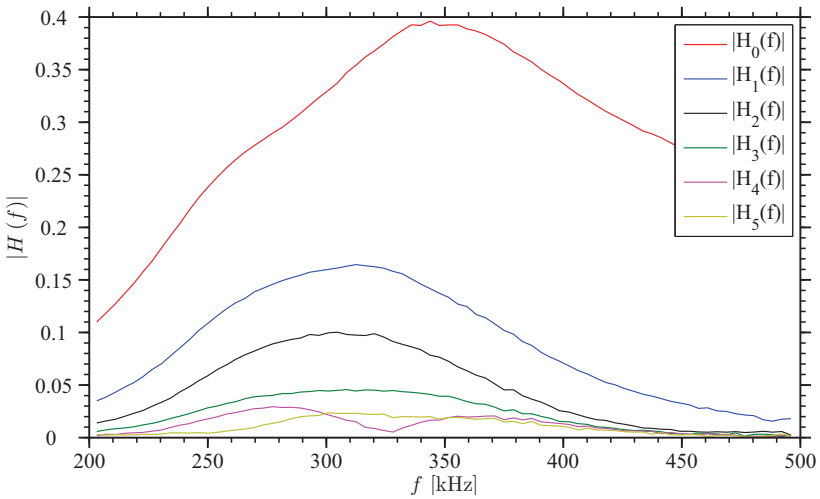

Figure 7.4.9: Absolute value of the channel coefficients $\left\{\overline{H}_{z,k},\ z = 0,\ 1,\ 2,\ 3,\ 4,\ 5\right\}$ versus frequency (i.e., versus k for a specific powerline channel.

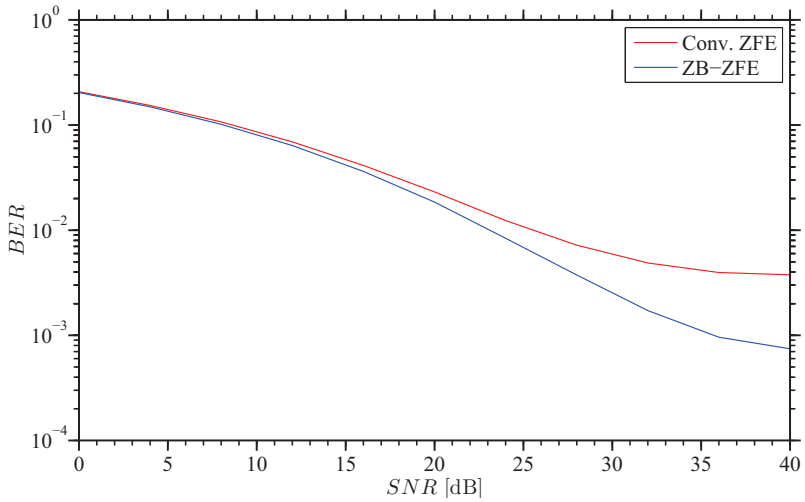

Figure 7.4.10: Average BER provided by a ZB-ZFE with $Z_E = 1$ and a conventional ZFE. Averaging over the communication channel involves 24 distinct powerline channels measured in a given residential scenario.

Chapter 8

Bit and Power Loading Techniques for OFDM Communications over Indoor Powerline Channels

The goal of this Chapter is the development of bit and power loading algorithms based on the LPTV channel model presented in Chapter 7*. The performance of the developed algorithms is assessed by mean of a MatLab simulator based on a database of experimentally acquired channel responses and on a database of experimentally acquired noise sequences. In our simulations the frequency band* $[200, 500]$ *kHz is considered since it is employed in various low data rate standard [96]*

The remaining part of this Chapter is organized as follows. In Section 8.1 a brief overview of the literature on bit/power loading for mulaticarrier systems operating over LPTV channels is provided. The architecture of the PLC OFDM communication system considered in the assessment of the developed bit/power loading algorithms is described in Section 8.2. A derivation of these algorithms is illustrated in Section 8.3, whereas their performance is analysed in Section 8.4. Finally, some conclusions are provided in Section 7.5.

8.1 Bit and power loading for LPTV channels: state of the art

Recent works have evidenced that indoor powerline channels are not stationary and, in particular, are characterized by both long-term and short-term variations [28]. Long term variations are due to the connection/disconnection of power loads, are characterized by a time support

of few seconds and can be straighforwardly modelled resorting to Markov chains [120]. On the contrary, short-term variations mainly depend on the presence of thyristors and rectifying circuits, and are characterized by a time support of few tens of milliseconds [132]. These short term changes influence the channel transfer function at frequencies below[1] 3 MHz and are synchronous to the mains frequency [132]. For this reason, an accurate representation of indoor powerline channels requires the adoption of LPTV models (e.g., the Switching Model (SM), [120, 132, 147], the ACR, [71, 73, 123] or the Zadeh's representation. It is also important to point out that the dependence of powerline channel properties on frequency can be also related to the presence of multipath and to the specific features of powerline noise [75, 128, 129]. In fact, at frequencies below 11 MHz powerline noise is coloured and is not characterized by a Gaussian distribution, whereas at frequencies beyond 11 MHz the standard AWGN model holds.

It is well known that, if a communication channel is slowly time-varying in both its transfer function and noise power spectrum, standard bit and power loading techniques can be employed to optimize an OFDM tramission over it, provided that Channel State Information (CSI) is fed back from the receive side to the transmit one [101]. On the contrary, if it exhibits substantial short time variations, computationally efficient loading algorithms able to quickly redistribute power/bits over subcarriers in response to such variations need to be employed. In the last years various research efforts have been devoted to devise such algorithms for multicarrier signalling over powerline channels [147, 149, 150, 151, 152, 153, 154, 155, 158]. In particular, algorithms able to cope with unexpected time variations and/or impulsive noise bursts and based on the concept of SNR margin have been proposed in [149, 153, 154], the use of the so-called Leke-Cioffi algorithm has been investigated in [150], iterative water filling has been studied in [151] and the so called *knapsack algorithm* has been proposed in [152]; in addition, the trade/off between data rate, BER and detection complexity has been analysed in [155], where a new metric, called *goodput,* has been introduced. However, in none of the just mentioned contributions the assumption of periodicity in powerline channel behavior is exploited. In fact, as far as we know, the only references developing bit and power loading techniques for powerline channels modelled as LPTV systems are [147, 158]. In particular, in [147] two different types of channel models are taken into consideratuion, namely the *commuted LPTV channel*, which is a combination of a high and a low transfer function exhibiting sharp transition and the *harmonic LPTV channe*l, which is a combination of transfer functions

[1] Indoor powerline channels can be deemed time-invariant at frequencies beyond 3 MHz, so that the well known stationary multipath model [14] can be employed to represent their behavior in that frequency range.

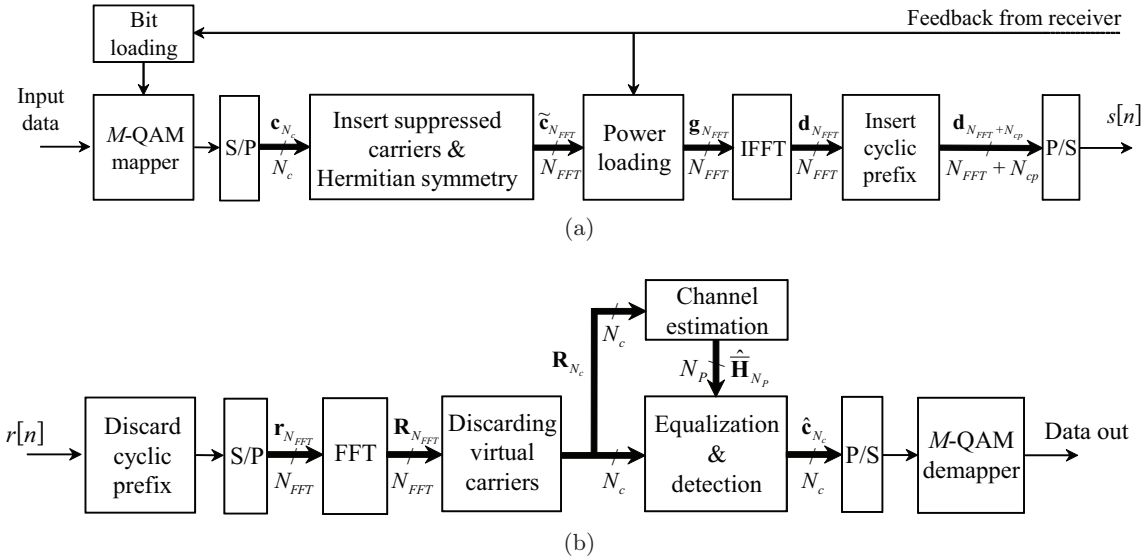

Figure 8.2.1: Block diagrams of the OFDM transmitter (a) and receiver (b).

characterized by a progressive variation. It is also worth mentioning that: a) the proposed channel model is based on a simplified powerline network topology and on a set of sinusoidal time varying impedances that simulate the behavior of home appliances; b) an (unrealistic) AWGN model is employed for powerline noise. The devised algorithm tries to maximize the overall bit rate under a constraint on the transmitted power and the maximum admissible BER. This leads to a periodic distribution of bits versus frequency along one period of the channel. A different conceptual approach is adopted in [158], where bit and power loading algorithms aiming at the minimization of the outage probability (i.e., the probability that the channel capacity decreases below a specific threshold or the BER increases over a specific threshold) are developed. In the case, performance of various loading algorithms is evaluated for a specific network topology characterized by 23 possible links (i.e., channels); moreover, each channel is characterized by colored background noise and a commuted impedence model, so that the channel response changes between two states only, depending on the voltage of the mains.

8.2 Communication System Model

The rationale behind the proposed algorithm consists of exploiting the LPTV nature of the channel and the cyclostationarity of the noise in allocating power and bits over subcarriers and time. The transfer function of the LPTV channel can be certainly estimated and modelled resorting to the techniques developed in Chapter 7. However, a Periodically Time Varying (PTV) noise model needs to be developed; this problem is tackled in Section 8.3.3.

To exploit the LPTV behavior of powerline channels the OFDM communication system proposed in this work adopt a periodic medium access method; the block diagram of the OFDM transmitter and OFDM receiver are shown in Fig. 8.2.1a and 8.2.1b, respectively. Note that the considered communication system is quite similar to that introduced in Chapter 7 (in particular, since the channel bandwidth $B = 300\,\text{kHz}$ is comparable to the central frequency $f_c = 350\,\text{kHz}$, even in this case the transmitted signal is generated directly in pass-band, i.e. without resorting to frequency upconversion), but now includes two subsystems for power and bit loading, and a feedback channel. This makes the description of the system more complicated; since the size of QAM constellations changes from subcarrier to subcarrier and, for a given subcarrier, changes from OFDM symbol to OFDM symbol.

Let us analyse now transmitter processing, focusing on what happens in a single period of the communication channel in order to simplify the notation. First of all, the maximum number of OFDM symbols N_{ts} that can be transmitted within one channel period is evaluated as

$$N_{ts} = \left\lfloor \frac{T_0}{T_{sy}} \right\rfloor \tag{8.2.1}$$

where$\lfloor x \rfloor$ denotes the integer part of x, T_0 is the period of the channel and T_{sy} is the OFDM symbol interval. Without loosing generality, the period of the LPTV channel is divided in N_{ts} time slots synchronized with the mains, each hosting the transmission of a single OFDM symbol. Similarly, if N_c is the number of useful carriers of the OFDM system, then the available spectrum can by divided in N_c frequency slots, so that $N_{ts} \times N_c$ Time-Frequency Slot (TFS) available in the considered channel period. Since time-varying bit and power loading are accomplished, the (i, k) TFS, associated with the i-th slot and the k-th subcarrier (with $0 \leq i < N_{ts}$ and $0 \leq k < N_c$) is characterized by a $\Theta_{i,k}$-ary QAM constellation and power $P(i, k)$. It is also important to point out that the adopted periodic medium access method leads to starting the transmission of the l-th OFDM symbol at time instant

$$t_{TX}[l] = \left\lfloor \frac{l}{N_{ts}} \right\rfloor T_0 + \mathrm{mod}(l, N_{ts})\, T_{sy} + \beta_0, \qquad l = 0, 1, ... \tag{8.2.2}$$

where *mod* is the integer remainder operator and β_0 is an initial time offset. Note that:a) $\lfloor l/N_{ts} \rfloor$ identifies the number of channel period, while $\mathrm{mod}(l, N_{ts})$ is the index of the TFS exploited for the symbol transmission; the channel is in the last $T_0 - N_{ts}T_{sy}$ sec of each of its periods.

Once bit allocation for the considered slot has been evaluated (this is based on the bit loading algorithm described in Subsection 8.3.2), the signal associated with the transmission of the l-th OFDM symbol is generated as follows (the index of the involved time slot is $\overline{n} = \mathrm{mod}(l, N_{ts})$). The input binary stream is partitioned into N_c blocks, each consisting of $\log_2(\Theta_{\overline{n},k})$ bits with $k = 0, 1, ..., N_c - 1$, and each block is mapped to a channel symbol belonging to a $\Theta_{\overline{n},k}$-ary QAM constellation. The resulting stream of channel symbols undergoes a serial-to-parallel conversion which produces a N_c-dimensional vector $\mathbf{c}_{N_c}^{(l)} \triangleq \left[c_0^{(l)}, c_1^{(l)}, \ldots, c_{N_c}^{(l)}\right]^T$, containing the N_c consecutive channel symbols. As already shown in Chapter 7, the new N_{FFT}-dimensional vector $\widetilde{\mathbf{c}}_{N_{FFT}}^{(l)}$ is generated from l-th useful data vector $\mathbf{c}_{N_c}^{(l)}$

$$\widetilde{\mathbf{c}}_{N_{FFT}}^{(l)} = \left[c_0^{(l)}, c_1^{(l)}, \ldots, c_{N_{FFT}-1}^{(l)}\right]^T \tag{8.2.3}$$

$$= \left[\left(\mathbf{0}_{N_{pre}}\right)^T, \mathbf{c}_{N_c}^{(l)}, \left(\mathbf{0}_{2N_{post}}\right)^T, \left(\mathbf{c}_{N_c}^{(l)}\right)^{\ddagger}, \left(\mathbf{0}_{N_{pre}}\right)^T\right]^T \tag{8.2.4}$$

where $\mathbf{0}_N$ denotes a N-dimensional null column vector and $()^{\ddagger}$ denotes the flipped[2] Hermitian transpose. Then the vector $\widetilde{\mathbf{c}}_{N_{FFT}}^{(l)}$ undergoes power loading which produces the power adapted data vector

$$\mathbf{g}_{N_{FFT}}^{(l)} = [g_0^{(l)}, g_1^{(l)}, ..., g_{N_{FFT}-1}^{(l)}]^T \triangleq \mathbf{G}_{\overline{n}}^T \odot \widetilde{\mathbf{c}}_{N_{FFT}}^{(l)}, \tag{8.2.5}$$

where $\mathbf{G}_n = [G_{n,0}, G_{n,1}, ..., G_{n,N_c-1}]^T$ is the i-th row of the $N_{ts} \times N_c$ matrix $\mathbf{G}$ collecting the gains generated by the power loading algorithm, whereas $\odot$ and $()^T$ denote the Hadamard product and the transposition operator, respectively.

Then the vector $\mathbf{g}_{N_{FFT}}^{(l)}$ undergoes to an IFFT of order N_{FFT} leading to the real vector $\mathbf{d}_{N_{FFT}}^{(l)}$. This ensures that:

[2]Flipping consists of reversing the order of the elements of the given vector.

- the N_c data symbols $\mathbf{c}_{N_c}^{(l)}$ are transmitted over N_c adjacent subcarriers centered at the frequencies $\{f_k = k/(N_{FFT}T_s)\}$ with $k = N_{pre}, N_{pre}+1, ..., N_{pre}+N_c-1$, which will be allocated in the band of interest $200 - 500$ kHz;

- $N_{sc} = N_{pre} + N_{post}$ subcarriers are suppressed in the band $0 - f_s/2$, where $f_s = 1/T_s = 2$ MHz is the maximum sampling frequency of the OFDM simulator (see Section 8.4);

- $N_{FFT} \triangleq (N_c + N_{sc})$.

Appending a CP of N_{cp} symbols to $\mathbf{d}_{N_{FFT}}^{(l)}$ produces the cyclically extended vector $\mathbf{d}_{N_{FFT}+N_{cp}}^{(l)}$. After parallel-to-serial conversion, the vector $\mathbf{d}_{N_{FFT}+N_{cp}}^{(l)}$ undergoes transmit filtering with (real) impulse response $p[n]$ yielding the OFDM real signal $s[n]$. Note that, if $N_0 = T_0 \cdot f_s$ denotes the period of the channel in number of samples, the parameter N_{ts} can be expressed as

$$N_{ts} \triangleq \left\lfloor \frac{N_0}{N_{FFT} + N_{cp}} \right\rfloor \tag{8.2.6}$$

and the overall duration of a time slot is given by $T_{ts} = (N_{FFT} + N_{cp})\, T_s$. Moreover, the index of the sample associated with the start of the transmission of the l-th OFDM symbol is

$$n_l^{TX} = \left\lfloor \frac{l}{N_{ts}} \right\rfloor N_0 + \mathrm{mod}\,(l, N_{ts})\,(N_{FFT} + N_{cp}) + \bar{\beta}_0, \qquad l = 0, 1, ... \tag{8.2.7}$$

with $\bar{\beta}_0 \triangleq \beta_0 f_s$.

Following [50, 132], the poweline communication channel is modelled as a discrete-time LPTV system characterized by a period[3] N_0. Then, if $\{h_{n,i}\}$ denotes the time-variant impulse response[4] of the overall communication channel (which includes both the transmit filter and the receive filter matched to it); the n-th received signal sample $r[n]$ can be expressed through the modified Zadeh model (see Chapter 7) of order Z as

$$r[n] = \sum_{z=-Z}^{Z} \left[\sum_{m=0}^{M-1} \tilde{H}_{z,m} s[n-m] \right] \exp\left(j \frac{2\pi z n}{N_0} \right) + w[n] \tag{8.2.8}$$

[3]Note that $N_0 = T_0/T_s$, where T_0 is the period of the time varying impulse response $h(t, \tau)$ of the communication channel.

[4]This is defined as the response at time n to a unitary pulse applied $n - i$ samples earlier.

where

$$\tilde{H}_{z,m} \triangleq \frac{1}{N_0} \sum_{n=0}^{N_0-1} h_{n,m} \exp\left(-j\frac{2\pi zn}{N_0}\right), \tag{8.2.9}$$

is the kth coefficient of the DFT of $\{h_{n,i}\}$,$w[n]$ represents the contribution of the filtered additive channel noise and M is the number of taps of each filter.

The OFDM receiver operates on a symbol-by-symbol basis and is endowed with ideal timing synchonization; for this reason, in the following the detection of the single OFDM symbol $\tilde{\mathbf{c}}^{(l)}_{N_{FFT}}$ is described. To carry out the detection of the l-th OFDM symbol, the receiver process the vector $\mathbf{r}^{(l)}_{N_{FFT}} = \left[r^{(l)}_0, r^{(l)}_1, ..., r^{(l)}_{N_{FFT}-1}\right]^T$ collecting the samples

$$\left\{r[n], n = n^{TX}_l + N_{cp}, n^{TX}_l + N_{cp} + 1, \ldots, n^{TX}_l + N_{cp} + N_{FFT} - 1\right\} \tag{8.2.10}$$

Note that in the received signal model the N_{cp} samples

$$\left\{r[n], n = n^{TX}_l, n^{TX}_l + 1, ..., n^{TX}_l + N_{cp} - 1\right\} \tag{8.2.11}$$

correspond to the cyclic prefix of the lth OFDM symbol and are discarded by the receiver. The vector $\mathbf{r}^{(l)}_{N_{FFT}}$ feeds a DFT of order N_{FFT} (implemented as a *fast Fourier transform*, FFT) generating the frequency-domain vector $\mathbf{R}^{(l)}_{N_{FFT}} = [R_0, R_1, ..., R_{N_{FFT}-1}]^T$, where

$$\begin{aligned} R^{(l)}_q &\triangleq \mathrm{DFT}_{N_{FFT}}\left[\mathbf{r}^{(l)}_{N_{FFT}}\right] \\ &= \frac{1}{N_{FFT}} \sum_{n=0}^{N_{FFT}-1} r^{(l)}_n \exp\left(-j\frac{2\pi nq}{N_{FFT}}\right). \end{aligned} \tag{8.2.12}$$

Expressing the LPTV channel through the Zadeh's representation [50, 156] yields the frequency-domain received vector as [156]

$$\mathbf{R}^{(l)}_{N_{FFT}} = \mathbf{A}^{(l)} \tilde{\mathbf{d}}^{(l)}_{N_{FFT}} \tag{8.2.13}$$

where $\mathbf{A}$ is the $N_{FFT} \times N_{FFT}$ channel matrix whose element $A_{q,k}$ is given by

$$A^{(l)}_{q,k} = \sum_{z=-Z}^{Z} H_{z,k} \tilde{A}_{q,z,k} \exp\left(\frac{j2\pi z n^{TX}_l}{N_0}\right), \tag{8.2.14}$$

$\{H_{z,k}\}$ are coefficients related to the Zadeh's representation of order Z of the LPTV channel (see [156, 50] for further details) and

$$\tilde{A}_{q,z,k} = \frac{1}{N_{FFT}} \sum_{n=0}^{N_{FFT}-1} \exp\left(-j2\pi n \left(\frac{q-k}{N_{FFT}} - \frac{z}{N_0}\right)\right) \tag{8.2.15}$$

$$= \exp\left(-j\pi\delta\left(N_{FFT}-1\right)\right) \frac{\sin\left(\pi N_{FFT}\delta\right)}{\sin\left(\pi\delta\right)}, \tag{8.2.16}$$

with

$$\delta = \frac{q-k}{N_{FFT}} - \frac{z}{N_0}, \tag{8.2.17}$$

The power adapted data vector $\hat{\mathbf{d}}_{N_c}^{(l)}$ can be estimated mitigating the channel distortions by means of a ZFE [156]. This requires evaluating the equalized vector

$$\mathbf{z}_{N_{FFT}}^{(l)} = \left(\mathbf{A}^{(l)}\right)^{-1} \mathbf{R}_{N_{FFT}}^{(l)} \tag{8.2.18}$$

and taking a decision $\hat{\mathbf{d}}_{N_{FFT}}^{opt}$ on $\hat{\mathbf{d}}_{N_c}^{(l)}$ on the basis of a minimum distance rule applied to this vector; then, the vector $\hat{\mathbf{d}}_{N_c}^{(l)}$ collecting the N_c symbols associated with the useful subcarriers (and identified by the values $N_{pre}, N_{pre}+1, ..., N_{pre}+N_c-1$ of the subcarrier index) are extracted from $\hat{\mathbf{d}}_{N_{FFT}}^{opt}$. Finally, an estimate of the useful data vector $\mathbf{c}_{N_c}$ is evaluated as

$$\hat{\mathbf{c}}_{N_c}^{(l)} = \left(\mathbf{G}^{(l)}\right) \odot \hat{\mathbf{d}}_{N_c}^{(l)}, \tag{8.2.19}$$

so that, after parallel-to-serial conversion, the stream of channel symbols is converted into a stream of output bits.

8.3 Loading Algorithms

The goal of bit and power loading consists of maximizing the bit rate B_r of the communication system while keeping a *bit error rate* (BER) below a target value BER_{max}. In addition, the transmitted signal needs to meet the *power spectral density* (PSD) mask $PSD_{TX}(f)$, which establishes the maximum power density that can be injected in the power network to prevent interference with other devices. In this case, a constraint on the PSD of the transmitted signal over a single period of the LPTV channel is set; for this reason, the PSD associated with a given OFDM symbol can exceed the limit $PSD_{TX}(f)$, provided that the constraint is met if $PSD_{TX}(f)$ is averaged over N_{ts} time slots. More precisely, it is required that

$$\sum_{n=0}^{N_{ts}-1} P_{n,k} \leq N_{ts} \left(PSD_{TX} \left(f_k \right) \cdot \Delta f \right) \tag{8.3.1}$$

where f_k represents the frequency of the kth subcarrier, Δf is the frequency spacing between adjacent subcarriers and $k = 0, 1, ..., N_c - 1$. Note that the resource allocation problem with the above mentioned constraints can be solved by tackling the following two independent subproblems:

- evaluation of the optimal power distribution $P\left(n, k\right)$ (with $0 \leq n < N_{ts}$ and $0 < k \leq N_c$) suitable to maximize the bit rate B_r under the power constraint 8.3.1;

- evaluation of the bit loading strategy (i.e. the strategy allocating QAM constellations on the useful subcarriers) suitable to maximize the bit rate B_r under the constraint $BER < BER_{max}$.

In fact, the constraint on the power budget affects only the power loading algorithm, while the constraint on the BER affects only the bit loading. In the following 3 Subsections a power loading algorithm, a bit loading algorithm and a method to estimate the PSD of the noise are illustrated.

8.3.1 Power loading algorithm

As already stated above, the goal of the power loading algorithm is the maximization of the bit rate of the communication system under a constraint on the power budget. The capacity C of the channel is given by:

$$C = \Delta f \sum_{i=0}^{N_{ts}-1} \sum_{k=N_{pre}}^{N_{pre}+N_c-1} \log_2 \left(1 + \frac{\left| A_{k,k}^{(i)} \right|^2 \cdot P_{i,k}}{\Delta f \cdot PSD_N \left(i, k \right)} \right) \tag{8.3.2}$$

where Δf is the frequency spacing of OFDM carriers and PSD_N denotes the power spectral density of the channel noise affecting the k-th subcarrier in i-th slot. The proposed power loading technique aims at solving the following set of N_c indipedent optimization problems (each referring to a distinct subcarrier frequency)

$$\begin{cases} \left\{P_{0,k}^{(L)}, P_{1,k}^{(L)}, \ldots, P_{N_{ts}-1,k}^{(L)}\right\} = \arg\max_{\tilde{\mathbf{P}}} \Delta f \sum_{i=0}^{N_{ts}-1} \log_2 \left(1 + \frac{\left|A_{k,k}^{(i)}\right|^2 \cdot \widetilde{P}_i}{\Delta f \cdot PSD_N(i,k)}\right) \\ \sum_{i=0}^{N_{ts}-1} P_{i,k} = N_{ts}\Delta f \cdot PSD_{TX}\left(f_k\right) \end{cases} \tag{8.3.3}$$

with $\tilde{\mathbf{P}} = \left[\tilde{P}_{0,k}, \tilde{P}_{1,k}, \ldots, \tilde{P}_{N_{ts}-1,k}\right]^T$ and $k = 0, 1, \ldots N_c - 1$, $n = 0, 1, \ldots N_{ts} - 1$ and the quantities $\left\{A_{k,k}^{(i)}\right\}$ are related to the channel gains at the frequencies of the useful carriers ($\{f_k\}$ $k = 0, 1, \ldots N_c - 1$); in the following $\mathbf{P}^{(L)} = [P_{l,m}^{(L)},]$ the matrix of the subcarrier powers evaluated in this step.

This approach ensures that for each frequency the average power spectral density computed on a channel period is equal to $PSD_{TX}\left(f\right)$. Note that each optimization problem of 8.3.3 can be viewed as a water filling problem along the time dimension instead of the usual frequency dimension.

8.3.2 Bit loading

The proposed bit loading algorithm has been devised in a way to allow a simple implementation on a standard hardware platform. The inputs required by the proposed algorithm are:

1. the maximum admissible bit error rate BER_{max};
2. the PSD mask for the transmitter $PSD_{TX}\left(f\right)$;
3. the power distribution $\mathbf{P}^{(L)}$ generated by the power loading algorithm illustrated in the previous Subsection;
4. an estimate of the time varying noise PSD along a channel period PSD_{noise} (this can be obtained employing the method presented in Subsection 8.3.3);
5. the channel gains $A_{k,k}^{(n)}$ for $n = 0, 1, \ldots N_{ts} - 1$ and $k = 0, 1, \ldots N_c - 1$.

The bit loading algorithm operates by comparing the SNR of each TFS with the values of a look up table which lists the minimum SNR required to achieve a BER equal to BER_{max} versus the QAM constellation size Θ. The entries of the look up table can be computed as follows. The bit error probability for the coherent detection of a Θ-ary QAM can be expressed as

$$P^e = \frac{\Theta - \sqrt{\Theta}}{\Theta} Q - 4 \frac{1 - 2\sqrt{\Theta} + \Theta}{\Theta} Q^2, \tag{8.3.4}$$

where

$$Q = \frac{1}{2} \mathrm{erfc}\Big(\alpha \sqrt{SNR}\Big), \tag{8.3.5}$$

$$\alpha = \sqrt{\frac{3}{\Theta - 1}}, \tag{8.3.6}$$

$$SNR = \frac{P\,|A|^2}{PSD_{noise}\,(f_k)\,\Delta f}, \tag{8.3.7}$$

Here P is the power of transmitted signal, PSD_{noise} is the noise power spectral density and $\overline{A}$ is the channel gain. The minimum value of signal to noise ratio $\overline{SNR}\,(\Theta, BER_{max})$ required to achieve BER equal to BER_{max} with a Θ-ary QAM can be obtained inverting 8.3.4 with $P_e = BER_{max}$. This requires the following two steps:

1. the computation of the value of $\overline{Q}$ such that

$$BER_{max} = \frac{\Theta - \sqrt{\Theta}}{\Theta} \overline{Q} - 4 \frac{1 - 2\sqrt{\Theta} + \Theta}{\Theta} \overline{Q}^2 \tag{8.3.8}$$

2. The computation of $\overline{SNR}$ as

$$\overline{SNR}\,(\Theta, BER_{max}) = \left[\frac{\mathrm{erfc}^{-1}\left(2\overline{Q}\right)}{\alpha_{i,k}\Theta} \right]^2 \tag{8.3.9}$$

The bit loading is fed by the power distribution $\mathbf{P}^{(L)}$ returned by the power loading and operates as follows (the steps the algorithm consists of are described for the $\overline{k}$-th sucarrier):

1. It sets the $N_{ts} \times N_c$ matrix of the power distribution $\mathbf{P} = \mathbf{P}^{(L)}$;

2. it computes the maximum size of QAM constellation that can be supported for each time slot along the $\overline{k}$-th subcarrier with a BER equal to BER_{max} as

$$\Theta_{n,\overline{k}} \;=\; \begin{cases} 0 \quad \text{if } SNR\left(n, \overline{k}\right) < \overline{SNR}\,(4, BER_{max}) \\ \max\left\{\Theta \mid SNR\left(n, \overline{k}\right) \geq \overline{SNR}\,(\Theta, BER_{max})\right\} \quad \text{otherwise} \end{cases} \tag{8.3.10}$$

with $n = 0, 1, \ldots N_{ts} - 1$.

Therefore, the set $TFS_{ON}^{(\overline{k})}$ of the TFSs exploited in data trasmission is given by

$$TFS_{ON}\left(\overline{k}\right) = \left\{n \mid \Theta_{n,\overline{k}} > 0\right\} \tag{8.3.11}$$

for the $\overline{k}$-th subcarrier. This produces a bit distribution denoted Θ^C in the following to evidence that is a *corse* distribution. Indeed, a better (*fine*) distribution can be obtained by adjusting the power distribution as follows (the $\overline{k}$-th subcarrier is considered again):

1. For each TFS associated with the $\overline{k}$-th carrier the power is set to the minimum value matching the constraint on the BER, i.e. the rule
$$P_{n,\overline{k}} = \overline{SNR}\left(\Theta_{n,\overline{k}}^C, BER_{max}\right)\left(PSD_N\left(f_k\right)\Delta f\right) \qquad n \in TFS_{ON}\left(\overline{k}\right) \tag{8.3.12}$$
is used.

2. The power surplus $P_{\overline{k}}^S$ is evaluated as
$$P_{\overline{k}}^S = PSD_{TX} \cdot \Delta f \cdot N_{ts} - \sum_{n \in TFS_{ON}\left(\overline{k}\right)} P_{n,\overline{k}} \tag{8.3.13}$$

3. The additional power $P_{n,\overline{k}}^{Add}$ required to extend the size of the constellation from $\Theta_{n,\overline{k}}$ to $4\Theta_{n,\overline{k}}$ for the TFS $(n,\overline{k})$ in the ON state or to turn on that TFS in the OFF state is given by
$$P_{n,\overline{k}}^{Add} = \begin{cases} \overline{SNR}\left(4\Theta_{n,\overline{k}}^C, BER_{max}\right)\Delta f - P_{\overline{k}}^S & n \in TFS_{ON}\left(\overline{k}\right) \\ \overline{SNR}\left(4, BER_{max}\right)\Delta f & \text{otherwise} \end{cases} \tag{8.3.14}$$

4. By defining $\check{P}_{\overline{k}}^{Add} \triangleq \text{sort}\left(P_{n,\overline{k}}^{Add}\right)$ the set $\left\{P_{n,\overline{k}}^{Add}, n=0\right\}$ arranged in ascending order and $\check{N}_{\overline{k}} \triangleq \arg_{(\bullet,\overline{k})}\left[\check{P}_{\overline{k}}^{Add}\right]$ the set of theb values of the index n index associated with the elements of $\check{P}_{\overline{k}}^{Add}$. The maximum number N_u of costellations that can be updated is evaluated as
$$N_u = \max\left\{N \middle| \sum_{n=0}^{N-1} \check{P}_{\overline{k}}^{Add} \leq P_{\overline{k}}^S\right\} \tag{8.3.15}$$

5. Therefore a *fine* constellation distribution $\boldsymbol{\Theta}^{(F)}$ can be obtained as (this matrix is initialized as $\boldsymbol{\Theta}^{(F)} = \boldsymbol{\Theta}^{(C)}$)
$$\Theta_{\check{N}_{\overline{k}}[m],\overline{k}}^F = \begin{cases} 4\Theta_{\check{N}_{\overline{k}}[m],\overline{k}}^C & \text{if } \Theta_{\check{N}_{\overline{k}}[m],\overline{k}}^C > 0 \\ 4 & \text{otherwise} \end{cases} \qquad m = 0, 1, \ldots N_u - 1 \tag{8.3.16}$$

6. Finally, the *fine* power distribution is given by

$$P^{F}_{\check{N}_{\overline{k}}[m],\overline{k}} = P_{\check{N}_{\overline{k}}[m],\overline{k}} + P^{Add}_{\check{N}_{\overline{k}}[m],\overline{k}} \qquad m = 0, 1, \ldots, N_u - 1 \tag{8.3.17}$$

8.3.3 Noise modelling

A specific method for modelling the periodic time varying behavior of powerline noise has been developed. This method exploits the OFDM receiver to estimate the variance of the noise on each carrier. By sampling the noise for L subsequent periods of the channel, the variance of the real and imaginary part of the noise at the output of the FFT block is estimated for each TFS as

$$\hat{\sigma}^2_{real}(k,n) = \frac{1}{(L-1)} \sum_{l=0}^{L-1} \left(\mathrm{Re}\left\{ R_k^{(n+lN_{ts})} \right\} - \mathrm{E}\left\{ \mathrm{Re}\left\{ R_k^{(n+lN_{ts})} \right\} \right\} \right)^2 \tag{8.3.18}$$

and

$$\hat{\sigma}^2_{imag}(k,n) = \frac{1}{(L-1)} \sum_{l=0}^{L-1} \left(\mathrm{Im}\left\{ R_k^{(n+lN_{ts})} \right\} - \mathrm{E}\left\{ \mathrm{Im}\left\{ R_k^{(n+lN_{ts})} \right\} \right\} \right)^2 . \tag{8.3.19}$$

respectively. It is worth remembering that powerline noise is not Gaussian for frequencies below 1 MHz [128], so that in principle (8.3.4) does not hold for powerline communications. However, it has been shown that modeling the noise at the output of an OFDM demodulator as a coloured Gaussian process provides good accuracy in terms of error performance [128], so that the noise can be modelled at the output of the FFT block for each TFS as a complex random variable consisting of iid Gaussian rvs with variance

$$\hat{\sigma}^2(k,n) = \max\left\{ \hat{\sigma}^2_{real}(k,n), \hat{\sigma}^2_{imag}(k,n) \right\}. \tag{8.3.20}$$

Finally, an estimate of the noise PSD can be evaluated as

$$\widehat{PSD_N}(i,k) \simeq \frac{2\hat{\sigma}^2}{\Delta f} \tag{8.3.21}$$

8.4 Simulation and numerical results

All the algorithms considered in this Chapter have been tested using a set of measurements acquired in a residential house located in Maranello (Modena, Italy). In particular, the experimental data include a data base collecting the TVTF of 24 powerline channels and for

Parameter	Value
Sampling frequency	$f_s = 2$ MHz
Order of the FFT	$N_{FFT} = 512$
Length of the cyclic prefix	$N_{CP} = 60$
Number of useful carriers	$N_c = 76$
Useful band	$203.1 - 496.1$ kHz
Number of OFDM symbol per mains period	$N_{ts} = 34$

Table 8.1: Parameters of the OFDM modulator and demodulator.

each channel a set of noise sequences acquired by means of the channel sounder described in [91]. Note that the channel impulse responses and the noise sequences have been acquired synchronously to the mains on subsequent mains periods. Then, the measured powerline channel have been modeled through the Zadeh's representation [132] with sampling frequency $f_s = 2$ MHz, order $Z = 4$ and memory $M = 400$ (corresponding to $200\,\mu s$).

The values of the parameters of the OFDM modulator and demodulator are listed in Table 8.1.

Three different approaches for bit and power loading have been considered in this work:

1. A standard bit loading algorithm which operates in the presence of the maximum power allowed by the PSD mask over each OFDM symbol;

2. the bit loading algorithm [147] (denoted as Tunc-Perrins-Lampe, TPL, in the following) which limits the total power spent by the transmitter over each period of the LPTV channel;

3. the proposed bit loading algorithm (denoted as Gianaroli-Pancaldi-Vitetta, GPV, hereafter) which limits the power transmitted over each subcarrier to meet the PSD mask over each period of the LPTV channel.

At the beginning of numerical analysis one of the measured powerline channels has been randomly picked out and exploited for performance assessment; in particular, the TVTF and noise PSD characterizing the selected channel are illustrated in Fig. 8.4.1 and 8.4.2, respectively, whereas the resulting *signal-to-noise ratio* (SNR) at the receiver, which accounts also the PSD mask, is shown in Fig. 8.4.3 (see eq. (8.3.7)). Note that variations as large

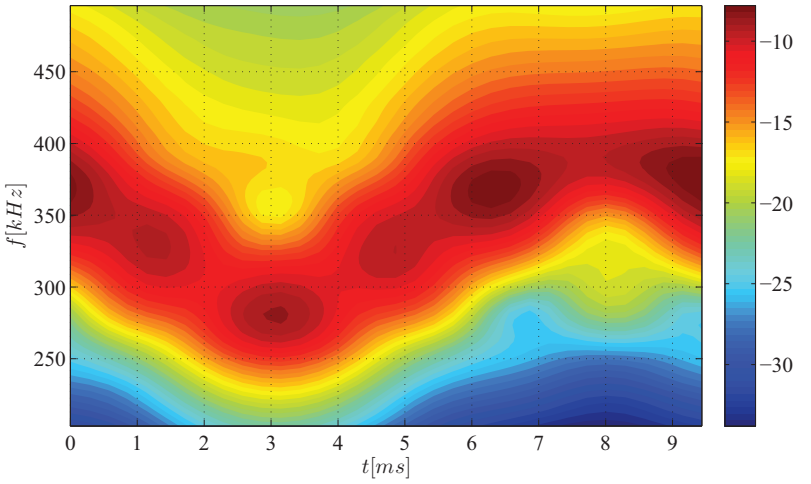

Figure 8.4.1: Absolute magnitude of the TVCFR in dB.

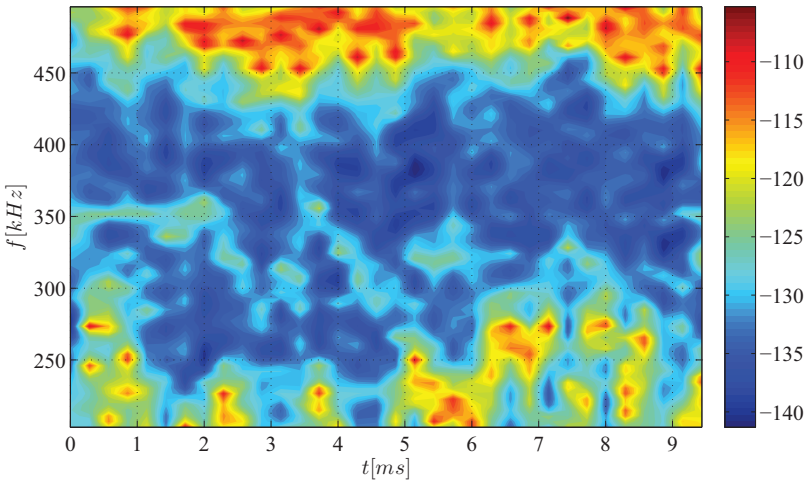

Figure 8.4.2: Time varying PSD of the noise in dB/Hz.

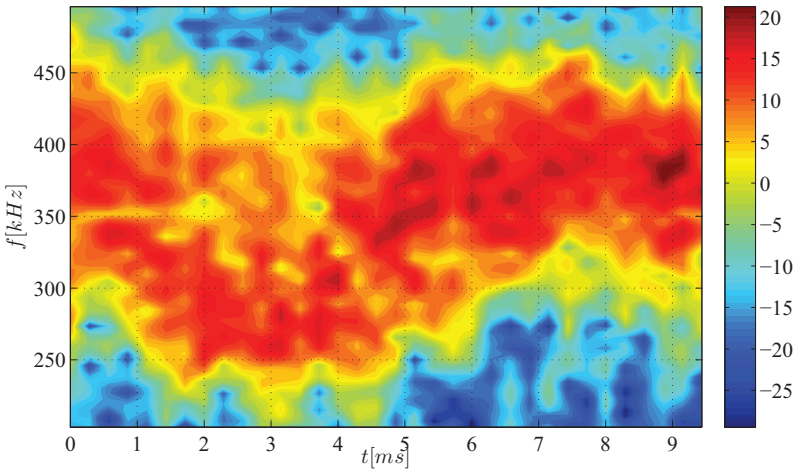

Figure 8.4.3: SNR at the receive side in dB.

	Channel off	4-QAM	16-QAM	64-QAM	B_r	BER
standard	65.7%	28.3%	6%	0.1%	209 kbps	$5.3 \cdot 10^{-6}$
TPL	74.7%	19.4%	6%	0%	162 kbps	$2 \cdot 10^{-4}$
proposed GPV	48%	26.1%	23%	2.9%	420 kbps	$9.8 \cdot 10^{-5}$

Table 8.2: Performance results evaluated for the standard, TPL and GPV algorithms for bit and power loading.

as 40 dB are visible in TVTF, noise PSD and SNR. Then, the performance of the all the considered bit/power loading algorithms has been assessed by computer simulation; the results, summarized in Table 8.2, have been obtained assuming the PSD mask

$$PSD_{TX}(f) = \begin{cases} -110\,\text{dBm/Hz} & 203.1\,\text{kHz} \leq f \leq 496.1\,\text{kHz} \\ 0 & \text{otherwise} \end{cases}, \tag{8.4.1}$$

a maximum constellation size $Q_{max}(n,k) = 1024$, a target maximum BER $BER_{max} = 10^{-4}$, $L = 20$ channel periods (corresponding to 200 ms) for noise estimation (8.3.18)-(8.3.19) and 100 channel periods (i.e., 1 s) for data transmission. The performance of the bit loading techniques in terms of allocated constellation size $Q(n,k)$ is illustrated in Fig. 8.4.4. Note that:

- the periodicity of the channel transfer function and noise statistical properties (see Figs.

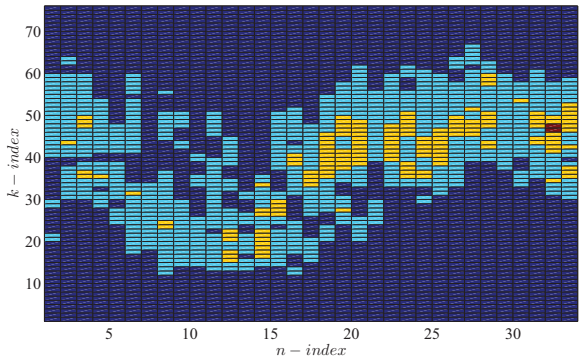

(a)

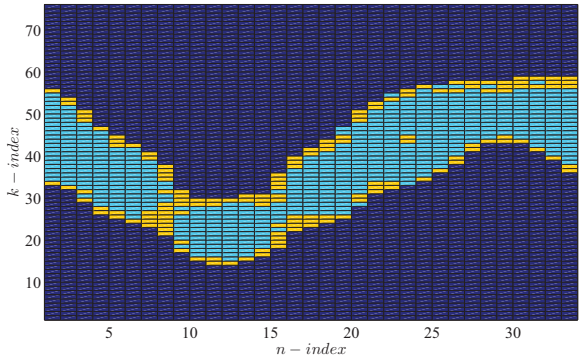

(b)

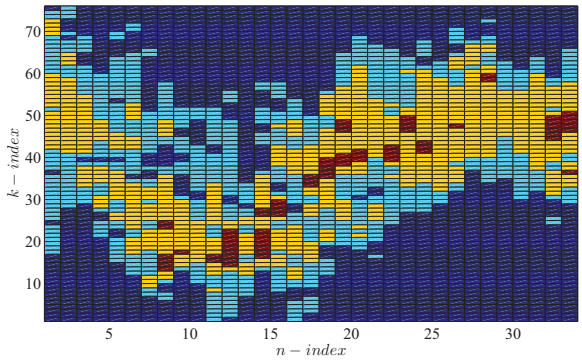

(c)

Figure 8.4.4: Bit allocation over the TFSs of a channel period when the (a) standard, (b) TPL and (c) GPV algorithms are employed for the same communication channel ; blue denotes $Q(n,k)=0$, cyan $Q(n,k)=4$, yellow $Q(n,k)=16$ and red $Q(n,k)=64$.

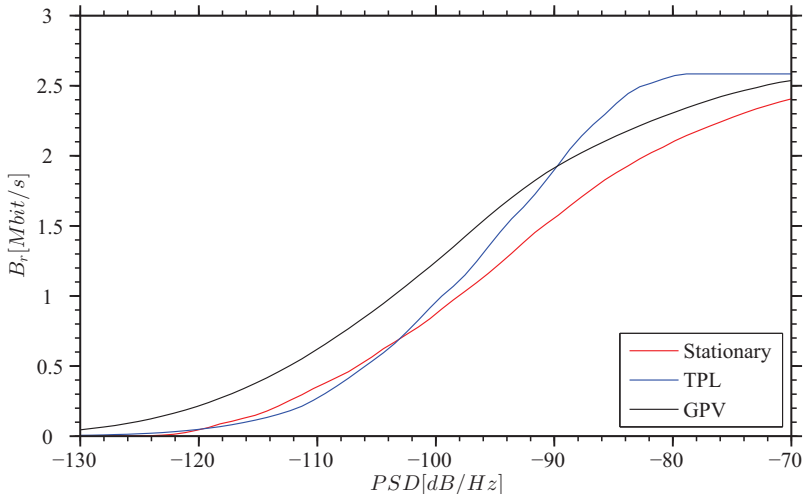

Figure 8.4.5: Bit rate achieved by the standard, TPL and GPV algorithms versus the transmitted PSD.

8.4.1 and 8.4.2, respectively) entails a periodicity in bit allocation;

- bit allocation follows the behaviour of the SNR (see Fig. 8.4.3), i.e. large constellation sizes $Q(n,k)$ are associated with TFSs characterized by large SNRs;
- the smart bit allocation of the GPV algorithm allows to turn on a larger number of TFSs with respect to its counterparts;
- the proposed GPV technique outperforms the standard approach in terms of bit rate because larger constellation sizes can be supported still satisfying the BER constraint $BER_{max} = 10^{-4}$; in fact in the considered scenario the GVP algorithm can achieve a bit rate of 420 kbps with a BER of $9.8 \cdot 10^{-5}$ against 209 kbps with a BER of $5.3 \cdot 10^{-6}$ for the standard technique;
- the TPL algorithm is outperformed by the standard and GVP algorithms in terms of both bit rate and BER (this result will be motivated at the end of this Section).

The performance of the three algorithms in terms of bit rate and BER has been also assessed feeding the OFDM simulator with sequences of measured noise; in this case only 20 channel periods are available in practice, so that about $20 \cdot N_{ts} = 680$ OFDM symbols have been transmitted (roughly corresponding to the transmission of 100 kbits). Consequently, since in

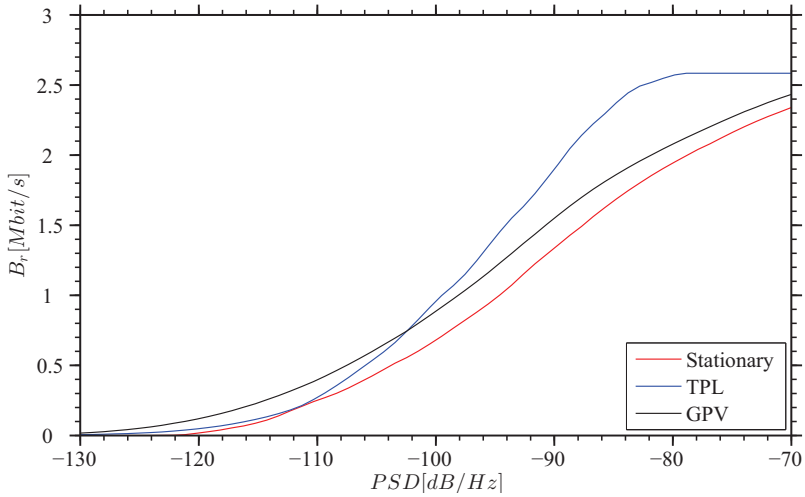

Figure 8.4.6: Bit rate achieved by the standard, TPL and GPV algorithms in the presence of measured noise.

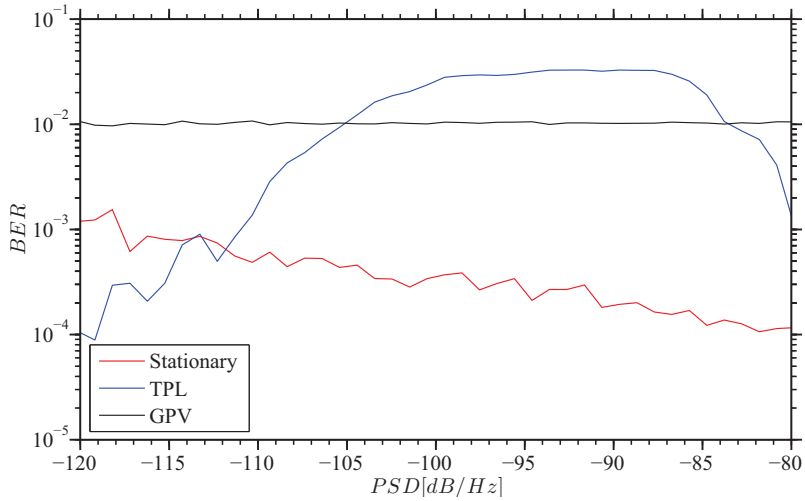

Figure 8.4.7: BER performance provided by the standard, TPL and GPV algorithms versus the transmitted PSD.

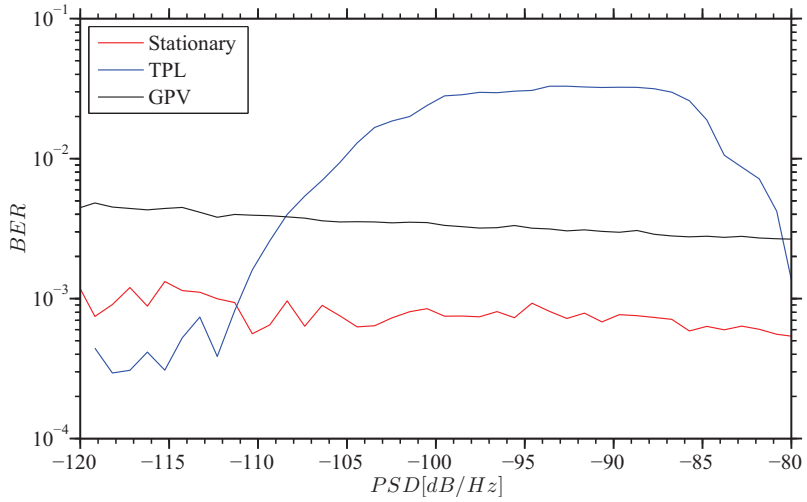

Figure 8.4.8: BER performance provided by standard, TPL and GPV algorithms in the presence of measured noise.

these conditions statistically meaningful values BER should not exceed 10^{-2}, the performance of of the GPV algorithm has been assessed for larger target BER ($BER_{max} = 10^{-2}$). In addition, the performance of the same communication system has been assessed in the presence of Gaussian noise over each subcarrier (in practice, the real and imaginary parts of each noise sample has been modelled as iid Gaussian rvs; see (8.3.18)-(8.3.19)) for comparison. The bit rate achieved by the system operating in the presence of modelled (Gaussian) and measured noise is illustrated in Fig. 8.4.5 and 8.4.6, respectively, versus the transmitted PSD (which is constant over the band of interest $200 - 500$ kHz), whereas the BER performance achieved in the presence of modelled (Gaussian) and measured noise is illustrated in Fig. 8.4.7 and 8.4.8, respectively. Note that the proposed GPV algorithm outperforms its counterparts when the PSD is smaller than 10^{-10} W/Hz, i.e. for low SNRs, whereas the TPL technique can outperform the proposed GPV algorithm for a PSD larger than 10^{-10} W/Hz. This behavior can be related to the different power constraints set for the GPV and TPL techniques; in fact, the former technique is forced to meet the PSD mask on a subcarrier by subcarrier basis, whereas the latter one can focus all the available power on the best TFSs. In particular, in the considered scenario, the TPL algorithm takes advantage of 45 useful subcarriers over the 76 available ones, but 37 subcarriers (over the 45 active ones) fall above the PSD mask (constant over the band of interest $200 - 500$ kHz). Furthermore, the TPL technique cannot

meet the target $BER_{max} = 10^{-2}$ for the following two reasons: a) a substantial approximation is introduced in eq. (7) of [147]; b) the unrealistica assumption of stationary AWGN is made in [147] (powerline noise is neither stationary nor white below 1 MHz [128]). Finally, it is worth pointing out that:

- the bit rate achievable in the presenec simulated (Gaussian) noise is larger than that referring to the case of measured noise;
- the BER performance achieved by the system operating in the presence of simulated (Gaussian) noise is larger than that with measured noise.

This behavior can be mainly related to the unrealistic assumption that the in-phase and quadrature components of the noise are iid; in fact, real world powerline noise is characterized by correlated components. Consequently, the bit rate decreases when employing measured noise because the the variance of channel noise is overestimated (see (8.3.20)); however, the BER gets smaller as well since the OFDM demodulator operates in more favourable conditions.

8.5 Conclusions

In this Chapter it has been shown that the knowledge of periodic time varying properties of powerline channels can be exploited to improve the bit rate of an OFDM link. In particular, bit/power loading algorithms have been developed under the assumptions of: a) specific constraints on the maximum admissible BER and on the maximum average transmitted power; b) knowledge of the parameters of a Zadeh-based LPTV model of the communication channel. Numerical simulations and experimental results referring to specific indoor scenarios have evidenced that the proposed algorithms can substantially outperform other techniques developed for linear time invariant channels or for LPTV channels.

Chapter 9

Conclusions

In this thesis several important research issues regarding indoor powerline communication systems have been addressed. The main goal has been the development of innovative techniques able to improve the performance of powerline communications systems without requiring a bandwidth increase. To this aim, the nature of powerline communication channels has been investigated under different points of view. In the first part of the research activities (see the first two chapters of this manuscript) powerline communication channels have been modeled as time invariant systems. In particular, a statistical channel simulator based on a Monte Carlo method has been developed and some experimental data have been acquired to validate the proposed tool and to characterize the input impedance of home appliances. The acquired data have evidenced the impact of accurate characterization of power load on the accuracy of the results achievable through the channel simulator. In particular, it has been shown that a good accuracy in the simulation of powerline channels at low frequency is achieved if home appliances are modeled as complex impedances. In the following two chapters the problem of powerline noise modeling has been addressed. In particular, in Chapter 3 the development of a model for the cyclostationary contributions of powerline noise has been studied. Various realizations of powerline noise have been acquired in the laboratories of the Department of Engineering "Enzo Ferrari" in order to assess the capability of the model to fit the cyclic autocorrelation function of measured noise. In Chapter 4 the effect of noise modeling on the error performance of a simulated powerline communication system employing OFDM has been analysed. In particular, the impact of the noise probability density function and power spectral density on error performance has been investigated. Simulation results have evidenced that the most important property to be accounted for by a noise model is the power

spectral density. The second part of the thesis has dealt with the analysis and modeling of time varying properties of powerline channels. To carry out this research activity, a specific channel sounder for powerline communication channels has been designed end implemented using a FPGA development board. Experimental results provided by this channel sounder have evidenced that indoor powerline channels can be represented as linear periodically time varying systems. A discrete time model for this class of systems has been derived starting from the so called Zadeh's series representation. The devised model achieve excellent performance in terms of both complexity and accuracy. The problem of estimating the parameters of this channel model has been also investigated; in particular, it has been shown that a simple and accurate frequency domain estimator can be employed. In the last part of this thesis, the developed channels models have been exploited to derive innovative communication techniques for OFDM powerline communication systems. More specifically, an OFDM equalizer and an OFDM bit loading algorithm, based on the knowledge of the time varying characteristics of powerline channels, have been proposed. The performance of these algorithms has been assessed resorting to computer simulations approach and some experimental tests. The results have evidenced that in indoor powerline communications reliable communications at 1 MBit/s can be achieved by a multicarrier communication system with a bandwidth of about 300 kHz.

Publications List

Journal (published):

1. F. Gianaroli, A. Barbieri, F. Pancaldi, A. Mazzanti and G. M. Vitetta, “A Novel Approach to Power-Line Channel Modeling”, IEEE Trans. Power Del., vol. 25, no. 1, pp. 132-140, Jan. 2010.

2. F. Gianaroli, F. Pancaldi, E. Sironi, M. Vigilante, G. M. Vitetta and A. Barbieri, “Statistical Modeling of Periodic Impulsive Noise in Indoor Power-Line Channels”, IEEE Trans. Power Del., vol. 27, no. 3, pp. 1276-1283, July 2012.

3. F. Gianaroli, F. Pancaldi, and G. M. Vitetta, “On the Impact of Load Characterization on Statistical Modeling of Powerline Channels”, IEEE Trans. Smart Grid, vol.4, no.2, pp.677,685, June 2013.

4. F. Gianaroli, F. Pancaldi, and G. M. Vitetta, "Design and Implementation of a Wideband Channel Sounder for Low-Voltage Powerlines”, IEEE Trans. Smart Grid, Sept. 2013.

Conference (published):

1. F. Gianaroli, F. Pancaldi and G. M. Vitetta, "Broadband system models based on Zadeh’s representation for indoor powerline channels: An experimental validation" Communications (ICC), 2013 IEEE International Conference on , vol., no., pp.4304,4309, 9-13 June 2013.

Journal (submitted):

1. F. Gianaroli, F. Pancaldi, and G. M. Vitetta, “On the Use of Zadeh’s Series Expansion for Modelling and Estimation of Broadband Indoor Powerline Channels”, submitted to the IEEE Trans. On Power Delivery, September 2013.

2. F. Gianaroli, F. Pancaldi, and G. M. Vitetta, "The Impact of Statistical Noise Modelling on the Error Rate Performance of OFDM Powerline Communications", submitted to the IEEE Trans. On Communications, September 2013.

3. F. Gianaroli, F. Pancaldi, and G. M. Vitetta, "Channel Estimation and Equalization for OFDM Indoor Powerline Communications", submitted to the IEEE Trans. On Communications, December 2013.

Bibliography

[1] M. Schwartz, "History of communications-Carrier-wave telephony over power lines: Early history", *IEEE Commun. Mag.*, vol. 47, no. 1, pp. 14–18, Jan. 2009.

[2] S. Galli, A. Scaglione, W. Zhifang , "For the Grid and Through the Grid: The Role of Power Line Communications in the Smart Grid", *Proceedings of the IEEE*, vol. 99, no. 6, pp. 998-1027, June 2011.

[3] K. Dostert, **Power Line Communications**, Prentice Hall, 2001.

[4] D. Clark, "Powerline communications: Finally ready for primetime?", *IEEE Internet Comput.*, vol. 2, no. 1, pp. 10–11, Jan. 1998.

[5] H. Meng, S. Chen, Y. L. Guan, C. L. Law, P. L. So, E. Gunawan and T. Lie, "Modeling of transfer characteristics for the broadband powerline communication channel", *IEEE Trans. Power Del.*, vol. 19, no. 3, pp. 1057–1064, Jul. 2004.

[6] M. Gotz and K. Dostert, "Power Line Channel Characteristics and Their Effect on Communication System Design", *IEEE Commun. Mag.*, vol. 42, no. 4, pp 78-86, Apr. 2004.

[7] A. Majumder and J. Caffery, "Power line communications", *IEEE Potentials*, vol.23, no.4, pp. 4-8, Oct.-Nov. 2004.

[8] N. Pavlidou, A. J. H. Vinck, J. Yazdani and B. Honary, "Power line communications: State of the art and future trends", *IEEE Commun. Mag.*, vol. 41, pp. 34–40, Apr. 2003.

[9] H. Hrasnica, A. Haidine and R. Lehnert, **Broadband Powerline Communications Networks: Network Design**, New York: Wiley, 2004.

[10] D. Anastasiadou and T. Antonakopoulos, "Multipath characterization of indoor power-line networks", *IEEE Trans. Power Del.*, vol. 20, no.1, pp. 90–99, Jan. 2005.

[11] D. Sabolic, A. Bazant and R. Malaric, "Signal Porpagation Modeling in Power-Line Communication Networks", *IEEE Trans. Power Del.*, vol. 20, no.4, pp. 2429-2436, Oct. 2005.

[12] S. Galli and T. C. Banwell, "A deterministic frequency-domain model for the indoor power line transfer functions", *IEEE J. Sel. Areas Commun.*, vol. 24, no. 7, pp. 1304–1316, July 2006.

[13] H. Philipps, "Modeling of powerline communication channels", in *Proc. 3rd Int. Symp. Powerline Communications and its Applications*, Lancaster, U.K., 1999, pp. 14–21.

[14] M. Zimmermann and K. Dostert, "A Multipath Model for the Power line Channel", *IEEE Trans. Commun.*, vol.50, no. 4, Apr. 2002, pp. 553–59.

[15] L. Liu, T. Cheng and L. Yanan, "Analysis and Modeling of Multipath for Indoor Power Line Channel", *10th International Conference on Advanced Communication Technology, 2008 (ICACT 2008)*, vol.3, pp.1966-1969, 17-20 Feb. 2008.

[16] I. C. Papaleonidopoulos, C. N. Capsalis, C. G. Karagiannopoulos and N. J. Theodorou, "Statistical analysis and simulation of indoor singlephase low voltage power-line communication channels on the basis of multipath propagation", *IEEE Trans. Consum. Electron.*, vol. 49, no. 1, pp. 175–183, Feb. 2003.

[17] M. Tlich, A. Zeddam, F. Moulin and F. Gauthier, "Indoor Power-Line Communications Channel Characterization Up to 100 MHz—Part I: One-Parameter Deterministic Model", *IEEE Trans. Power Del.*, vol. 23, no. 3, pp. 1392-1401, July 2008.

[18] J. A. Cortes, F. J. Canete, L. Diez and J. T. Entrambasaguas, "Characterization of the cyclic short-time variation of indoor power-line channels response", in *Proc. Int. Symp. Power Line Commun.*, Apr. 6–8, 2005, pp. 326–330.

[19] M. Gebhardt, F. Weinmann and K. Dostert, "Physical and Regulatory Constraints for Communication over the Power Supply Grid", *IEEE Commun. Mag.*, vol. 41, no. 5, pp. 84-90, May 2003.

[20] P. A. Janse van Rensburg and H. C. Ferreira, "Design of a bidirectional impedance-adapting transformer coupling circuit for low-voltage power-line communications", *IEEE Trans. Power Del.*, vol. 20, no. 1, pp. 64–70, Jan. 2005.

[21] T1-1-X65 RF transformer datasheet. Available online at http://www.minicircuits.com/products/transformers_pic_c.html#config_c.

[22] Mini Circuits application note, "How RF Transformers Work," available online at http://www.minicircuits.com/pages/pdfs/howxfmerwork.pdf.

[23] Tonello, Andrea M., and Fabio Versolatto, "New results on top-down and bottom-up statistical PLC channel modeling", *Third Workshop on Power Line Communications*. 2009.

[24] S. Galli and O. Logvinov, "Recent Developments in the Standardization of Power Line Communications within the IEEE", *IEEE Commun. Mag.*, vol. 46, no. 7, pp. 64-71, July 2008.

[25] F. J. Canete, L. Diez, J. A. Cortes and J. T. Entrambasaguas, "Broadband Modelling of Indoor Power-Line Channels", *IEEE Trans. Consumer Electronics*, vol. 48, no. 1, pp.175-183, Feb. 2002.

[26] I. C. Papaleonidopoulos, C. A. Ioannou, C. G. Karagiannopoulos and N. J. Theodorou, "Branched-Bus HF Power-Delay-Profile Approach of Indoor PLC Channels", *Proc. IEEE International Symposium on Power Line Communications and Its Applications* (ISPLC 2005), pp. 147 - 151, 2005.

[27] S. Barmada, A. Musolino and M. Raugi, "Innovative Model for Time-Varying Power Line Communication Channel Response Evaluation", *IEEE J. Sel. Areas Commun.*, vol. 24, no. 7, pp. 1317–1326, July 2006.

[28] F. J. Canete Corripio, J. A. Cortes Arrabal, L. Diez del Rio and J. T. Entrambasaguas Munoz, "Analysis of the Cyclic Short-term Variation of Indoor Power

Line Channels", *IEEE J. Select. Areas Commun.*, vol. 24, no. 7, pp. 1327-1338, July 2006.

[29] H. Hrasnica, A. Haidine and R. Lehnert, **Broadband Powerline Communications Networks**, John Wiley & Sons, 2004.

[30] S. Sancha, F. J. Canete, L. Diez and J. T. Entrambasaguas, "A Channel Simulator for Indoor Power-line Communications", *Proc. IEEE International Symposium on Power Line Communications and Its Applications* (ISPLC 2007), pp. 104 - 109, 2007.

[31] G. Moreno-Rodriguez and L. T. Berger, "An IIR-Filter Approach to Time Variant PLC-Channel Modelling", *Proc. IEEE International Symposium on Power Line Communications and Its Applications* (ISPLC 2008), pp. 87-92, 2008.

[32] H. Phillips, "Modelling of Powerline Communication Channels", *Proc. 3rd Int. Symp. Powerline Communications and its Applications*, pp. 14–21, Lancaster, U.K., 1999.

[33] H. Philipps, "Performance measurements of powerline channels at high frequencies", *Proc. 2nd Int. Symp. on Powerline Communications and Its Applications*, pp. 229–237, Tokyo, Japan, 1998.

[34] T. Esmailian, F. R. Kschischang and P. G. Gulak, "In-building power lines as high speed communication channels: channel characterization and a test channel ensemble", *Int. J. Commun. Syst.*, vol. 16, 2003.

[35] J. Anatory, M. M. Kissaka and N. H. Mvungi, "Channel Model for Broadband Power-Line Communication", *IEEE Trans. Power Del.*, vol. 22, no.1, pp. 135–141, Jan. 2007.

[36] H. Chaouche, M. Tlich, P. Pagani and A. Zeddam, "Deterministic Modelling of Powerline Channels and Impact of Domestic Appliances Impedances", *Proc. IEEE 1st IFIP Wireless Days* (WD '08), pp. 1-5, 2008.

[37] X. Ding and J. Meng, "Channel Estimation and Simulation of an Indoor Power-Line Network via a Recursive Time-Domain Solution", *IEEE Trans. Power Del.*, vol. 24, no.1, pp. 144–152, Jan. 2009.

[38] M. Tlich, A. Zeddam, F. P. Gauthier and P. Pagani, "Wideband Indoor Transmission Channel Simulator for Power Line: WITS Software", *IEEE Trans. Power Del.*, vol. 25, no.2, pp. 702–713, Apr. 2010.

[39] F. Gianaroli, A. Barbieri, F. Pancaldi, A. Mazzanti and G. M. Vitetta, "A Novel Approach to Power-Line Channel Modeling", *IEEE Trans. Power Del.*, vol. 25, no.1, pp. 132–140, Jan. 2010.

[40] J. A. Cortes, L. Diez, F. J. Canete and J. J. Sanchez-Martinez, "Analysis of the Indoor Broadband Power-Line Noise Scenario", to appear on *IEEE Trans. Electromagnetic Compatibility*, 2010.

[41] S. Galli, "A Simple Two-Tap Statistical Model for the Power Line Channel", *Proc. IEEE International Symposium on Power Line Communications and Its Applications* (ISPLC 2010), pp. 242-248, 2010.

[42] A. M. Tonello and F. Versolatto, "Bottom-up Statistical PLC Channel Modeling–Part I: Random Topology Model and Efficient Transfer Function Computation", *IEEE Trans. Power Del.*, vol. 26, no.2, pp. 891–898, Apr. 2011.

[43] R. M. Vines, H. J. Trussel, K. C. Shuey and J. B. O'Neal, "Impedance of the Residential Power-Distribution Circuit", *IEEE Trans. Electromagnetic Compatibility*, vol. 27, no. 1, pp. 6-12, Feb. 1985.

[44] S. Tsuzuki, S. Yamamoto, T. Takamatsu and Y. Yamada, "Measurement of Japanese Indoor Power-Line Channel", *Proc. IEEE International Symposium on Power Line Communications and Its Applications* (ISPLC 2001), pp. 79-84, 2001.

[45] D. Anastasiadou and T. Antonakopoulos, "Measurements-based Method for Impedance Characterization of Residential Loads", *Proc. IEEE Instrumentation and Measurement Technology Conference* (IMTC 2004), pp. 669-674, May 2004.

[46] J. Anatory, N. Theethayi and R. Thottappillil, "Channel Characterization for Indoor Power-Line Networks", *IEEE Trans. Power Del.*, vol. 24, no. 4, pp. 1883–1888, Oct. 2009.

[47] A. M. Tonello and F. Versolatto, "Bottom-up Statistical PLC Channel Modeling–Part II: Inferring the Statistics", *IEEE Trans. Power Del.*, vol. 25, no. 4, pp. 2356–2363, Oct. 2010.

[48] Er Liu *et al.*, "Broadband Characterization of Indoor Powerline Channel and Its Capacity Consideration", *Proc. IEEE International Conference on Communications* (ICC 2005), vol. 2, pp. 901–905, 2005.

[49] S. Y.-di Lien and M. Cherniakov, "Analytical Approach for multipath Delay Spread Power Distribution", *Proc. IEEE Global Telecommunications Conference* (GLOBECOM'98), vol. 6, pp. 3680–3685, 1998.

[50] F. Gianaroli, F. Pancaldi and G. M. Vitetta, "Broadband System Models Based on Zadeh's Representation for Indoor Powerline Channels: An Experimental Validation", *accepted for presentation at the International Conference on Communications 2013.*

[51] J.-M. Molina-Garcia-Pardo, J.-V. Rodríguez and L. Juan-Llacer, "MIMO Channel Sounder Based on Two Network Analyzers", *IEEE Trans. Instrum. Meas.*, vol. 57, no. 9, pp. 2052-2058, Sep. 2008.

[52] B. T. Maharaj, J. W. Wallace, M. A. Jensen and L. P. Linde, "A Low-Cost Open-Hardware Wideband Multiple-Input–Multiple-Output (MIMO) Wireless Channel Sounder", *IEEE Trans. Instrum. Meas.*, vol. 57, no. 10, pp. 2283-2289, Oct. 2008.

[53] F. J. Canete, L. Diez, J. A. Cortes, J. J. Sanchez-Martinez and L. M. Torres, "Time-Varying Channel Emulator for Indoor Power Line Communications", *Proc. IEEE Global Telecommunications Conference* (GLOBECOM 2008), pp. 1-5, 2008.

[54] M. Bauer, W. Liu and K. Dostert, "Channel Emulation of Low-Speed PLC Transmission Channels", *Proc. IEEE International Symposium on Power Line Communications and Its Applications* (ISPLC 2009), pp. 267-272, 2009.

[55] M. Sebeck and G. Bumiller, "Power-Line Analysing Tool for Channel Estimation, Channel Emulation and Noise Characterisation", iAd Gmbh, available online at http://www.iad-de.com/plcsym/platopaper01.pdf

[56] Com Block, COM-1232 "Channel Emulator", online at http://comblock.com/download/com1232.pdf

[57] CENELEC EN 50065-1, "Signalling on low-voltage electrical installations in the frequency range 3 Hz to 148,5 kHz - Part 1: General requirements, frequency bands and electromagnetic disturbances", 2011.

[58] S. Galli and O. Logvinov,"Recent Developments in the Standardization of Power Line Communications within the IEEE", *IEEE Commun. Mag.*, vol. 46, no. 7, pp. 64-71, July 2008.

[59] F. J. Canete Corripio, J. A. Cortes Arrabal, L. D. del Rio and J. T. Entrambasaguas Munoz, "Analysis of the Cyclic Short-Term Variation of Indoor Power Line Channels", *IEEE J. Selected Areas Commun.*, vol. 24, no. 7, pp. 1327- 1338, July 2006.

[60] Altera, "Stratix III 3SL150 Development Board Reference Manual", online at http://www.altera.com/literature/manual/rm_stratixiii_dev_kit_host_board.pdf

[61] Altera, "Stratix III FPGAs vs. Xilinx Virtex-5 Devices: Architecture and Performance Comparison", online at http://www.altera.com/literature/wp/wp-01007.pdf

[62] Altera, "Data Conversion HSMC Reference Manual", online at http://www.altera.com/literature/manual/rm_data_conversion_hsmc.pdf

[63] F. Gianaroli, F. Pancaldi and G. M. Vitetta, "The Impact of Load Characterization on the Average Properties of Statistical Models for Powerline Channels", *IEEE Trans. on Smart Grid*, vol.4, no.2, pp.677,685, June 2013.

[64] Coilcraft, "Low Pass LC Filter Modules", datasheet available online at: "http://www.coilcraft.com/pdfs/lcfilt.pdf"

[65] Coilcraft, "Wideband Transformers", datasheet available online at: "http://www.coilcraft.com/pdfs/wb.pdf"

[66] Texas Instruments, OPA842 "Wideband, Low Distortion, Unity-Gain Stable, Voltage-Feedback Operational Amplifier", datasheet available online at: "http://www.ti.com/lit/gpn/opa842"

[67] Texas Instruments, OPA846 "Wideband, Low-Noise, Voltage-Feedback Operational Amplifier", datasheet available online at: "http://www.ti.com/lit/gpn/opa846"

[68] Texas Instruments, OPA2677 "Dual, Wideband, High Output Current Operational Amplifier", datasheet available online at: "http://www.ti.com/lit/gpn/opa2677"

[69] P. P. Chu, **FPGA Prototyping by Verilog Examples**, John Wiley & Sons, 2008.

[70] S. G. Mallat, **A Wavelet Tour of Signal Processing: The Sparse Way**, Third Edition, Elsevier Academic Press, 2009.

[71] A. S. Mehr and T. Chen, "On Alias-Component Matrices of Discrete-Time Linear Periodically Time-Varying Systems", *IEEE Signal Processing Lett.*, vol. 8, no. 4, pp. 114-116, Apr. 2001.

[72] Y. Dorfan, A. Feuer and B. Porat, "Modeling and identification of LPTV systems by wavelets", *Elsevier Signal Processing*, no. 84, pp. 1285-1297, 2004.

[73] W. Yin and A. S. Mehr, "Least square identification of alias components of linear periodically time-varying systems and optimal training signal design", *IET Signal Processing*, vol. 4, no. 2, pp. 149-157, 2010.

[74] E. Louarroudi, R. Pintelon, J. Lataire and G. Vandersteen, "Estimation of Non-parametric Harmonic Transfer Functions for Linear Periodically Time-Varying Systems Using Periodic Excitations", *IEEE Instrumentation and Measurement Technology Conference* (I2MTC), pp. 1-6, 2011.

[75] F. Gianaroli, F. Pancaldi, E. Sironi, M. Vigilante, G. M. Vitetta and A. Barbieri, "Statistical Modeling of Periodic Impulsive Noise in Indoor Power-Line Channels", *IEEE Trans. Power Del.*, vol. 27, no. 3, pp. 1276-1283, July 2012.

[76] H. Meng, Y. L. Guan and S. Chen, "Modeling and Analysis of Noise Effects on Broadband Power-Line Communications", *IEEE Trans. Power Del.*, vol. 20, no. 2, pp. 630–636, Apr. 2005.

[77] M. Tlich, H. Chaouche, A. Zeddam and P. Pagani, "Novel Approach for PLC Impulsive Noise Modelling", *Proc. IEEE International Symposium on Power Line Communications and Its Applications (ISPLC '09)*, pp. 20–25, 2009.

[78] References J. A. Cortes, L. Diez, F. J. Cañete and J. Lopez, "Analysis of the Periodic Impulsive Noise Asynchronous with the Mains in Indoor PLC Channels", *Proc. IEEE International Symposium on Power Line Communications and Its Applications (ISPLC '09)*, pp. 26–30, 2009.

[79] N. Andreadou and F.-N. Pavlidou, "Modeling the Noise on the OFDM Power-Line Communications System", *IEEE Trans. Power Del.*, vol. 25, no. 1, pp. 150–157, Jan. 2010.

[80] N. Andreadou and F.-N. Pavlidou, "PLC Channel: Impulsive Noise Modelling and Its Performance Evaluation Under Different Array Coding Schemes", *IEEE Trans. Power Del.*, vol. 24, no. 2, pp. 585–595, Apr. 2009.

[81] K. S. Al-Mawali, F. S. Al-Qahtani and Z. M. Hussain, "Adaptive Power Loading for OFDM-Based Power Line Communications Impaired by Impulsive Noise", *Proc. IEEE International Symposium on Power Line Communications and Its Applications (ISPLC '10)*, pp. 178–182, 2010.

[82] S. Winder, **Analog and Digital Filter Design**, second edition, Newnes, 2002.

[83] References W. A. Gardner, "Cyclostationarity: Half a century of research", *Signal Processing*, vol. 86, no. 4, pp. 639–697, Apr. 2006.

[84] K. W. Hipel and A. I. McLeod, **Time Series Modelling of Water Resources and Environmental Systems**, Elsevier, 1994.

[85] P. J. Brockwell and R. A. Davis, **Time Series: Theory and Methods**, second edition, Springer, 2006.

[86] Y. Chakhchoukh, "A New Robust Estimation Method for ARMA Models", *IEEE Trans. Signal Processing*, vol. 58, no. 7, pp. 3512–3522, July 2010.

[87] S. A. Fattah, W.-P. Zhu and M. O. Ahmad, "A Novel Technique for the Identification of ARMA Systems Under Very Low Levels of SNR", *IEEE Trans. Circuits Syst. I*, Reg. Papers, vol. 55, no. 7, pp. 1988–2001, Aug. 2008.

[88] http://www.mathworks.com/help/toolbox/ident/ref/armax.html

[89] L. Ljung, **System Identification: Theory for the User**, Prentice Hall PTR, 1999.

[90] H. Farhangi, "The path of the smart grid", *IEEE Power & Energy Mag.*, vol. 8, no. 1, pp. 18-28, Jan/Feb. 2010.

[91] F. Gianaroli, F. Pancaldi and G. M. Vitetta, "Design and Implementation of a Wideband Channel Sounder for Low-Voltage Powerlines", *IEEE Trans. Smart Grid*, vol.5, no.1, pp. 210–219, Jan. 2014

[92] M. A. Tunc, E. Perrins and L. Lampe, "Reduced complexity LPTV-aware bit loading for channel adaptation in broadband PLC", *Proc. IEEE International Symposium on Power Line Communications and Its Applications* (ISPLC 2012), pp. 206-211, 2012.

[93] F. Rouissi, V. Degardin, A. Ghazel, M. Lienard and F. Gauthier, "Impulsive Noise Modelling Using Markov Chains in Indoor Environment - Comparison With Stochastic Model", *Proc. IEEE 12th International Conference on Electronics, Circuits and Systems* (ICECS 2005), 2005.

[94] M. Katayama, T. Yamazato and H. Okada, "A Mathematical Model of Noise in Narrowband Power Line Communication Systems", *IEEE J. Selected Areas Commun.*, vol. 24, no. 7, pp. 1267-1276, July 2006.

[95] S. Katar, B. Mashbum, K. Afkhamie, H. Latchman and R. Newrnan, "Channel Adaptation based on Cyclo-Stationary Noise Characteristics in PLC Systems", *Proc. IEEE International Symposium on Power Line Communications and Its Applications* (ISPLC 2006), pp. 16-21, 2006.

[96] M. Nassar, A. Dabak, I. H. Kim, T. Pande and B. L. Evans, "Cyclostationary noise modeling in narrowband powerline communication for Smart Grid applications", *Proc. IEEE International Conference on Acoustics, Speech and Signal Processing* (ICASSP 2012), pp. 3089-3092, 2012.

[97] J. Lin and B. L. Evans, "Cyclostationary noise mitigation in narrowband powerline communications", *Proc. IEEE Asia-Pacific Signal & Information Processing Association Annual Summit and Conference* (APSIPA ASC 2012), 2012

[98] .V. Guillet and G. Lamarque, "Unified background noise model for Power Line Communication", *Proc. IEEE International Symposium on Power Line Communications and Its Applications* (ISPLC 2010), pp. 131-136, 28-31 Mar. 2010.

[99] R. Hashmat, P. Pagani, T. Chonavel and A. Zeddam, "A Time-Domain Model of Background Noise for In-Home MIMO PLC Networks", *IEEE Trans. Power Del.*, vol. 27, no. 4, pp. 2082-2089, Oct. 2012

[100] P. A. C. Lopes, J. M. M. Pinto and J. B. Gerald, "Dealing With Unknown Impedance and Impulsive Noise in the Power-Line Communications Channel", *IEEE Trans. Power Del.*, vol. 28, no. 1, pp. 58-66, Jan. 2013.

[101] G. M. Vitetta, D. P. Taylor, G. Colavolpe, F. Pancaldi and P. A. Martin, **Wireless Communications: Algorithmic Techniques**, John Wiley & Sons, 2013.

[102] H. Hrasnica, A. Haidine and R. Lehnert, **Broadband Powerline Communications Networks**, John Wiley & Sons, 2004.

[103] M. Zimmermann and K. Dostert, "Analysis and modeling of impulsive noise in broad-band powerline communications", *IEEE Trans. Electromagnetic Compatibility*, vol. 44, no. 1, pp. 249-258, Feb. 2002

[104] .D. Middleton, "Statistical-physical models of electromagnetic interference", *IEEE Trans. Electromagnetic Compatibility*, vol. EMC-19, no. 3, pp. 106-127, Aug. 1977.

[105] Wang Bo, Qi Yinghao, Huang Peiwei and Cai Wenhao, "Indoor powerline channel simulation and capacity analysis", *Proc. IET Conference on Wireless, Mobile and Sensor Networks* (CCWMSN07), pp. 154-157, 12-14 Dec. 2007.

[106] V. Bhatia and B. Mulgrew, "Non-parametric likelihood based channel estimator for Gaussian mixture noise", *Elsevier Signal Processing*, vol. 87, no. 11, pp. 2569–2586, Nov. 2007.

[107] T. Esmailian, F. R. Kschischang and P. G. Gulak, "Characteristics of inbuilding power lines at high frequencies and their channel capacity", *Proc. IEEE International Symposium on Power Line Communications and Its Applications* (ISPLC 2000), pp. 52–59, 2000.

[108] L. Di Bert, P. Caldera, D. Schwingshackl and A. Tonello, "On noise modeling for power line communications", *Proc. IEEE International Symposium on Power Line Communications and Its Applications* (ISPLC 2011), pp. 283-288, 3-6 Apr. 2011.

[109] D. Benyoucef, "A new statistical model of the noise power density spectrum for powerline communication", *Proc. IEEE International Symposium on Power Line Communications and Its Applications* (ISPLC 2003), pp. 136-141, Mar. 2003.

[110] M. Zimmermann and K. Dostert, "An analysis of the broadband noise scenario in powerline networks", *Proc. IEEE International Symposium on Power Line Communications and Its Applications* (ISPLC 2000), pp. 131-138, 2000.

[111] M. Nassar, K. Gulati, Y. Mortazavi and B. L. Evans, "Statistical Modeling of Asynchronous Impulsive Noise in Powerline Communication Networks", *Proc. IEEE Global Telecommunications Conference* (GLOBECOM 2011), 5-9 Dec. 2011.

[112] C. M. Bishop, **Pattern recognition and machine learning**, New York: Springer, 2006.

[113] L. Liporace, "Maximum likelihood estimation for multivariate observations of Markov sources", *IEEE Trans. Information Theory*, vol. IT-28, no. 5, pp. 729-734, Sep. 1982.

[114] K. Fan, "Les fonctions definies-positives et les fonctions completement monotones", *Memorial des Sciences Math.*, CXIV, 1950.

[115] T. K. Moon, "The expectation-maximization algorithm", *IEEE Signal Processing Mag.*, vol. 13, no. 6, pp. 47-60, Nov. 1996.

[116] M. Bouvet and S. T. Schwartz, "Comparison of Adaptive and Robust Receivers for Signal Detection in Ambient Underwater Noise", *IEEE Trans. Acoustics Speech Signal Processing*, vol. 37, no. 5, pp. 621-626, May 1989.

[117] S. Galli, "A Simplified Model for the Indoor Power Line Channel", *Proc. IEEE Int. Symp. Power Line Communications and Its Applications* (ISPLC '09), pp. 13-19, 2009.

[118] P. Pagani, A. Ismail and A. Zeddam, "Path Identification in a Power-Line Network Based on Channel Transfer Function Measurements", *IEEE Trans. Power Del.*, vol. 27, no. 3, pp. 1081-1089, July 2012.

[119] A. M. Tonello, F. Versolatto, B. Bejar and S. Zazo, "A Fitting Algorithm for Random Modeling the PLC Channel", *IEEE Trans. Power Del.*, vol. 27, no. 3, pp. 1477-1484, July 2012.

[120] S. Sancha, F. J. Canete, L. Diez and T. J. Entrambasaguas, "A Channel Simulator for Indoor Power-line Communications", *Proc. IEEE Int. Symp. Power Line Communications and Its Applications* (ISPLC '07), pp. 104-109, 2007.

[121] S. Galli, "A Novel Approach to the Statistical Modeling of Wireline Channels", *IEEE Trans. Commun.*, vol. 59, no. 5, pp. 1332-1345, May 2011.

[122] G. B. Giannakis and A. V. Dandawate, "Polyspectral analysis of (almost) cyclostationary signals: LPTV system identification and related applications", *Proc. 25th Asilomar Conf. Signals, Systems and Computers*, vol. 1, pp. 377-382, 4-6 Nov. 1991.

[123] A. S. Mehr and C. Tongwen, "Representations of linear periodically time-varying and multirate systems", *IEEE Trans. Signal Processing*, vol. 50, no. 9, pp. 2221-2229, Sep. 2002.

[124] W. Yin, **Identification of Linear Periodically Time-Varying (LPTV) Systems**, PhD thesis, University of Saskatchewan, 2009.

[125] L. A. Zadeh, "Frequency Analysis of Variable Networks", *Proc. of the IRE*, vol. 38, no. 3, pp. 291-299, Mar. 1950.

[126] S. Galli and A. Scaglione, "Discrete-Time Block Models for Transmission Line Channels: Static and Doubly Selective Cases", *Cornell University Library*, available online at http://arxiv.org/abs/1109.5382.

[127] A. Bjorck, **Numerical methods for Least Squares Problems**, Society for Industrial and Applied Mathematics, 1996.

[128] F. Gianaroli, F. Pancaldi and G. M. Vitetta, "The Impact of Statistical Noise Modelling on the Error Rate Performance of OFDM Powerline Communications", *submitted for publication on IEEE Trans. Commun.*

[129] T. Guzel, E. Ustunel, H. B. Celebi, H. Delic and K. Mihcak, "Noise Modeling and OFDM Receiver Design in Power-Line Communication", IEEE Trans. Power Del., vol. 26, no. 4, pp. 2735-2742, Oct. 2011.

[130] P. J. Huber, **Robust Statistics**, John Wiley & Sons, 1981.

[131] W. J. J. Rey, **Introduction to Robust and Quasi-Robust Statistical Methods**, Springer, 1983.

[132] F. Gianaroli, F. Pancaldi and G. M. Vitetta, "On the Use of Zadeh's Series Expansion for Modelling and Estimation of Broadband Indoor Powerline Channels", *submitted for publication on the IEEE Transactions on Power Delivery.*

[133] B. Adebisi, C. L. Giovaneli, B. Honary and M. Mowlavi, "Low Complexity Turbo Equalization for Power Line Communications", *Proc. IEEE Int. Symp. Power Line Communications and Its Applications* (ISPLC '07), pp. 385-389, 2007.

[134] T. C. Chuah, "Adaptive Robust Turbo Equalization for Power-Line Communications", *IEEE Trans. Power Del.*, vol. 22, no. 4, pp. 2172-2179, Oct. 2007.

[135] Y. H. Ng and T. C. Chuah, "Single-Carrier Cyclic Prefix-Assisted PLC Systems with Frequency-Domain Equalization for High-Data-Rate Transmission", *IEEE Trans. Power Del.*, vol. 25, no. 3, pp. 1450-1457, July 2010.

[136] K. Xie and J. Li, "Combating Impulsive Noise and ISI in Power Line Communication Systems", *Proc. IEEE 46th Annual Conference on Information Sciences and Systems* (CISS 2012), 2012.

[137] H. Lin, C. Lèlè and P. Siohan, "Equalization with Interference Cancellation for Hermitian Symmetric OFDM/OQAM Systems", *Proc. IEEE Int. Symp. Power Line Communications and Its Applications* (ISPLC '08), pp. 363-368, 2008.

[138] H. Kunishima, H. Koga, O. Muta and Y. Akaiwa, "Joint Use of Adaptive Equalization and Cyclic Noise Cancellation for Band-limited OQAM Based Multi-Carrier Transmission in Power-Line Communication Systems", *Proc. IEEE Int. Symp. Power Line Communications and Its Applications* (ISPLC '08), pp. 380-385, 2008.

[139] C. Luo, S. Cheng, L. Xiong, J. Nguimbis, Y. Zhang and J. Ma, "A Nonlinear Equalization Method Based on Multilayer Perceptron for OFDM Power-Line Communication", *IEEE Trans. Power Del.*, vol. 20, no. 4, pp. 2437-2442, Oct. 2005.

[140] M. Raugi and M. Tucci, "Power-Line Communications Channel Estimation and Tracking by a Competitive Neural Network", *IEEE Trans. Consumer Electronics*, vol. 52, no. 4, pp. 1213-1219, 2006.

[141] M. V. Ribeiro, "On Fuzzy-DFE-LMS and Fuzzy-DFE-RLS Algorithms to Equalize Power Line Channels", *Proc. IEEE Int. Symp. on Industrial Electronics* (ISIE '03), vol. 2, pp. 1001-1006, 2003.

[142] W. K. Wong and H. S. Lim, "An Extended Kalman Filter Based Fuzzy Adaptive Equalizer for Powerline Channel", *Proc. IEEE Int. Symp. Power Line Communications and Its Applications* (ISPLC '05), pp. 250-254, 2005.

[143] M. V. Ribeiro, M. B. Loiola and R. R. Lopes, "Turbo-Fuzzy Equalization for Single-Carrier Power Line Channels", *Proc. IEEE Int. Symp. Power Line Communications and Its Applications* (ISPLC '07), pp. 167-172, 2007.

[144] G. B. Giannakis, G. Zhou and M. K. Tsatsanis, "On Blind Channel Estimation with Periodic Misses and Equalization of Periodically Varying Channels", *Proc. IEEE 26th Asilomar Conference on Signals, Systems and Computers*, vol. 1, pp. 531-535, 1992.

[145] T. K. Moon and W. C. Stirling, **Mathematical methods and algorithms for signal processing**, Prentice Hall, 2000.

[146] G. H. Golub and C. F. Van Loan, **Matrix Computation**, Third Edition, The John Hopkins University Press, 1996.

[147] M. A. Tunc, E. Perrins and L. Lampe, "Reduced complexity LPTV-aware bit loading for channel adaptation in broadband PLC", *Proc. IEEE Int. Symp. Power Line Communications and Its Applications* (ISPLC '12), pp. 206 - 211, 2012.

[148] M. Nassar, J. Lin, Y. Mortazavi, A. Dabak, Il Han Kim, and B. L. Evans, "Local Utility Power Line Communications in the $3-500$ kHz Band", *IEEE Signal Processing Mag.*, pp. 116-127, Sep. 2012.

[149] N. Papandreou and T. Antonakopoulos, "Dynamic Bit-Loading in pDSL Communications Systems", *Proc. IEEE Int. Symp. Power Line Communications and Its Applications* (ISPLC '05), pp. 356 - 360, 2005.

[150] S. Morosi, D. Marabissi, E. Del Re, R. Fantacci and N. Del Santo, "A rate Adaptive Bit-Loading Algorithm for In-Building Power-Line Communications Based on DMT-Modulated Systems", *IEEE Trans. Power Del.*, vol. 21, no. 4, pp. 1892-1897, Oct. 2006.

[151] D. Jiang, "Optimal Bit Loading Algorithm for Power-Line Communication Systems subject to Individual Channel Power Constraints", *Proc. IEEE Int. Conf. Commun. Technology* (ICCT '06), pp. 1-4, 2006.

[152] T. Hayasaki, D. Umehara, S. Denno and M. Morikura, "A bit-Loaded OFDMA for in-home power line communications", *Proc. IEEE Int. Symp. Power Line Communications and Its Applications* (ISPLC '09), pp. 171 - 176, 2009.

[153] K. S. Al-Mawali, A. Z. Sadik and Z. M. Hussain, "Adaptive power loading for OFDM-based power line communications impaired by impulsive noise", *Proc. IEEE International Symposium on Power Line Communications and Its Applications* (ISPLC 2010), pp. 178-182, 2010.

[154] K. S. Al-Mawali, F. S. Al-Qahtani and Z. M. Hussain, "Simple discrete bit-loading for OFDM systems in power line communications", *Proc. IEEE International Symposium on Power Line Communications and Its Applications* (ISPLC 2011), pp. 267-270, 2011.

[155] M. Biagi, V. Polli and T. Patriarca, "Power-Constrained Physical-Layer Goodput Maximization for Broadband Power Line Communication Links", *IEEE Trans. Commun.*, vol. 59, no. 3, pp. 695-700, Mar. 2011.

[156] F. Gianaroli, F. Pancaldi, and G. M. Vitetta, "Channel Estimation and Equalization for OFDM Indoor Powerline Communications", submitted to the *IEEE Trans. On Communications*, December 2013.

[157] Honda, S.; Umehara, D.; Hayasaki, T.; Denno, S.; Morikura, M., "A fast bit loading algorithm synchronized with commercial power supply for in-home PLC systems," Power Line Communications and Its Applications, 2008. ISPLC 2008. IEEE International Symposium on , vol., no., pp.336,341, 2-4 April 2008

[158] Shin, J.; Jeong, J., "Improved Outage Probability of Indoor PLC System for Multiple Users Using Resource Allocation Algorithms" *IEEE Trans. on Power Delivery* , accepted for the inclusion in a future issue

[159] Canete, F.J.; Cortés, J.A.; Díez, L.; Entrambasaguas, J.T., "A channel model proposal for indoor power line communications," *IEEE Communications Magazine*, vol.49, no.12, pp.166,174, December 2011